The Time-Dependent Flow Through Throttle Valves: A Computational and Experimental Investigation

by

Raimond W Alsemgeest

A thesis submitted in fulfillment
of the requirements for the degree of

Doctor of Philosophy in Engineering

The University of Warwick, School of Engineering

September 2004

Dedication

This thesis is dedicated to the memory of

William Joseph Dunlop MBE OBE

(1952-2000)

Contents

List of Figures

List of Tables

Nomenclature

Roman Symbols

A	=	area (m^2); empirical constant; general matrix
$\mathbf{a}$	=	acceleration ($m\ s^{-2}$)
a_o	=	speed of sound at stagnation conditions ($m\ s^{-1}$)
a	=	speed of sound at measurement location ($m\ s^{-1}$)
B	=	empirical constant
$\mathbf{b}$	=	general matrix
C	=	constant
C_p	=	pressure-drop coefficient
C_{pi}, C_{pe}	=	inlet and exit wall-pressure coefficient
C_d	=	coefficient of discharge
C_v	=	specific heat of gas at constant volume ($J\ kg^{-1}\ K^{-1}$)
$C_{1\varepsilon}$, $C_{2\varepsilon}$, C_μ	=	k-ε model constants
D_1, D_2	=	contraction inlet and exit diameter (m)
d	=	diameter (m)
E_{ij}	=	mean rate of deformation
E	=	anemometer/bridge voltage (V);
		empirical coefficient describing wall roughness in (3.10)
E_{AC}, E_{DC}	=	ac and dc voltages (V)
E_{off}	=	offset voltage (V)
e	=	internal energy (J)
e_1, e_2	=	HWA Wheatstone bridge voltages (V)

$\mathbf{F}$ = force (N)

$F(z)$ = general analytical function

F_e = function of wall curvature

f_c = cutoff frequency (Hz)

f_x, f_y, f_z = body forces in x, y, z directions (N)

f_μ = k-ε model constant

G = amplifier gain

G_i = function of wall curvature

h = height of response curve in Figure 2.8 (V); wall roughness (m)

$\mathbf{i}$, $\mathbf{j}$, $\mathbf{k}$ = unit normals in x, y, z directions

i = grid point; current (A); complex variable

K = kurtosis in measurements

K_u = probe sensitivity (m s^{-1} V^{-1})

k = thermal conductivity (W m^{-1} K^{-1}); turbulent kinetic energy (m^2 s^{-2})

L = characteristic length (m); contraction length (m)

l = mean free path of molecules (m); mixing length (m)

M = molecular mass (kg mol^{-1})

m = mass (kg); ratio of diameters, D_1/D_2

$\dot{m}$ = mass flow rate (kg s^{-1})

N = frequency (Hz); number of cells; sample size of discretised HWA signal

n = power law exponent; curve matching exponent

$\hat{\mathbf{n}}$ = unit normal

P, p = pressure (Pa)

p_o = total pressure (Pa)

p^{new} = new pressure field for SIMPLE/PISO algorithms (Pa)

p' = pressure correction factor for SIMPLE/PISO algorithms (Pa)

p^* = estimated pressure field for SIMPLE/PISO algorithms (Pa)

q = flow rate (m^3 s^{-1})

R = resistance (Ω); gas constant (J kg^{-1} K^{-1})

R_L = leads resistance (Ω)

$R_u(i), R_u(t)$ = autocorrelation functions (m^2 s^{-2})

R_w = wire resistance (Ω)

r = radial distance from pipe centreline (m)

S = size of reference cell (m); skew in measurements

T = temperature (K)

T_f = resolved temporal scale (s)

Ti = turbulence intensity

T_t = modelled temporal scale (s)

t = time (s)

$\mathbf{U}$ = mean velocity vector (m s^{-1})

U, V, W = mean steady velocity components (m s^{-1})

U_∞ = free-stream velocity (m s^{-1})

U_{ideal} = ideal velocity (m s^{-1})

U_{c1}, U_{c2} = centreline velocity at contraction inlet and exit (m s^{-1})

U_{we}, U_{wi} = wall velocity maxima and minima (m s^{-1})

$\mathbf{u}$ = velocity vector of components u, v, w (m s^{-1})

u, v, w = velocity components in x, y, z directions (m s^{-1})

u_B, u_N, u_T = velocity components perpendicular, normal and parallel to hot-wire in Figure 2.6 (m s^{-1})

u_i = instantaneous velocity of discretised sample (m s^{-1})

u', v', w' = time-varying fluctuating components of velocity (m s^{-1})

u^+ = non-dimensional velocity

u_τ = velocity scale

u^*, v^*, w^* = estimated velocity field for SIMPLE/PISO algorithms (m s^{-1})

$\overline{u}$ = mean velocity (m s^{-1})

$\overline{u_i' u_j'}$ = Reynolds stresses

V = volume (m^3)

X = non-dimensional curve match point

$\mathbf{x}$ = general matrix

x, y, z = Cartesian coordinates (m)

y^+ = non-dimensional wall distance

Greek Symbols

α = throttle opening angle (°); hot-wire pitch angle (°)

α_p = pressure under-relaxation factor for SIMPLE/PISO algorithms

β = hot-wire yaw angle (°)

Γ = diffusion coefficient

γ = ratio of specific heats for air

Δt = time step (s)

Δp = static pressure difference/drop (Pa)

Δx = grid spacing (m)

δ_{ij} = Kronecker delta

ϵ_1, ϵ_2 = linearity and repeatability error

ε = turbulent dissipation rate ($m^2\ s^{-3}$)

θ = flat plate incidence angle (°)

κ = Kaŕmań constant

μ = molecular viscosity (kg $m^{-1}\ s^{-1}$)

$\mu_u(i), \mu_u(t)$ = time and ensemble average (m s^{-1})

μ_t = turbulent/eddy viscosity (kg $m^{-1}\ s^{-1}$)

ν = kinematic viscosity ($m^2\ s^{-1}$)

ξ = function of wall curvature

ρ = density (kg m^{-3})

ϱ = residual value

σ_u = standard deviation of HWA signal (m s^{-1})

$\sigma_\varepsilon, \sigma_k$ = k-ε model constants

τ_w = time (s) in Figure 2.8; wall shear stress

$\upsilon_d, \upsilon_c, \upsilon_d$ = design-stage, instrument, and zero-order uncertainty

Φ = dissipation function; mean steady component of a general fluid quantity

ϕ = general scalar quantity; velocity potential

ϕ' = time-varying fluctuating component of a general fluid quantity

$\boldsymbol{\phi}$ = general vector quantity; mean general quantity

ψ = stream function

Non-Dimensional Numbers

C = Courant number

Kn = Knudsen number

M = Mach number

Nu = Nusselt number

Pr = Prandtl number

Re = Reynolds number

St = Strouhal number

Abbreviations

CAD = computer aided design

CFD = computational fluid dynamics

CFL = Courant-Friedrichs-Lewy

CC = constant current (anemometer)

CCD = charge coupled device

CR = contraction ratio

CT = constant temperature (anemometer)

CV = control volume

D = throttle valve diameter

DAQ = data acquisition

DES = detached eddy simulation

DI	=	direct injection
DFT	=	discrete Fourier transform
DNS	=	direct numerical simulation
FFT	=	fast Fourier transform
HC	=	hydrocarbon
HWA	=	hot wire anemometry
ICE	=	internal combustion engine
ISO	=	International Organisation for Standardisation
LE	=	leading edge
LES	=	large eddy simulation
LDA	=	laser doppler anemometry
LRSFM	=	low Reynolds number and heat flux equations
MARS	=	monotone advection and reconstruction scheme
PCD	=	pitch circle diameter
PCV	=	positive crankcase ventilation
PISO	=	pressure implicit with splitting of operators
PIV	=	particle image velocimetry
PTFE	=	polytetrafluorethylene
QUICK	=	quadratic upstream interpolation for convective kinetics
RANS	=	Reynolds-averaged Navier-Stokes
RSM	=	Reynolds stress model
RSS	=	root sum squares
SGS	=	sub grid-scale
SI	=	spark ignition
SIMPLE	=	semi-implicit method for pressure-linked equations
SN	=	single normal (hot-wire probe)
SY	=	single yawed (hot-wire probe)
TE	=	trailing edge

TVD = total variation diminishing

URANS = unsteady RANS

VLES = very large eddy simulation

VRP = variable resistance pressure

WOT = wide open throttle

Acknowledgements

I would like to thank my supervisors, Chris Shaw, and Peter Carpenter, for their support and guidance throughout this investigation, and above all, for their patience. I would also like to thank Jaguar Cars for the opportunity to carry out this work, and for providing funding for the project. In particular, Steve Pierson and Steve Richardson, without whom much of this work would not have been possible.

Having thanked those that made the project possible, I would like to acknowledge those that made it happen; that is, of course, those in the same boat struggling to stay afloat. Firstly, I'd like to thank the "old-school CFD boys", Jason, Reza, Alex, and the godfather, Martin, who have always been on hand to share in the merriment along the way, and who have offered valuable advice and support in times of need. Warwick will never be quite the same without "Baby's got blue skies" echoing in the halls. The later additions to the group, Gianni, Rich, and Karen, and the honorary members, Pascal and Ross, have been equally supportive and inspirational, whereas Gianni's coffee has simply been mind-blowing.

I'd like to thank those outside the CFD bubble, particularly my house-mates who have sometimes taken the brunt of a bad day, and all those around me who have been a part of my life. Finally, Mum and Dad, thanks.

Declaration

I hereby declare that the work contained in this thesis is the authors own work. It has not been submitted for a degree at any other university.

Chapter 1

Introduction

1.1 Background Information

The automotive industry is, perhaps, and that is left open to debate, one of the most important engineering fields, and one which is increasingly influential on our everyday lives. Automotive engineering brings together all aspects of engineering knowledge to produce the one product that so many people have become dependent upon. The industry itself is vast and many tangents can be drawn from it, hence here we must define the area of interest to which this work relates. The initial concept for the work carried out stems from the passenger car industry; however, the work has more far-reaching benefits and implications.

As passenger vehicles become increasingly popular and increasingly advanced, so the need increases to understand more of the operation of all aspects of the vehicle. This work stems from a need to gain understanding of the flow of breather and blow-by gases within an internal combustion engine (ICE) with the long-term aim of fully understanding the processes involved to enable improved engine design and reduced pollutant production. The latter is a significant driving force as legislation becomes more strict on the level of pollutants emitted from vehicles and engines. This work therefore not only reflects on passenger vehicles, but any other industry or product that uses ICEs.

Here, the investigation is concerned with a (port) fuel-injected engine of V8 configuration as used in a production passenger vehicle. The two banks of cylinders defining

the 'V' of the engine are separated by an angle of 90° (known as the V-angle). Owing to space restrictions stipulated by the external shape of the car, the space between the cylinder banks is used to house the plenum that feeds air to the cylinders of the engine via the primary runners; the length of which has considerable effect on the state of tune of an engine owing to pressure wave effects (Heywood, 1988). As such the primary runners wrap around the plenum chamber to provide the necessary length for optimum engine tuning in this configuration. Figure 1.1 shows a schematic of the V8 engine used here, complete with plenum, intake, and breather systems.

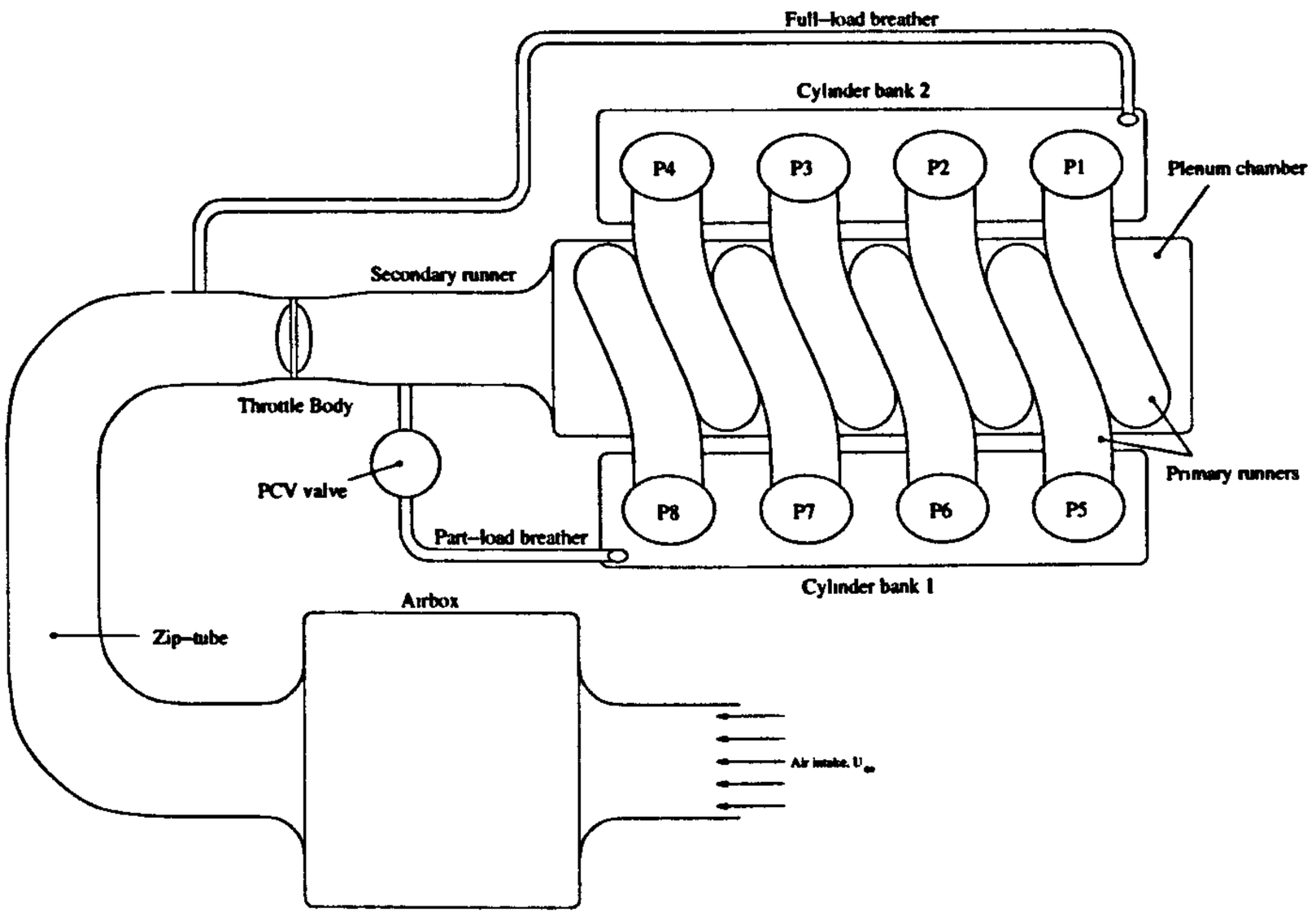

Figure 1.1: Schematic showing a V8 engine intake system incorporating air filtration system, throttle body, plenum chamber, plenum runners, cylinder banks and breather tubes. Not to scale.

Air is drawn through the throttle valve via the zip-tube and filtered air-box before entering the plenum chamber where the flow is split to feed each of the cylinders. Note that air is fed to two cylinders at a time owing to the timing of the engine, hence a pulsed flow is experienced. Internally, the V8 crankcase is sectioned into quarters such that opposite pistons from each bank are paired and use the same crankshaft weights, i.e. P1-P5, P2-P6, P3-P7, P4-P8. The lower section of the crankcase incorporates an oil sump which forms part of a splash lubrication system for the lower engine and brings

about the need for filtering the crankcase gases to remove the fine oil mist present. Also shown on the diagram are the breather system tubes which will be discussed in the following section.

1.2 Blow-By Gases and the Breather System

Blow-by gases are defined as combustion gases that leak past the pistons into the crankcase of a reciprocating engine during operation (Heywood, 1988). Once within the crankcase volume these gases mix with the fine oil spray produced by the motion of the engine. Legislation prohibits these combustion products from being vented to atmosphere directly, rather they must be re-introduced into the engine to be re-burnt in the combustion process. In order to facilitate this, the crankcase volume is kept at a negative relative pressure (to atmosphere) such that should a leak occur, air is drawn into, as opposed to forced out of, the crankcase, and a breather system is incorporated into the system to feed the gases (i.e. breather gases) back into the intake system (see Figure 1.1.

During the compression and expansion stroke of an engine cycle, where operational pressures are at their highest, fuel-air and combustion gases leak past the piston and enter the crankcase volume. Here they mix with the fine oil spray generated by the splash lubrication system of the engine, and through the general action of the engine itself. Hence air-oil separators are incorporated into the breather system to filter out the oil from the mixture, as allowing it to pass into the combustion process leads to further pollution in addition to contamination of intake components.

The breather system operates by purging the crankcase of blow-by gases with fresh air from the intake system. As air flows through the throttle valve a pressure differential is generated across the valve blade and this pressure gradient is used to drive the flow through the breather system. Downstream of the valve, the part-load breather experiences a low pressure whereas the full-load breather situated upstream of the valve experiences a high pressure thus driving clean air though the crankcase and reintroducing the filtered blow-by gases downstream of the valve. A PCV (positive crankcase

ventilation) valve is present within the part-load breather that ensures the flow throughout the breather system is in one direction (Krause, Spies, Bell & Ebert, 1995). At wide open throttle (WOT) conditions this no longer holds true as the pressure differential across the valve diminishes significantly or entirely; thus there is no driving force to purge the crankcase. Under WOT conditions, the blow-by gases build up the pressure within the crankcase volume therefore forcing reversed flow through the full-load breather (hence the terminology) (Jaguar Cars Ltd., 1999). This is an undesired effect, as contamination of the valve can occur and the crankcase is no longer being purged of its gases.

The increasing number of cars on the road, and the increasing concerns over pollution and the environment have meant that legislation on pollutant emissions has tightened and will continue to do so in the future (Schäfer & van Basshuysen, 1995). Therefore improvements need to be made to many aspects of an engine in order to reduce overall emissions. The reduction of blow-by gases, and the understanding of the flow of these gases through the engine is just one step in improving the overall product.

1.3 Computational Predictions

Not only have vehicles and engines become more advanced, but so too have the methods of analysis, design and testing increased in complexity, accuracy and speed; in fact to a higher degree than the vehicles. Arguably, the main driving force for these methods is the ever-increasing performance of computer technology and the reduction of computing costs. Computers are now used in every aspect in the creation, analysis, and use of a vehicle and engine through use of embedded systems, control systems, simulations, design tools, data analysis, information exchange, and so forth. Analysis tools are of interest here, with particular interest in the use of computers to predict fluid flows, i.e. computational fluid dynamics, or CFD.

CFD has become a far more cost-effective analysis tool over the last decade leading to increased usage of CFD for flow predictions by many engineering sectors and companies as opposed to the almost purely academic status it acquired in the past. Increased

usage of CFD within the industry is allowing it to become an established design tool for product evaluation and testing, alongside increasing the overall knowledge base for reference. Care is needed, however, to ensure that the predictions generated represent physically correct flows, preferably through use of some experimental procedures. Only when sufficient comparisons have been made for a particular flow should computational results be trusted, and even then one should scrutinise the results carefully.

Here, CFD has been used to investigate unknown flow phenomena alongside the use of experimental methods to validate and verify the predictions obtained. Although CFD is being used as a design tool, its use alone to develop a product is still questionable, as the predictions obtained depend on many factors and can easily produce incorrect and non-physical flows. As such, experimental validation of CFD results is still required, in particular where experimental investigations have not been previously carried out. Within industry, validation of results, let alone full verification, is not always possible and previous work or external data must be relied upon. The terms validation, verification, and calibration will be discussed in subsection 2.5.

Here a commercial CFD package is used that allows modelling of practically any fluid flow in three dimensions, including compressible flows, transient flows, turbulent flows and heated flows. The code used is STAR-CD v3150 (Computational Dynamics Ltd., 2001) which includes its own pre-processing and post-processing program PROSTAR, thus allowing for the majority of operations to be carried out in one environment. However, discretisation of the computational domain is taken care of using the grid-generation package ICEM-Tetra (ICEM CFD Engineering, 1998) which creates tetrahedral grids using an octree method (George, 1991).

1.4 Experimental Measurements

CFD predictions alone are inadequate to analyse a flow unless the models used have been calibrated specifically for a particular application. It is very easy to generate physically incorrect flows using CFD simulations that look plausible. Poor predictions can be a result of any number of possibilities including poor conceptual modelling, poorly

defined boundaries and domains for the flow in question, and inappropriate application of modelling techniques. To ensure that the predictions represent reality the CFD models should be validated, and this is normally achieved through comparison with experimental measurements of similar flows. This should highlight any poor modelling assumptions and limitations of the models.

Here a flow-rig has been designed and built for the sole purpose of validating the computational predictions. Measurements of the physical flow though a throttle body have been made using a hot-wire anemometer and these have been compared to the predictions.

1.5 Aims

With the increasing need to reduce pollution levels and produce more efficient engines, devices such as the crankcase breather are becoming more important. The interaction of different engine components therefore becomes increasingly relevant in evaluation of total engine performance. This investigation aims to increase understanding of the flows through a throttle valve by investigating the detailed characteristics of flow through a throttle valve at various opening angles and flow rates using computational predictions. The use of CFD to model such flows will be validated using experimental measurements. The outcome of the investigation may yield insight into the use of computational methods as a tool for engine design.

1.6 Objectives

The main objectives of this investigation are:

- To predict the flow through throttle valves at a range of opening angles using a commercial CFD code.
- To investigate the flow through a throttle valve using experimental techniques.
- To compare the results of the physical experiments to the computational predictions.

- To assess the limitations of the computational methods as a design tool.

1.7 Document Layout

Chapter 2 discusses blow-by gases and breather systems in more detail along with their influence on pollution and legislation. Previous numerical and experimental investigations of flows similar to those considered here are discussed, followed by details of the modelling and measurement techniques used.

Following on, chapter 3 is devoted to the computational simulations carried out. This first introduces the problem and describes the implementation of the models and methods used throughout. This is followed by a presentation of key results and a discussion thereof.

Chapters 4 and 5 describe the experimental equipment and techniques used in the experimental investigation. The former describes the design and building of the flow rig used to carry out the experiments. The latter first describes the methods used to investigate the flow and then presents the findings of the investigation before subsequent analysis and discussion.

Comparisons between the computational and experimental findings and discussion thereof are presented in chapter 6 with concluding remarks and suggestions for further work following in chapter 7. Appendices are given at the end of the document, followed by the bibliography.

Chapter 2

Literature Review

2.1 Introduction

This chapter gives a brief insight into the methods and techniques used within this investigation, and reviews some of the previous work carried out in related fields. The chapter first introduces some work and information on engines and their operation with relevant links to the current work. Experimental methods are then introduced followed by detail on computational methods. Finally the hot-wire method is discussed is some detail owing to its use here.

2.2 Internal Combustion Engines and Pollution

2.2.1 Transport Trends and Air Pollution

The main role of the internal combustion engine is as a power-plant for applications such as automobiles, other vehicles, pumps, and power-generation equipment. Perhaps their most common role is as the power-plant for the automobile that forms part of the everyday life for millions of people around the world. Every year an increasing number of road vehicles are produced leading to greater freedom for a wider population; however, this is accompanied by a less welcome increase in congestion and pollution; particularly air and noise pollution.

Over the past two decades, motor vehicle production in the UK alone has seen a

20% increase in volume[1,2] and although a proportion of these vehicles are exported abroad, there are increasing numbers of new vehicle registrations on Britain's roads each year[2,3,4]. In addition, the number of licensed cars on Britain's roads has increased on a yearly basis alongside new vehicle registrations. Thus the number of new vehicles introduced outweighs those scrapped with approximately 45% of household cars over 7 years of age[4,5]. Other vehicles have also shown an increase in new registrations. For example, motorcycles have shown a doubling of registrations over the last 5 years, small goods vehicles have quadrupled registrations over the last ten years, and the net total vehicle registrations over the last decade has shown an approximate 40% increase from 85,000 vehicle registrations in 1990 to approximately 120,000 registrations in 2000[2]. People are becoming more dependent on their cars for general transport, as reflected by an increase in the percentage of households with two or more cars over the past two decades, whilst a drop in the number of households with no car is seen over the same period[1]. At the same time the distance covered by motorised vehicular traffic is steadily increasing and a trend towards private transport over public transport is also apparent[4], see Figure 2.1 and Figure 2.2.

With the ever-increasing number of motorised vehicles, concern is being aired over the levels of congestion and pollution produced by these vehicles, and also of pollution from other energy sources. The combustion process, i.e. the burning of the fuel-air mixture within the cylinder, generates polluting by-products that are exhausted to atmosphere. It is these pollutants that are the main cause for concern, leading to increasingly strict legislation governing the level emissions. Fuel used in internal combustion engines contains hydrocarbons that, under stoichiometric combustion (i.e. theoretical or complete combustion where sufficient oxygen is available), oxidize completely to produce only water, carbon dioxide, and sulphur dioxide (i.e. C$\Leftrightarrow$$CO_2$, H$\Leftrightarrow$$H_2O$, and

[1]Data sourced from footnotes 2-5 have been gathered from the Office of National Statistics (http://www.statistics.gov.uk). Details of sources can be found in appendix A.
[2]Department of Environment (DOE).
[3]Annual vehicle census / vehicle information database (DVLA).
[4]Department of transport, local government and the regions (DTLR).
[5]National travel survey (NTS).

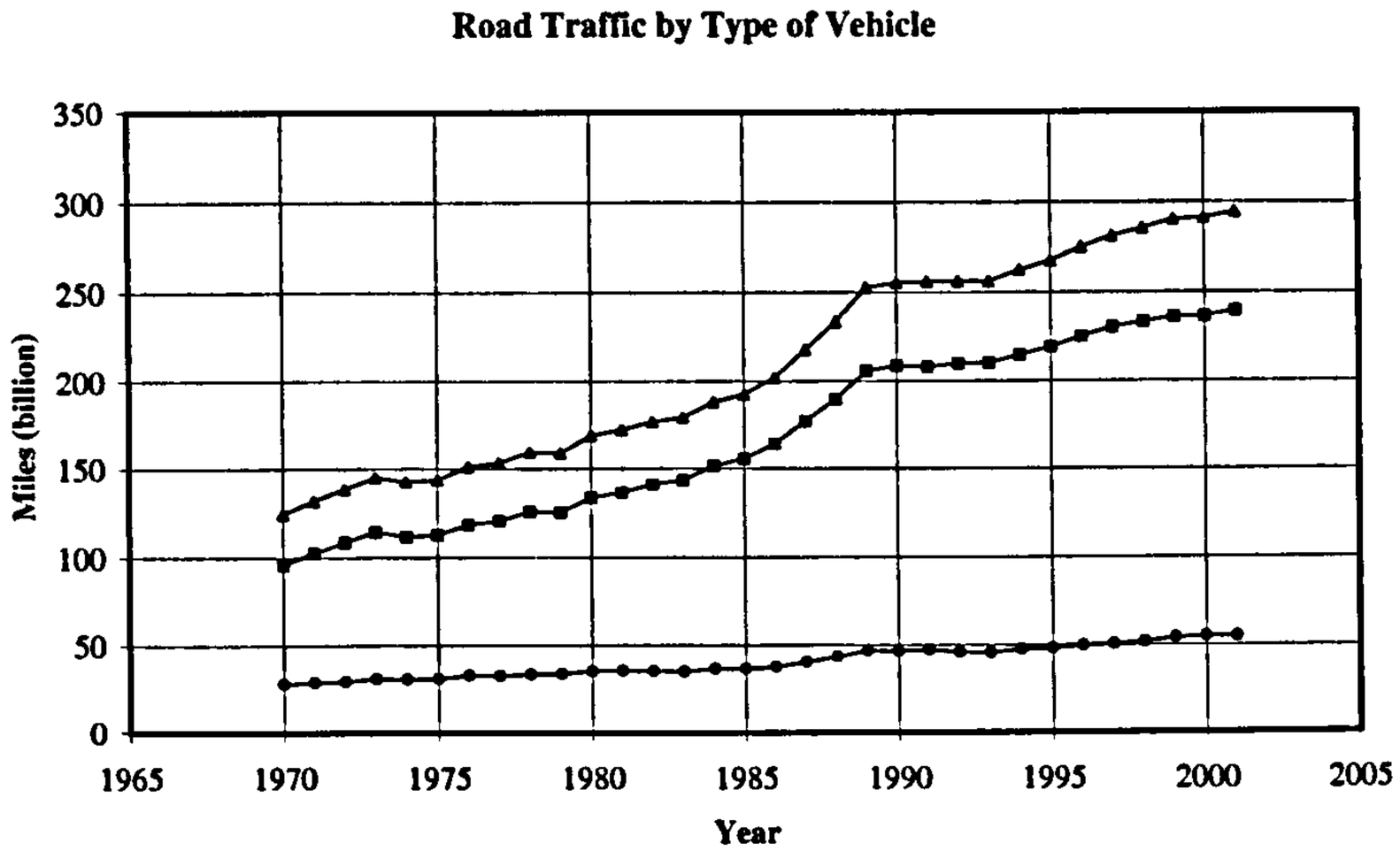

Figure 2.1: Graph illustrating the increase in the number of miles travelled by passenger vehicles within Great Britain in the period 1970-2001. ■ cars and taxis; • other vehicles; ▲ all vehicles. Data obtained from the DTLR[4].

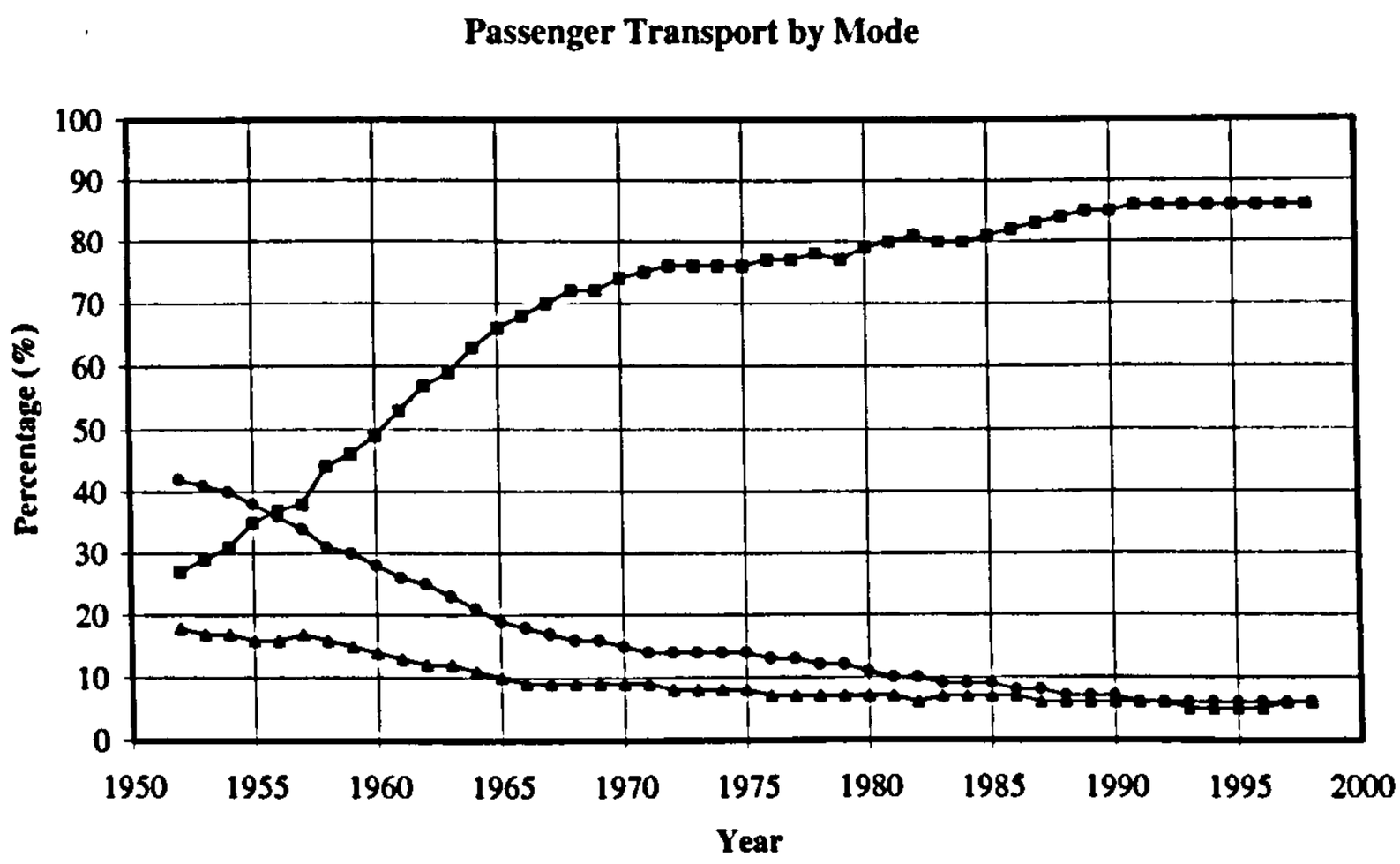

Figure 2.2: Graph illustrating the increase in dependence on private transport and the decline in use of public transport from 1952-1998 within Great Britain. ■ cars, vans and taxis; • buses and coaches; ▲ rail. Data obtained from the DTLR[4].

S⇔SO_2). However, many hydrocarbons contain additional oxygen that produces by-products when combusted (Schäfer & van Basshuysen, 1995) and it is these products that most governments of developed countries are particularly trying to lower in order to reduce overall pollution levels. In addition, as combustion is never ideal, a certain percentage of unburned mixture remains after combustion. For spark ignition (SI) engines this is typically 20 percent at light loads and 7 percent at full load (Heywood, 1988).

Many of the combustion products exhausted from an engine are harmful to life, and as such legislation by the EU (European Union) has limited the output of some of the exhaust products, namely:

- carbon monoxide (CO),
- unburned hydrocarbons (HC), e.g. benzapyrene and benzene; and
- nitrogen oxides (NO_x), a combination of nitrogen oxide, NO, and nitrogen dioxide, NO_2, with NO being dominant.

In addition to these legally limited substances, some further important pollutants contained within exhaust gases are, lead compounds (Pb), sulphur dioxide (SO_2), aldehydes (H-C-O compounds), particulates (including soot and smoke), and carbon dioxide (CO_2). Schäfer & van Basshuysen (1995) give an excellent account of the effects of these pollutants on the human body and the atmosphere, and also discuss in detail the generation of pollutants from a chemical viewpoint. Baruah (1986) also discusses the formation of these pollutants within SI engines and Abbass, Andrews, Bartle & Williams (1989) discuss hydrocarbons in direct-injection diesel engines.

Legislation put into place over the last few decades has had a considerable effect on the environment and future targets for air pollution are becoming more strict. The introduction of unleaded petrol in the mid eighties and the subsequent abolishment of leaded motor fuels in the late nineties has had considerable effect on the levels of lead in the environment. By 1999 the lead emission from road transport in the atmosphere

had dropped to 95% of the level of 1970 (from 6,363 to 327 tonnes with a peak in 1973 at 8,280 tonnes)[6]. Similar trends are also reported for other key pollutants of the combustion process, with carbon monoxide (CO), benzene, benzapyrene and nitrogen oxides (NO_x) all showing a reduction in the period 1970-1999[6]. Levels of carbon dioxide (CO_2) emissions from transport has, however, increased 100% in the same period, while CO_2 emissions from other sources show a decrease over the same period.

Similar trends to those described above are also reported by the Environment Agency whose findings have shown that in urban areas the number of days when air pollution is moderate to high has reduced over the last five years to such an extent that rural areas now experience more frequent high pollution levels[7]. A study by Booker (2000) has shown that the build up of particulates in urban areas increases dramatically with vehicle speed and traffic congestion levels. The same study looked at exposure levels of pollutants when cycling and driving into an urban environment. The studies showed that a cyclist is exposed to far higher levels of particulates than a driver of a modern car, i.e. the filtration systems in modern automobiles function exceptionally well. However, the emphasis of car design is not to improve the filtering systems so much as reducing the levels of pollutants produced in the first place.

Pollutant reduction can take many forms, from use of catalytic converters, specific fuel types, state of engine tune, reduced weight, improved aerodynamics, among other methods. One of the simple ways of reducing emissions is through use of a crankcase breather system which is now compulsory equipment on any new vehicle. Such systems eliminate the emission to atmosphere of the gases that reside within the crankcase by recycling them through the engine. Such systems form the basis of this investigation and are discussed in subsection 2.2.2.

[6]DEFRA (Department for environment, food and rural affairs, from the UK national air quality information archive (based on estimated figures). See appendix A.

[7]Environment Agency.

2.2.2 Breather Systems and Blow-By Gases

Blow-by gases contain a mixture of unburnt fuel mixture, burnt HCs, and engine oil. The proportion of these components and the overall level of blow-by depend on engine operating conditions, engine design, the level of engine wear, and engine temperature. Perhaps the most influential factor on the level of blow-by produced is the design and layout of the piston, piston rings, and cylinder of the engine, as this is the primary source of blow-by (other sources include the leakage of gas past valve guides). Figure 2.3 shows a basic schematic layout of the piston and ring assembly in relation to the cylinder wall.

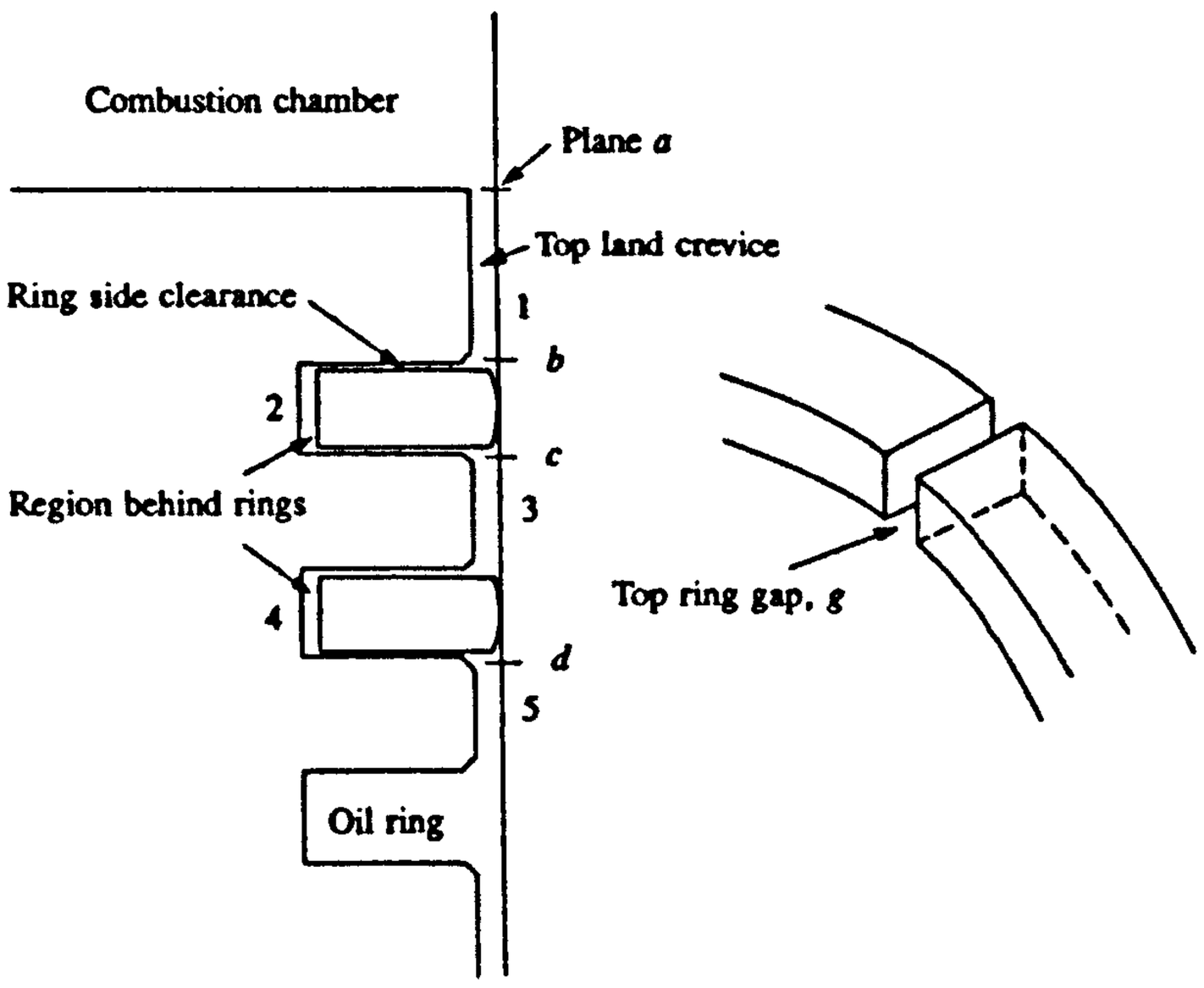

Figure 2.3: Schematic showing piston and ring assembly for a spark-ignition engine. Taken from Heywood (1988).

Figure 2.3 shows the main crevice volumes within the cylinder that are exposed to combustion, and the gaps present around the piston rings. Of all the crevice volumes present, the top land crevice is by far the largest (based on cold engine measurements (Heywood, 1988)), and its size affects the level of HC emissions produced by an engine. Although this is the largest of the crevice volumes, it has only a limited effect on the

level of HCs entering the crankcase via blow-by. Wentworth (1968) suggests that by removing the top land crevice, a 47 to 74 percent reduction of unburnt HCs within the cylinder volume is possible. Namazian & Heywood (1982) also show this but note that although there is a reduction in HCs returning to the cylinder, there is no effect on the level of HCs passed to the crankcase via blow-by. Blow-by levels are more significantly affected by the size of the gap behind the rings, and the ring gaps, with larger volumes and gaps leading to higher blow-by and a larger return of HCs to the cylinder. Each of these volumes undergoes considerable change throughout the engine cycle owing to the motion of the piston and the massive pressure differences that occur during the cycle (approximately 2000 kPa for SI engines (Heywood, 1988)). Motion of the piston and rings is studied numerically by Herbst & Priebsch (2000) who analyse the effects of the motion on the level of oil consumption in an engine. Their study briefly looks at the effect of altering the piston ring shape and ring-gap on the motion of the rings and finds this has significant effect on the blow-by produced.

Shayler, Winborn & Scarisbrick (2000) investigate the cold-start conditions on the level of blow-by and HC emissions from an engine. The levels of hydrocarbons in the breather system of an engine was studied and the source of these investigated. As well as blow-by, a further source of HCs in the breather is the desorption of fuel from the sump oil. However, their findings show that this accounts for only a small amount of the HCs with blow-by responsible for the bulk of HC content. The absorption properties of the sump oil were found to reduce with increasing temperature, and hence this leads to a higher concentration of hydrocarbons in the breather flow than for a cold engine where the oil is able to more efficiently absorb the gases (typically 85% absorption efficiency for cold oil versus 5% for hot oil). The fact that the oil is able to absorb the gases increases the need for their removal in order to prevent excessive contamination of the oil and sludge formation (Dhariwal, 1997).

A fine oil mist is generated in the crankcase through the motion of the crank and any of this oil mist escaping through the breather system enters the combustion chamber. Oil entering the combustion chamber does not fully combust hence leading to increases

in the levels of hydrocarbons and particulates that leave the exhaust system (Krause et al., 1995). This has lead to the development and analysis of increasingly effective filtering systems to remove the oil mist from the breather gases, including active systems (Koch, Hardt & Haubner, 2001), and methods of prediction (Satoh, Kawai, Ishikawa & Matsuoka, 2000).

The content of the breather and blow-by gases also leads to problems with their measurement. Ebner & Jaschek (1998) have investigated blow-by flow-rate meters and note that conventional measurement equipment can seldom be used for measurement of blow-by gases owing to their composition and the risk of contamination. Here contamination is also a concern owing to the blow-by gases being fed through the throttle body under WOT conditions. As the breather system inlet and outlet are situated to either side of the throttle valve, it is clear that the throttle plays an important role in driving the flow through the breather system, and hence its study is warranted. Several authors have previously studied such flows, but many of these investigations have been limited to specific areas of interest that do not highlight the main flow structures. Some of these investigations are described below.

2.3 Fluid Flows

2.3.1 Butterfly Valve Flows

The throttle body used in this investigation is essentially a butterfly valve used to control the airflow into the engine. Butterfly valves have been used as a flow controller for a long time and are used in a wide variety of applications. They are typically used for industrial applications to control the flow of liquids on a large scale. The butterfly valve is a popular choice for flow control applications owing to its simplicity, low cost, low weight and good flow characteristics. When fully opened, the butterfly valve offers very little flow resistance and also offers a full range of movement to a fully sealed position (Danbon & Solliec, 2000; Eom, 1988; Kimura, Tanaka, Fujimoto & Ogawa, 1995).

For the majority of industrial applications the performance of the butterfly valve

is evaluated through the pressure-loss coefficient which is typically the pressure drop across the valve non-dimensionalised by the dynamic pressure of the upstream flow, i.e. $C_p = \Delta p / \left({}^1/_2 \rho U_\infty^2\right)$ as used by Cohn (1951), Eom (1988), and Kimura et al. (1995). Investigations into the pressure loss characteristics of the valve by these authors have shown a considerable reduction in pressure drop at the full open positions owing to the negligible pressure drop across the valve. The findings show that losses remain low for approximately 30° before the losses rise and become significant.

The shape of the valve has been found to have only minimal effect on the level of pressure losses found. Typically, variation of the pressure loss with valve shape is most notable in the middle of the valve-opening range. In this region, a valve with its pivot blended into the blade and thin tips provides the least losses whilst the worst performers are valves with a thick blade or an asymmetric valve (Cohn, 1951). Kimura et al. (1995) also study the shape of the pivot on the performance of a slender valve and show that a round pivot (as used here) shows almost double the pressure loss at full opening than a valve with a more square pivot or no pivot. A pivot that is waisted in the centre of the valve also reduces losses as less blockage is presented to the oncoming flow. Away from the fully open positions, the different pivot shapes make little difference to the losses.

Valve shape is investigated by Morris & Dutton (1989*a*) in order to establish the effect on torque load on a valve in a compressible flow field. The study evaluates a 2D symmetric circular arc disc (an elliptic cross section with sharp edges) and a flat valve with tapered ends at various angles of inclination. Their main findings indicate that the separation and re-attachment of the flow on the valve has significant effects on the torque loading of the valve owing to the large changes in pressure distribution. Each shape shows positive results depending on the opening angle, for example, at the fully open position the circular arc valve shows no loading, while the flat valve showed flow separation leading to a closing torque acting on the valve. Further effects of the compressible flows around butterfly valves are considered by Addy, Morris & Dutton (1985), Morris (1987), and Morris & Dutton (1989*b*).

The torque loading of valves is also investigated by Solliec & Danbon (1999), and

in a subsequent paper (Danbon & Solliec, 2000), where the effect of an upstream elbow is considered on the torque loading. These studies are of use for large-scale industrial applications where the torque loading on the valve places additional load on the valve actuators that can be very expensive. In a similar manner to the pressure-loss coefficient, the aerodynamic torque on the valve is characterised by a non-dimensional coefficient that usually uses the static pressure drop across the valve for normalisation. The authors note that the pressure drop is easily obtained for the ideal situation where the valve is between lengths of straight pipe, but that in most applications the valve is typically placed near to storage tanks, elbows, pumps and other critical areas that affect the pressure drop across the valve (Solliec & Danbon, 1999). As such they devise a new torque coefficient using the dynamic pressure as a normalisation factor and show that the new coefficient is more representative of the actual torque loading on the valve with minimal variation owing to different pipe configurations. The overall findings of the papers suggest that the mean torque on the valve is not affected by the elbow, but significant changes to the flow structure occur including increased buffeting.

Morris & Dutton (1991) have also looked at the torque characteristics of a valve downstream of an elbow and show greater variation than the work of Danbon & Solliec (2000). However, they use the standard torque coefficient that was shown by Danbon & Solliec (2000) to give greater variations in values. In addition there are geometric differences in the valve and pipes of the two investigations. Their findings also indicate that greater variation in performance is found with a valve close to the elbow, and that these variations are largely suppressed by placing the valve approximately eight diameters downstream of the elbow.

Numerical investigations into the flow through butterfly valves have also been focused on specific applications and have been limited to steady-state simulations. These do, however, offer an insight into the flow fields around the valve that are lacking in many of the previously discussed works. Lacor & Hirsch (1988) have investigated the flow in proximity to a butterfly valve using the Euler equations. The computational domain comprises of a wedge-shaped valve in a circular tube that extends ten diameters

upstream and downstream of the valve; however, only half the domain is modelled by making use of the valve symmetry. Results are presented for a valve inclination of 30° to the fully opened position for two different flow-rates. The results show the presence of vortex sheets emanating from the valve tips with a total pressure loss occurring across each. Downstream of the valve the flow is predicted to be highly rotational with a large vortex rolling up in the half of the domain that entrains the vortex sheets. Comparison of the results to previous experimental work shows that the inviscid calculations are able to correctly predict the operating point of the valve, i.e. the pressure drop for a given mass-flow rate.

Huang & Kim (1996) have investigated the three-dimensional incompressible flow around a flat-plate-style butterfly valve for a range of opening angles using steady-state simulations. The simulations are carried out using a grid of approximately 13000 cells with the domain extending 2D upstream and 8D downstream of the valve. A Reynolds–Averaged Navier–Stokes (RANS) modelling approach has been used with the k-ε turbulence model to model the turbulent features of the flow. The results of the simulations reveal similar separation from the valve tips as found by Lacor & Hirsch (1988); however, although the large axial vortices downstream of the valve have been predicted, they are less well established. Flow in the wake of the valve is studied for the range of angles and reveals recirculation behind the valve. However, it fails to capture any fine detail of the flows. Comparison of the pressure-loss coefficient to experimental values show the predictions to be fairly accurate. Some of the shortcomings of the investigation are acknowledged by the authors to be as a result of the limitations of the computer resources.

Chen & Chen (1995) have performed a numerical investigation into the flow through a throttle body at idle conditions, i.e. at very small valve openings. The study assumes a steady-state compressible flow and only half the domain is modelled with a symmetry plane used to reflect this. Both the standard k-ε and the k-ε-RNG turbulence models have been used in the prediction, the latter intended to improve the findings. However, their findings show no significant differences between the two models and hence the

k-ε models were presented. The study is more concerned with the flow rate through the valve at these small openings with loose- and tight-fitting valves, as opposed to any general flow features. A considerable difference in flow rate was observed with approximately 5 times the flow rate for a loose-fitting valve than a tight valve; the corresponding flow areas being an approximate 2:1 ratio. Such a change can have significant effects on the fuelling of an idling engine.

2.3.2 Bluff-Body Flows and Unsteady Flows

Flow through a throttle valve is essentially a confined bluff-body flow, and there are some similarities with general bluff-body flows that will be discussed. An obvious analogy of the throttle valve is the flow over an inclined flat plate, that has been studied extensively in the past. Flows over an inclined flat plate separate at the leading and trailing edges thus generating vortex sheets in a similar manner to that discussed above for valve flows. Such vortex streets can roll up into spirals and subsequently form circular vortices (Saffman & Baker, 1979). However, although this is true in a two-dimensional sense, a three-dimensional flow presents a much more complicated flow interaction. In general, the separated flow over an inclined flat plate does become unsteady and vortex shedding occurs in a form similar to a von Kármán vortex street. However, a vortex street does not have to be associated with vortex shedding from a body and may be a consequence of an unstable wake velocity profile as is shown by Tritton (1988) for the flow behind a flat plate parallel to the flow direction.

Studies by Abernathy (1962) evaluate the flow over inclined flat plates over a range of incidence angles and a range of flow constrictions. He uses a small-scale wind tunnel to perform tests and shows that vortex shedding from the valve remains even with a higher constriction. These findings are discussed in later chapters. Interestingly the findings show that the separation of the free shear layers from the leading and trailing edges of the valve are independent of the level of constriction. However, the highest constriction of the study falls far short of that of a throttle valve.

Flow past bluff bodies almost always results in some degree of unsteady wake, usually

in the form of vortex shedding owing to instability of the flows (Tritton, 1988). This vortex shedding is exploited in vortex flow-meters where the flow-rate in a pipe is found by indirect measurements of the vortex shedding from a bluff body (Igarashi, 1999). In an investigation to improve the standard vortex shedder used in a vortex meter, Igarashi (1999) shows that for a large blockage ratio (>50%), the vortex shedding is suppressed owing to the jetting of the flow between the vortex shedder and the walls of the domain. Abernathy (1962), however, shows that the vortex shedding continues for higher blockage ratios.

The vortices shed in the wake of a bluff body flow extend far downstream and maintain a high degree of interaction (Prasad & Williamson, 1997; Williamson, 1996). Many flows show this behavior, from the vortex shedding of a circular cylinder, to that behind a square cylinder. Although not reported in the findings above, it is likely that the wake of the throttle valve will exhibit unsteady effects that may influence the performance of the valve, and the engine to which it is attached.

It is clear from the above findings that flow behind the butterfly valve and other bluff bodies is highly complex and turbulent and that this is of importance in engine intake design as this has immediate effects on the flow entering the plenum system. The study here hopes to model the flows through the valve and highlight the flow structures of interest, and validate these through experimental measurements. The flows in either case are described by the governing equations of fluid flow which are now presented.

2.4 The Governing Equations of Fluid Dynamics

The governing equations are mathematical statements of the fundamental physical principles that apply to all fluid flows, namely the conservation of mass, Newton's second law, and the conservation of energy. These equations describe the fluid flows discussed above and any other flow of a Newtonian fluid and are used by the computational methods outlined in the later sections.

2.4.1 The Continuity Equation

The physical principle behind the continuity equation is that for a given control volume the mass is conserved through the volume. So for an individual fluid element the rate of increase of mass in the element is equal to the net rate of flow of mass into the element (Versteeg & Malalasekera, 1995). By considering an individual control volume fixed in space, and evaluating the individual components of velocity passing through the volume, the conservation form of the mass continuity equation can be derived as,

$$\frac{\partial \rho}{\partial t} + \nabla \cdot (\rho \mathbf{u}) = 0, \tag{2.1}$$

where ρ is the density, t is time, and the velocity is given by $\mathbf{u} = (u\mathbf{i} + v\mathbf{j} + w\mathbf{k})$ (Anderson, 2000).

2.4.2 The Momentum Equations

The momentum equations are based on Newton's second law of motion, i.e. the rate of change of momentum is equal to the sum of forces acting on a volume of fluid, or $\mathbf{F} = m\mathbf{a}$. For a given flow, the forces acting on the fluid particles are a combination of surface forces and body forces. Surface forces are typically represented as individual terms in the equations whilst the body forces are usually incorporated as source terms (Anderson, 2000; Versteeg & Malalasekera, 1995). Again consideration of a stationary control volume in a flow yields the conservative form of the momentum equations in the x, y, and z directions for Newtonian fluids,

$$\frac{\partial(\rho u)}{\partial t} + \nabla \cdot (\rho u \mathbf{u}) = -\frac{\partial p}{\partial x} + \nabla \cdot (\mu \nabla u) + f_x, \tag{2.2}$$

$$\frac{\partial(\rho v)}{\partial t} + \nabla \cdot (\rho v \mathbf{u}) = -\frac{\partial p}{\partial y} + \nabla \cdot (\mu \nabla v) + f_y, \tag{2.3}$$

$$\frac{\partial(\rho w)}{\partial t} + \nabla \cdot (\rho w \mathbf{u}) = -\frac{\partial p}{\partial z} + \nabla \cdot (\mu \nabla w) + f_z, \tag{2.4}$$

where μ is the dynamic viscosity of the fluid, and f are the body forces acting on the fluid. These are more commonly termed the Navier–Stokes equations for Newtonian

fluids, so named in honour of the Frenchman, M. Navier, and the Englishman, G. Stokes, who independently obtained the equations in the first half of the nineteenth century (Anderson, 2000).

2.4.3 The Energy Equation

The final governing equation describing fluid flows is the energy equation which is based on the principle that energy is conserved within a fluid. This is the first law of thermodynamics which states that the rate of change of energy of a fluid particle is equal to the rate of heat addition to the fluid particle plus the rate of work done on the particle (Versteeg & Malalasekera, 1995). Thus for a stationary control volume the conservative form of the energy equation is given as,

$$\frac{\partial(\rho e)}{\partial t} + \nabla \cdot (\rho e \mathbf{u}) = -p\nabla \cdot \mathbf{u} + \nabla \cdot (k\nabla T) + \Phi + f_e, \tag{2.5}$$

where e represents the internal energy, T is the fluid temperature, k is the thermal conductivity, and Φ is the dissipation function that represents the rate at which kinetic energy is converted into internal energy by viscous effects.

2.4.4 Equations of State

The partial differential equations (2.1) to (2.5) represent the governing equations of fluid flow. Observation shows that for the five equations, there are seven unknown quantities, ρ, p, u, v, w, e, T, and hence the set of equations is not closed. In order to close the set of equations, the equation of state is defined as,

$$p = p(\rho, T), \tag{2.6}$$

which for a perfect gas is described in chapter 3. A final equation is used to close the set of equations which is the thermodynamic relationship between the state variables,

$$e = e(T, p), \tag{2.7}$$

which for a calorically perfect gas the relationship is given as,

$$e = C_v T, \tag{2.8}$$

where C_v is specific heat of the gas at constant volume (Anderson, 2000).

Historically the momentum equations for a viscous flow, i.e. equations (2.2) through (2.4) have been termed the Navier–Stokes equations. However, it is common, particularly for numerical simulations, for the Navier–Stokes terminology to include the entire set of equations (2.1) through (2.5), leading to the terminology of a "Navier–Stokes solution". Computational modelling of flows using these fundamental equations is now discussed.

2.5 Computational Modelling of Fluid Flows

2.5.1 Zero and One-Dimensional Modelling

These modelling techniques are often used in complex flow systems, for example the internal combustion engine, to obtain global flow properties using a simplified approach. For engine-based flows the simplified models are usually thermodynamic or fluid dynamic in nature depending on the underlying equations used (Heywood, 1988). Zero-equation models relate to thermodynamic processes where the flow, geometric features, and fluid motion cannot be modelled. One-dimensional models give a basic representation of the flow properties by reducing the governing equations to one dimension therefore greatly simplifying the flow. Given the level of complexity of engine flows, such models do not fully represent the flows or processes, but are limited to specific areas and many assumptions are usually made in the development of the models.

Perhaps the most relevant to the work carried out here is the modelling of intake and exhaust flows. Such flows are of importance as they are directly responsible for the performance of an engine. Typically these flows are modelled by one of three different techniques which are briefly described below and full detail of the methods can be found in the text by Heywood (1988).

Quasi-Steady Flow Models

Quasi-steady models use steady one-dimensional flow equations to calculate the flow through a series of interconnecting components that make up the system of interest.

Each individual component is defined by its geometry and an empirically defined discharge coefficient. Such models are widely used for engine simulations to predict the mass flow rates into and out of the cylinders and have been used here to predict the overall flow into the plenum chamber of the engine. Owing to their inherent simplifications, such models are unable to predict any flow structures or any transient effects of the flow such as the variation of volumetric efficiency with engine speed (Heywood, 1988).

Filling and Emptying Models

These models represent the components of an engine as finite control volumes, or a series of finite control volumes, where the mass of gas contained in each is able to vary in time. For example, the entire intake system can be modelled as a single control volume, or as a series of control volumes describing the individual components of the intake system such as the throttle, plenum chamber, and inlet manifold. Using the continuity and energy equations, and information regarding the flow-rates into and out of each volume, the gas state within each volume is found. As is discussed by Heywood (1988), such models are able to model time-varying characteristics of manifold flows if they are averaged over the entire system under consideration, but are unable to predict the spatial variation of pressure due to the unsteady gas dynamics in the manifolds.

Gas Dynamic Models

For a number of years gas-dynamic models have been used to study the gas-exchange processes within internal combustion engines. Typically such models solve the mass, momentum and energy equations (equations (2.1) through (2.4)) for unsteady compressible flows reduced to their one-dimensional forms. The resulting equations are hyperbolic and are typically solved using the method of characteristics or finite difference methods. The former method involves the transformation of the partial differential equations into ordinary differential equations (the compatibility equations) that hold only along the characteristic lines for the system which are normally solved numerically

(Anderson, 1982; Heywood, 1988).

Finite difference methods prove to be a more efficient and flexible method of solving the one-dimensional equations than the method of characteristics. These methods rely on the computational domain being split into a series of grid points that are spaced by Δx in the spatial coordinate and Δt in the time coordinate. However, the spacing is not necessarily even. Using the Lax-Wendroff method as an example, the values of the flow variables, ϕ_i, at each grid point, i, at time $t = 0$ are assumed and used as initial conditions to the problem. A Taylor expansion in time is used to calculate values of ϕ_i at a new time t, i.e. $\phi_i\,(t + \Delta t)$,

$$\phi_i^{t+\Delta t} = \phi_i^t + \left(\frac{\partial \phi}{\partial t}\right)_i^t \Delta t + \left(\frac{\partial^2 \phi}{\partial t^2}\right)_i^t \frac{(\Delta t)^2}{2} + \cdots \tag{2.9}$$

The spatial derivatives of the continuity equation are replaced by their central differences and because the initial flow field is assumed, this provides the first derivative of density, $\partial \rho / \partial t$ at time t and grid position i, that can be substituted into equation (2.9). The remaining terms of equation (2.9) are then found by differentiation of the continuity equation with respect to time and space, with the space derivatives replaced with their central differences. The same treatment is also applied to the momentum equation. This gives rise to secondary differentials from the known flow field that are substituted into the equations to obtain a value of the second differential, $\partial^2 \rho / \partial t^2$. This procedure is repeated for the next time-step to obtain $\rho\,(t + \Delta t)$, and then the whole procedure is applied to the momentum and energy equations to obtain $u\,(t + \Delta t)$, and $e\,(t + \Delta t)$. This is repeated for a large number of time-steps such that the steady-state solution is reached. It is clear that such calculations require a computational resource in order to solve the equations quickly.

These methods have been used successfully to predict the mass-flow rates through the inlet and exhaust valves of an engine over a complete engine cycle (Heywood, 1988). Given these predicted flow rates the volumetric efficiency of an engine can be calculated, and the findings of Heywood (1988) show that good agreement is found between the numerical predictions and experimental measurements. A similar method has been used

to calculate the flows through the intake and exhaust system of the V8 engine under consideration here. The 1D code, MANDY, has been used to calculate the mass-flow through the inlet system and these have been used as boundary conditions for the CFD predictions (Jaguar Cars Ltd., 1999). Thus one-dimensional techniques prove to be useful for the evaluation of global flow quantities, but unable to provide information of the details of the flow. In order to achieve this, multi-dimensional approaches are required that solve the full set of governing equations. However, the one-dimensional analysis is often used to provide the boundary conditions for such flows, as has been done by Onorati, Ferrari & D'errico (2000). The authors of this paper have used a two-dimensional code to model the flows in a divergent duct, sudden expansion, and Helmholtz resonator that form part of an exhaust system of a diesel engine. These regions have been coupled by a one-dimensional gas-dynamic code that also predicts the flow within the cylinder of the engine. In combining the codes in this manner the computational times are drastically reduced as the full flow fields are not resolved in the cylinder, exhaust port and runners, but the 1D code is able to predict the bulk flow properties which are used as boundary conditions by the 2D code. The results show good agreement with experimental values, and show the prediction of unsteady pressure variations brought about by the engine motion.

2.5.2 Multi-Dimensional Computational Modelling

The preceding sections have shown that one-dimensional flow simulations are able to provide solutions to duct and manifold flows where the bulk flow properties are required. Thus such an approach could be used to predict the bulk flow properties through a throttle valve over a range of engine operation. However, the butterfly valve and bluff-body flows discussed in previous sections have been shown to be highly three-dimensional, rotational and often unsteady, and a one-dimensional code is unable to resolve these flow features. In addition, as one-dimensional codes cannot predict the entire flow field, they are unable to fully evaluate the effects of geometric changes that are often encountered in the design process. In order to achieve these goals, multi-dimensional techniques

must be employed that solve the governing partial differential equations.

Multi-dimensional techniques use similar ideas to that described above for the one-dimensional techniques. In order to solve a flow, the volume of fluid in question must be discretised by creating a mesh of points within it. Depending on the method used for the discretisation, these grid points will be handled in different ways. Historically, the first discretisation practice to be used was the finite difference method, as employed by the one-dimensional Lax-Wendroff technique described above. By using the finite difference formulation the flow variables at each of the grid points are used to solve the discretised governing flow equations, and hence the discretisation of the volume remains as grid points alone (Shaw, 1992).

The use of the finite element method is typically associated with stress analysis of solid structures; however, it is also commonly used to solve fluid flows. When using this method the discretised points of the fluid volume are used to define elements over which simple variations of the dependent flow variables are assumed. The method allows unstructured grids to be used which are a distinct advantage for some complex geometries. Full details of the method are found in the standard reference text by Zienkiewicz & Taylor (1989).

For the finite volume method, the grid of points within the volume are arranged such that individual volumes or cells are created. A solution to the flow is found by considering the flux of the dependent variables across the faces of the cells. Many finite volume codes of the past have demanded that a structured grid topology be used; however, the use of unstructured grids is now more popular using this technique. As this method has been used for the present investigation, it is described in more detail below.

Transport Equations for the Finite Volume Method

Evaluation of the governing equations (2.1) to (2.5) reveals that each has a similar format and therefore they can be represented by a global conservative transport equation,

$$\frac{\partial(\rho\phi)}{\partial t} + \nabla \cdot (\rho\phi\mathbf{u}) = \nabla \cdot (\Gamma\nabla\phi) + f_\phi, \tag{2.10}$$

where ϕ is a general variable that represents both scalar and vector quantities, and Γ is the diffusion coefficient. Equation (2.10) is the basis of the finite volume formulation. By replacing ϕ in equation (2.10) with the relevant dependent variables, i.e. $1, u, v, w$, and e, and using appropriate values for the diffusion coefficient and source term, the conservative governing equations (2.1) to (2.5) are obtained.

The key step of the finite volume method is the integration of the governing equations over a three-dimensional control volume. Considering equation (2.10), integration over a control volume (CV) yields,

$$\int_{CV} \frac{\partial(\rho\phi)}{\partial t} dV + \int_{CV} \nabla \cdot (\rho\phi\mathbf{u})\, dV = \int_{CV} \nabla \cdot (\Gamma\nabla\phi)\, dV + \int_{CV} f_\phi dV. \tag{2.11}$$

The convective and diffusive terms can be rewritten as integrals over the entire surface of the control volume using Gauss' divergence theorem that for a vector, ϕ, states that (Versteeg & Malalasekera, 1995),

$$\int_{CV} \nabla \cdot \boldsymbol{\phi}\, dV = \int_A \hat{\mathbf{n}} \cdot \boldsymbol{\phi}\, dA, \tag{2.12}$$

where, $\hat{\mathbf{n}}$ is a unit vector normal to control-surface element dA, and hence $\hat{\mathbf{n}} \cdot \boldsymbol{\phi}$ represents the component of vector $\boldsymbol{\phi}$ in the normal direction. Application of Gauss' divergence theorem to equation (2.11), and integration over time for transient calculations yields the general form of the finite volume transport equation:

$$\int_{\Delta t} \frac{\partial}{\partial t} \left\{ \int_{CV} (\rho\phi)\, dV \right\} dt + \int_{\Delta t} \int_A \hat{\mathbf{n}} \cdot (\rho\phi\mathbf{u})\, dA\, dt$$

$$= \int_{\Delta t} \int_A \hat{\mathbf{n}} \cdot (\Gamma_\phi \nabla\phi)\, dA\, dt + \int_{\Delta t} \int_{CV} f_\phi\, dV\, dt. \tag{2.13}$$

Note that the order of differentiation and integration has changed for term one on the left-hand side in order to emphasise the physical meaning of the equation. The term represents the rate of change of the total amount of the fluid property ϕ in the control volume (Versteeg & Malalasekera, 1995).

The integration of equation (2.13) is applied to the individual cell faces of each discretised volume and over each time interval for the flow. STAR-CD introduces several approximations to the equation. The first term is averaged over the time interval as suggested by the form of the equation. The diffusion term (third term) is approximated by face-centre averaged values, and the final term represents any sources and sinks of the transported property and any additional flux terms. Approximation of the convective term (term 2) is defined by the user with several low-order and high-order discretisation schemes available (Computational Dynamics Ltd., 2001).

Spatial Flux Discretisation

The choice of spatial flux discretisation for the convective terms of the finite volume equation can have significant effect on the accuracy and stability of the flow solutions produced. The two main classes of discretisation scheme are low-order and high-order schemes. A low-order scheme typically generates a form of the finite volume equation that is easier to solve, and the scheme tends to preserve the physical bounds of the flow. However, such schemes are more prone to numerical diffusion that can be ameliorated through grid refinement (Abbott & Basco, 1989). Higher-order schemes tend to improve the capture of steep gradients within the flow but can also more readily lead to non-physical flows. Numerical dispersion is often found in higher-order schemes which is a result of the numerical solution overshooting the bounds of the dependent variables (Hirsch, 1990).

STAR offers only the first-order upwind-difference scheme as a low-order scheme. First-order schemes are typically no longer used for a full flow solution, and many journals no longer accept work produced using first-order schemes (Freitas, 1995). However, it is acceptable to use a first-order scheme to start a solution that is later continued with a higher-order scheme. A wider choice of schemes is, however, available for higher-order schemes, although some of these are dependent on the mesh types used. The central-differencing scheme uses linear interpolation between cell faces to calculate the variables. Although the scheme is a common in commercial CFD codes, its use should

be limited as it has a tendency to become unbounded if the Peclet number (the ratio of convection to diffusion) is greater than 2 (Versteeg & Malalasekera, 1995). In addition the scheme is ambiguous to flow direction.

The quadratic upstream interpolation for convective kinetics (QUICK) scheme uses quadratic interpolation between cell values and is of third-order for a uniform mesh. The scheme can be slightly dispersive (Versteeg & Malalasekera, 1995) and is not recommended for use with tetrahedral meshes (Computational Dynamics Ltd., 2001). Hayase (1999) has investigated the QUICK and central-differencing schemes for the fully developed turbulent flow through a square duct using several levels of grid refinement. He shows that the QUICK scheme offers monotonic convergence with reduced grid sizes despite offering a poor initial agreement with DNS data. The results obtained with central differencing scheme show improved initial agreement, but a non-monotonic convergence with grid size that can be misleading.

STAR offers several blended higher-order schemes that contain a built-in adaptive filter that removes any non-physical phenomena should they arise. This is achieved by blending of the central- and upwind-differencing schemes based on face-related weighting factors. Such schemes revert to a low-order scheme when non-physical flows occur leading to increased smearing of the solutions.

Computational Dynamics Ltd. (2001) have developed a monotonic high-order scheme that remains second-order accurate even when used on highly skewed and irregular grids. The scheme is known as the monotone advection and reconstruction scheme (MARS) and also uses a filtering technique to alternate between central- and upwind-differencing. This scheme has been shown to offer good predictions (Freitas, 1995) and has been used for the current predictions. It is discussed further in chapter 3, along with the solution algorithm used.

Turbulence Modelling

The majority of engineering flows are turbulent in nature and hence this needs to be taken into account when performing numerical simulations of these flows. The governing

equations of fluid flow describe the motion of the both laminar and turbulent flows and hence should provide sufficient information when discretised to provide solutions to turbulent flows. However, given that the range of length scales in a turbulent flow may reach as low as 100 μm, the number of grid points required to capture the full range of length scales over a decent sized domain would be phenomenal (Versteeg & Malalasekera, 1995). In addition, the frequency of the fastest events in the flow are of the order of 10 kHz and therefore to sufficiently capture the temporal changes in the flow a time-step of the order of 100 μs would be required. To generate a solution resolved to such a degree for general flows would require computers far more powerful than those currently available.

However, the rise in computing power has seen an increase in such studies that are formally known as direct numerical simulation, or DNS. Such simulations are currently limited to relatively small computational domains and simple geometries for turbulent flows of low Reynolds number. Typical examples are the flows over flat plates and the vortex shedding behind a circular cylinder and bluff bodies at low Reynolds numbers (Sohankar, Norberg & Davidson, 2001). DNS offers great insight into the turbulent flow structures that have previously been incredibly difficult to examine, hence increasing our overall knowledge of turbulent flows. Such is the confidence in DNS simulations that their results are now often used as validation tools for other simulation techniques.

The use of DNS is, however, very restrictive and it will be some time before complex flows at high Reynolds number can be realistically analysed. Thus alternate methods are used to simulate turbulence in the flow that typically rely on some form of semi-empirical mathematical model to account for the turbulent features of a flow.

Large eddy simulation (LES) is one such example where a turbulence model is used to model the small-scale turbulent structures found in the proximity of walls and solid boundaries. The large-scale eddies away from the wall are resolved directly by the computational grid that remains relatively large in comparison to those used for DNS studies. Although LES is also very computationally intensive, it is now becoming more mainstream with the advent of more powerful and cheaper computer resources. Until

now, typical flows studied with LES are the vortex shedding from cylinders (Jordan & Ragab, 1998) and other bluff bodies, and duct flows, although most flows can be considered.

The Unsteady Reynolds-Averaged Navier-Stokes Equations

More commonly used in industry is the approximation that leads to the Reynolds-Averaged Navier-Stokes equations, often written as the RANS equations. RANS modelling techniques typically produce faster solutions than the LES methods and have a proven track record with solutions to many practical engineering flows documented.

The key to the RANS method, as the name implies, is the Reynolds averaging of the Navier-Stokes equations to yield a new set of equations that include terms that model the turbulence in the flow. This is achieved by first considering the flow properties to be time dependent which is the case for all turbulent flows. Now the general fluid property, ϕ, of equation (2.10) can be expressed as the sum of a steady mean component, Φ, and a time-varying fluctuating component, ϕ', i.e. $\phi(t) = \Phi + \phi'(t)$, and this applies to each of the flow variables.

In order to model the effects of these fluctuations, the flow variables in the governing equations (2.1) through (2.5) are replaced by their mean and fluctuating components. A time-average of these equations is then performed which yields the Reynolds–Averaged Navier–Stokes equations as summarised below:

The mass-continuity equation:

$$\frac{\partial \rho}{\partial t} + \nabla \cdot (\rho \mathbf{U}) = 0. \tag{2.14}$$

The Reynolds equations:

$$\frac{\partial(\rho U)}{\partial t} + \nabla \cdot (\rho U \mathbf{U}) = -\frac{\partial P}{\partial x} + \nabla \cdot (\mu \nabla U) + \left[-\frac{\partial\left(\rho\overline{u'^2}\right)}{\partial x} - \frac{\partial\left(\rho\overline{u'v'}\right)}{\partial y} - \frac{\partial\left(\rho\overline{u'w'}\right)}{\partial z} \right] + f_x, \quad (2.15)$$

$$\frac{\partial(\rho V)}{\partial t} + \nabla \cdot (\rho V \mathbf{U}) = -\frac{\partial P}{\partial y} + \nabla \cdot (\mu \nabla V) + \left[-\frac{\partial\left(\rho\overline{u'v'}\right)}{\partial x} - \frac{\partial\left(\rho\overline{v'^2}\right)}{\partial y} - \frac{\partial\left(\rho\overline{v'w'}\right)}{\partial z} \right] + f_y, \quad (2.16)$$

$$\frac{\partial(\rho W)}{\partial t} + \nabla \cdot (\rho W \mathbf{U}) = -\frac{\partial P}{\partial z} + \nabla \cdot (\mu \nabla W) + \left[-\frac{\partial\left(\rho\overline{u'w'}\right)}{\partial x} - \frac{\partial\left(\rho\overline{v'w'}\right)}{\partial y} - \frac{\partial\left(\rho\overline{w'^2}\right)}{\partial z} \right] + f_z. \quad (2.17)$$

Note that these equations represent the unsteady time-averaged form of the governing equations and thus are more correctly termed the URANS equations. The format of the equations is similar to the original governing equations; however, the time-average yields additional terms on the right-hand side of each of the momentum equations (2.15) to (2.17). These additional terms represent the convective momentum transfer due to the velocity fluctuations and are commonly known as the Reynolds stresses (Versteeg & Malalasekera, 1995). They are typically represented in suffix notation as, $-\rho\overline{u_i' u_j'}$.

Herein lies the need for turbulence modelling. By time-averaging the governing equations, six additional unknown quantities are obtained and thus the full set of equations cannot be solved as the problem is not closed. Thus the role of the turbulence model is to predict the Reynolds stresses in equations (2.15) through (2.17) hence closing the set of equations.

The classical models used in RANS modelling consist of zero-equation models, two-equation models, Reynolds-stress equation models, and algebraic-stress models (Versteeg & Malalasekera, 1995). Of these, the mixing-length model and k-ε model are by far the most popular and well documented, and the k-ε model is the more generally applied model and hence will be briefly described here.

The k-ε Turbulence Model

Turbulent viscosity models, such as the k-ε model, assume that the Reynolds stresses are related to the mean rate of strain of the flow as proposed by Boussinesq and hence this is termed the Boussinesq hypothesis:

$$-\rho\overline{u_i'u_j'} = \mu_t\left(\frac{\partial U_i}{\partial x_j}+\frac{\partial U_j}{\partial x_i}\right)-\frac{2}{3}\rho\delta_{ij}k = 2\mu_t E_{ij}-\frac{2}{3}\rho\delta_{ij}k. \tag{2.18}$$

Here, μ_t is the turbulent or eddy viscosity, δ_{ij} is the Kronecker delta, and E_{ij} is the simplified representation of the mean rate of deformation. It is the role of the turbulence model to specify the value of the turbulent viscosity. By dimensional analysis this can be expressed in terms of a velocity and length scale, which for the k-ε model are defined in terms of k and ε to give,

$$\mu_t = \rho C_\mu f_\mu \frac{k^2}{\varepsilon}, \tag{2.19}$$

where C_μ is a dimensionless constant, and f_μ is unity for the high Reynolds number k-ε model (Versteeg & Malalasekera, 1995).

The standard k-ε model (Launder & Spalding, 1974) incorporates two transport equations that model the turbulent kinetic energy, k, and the rate of dissipation, ε. The governing equation for the turbulent kinetic energy is combined with the Boussinesq approximation and, after significant manipulation, the two model transport equations are given by Versteeg & Malalasekera (1995) as:

$$\frac{\partial(\rho k)}{\partial t}+\nabla\cdot(\rho k\mathbf{U}) = \nabla\cdot\left[\frac{\mu_t}{\sigma_k}\nabla k\right]+2\mu_t E_{ij}\cdot E_{ij}-\rho\varepsilon, \tag{2.20}$$

$$\frac{\partial(\rho \varepsilon)}{\partial t}+\nabla\cdot(\rho \varepsilon\mathbf{U}) = \nabla\cdot\left[\frac{\mu_t}{\sigma_\varepsilon}\nabla \varepsilon\right]+C_{1\varepsilon}\frac{\varepsilon}{k}2\mu_t E_{ij}\cdot E_{ij}-C_{2\varepsilon}\rho\frac{\varepsilon^2}{k}, \tag{2.21}$$

which enable the turbulent viscosity to be found from equation (2.19). The terms for the kinetic energy and dissipation are closely linked in the equations, and this improves the boundedness of the model.

Equation (2.18) implies the assumption of isotropic viscosity which limits the model in complex flows. Under such conditions the Reynolds stresses are rarely isotropic and hence advanced models such as the Reynolds-stress model offer improved predictions. Such models formulate equations to represent the Reynolds stresses thus leading to a more complex set of equations to solve. The accuracy of such methods for complex flows is improved but at the expense of requiring additional computational resources.

Details of the application of the model are described in chapter 3, including the implementation of boundary conditions and the use of wall functions. The results obtained using the k-ε turbulence model are discussed in chapter 6, including some of their shortcomings, particularly when used to model transient flows.

Uncertainty and Validation

With the advent of cheaper and faster computing technology, and improvement to commercial codes, CFD has rapidly become adopted as an additional design tool in the engineering industry. Where the methods were once largely of academic interest they have spread into all sectors of engineering, in particular the aerospace industry and now the automotive industry. Through use as a design tool, CFD is also being integrated into other multi-disciplinary applications, including such applications as fluid-structure interactions (Knight, Lucey & Shaw, 2001). Massive increases in the number of commercial users by the start of the century was predicted by Fisher & Rhodes (1996), and although the figures suggested have not been confirmed, it is clear that there is rapid growth in the industry today. The large growth of users has raised concern over the uncertainty of CFD and brings forth the need to raise awareness of its capabilities and limitations through increased documentation of validation cases (Casey & Wintergerste, 2000; Fisher & Rhodes, 1996; Freitas, 1995; Gosman, 1998).

In order to classify uncertainty and errors in CFD codes it is possible to break down the methods of quantification into three distinct definitions. Roache (1997) defines the following terms:

Verification is the process of ensuring that the computational code correctly solves

the mathematical equations. Verification of the flow gives no indication of the physical correctness of the solution, and only gives an indication of the numerical error of the code.

Validation is the procedure to check the extent to which the model accurately represents reality and hence this is also a check on the conceptual modelling error. Validation is typically carried out by comparison of the predicted flows to experimental measurements and hence good agreement of the two leads to a valid solution. Poor agreement shows that the model has been poorly defined, or that the incorrect model has been used for a flow.

Calibration is the process to access the ability of a CFD code to predict global quantities of interest for specific geometries of design interest. Typically this involves simulations of several similar flows to gauge the performance of the CFD code and model to the application at hand.

For the new CFD user, or experienced user tackling a new problem, previously validated test cases provide invaluable information as to the suitability of models or techniques to a particular flow. Such cases include solutions with both good and poor agreement with experimental measurements that therefore expand the available knowledge base and improves the overall quality of CFD simulations. Here, validation of the computational predictions has been performed by comparison to hot-wire and pressure measurements made of the physical flows. The computational domain and the physical flow volume are dimensionally similar, therefore providing like-for-like comparisons. Some of the relevant measurement techniques applicable to the flows under investigation are now presented.

2.6 Experimental Measurement Techniques

The above discussion raises the need for experimental measurements in order to validate computationally predicted fluid flows. However, in order to achieve this the accuracy of the measurements must also be high, otherwise there is no quantitative means by

which to validate the predictions. Whereas many past experimental investigations have been devised solely to examine a particular flow, the need for reduced uncertainty in CFD modelling has given rise to an increased number of specialised experimental investigations for the sole purpose of validation and calibration of the codes. For example, alongside the main flow measurements performed, it is often necessary to include measurements that can be used to improve the boundary-condition specification of the computational models. In addition, a series of complicated flow experiments can be used to calibrate the CFD code such that future design changes can be evaluated with the computational models with confidence, and therefore eliminate the need for further experiments to validate the models.

The measurement techniques used to carry out such investigations have advantages and disadvantages that must be evaluated in order to choose the most suitable type for the investigation in question. For example, it may be necessary that non-intrusive techniques are used owing to the sensitivity of the flow to disturbance, or a high response time is required to suitably capture the physics of the flow. Also, the choice of measurement technique depends on what physical quantities are of interest; for example, flow velocity, pressure fields, body forces, and visualisations.

Here the main aim of the measurements is to record oscillations of the flow velocity field, and hence velocity measurement techniques are the primary choice for the investigation. Some of the common measurement equipment is now described before a more detailed account is given of the hot-wire anemometry system that has been used for the flow measurements carried out here.

2.6.1 Mean Flow-Rate and Mean Velocity Measurement

In order to ensure that the experiments and computational model match, the inlet flow rate to the throttle body must be determined. Measurement of the inlet flow rate can be achieved by various means, provided that the measuring device causes minimal disturbance to the flow entering the throttle body. If this condition is satisfied the flow may be considered to be quasi one-dimensional and hence the use of Bernoulli's

equation to evaluate the flow speed is permitted. In using Bernoulli's equation, the pressure-gradient technique can be used to evaluate the flow rate via measurement of the differential pressure across a device (Fraden, 1993). This method relies on a flow restriction being placed in the flow of known properties, measuring the pressures at either side and then determining the flow rate by simple calculations from the known values. The schematic of Figure 2.4 shows a simplified differential pressure measurement device, based on the venturi meter (Linford, 1961).

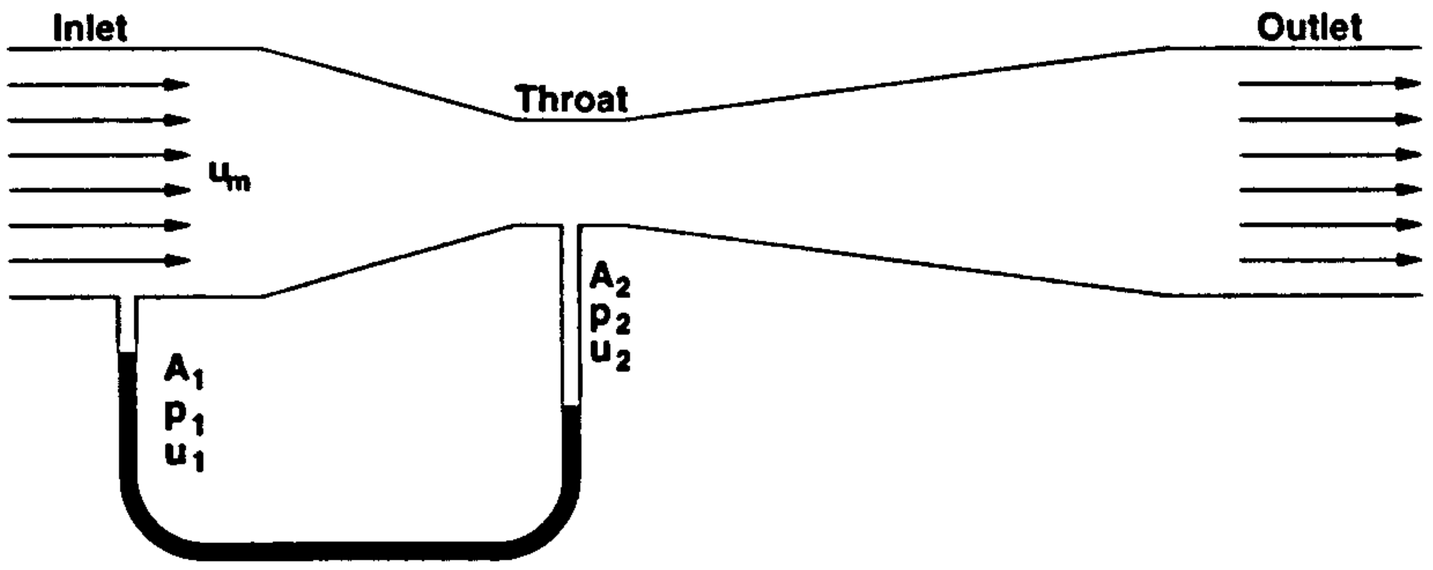

Figure 2.4: Schematic of a simplified venturi meter used to measure the flow-rate of a fluid. Not to scale.

Figure 2.4 shows the basic properties of a venturi meter which operates on the differential pressure principle. Geometric detail of the venturi has not been shown in the figure although much information exists on the subject, in particular the ISO (International Organisation for Standardisation) papers offer excellent guidelines to their design (ISO, 1991). The basic operation of the venturi and other differential pressure meters is straightforward. The cross-sectional areas of the upstream section and throat are known, and are denoted by A_1 and A_2 respectively. Static pressure is measured at both locations, denoted as p_1, and p_2 respectively. This gives the effective differential pressure which is sometimes converted to head loss (Linford, 1961). We can now apply Bernoulli's equation to the central streamline to evaluate the flow, where Bernoulli's equation is stated as,

$$p + \frac{1}{2}\rho u^2 = p_o. \tag{2.22}$$

Thus, applying equation (2.22) to the upstream and downstream locations, and us-

ing the one-dimensional continuity equation (from equation (2.1)), the ideal flow-rate through the venturi can be calculated from equation (2.23) as,

$$q_{ideal} = u_2 A_2 = A_2 \sqrt{\frac{2(p_1 - p_2)}{\rho\left(1 - \left(\frac{A_2}{A_1}\right)^2\right)}}. \tag{2.23}$$

Real flows will deviate from this value owing to frictional effects, and so to determine the actual flow rate an additional term, the coefficient of discharge, C_d is added (Shames, 1992). Thus, the actual flow rate is given by,

$$q_{actual} = C_d \, q_{ideal}. \tag{2.24}$$

The coefficient of discharge is usually found by experiment, however, the ISO has published values of C_d for several configurations of venturi meter (ISO, 1991). For compressible flows, equations (2.23) and (2.24) no longer hold and further equations need to be developed to establish the flow rate. Anderson (1982) shows that flows with a mean speed below one third of the speed of sound can be considered incompressible. For the experiments considered here, the inlet flow velocity has a maximum of approximately 75 m s^{-1}, which falls below this value, and hence equations (2.23) and (2.24) are valid. Many other pressure differential devices exist for the measurement of fluid flow, all of which operate on the same principles as described here. Examples include flow nozzles, square-edged orifice plates, gauze-restrictors, Dall tubes, Dall orifices, double-throat venturis, and others (Bradshaw, 1970; Fraden, 1993; ISO, 1991; Shames, 1992; Ward-Smith, 1980).

Venturi tubes and other differential pressure devices are well established and can easily be applied here. However, there are numerous problems which make their use impractical. The use of the differential pressure technique assumes that the flow entering the device is steady, smooth and of a normally turbulent state. This requires a long length of straight circular pipe to be placed upstream of the device to ensure that this condition is met. Linford (1961) states that usual practice is to use a straight circular pipe with a length of ten upstream diameters for this purpose but notes that there is

considerable disagreement between authors on the exact length required under differing circumstances.

In a similar manner, a length of straight circular pipe is also required immediately downstream of the measurement device to ensure pressure recovery and flow stabilisation occur. This is especially important for devices such as orifice plates and nozzles which tend to disturb the flow to a much higher degree than the venturi or Dall tube.

Owing to these limitations, such devices are not appropriate for the proposed experiments because of a lack of available space for the extensive pipe-work. A further problem exists in using such devices with low flow rates as will also be experienced here. Venturi meters have a stable operating range above a Reynolds number of 3×10^5, where Re is evaluated at the throat section (Ward-Smith, 1980). Below this value the coefficient of discharge (see equation (2.24)) is no longer constant, thus requiring complex calibration of the device. At these lower Reynolds numbers the flow through the venturi separates at the interface between the convergent duct and throat. This leads to a separation bubble forming in the region of adverse pressure gradient at the throat entrance and a consequent 'hump' being seen in the curve of C_d versus Re. For the experiments here, Re is predominantly below 2×10^5, hence measurement would prove difficult and an alternative must be used. Other differential pressure devices would also offer excess disturbance of the flow.

A device which operates by the principle of differential pressure measurement is the Pitot tube, although it is usually considered to be a direct velocity measuring instrument. The Pitot tube is a very common device for velocity measurement, making it readily available. Pitot tubes are simple to operate and are typically constructed in conjunction with static holes (Pitot-static tube) as shown in Figure 2.5.

When using the Pitot tube, steady flow is again assumed to exist which endorses the use of Bernoulli's equation (2.22). Inserting the probe in the flow such that its end is aligned into the oncoming flow causes the fluid to move around it and a stagnation point forms at the tip. Stagnation, or total pressure ($p + {}^1/_2\rho u^2$), is thus measured in the central tube of the device. By measuring the static pressure, p, through the series of

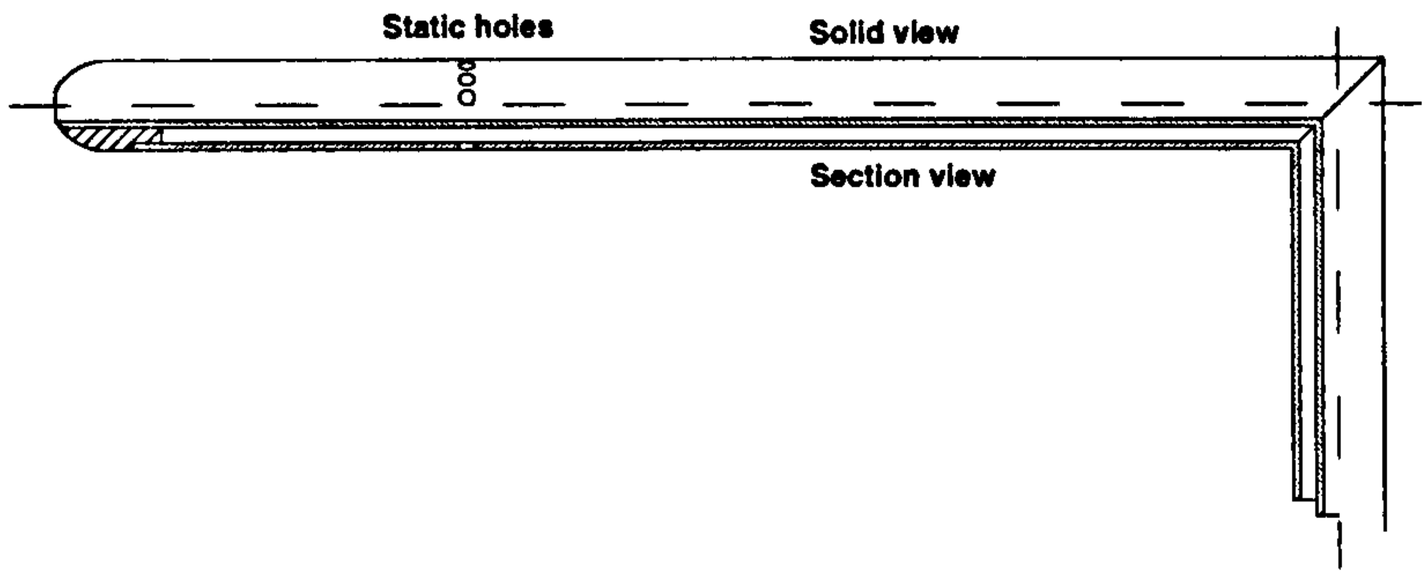

Figure 2.5: Basic construction of a standard NPL (National Physics Laboratory) type Pitot-static tube. Not to scale.

holes in the outer tube and calculating the differential pressure, the dynamic pressure, and consequently the flow velocity can be found.

The Pitot tube's main disadvantage here is that it is an obtrusive measurement technique thus adding disturbance to the flow being measured. Typically the device is used in a wind tunnel, and hence its disturbance to the global flow is minimal, and its blockage effect is nearly non-existent. For small-scale measurements these issues become more apparent and must be accounted for; this is discussed in chapter 5. The Pitot tube measures only the steady mean velocity at a point in the flow thus in order to measure the instantaneous velocity at a point in the flow other techniques are required and these are outlined below.

2.6.2 Laser Doppler Anemometry

Laser Doppler anemometry is the method of fluid velocity measurement by detecting the Doppler shift of laser light scattered by particles suspended within the flow. Such particles are either naturally occurring in the fluid or are artificially introduced by seeding the flow. Seeding particles should be naturally buoyant in the flow and remain small enough not to cause disturbance to the flow. The choice of suitable seeding material is dependent of the fluid medium and flow field, and generation of consistent particle sizes is often troublesome even when using special seeding apparatus (Durox, 1999).

The basic method of operation involves splitting of the laser beam such that one

beam is shone into the flow domain at incidence, and the second split beam is shone at a photo-detector. The photo-detector is positioned at an equivalent incidence angle to the flow as the first laser beam such that any laser light scattered by the suspended particles is detected. This scattered beam interferes with the secondary split beam from the laser source and the frequency of the interference is a measure of the flow velocity (Drain, 1980).

One of the main advantages of the LDA technique is that it is a non-intrusive technique thus offering no flow disturbance. The disadvantage of the method is that high-quality optical access is required in order to transmit and receive the laser beam to the measurement volume. Measurement of plenum system flows have been made by Shaw, Lee, Richardson & Pierson (2000) using a specially designed and built flow-rig made from glass and perspex. The measurements have been used to validate computational predictions of the plenum flows by measurement of the velocity components and turbulence intensities of the flow. Similar studies have been performed by Chen, Ganti, Lee & Yianneskis (1994) for the flow through a generic model inlet port of an internal combustion engine. Their findings suggest that measuring the fine details of the flow using LDA is difficult, a fact reflected by Buchhave, George & Lumley (1979) who give a detailed account of the measurement of turbulent flows using LDA.

2.6.3 Particle Image Velocimetry

Another non-intrusive measurement technique that makes use of optical methods is particle image velocimetry, or PIV. The method uses a pulsed laser- or light-sheet to illuminate a planar section of the flow that is seeded with small particles. A high-speed digital camera is used to capture two images of the flow in the plane at a fraction of a second apart. The frequency of the pulsed light sheet and image capture are timed to coincide such that the images capture the instantaneous flow field at the two instances in time. The resulting images show the seeding particles as stationary points and statistical imaging techniques are used to determine the positions of each particle at each time instant. This analysis is the most time-consuming part of the PIV process as each image

typically contains many thousands of pixels to analyse, and can contain many particles. The analysis process also determines the accuracy, reliability and spatial resolution of the measurements (Adrian, 1991). Knowing the position of a particle at two instances in time allows the velocity vector to be calculated and hence a picture of the entire flow field is produced. The timing of the system needs to be considered for any particular flow to ensure that the two snapshots show only small movement of the particles.

The obvious advantage of PIV techniques is that a large slice of the flow is captured at any one time as opposed to point measurements as made by other systems. However, this also places limitations on the application of the method as access for the optical equipment is required. Measurements in complex geometries can pose particular problems as the laser sheet is obstructed by the geometry and suitable access for the camera can be difficult. Results obtained with the technique lend themselves well to CFD validation as vector plots through a slice of the domain are obtained which are also typically presented for CFD simulations.

2.6.4 Hot-Wire Anemometry

Hot-wire anemometry, as the name suggests, is a method of recording the speed of a particular flow. However, a hot-wire anemometer is able to provide far more information than just the flow speed alone, depending on its configuration and the type of system used. Typically hot-wire anemometers are used for the measurement of instantaneous flow velocities, flow temperatures and perhaps most importantly, the turbulence quantities of a flow. Within the current investigation a hot-wire anemometer is used to capture basic flow information such as the frequency of flow oscillations, instantaneous one-dimensional point velocities, and some basic turbulence information of the flow downstream of the throttle valve. Comte-Bellot (1976) gives a brief introduction to the origins of hot-wire anemometry.

Principle of Operation

Hot-wire anemometers operate on the principle of heat transfer from the sensing probe to the surrounding moving fluid, essentially acting as a thermal transducer (Perry, 1982). Typically, a convective heat-transfer relationship involving the Nusselt (Nu), Prandtl (Pr), and Reynolds (Re) numbers exists of the form given in equation (2.25),

$$\mathrm{Nu} = A + B\mathrm{Re}^{1/2}, \tag{2.25}$$

where A and B are empirical calibration constants (Bruun, 1995). The most common form of this equation was proposed by Kramers (1946) who carried out heat-transfer experiments on three spheres in air, water and oil. A general formulation of equation (2.25) was found, but also for heat transfer to a perpendicular flow from a cylindrical wire, the following relationship was found,

$$\mathrm{Nu} = 0.42\mathrm{Pr}^{0.20} + 0.57\mathrm{Pr}^{0.33}\mathrm{Re}^{0.50}. \tag{2.26}$$

Several variations on the convective heat transfer laws exist and a brief discussion can be found in the work by Comte-Bellot (1976) and Collis & Williams (1959). It is not proposed to show the entire working relationships of heat-transfer, flow velocity, and bridge voltage output here.

Several alternative types and configurations of sensing element, or probe, exist that allow different flow quantities to be ascertained experimentally. For example, single-, double-, and triple-wire probes allow the measurement of the equivalent number of velocity components of a flow. In addition, different sizes and shapes of probes are available to suit a wide range of applications.

The term 'wire' derives from the construction of the probe itself. A typical single-wire probe consists of a short filament stretched between two supporting prongs designed to minimise flow disturbance. Each end of the filament is soldered to the supports, often with a small degree of slack to allow for distortion through heating and aerodynamic loading. Typically the filament is made from tungsten or platinum, with a diameter of approximately 5 μm, and length of 1.25 mm, although several different configurations

are available (Bruun, 1995). Depending on the manufacturing method, the exposed section of the element may extend the distance between the prongs, or if the wire has been exposed by etching of a Wollaston wire, then the ends of the wire may remain plated. Single-sensor probes that have the wire orientated perpendicular to the body and supports are often termed single-normal (SN) probes (Bruun, 1995). Figure 2.6 shows an SN probe with a wire-fixed coordinate system and the velocity components acting at the wire.

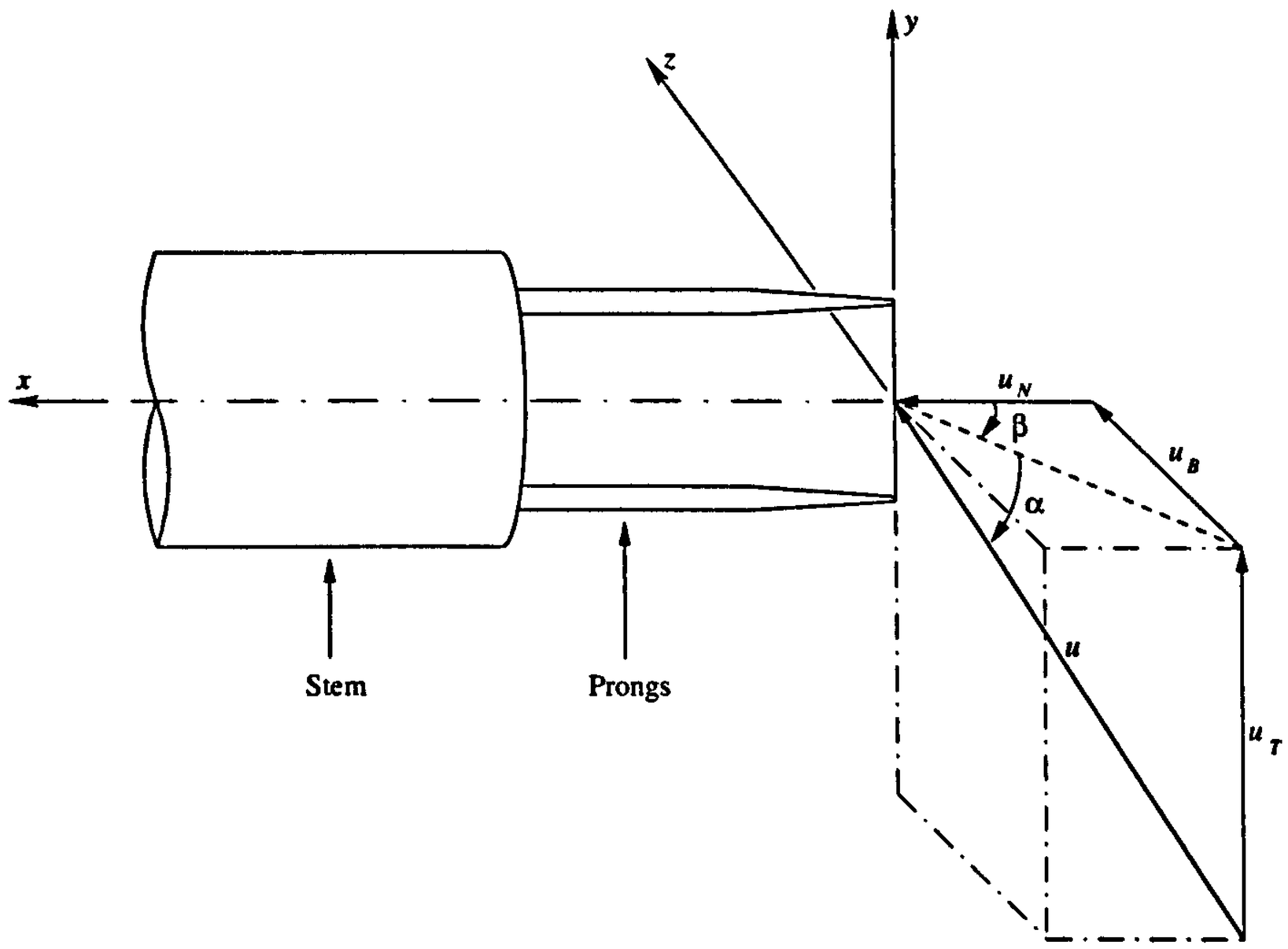

Figure 2.6: Schematic showing an SN probe with wire-fixed coordinate system defined with x along the probe axis, and y parallel to the wire axis. Also shown are the velocity components acting on the wire, where u_T is parallel to the wire, and u_B is perpendicular to both the wire and prongs.

Figure 2.6 shows the hot-wire prongs and stem and the fixed-wire coordinate system defined with x along the probe axis, and y orientated parallel to the wire axis. The incident velocity acting on the wire is defined **u** with components: u_N, normal to the wire along the probe axis; u_T, parallel to the wire; and u_B, perpendicular to both the wire and the prongs. The pitch and yaw angles are defined as α and β respectively.

Hot-film probes are also commonly used for flow studies. Such probes comprise

thin films (~ 0.1 μm) of (typically) nickel or platinum attached to thermally insulated bodies (Bruun, 1995). Common shapes include cylinders, cones and wedges, along with flush-mounting probes for surface flow studies. Hot-film probes are generally used where the acquisition of accurate turbulence quantities is not a priority. Such probes are typically more robust, more stable, and more consistent; however, they suffer from a larger relative size, hence introducing greater flow disturbance, and have a more complex frequency response.

Hot-wire anemometers operate in one of two ways, either constant current (CC) mode, or constant temperature (CT) mode. Constant-temperature anemometers are by far the most popular of the two, perhaps due to their simpler operation; a CT anemometer is used here. Operating in such a mode, the probe filament is maintained at a constant operational temperature, and hence resistance, by a feedback loop that is incorporated into the HWA circuit. For CC anemometers a current is applied that gives the desired bridge balance, and this is then fixed during operation. Figure 2.7 shows a schematic circuit diagram for a CT anemometer.

The probe forms the active arm of the anemometer bridge circuit and its filament is heated by an electric current. Figure 2.7 shows the wire with a resistance, R_w, connected in series with a resistance, R_L, which represents the leads resistance of the probe, cable and support (DISA Elekronik A/S, n.d.). The differential amplifier of gain, G, forms the feedback loop with its inputs being the voltage difference between the two halves of the Wheatstone bridge ($e_2 - e_1$); this voltage represents the change in filament resistance. The current output from the differential amplifier, i, is passed back into the bridge circuit thus maintaining the wire at a constant resistance. The output from the circuit, E, the bridge voltage, is directly proportional to the heat transfer from the wire, and hence is a measure of the velocity of the flow. In a typical circuit an offset voltage is applied to the amplifier output voltage which enables the system to be started and also improves stability (Perry, 1982).

In order to tune the dynamic frequency response on the anemometer the bridge needs to be balanced. Bridge balance is attained by balancing the left- and right-

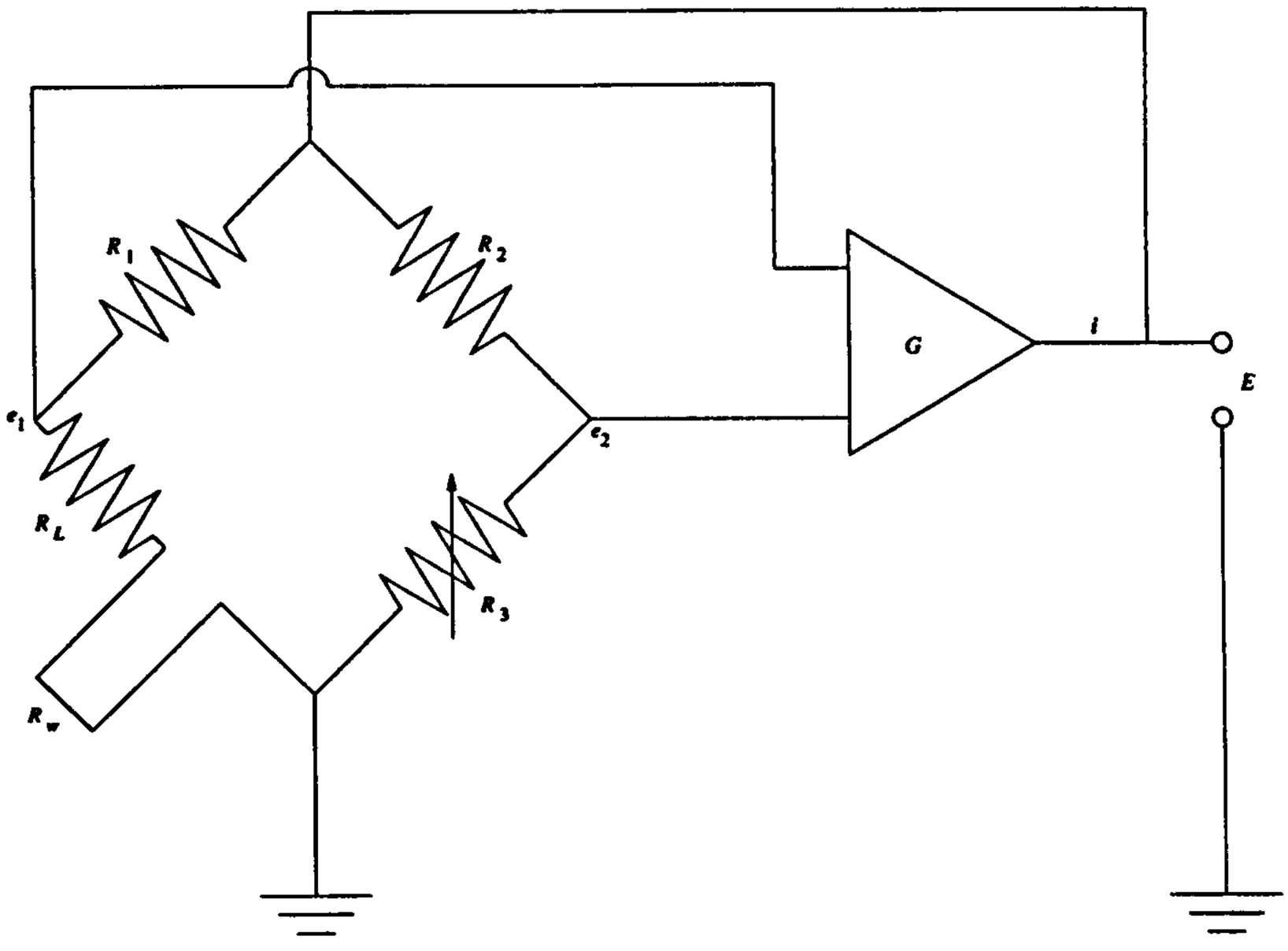

Figure 2.7: Circuit diagram for a hot-wire anemometer operating in CT mode showing the Wheatstone bridge and feedback loop. Reproduced from DISA Elekronik A/S (n.d.).

hand sides of the bridge, i.e. $(R_w + R_L)/R_1 = R_3/R_2$ (from Figure 2.7). For optimal frequency response, the bridge is equally balanced (i.e. a bridge ratio of 1:1); however, anemometers are often operated at bridge ratios in the range, $5 \leq R_2/R_1 \leq 20$ (Bruun, 1995). In practice, balancing is achieved by exposing the probe to a steady flow, with a velocity equal to at least the maximum velocity occurring during measurements, and applying an electrical square wave on the bridge offset voltage. Using a square wave is analogous to a step change in the velocity being measured, which is considerably easier than obtaining a precise step change in flow velocity, although techniques for velocity changes have been developed. The output from the anemometer is observed via an oscilloscope and the unit adjusted so that the response curve shown in Figure 2.8 is obtained.

Figure 2.8(a) shows the ideal response curve of a CT anemometer subjected to a square-wave test signal. Optimal frequency response requires that the undershoot is approximately 15% of the maximum output, as depicted. Bruun (1995) defines the

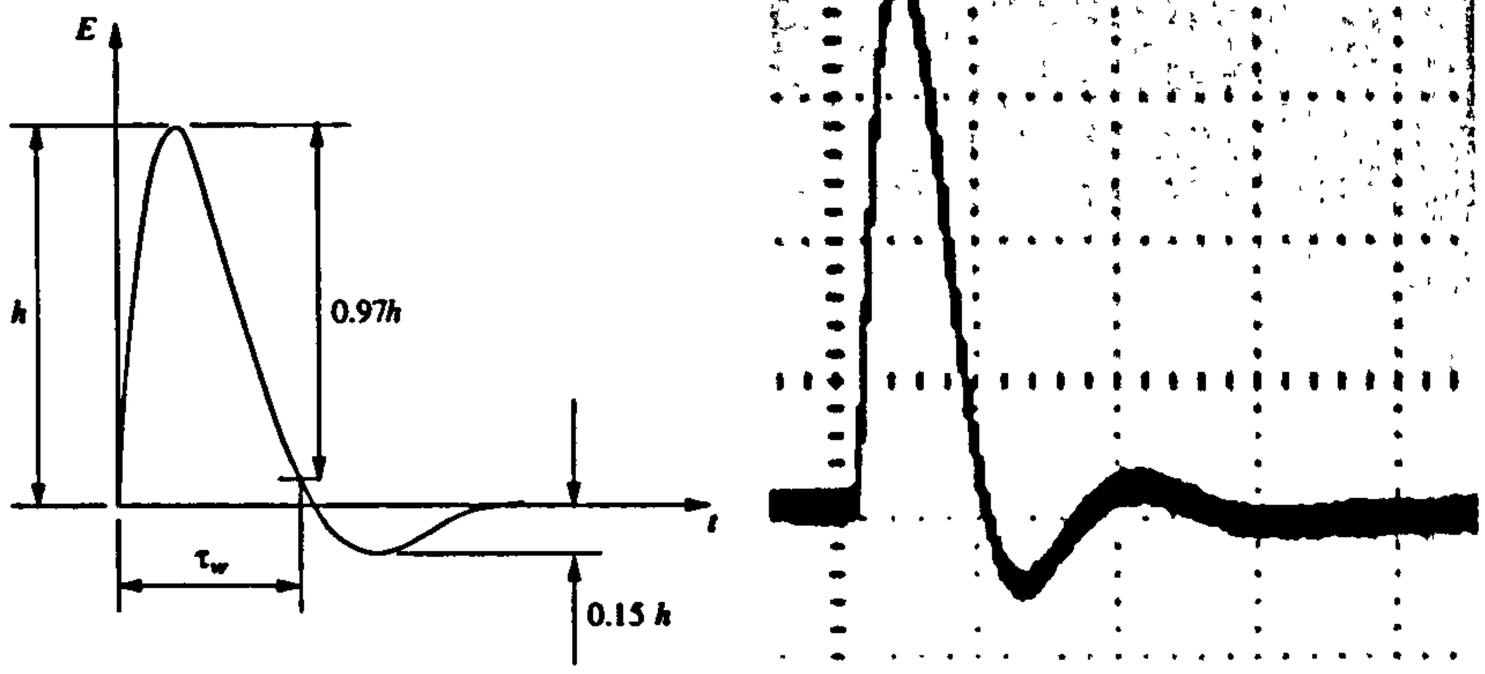

(a) Ideal response curve (b) Typical output

Figure 2.8: Square-wave test response of a CT anemometer, (a) ideal curve (Bruun, 1995); (b) a typical oscilloscope trace for the work carried out here.

value of τ_w as the time for the signal to decay to 3% of its maximum valve, and defines of the cutoff frequency (the upper limit of dynamic response) as, $f_c = 1/1.3\tau_w$. Here, with a 5 μm diameter wire of length 1.25 mm, a bridge ratio of 1:1 and a flow velocity of 60 m s^{-1}, this gives a cutoff frequency of approximately 150 kHz. Figure 2.8(b) shows a typical oscilloscope trace of a hot-wire response curve obtained here.

Perry (1982) discusses the commonly found output traces that are generated when tuning a system, including non-linear and higher-order traces. Typically a non-linear output will show asymmetry in the trace about the time axis (normally a series of pulses as in Figure 2.8(a) are generated with each consecutive pulse reflected in the time axis). Higher-order effects are apparent when there is oscillation in the signal and the damping is not sufficient to maintain the ideal curve.

In use, a hot-wire probe is carefully aligned within the flow to minimise disturbance. For single-sensor probes measuring a single velocity component, the probe is typically aligned such that the probe axis is parallel to the flow, i.e. the the sensing element in perpendicular to the flow direction. Single-sensor probes can perform two-component velocity measurements when orientated at an angle to the flow, or when a single-yawed

(SY) probe is used whereby the filament is inclined at an angle to the supports. In such a case the velocity of the flow is split into components relative to the filament. (Note that for the remainder of this work, reference is made only to SN probes.) In either scenario, the probe is best placed in a region of uni-directional non-circulatory flow owing to its directional ambiguity. For measurements in periodic flows, care must be taken in locating the probe to reduce the ambiguity of the results. This is best explained by example.

Consider a fluctuating flow with an underlying periodicity, as depicted in Figure 2.9(a), represented here by a sinusoidal function. In such a case, the voltage output of the hot-wire anemometer follows the velocity trace, as depicted in figure 2.9(b). Thus, the change of flow velocity is captured by the system. Now, consider the velocity fluctuating about a zero mean, i.e. a change of flow direction occurs, figure 2.9(c). Because of the hot-wire probe's ambiguity to changes in flow direction, the resulting output is the absolute value of the velocity trace, figure 2.9(d), that is, the hot-wire anemometer converts all negative velocity input to positive voltage output. On first inspection one might assume that this represents the true velocity fluctuation, and hence incorrect oscillation frequency could be assumed.

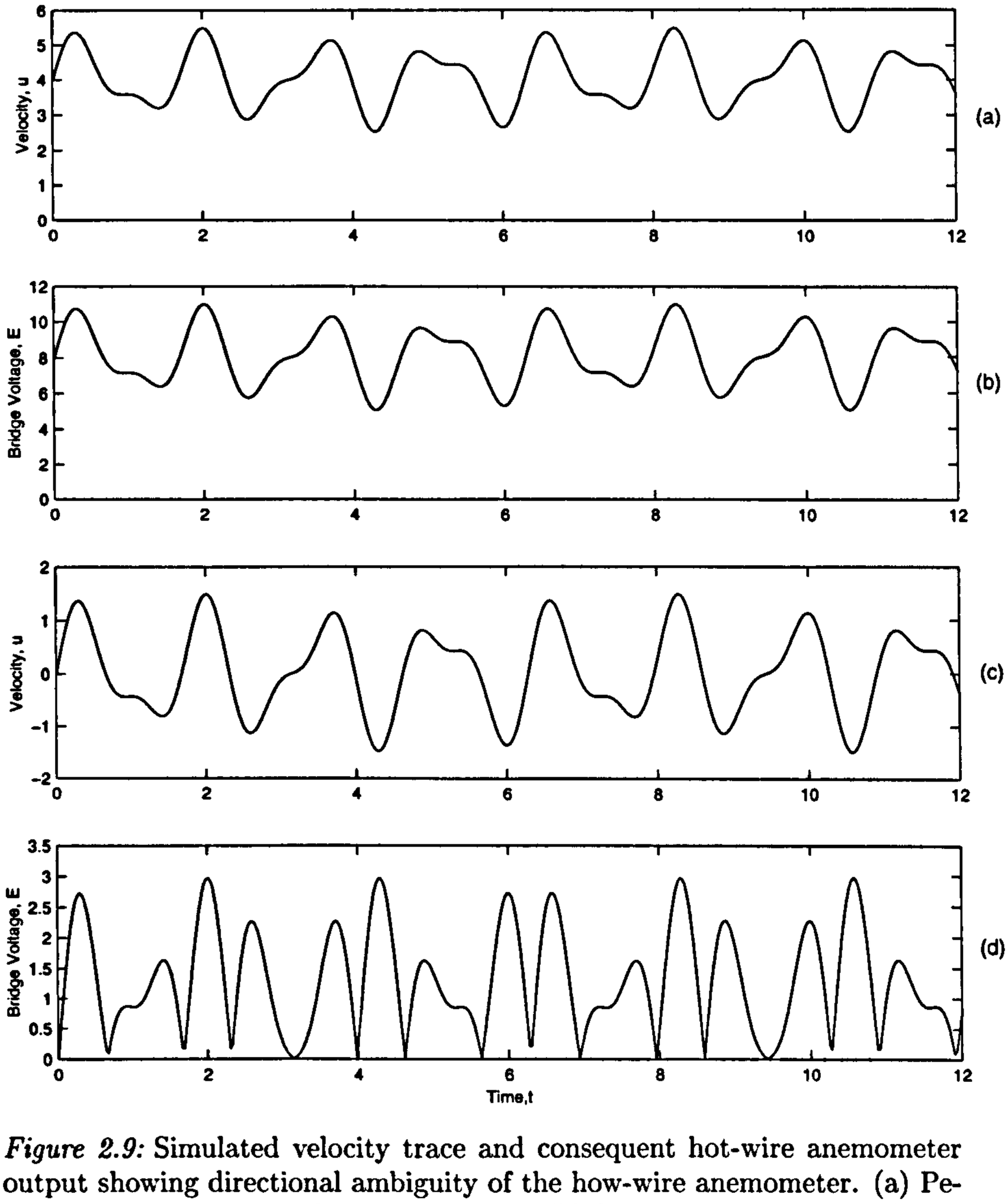

Figure 2.9: Simulated velocity trace and consequent hot-wire anemometer output showing directional ambiguity of the how-wire anemometer. (a) Periodic velocity trace with positive mean; (b) hot-wire output for velocity trace in (a); (c) periodic velocity trace with zero mean; (d) hot-wire output for velocity trace in (c).

This ambiguity stems from the heat transfer from the wire. The anemometer output reflects the amount of heat lost from the filament to the flow, which in turn is related to the perpendicular velocity magnitude of the flow past the wire. Hence, in the ideal (an infinite wire with no prongs or support), if the wire were to be placed in a uniform uni-directional flow and then rotated about its axis, no discernible change in the voltage output would be observed as the velocity magnitude of the flow past the wire, and hence the heat transfer from the wire, would remain constant.

Hot-Wire Calibration

In order to accurately measure the velocity of the flow, a probe first needs to be calibrated for its application because the anemometer does not measure absolute values. For SN probes, a relationship exists between the output voltage and the flow velocity. When considering one-component velocity measurements alone, as here, then the relationship is simply $E = E(u_N)$, where u_N is the velocity component normal to the wire axis. For yawed SN probes, this relationship does not hold as a dependence on the yaw angle exists, and hence also on the two components of the velocity.

Calibration involves exposing the hot-wire probe to a variable uni-directional steady flow with a low turbulence intensity. This flow must be perpendicular to the filament, and the stem orientation must be noted as this influences the recorded velocity (Bruun, 1995) and is discussed below. Typically, calibration is carried out using a specialised nozzle-calibration device, or within a wind-tunnel. Calibration requires that the flow velocity is varied and the anemometer output recorded, thus generating a series of data points. Bruun (1995) recommends that 10 to 30 evenly spaced points are recorded over the velocity range, although TSI Inc. (1997) suggest that this be biased such that approximately $^2/_3$ of the data points lie in the first 25% of the velocity range as $\mathrm{d}E/\mathrm{d}u$ is considerably larger in this region. The resulting curve shows the non-linear relationship between voltage and velocity.

Errors can easily creep into the calibration process at any stage and the user of the system needs to be aware of the main sources of error and how to best avoid excess.

Owing to the fact that no calibration facility is perfect, and that changes in the flow will always occur, it is commonly acknowledged that time-averaged readings of velocity and anemometer voltage should be taken during calibration. It is suggested (Bruun, 1995; Perry, 1982) that a measurement time in the order of 10 - 30 seconds is sufficient for such purposes. Likewise, the velocity is often found indirectly by measurement of dynamic pressure (i.e. $p_o - p_{atm} = \frac{1}{2}\rho\overline{u}^2$) through use of pressure transducers or manometers. These devices are often attached via tubing, and the volume of gas within these tubes requires time to react to the changes in the pressure, hence adequate time should be allowed for the fluid to settle before a reading is taken. There are also advantages and disadvantages for using dedicated calibration equipment such as a portable nozzle-calibration device. Such devices offer consistent results and ease of use; however, they also require that the probe be moved which in turn can lead to further problems with inconsistencies. Also, when using such a device the probe can present a large blockage to the flow leaving the nozzle which can lead to an incorrect velocity reading (Khan, MacKenzie & Bruun, 1987); this is discussed further below. Ideally a probe would be calibrated *in-situ* as this requires no movement of the probe, no disconnections of equipment, and utilises the same flow generation as the actual experiments. Usually this is not practical and other means are needed. Bruun (1995) has, however, successfully adapted part of a nozzle-calibration device to be used as a removable part of his experimental equipment such that the probe remains *in-situ* during calibration.

Calibration is carried out over a velocity range of interest. This range of velocities may be quite large, and hence errors can creep into the calibration procedure. For a more precise calibration a narrow velocity range should be considered to provide a more agreeable curve fit over the range in question. Should a large range of velocities need to be be studied, improvement in accuracy is achieved by segregating the range into a series of smaller ranges and performing multiple calibrations. Alternate calibration equations have been suggested that provide an improved curve fit over a larger velocity range (Siddall & Davies, 1972); however, such improvements are usually negligible (Bruun, 1995), as will be discussed below.

Norman (n.d.) notes that normal calibration techniques in gases can be flawed at high speeds owing to the effects of compressibility. In order to take the compressible effects into account, Norman (n.d.) included the density and mass-flux in the derivation of the heat transfer relationship, as King's law (see equation (2.27)) does not hold at high subsonic speeds. At these higher flow rates, cooling of the wire reaches a peak, and then drops off again, hence causing ambiguity in the calibration. Norman (n.d.) also notes that equation (2.25) is only valid if the Knudsen number is below 0.01; where the Knudsen number is defined as $\mathrm{Kn} = l_m/d_w$, and l_m is the mean free path of molecules, and d_w is the wire diameter. He suggests that a number of calibration curves should be carried out for different values of Kn. Results showed that the heat transfer reduces as Kn and the Mach number, M, increase, provided the stagnation temperature does not change considerably.

Hot-Wire Calibration Equations

Once a set of data points have been recorded, a relationship between the voltages and velocities must be established. Several possible equations exist that can be used for a response equation. Bruun (1995) outlines the most popular methods and their advantages and disadvantages and suggests that the choice is down to a balance of accuracy to ease of use. Perhaps the most common calibration equation is the power law proposed by King (1914), which is given as:

$$E^2 = A + Bu^n, \tag{2.27}$$

where A and B are empirical constants. King found that a value of $n = 0.5$ performed adequately for his investigations of flow around an infinitely long cylinder in cross flow. However, Bruun (1995) has reviewed work by several authors to conclude that an improved curve fit is obtained through use of a value of n in the range $0.4 - 0.45$. For example, Collis & Williams (1959) have developed an alternative heat-transfer law with dependence on the power of 0.45 for Reynolds numbers below that of the onset of vortex shedding from the wire. However, it is clear that the value of n is best investigated for the application at hand, and as such a least-squared curve-fitting method should

be used to find the optimum value of n. Perry (1982) also investigates the variation of parameter n and compares his results to a dynamic calibration (whereby the probe itself is moved with sinusoidal motion in a steady flow), again finding that the value of n depends on the specific flow in question. Bruun (1995) shows that use of an optimum value of n gives a substantial reduction in the error in local velocity reading over the entire velocity range.

Perry (1982) also investigates the claims of some authors that the longitudinal component of velocity also has a cooling effect on the wire, and hence that the probe should be sensitive to velocity fluctuations parallel to the wire. This was achieved by replacing the velocity component in the mean-flow direction, u, in equation (2.27) by $u_e^2 = u^2 + C^2 u_P^2$, where the subscripts e, and P, refer to the effective and parallel velocity components, and the constant, C, is equal to 0.2. Using a combination of the binomial theorem and Pythagora's rule, and assuming that fluctuations are small, Perry showed that the sensitivity of the wire was a function of $\overline{u}$ alone,

$$K_u = \frac{nB}{2\overline{E}(\overline{u})^{1-n}}, \tag{2.28}$$

where K_u represents the probe sensitivity, and $\overline{u}$ represents the mean velocity. Note the similarity to differentiation of equation (2.27) which represents the gradient $\mathrm{d}E/\mathrm{d}u$, although here equation (2.28) uses the mean velocity. This gradient is dependent on n, and in order to produce a more satisfactory calibration curve the use of dynamic calibration is suggested (Perry, 1982).

In addition to the basic power law of equation (2.27), several other calibration equations exist. These include extended power laws, whereby a further term is incorporated into the basic equation (Siddall & Davies, 1972), curve fitting by splines, and polynomial curve fits. These methods have been compared to the basic power law by Bruun (1995) who finds that for most purposes the simple power law and the polynomial curve fit provide adequate results.

Hot-Wire Orientation and Disturbance Issues

Khan et al. (1987) have investigated the blockage effect of a probe with respect to a calibration nozzle and note that considerable change in the recorded velocity is observed depending on the orientation of the probe stem. Comparisons between a plated and unplated probe (with 3 mm diameter stem) orientated parallel and perpendicular to a nozzle flow were made for a number of different nozzle areas (12 - 120 mm^2) and also within a wind-tunnel. Their findings indicate that with a parallel orientation, the probe tends to offer a much larger blockage to the nozzle, as expected. This blockage decreases as the nozzle area increases; however, the recorded velocity never reaches the same levels as those recorded in a wind-tunnel (effectively an infinite-area nozzle), thus showing the blockage should not be discounted even when using large nozzles. For a plated probe, a difference of 3% was observed in interpreted velocity between the smallest and largest nozzle areas, and a difference of 3 - 4% in interpreted velocity between the largest nozzle area and the wind-tunnel reading. This variation increases to approximately 4% and 8% respectively for an unplated parallel-orientated probe.

For a plated probe (DANTEC 55P01) orientated perpendicular to the flow (i.e. $\beta = 90°$) the difference in interpreted velocity readings was negligible for all nozzle areas with a maximum difference at low velocities ($\sim$10 m s^{-1}) of approximately 1%. For an unplated probe (a DANTEC 55P11, as used in this investigation), the blockage effect is greater again, although still reduced from the parallel-probe configuration (approx. 3% difference over the nozzle range). The reason for the difference between the probes is due to the probe and nozzle dimensions; a plated probe has the element removed from the prongs, whereas the element of an unplated probe extends to the ends of the prongs. The plated probe used had a prong spacing of 3 mm, and a prong length of 8 mm, and the smallest nozzle diameter used was 3.9 mm. The unplated probe has a prong spacing of 1.5 mm. Hence when the plated probe is exposed to the flow only the element and the very tips of the prongs are exposed, and in the case of the unplated probe a higher proportion of the prongs are also exposed to the flow. In both cases, as the area of the

nozzle is increased so more of the probe is exposed to the flow and thus the deviation of interpreted velocity increases. In this orientation, the difference in interpreted velocity between the 120 mm^2 nozzle and the wind-tunnel test was approximately 3.5% and 2.5% for the plated and unplated probe respectively.

In a related study, Comte-Bellot, Strohl & Alcaraz (1971) have investigated the aerodynamic disturbance caused by the probe prongs and stem for a number of probes and probe orientations. These authors set out to determine the effect that the separate parts of the probe have on the flow, i.e. the stem, and the prongs for most applications. This was carried out by using four hot-wire probes (DISA 55A25, DISA 55F11, a modified DISA 55A25, and a reference probe), a special probe to establish the perturbations from the prongs alone, and a plain DISA stem. The exact configuration and dimensions of the probes can be found in the paper by Comte-Bellot et al. (1971). The probes were tested in a jet flow with a velocity of 7 m s^{-1} at a location of $x/d = 0.25$, where the diameter, $d = 80$ mm, and x is the axial distance from the jet outlet. Rotation tests, whereby the probe pitch angle is varied through $\pm 90^{\circ}$ and velocities recorded, were carried out for each of the sensing probes. The results showed that a predominantly symmetrical relationship existed, i.e. the two perpendicular orientations read the same velocity. However, the modified probe showed a non-symmetric reading owing to the wire not being soldered perfectly central on the prongs; highlighting the need for extra care in repairing probes. Of the probes tested, it was found that the reference probe (a probe with long fine prongs) provided the least sensitivity to pitch angle, being almost independent of β. And the standard DISA 55A25 probe (similar topology to the DANTEC 55P11 used here) showed the largest sensitivity to pitch angle with a 20% increase in velocity at $\beta = \pm 90^{\circ}$.

Having established the symmetry in the readings, further tests were carried out by Comte-Bellot et al. (1971) to determine the individual effects of the stem and prongs. This was achieved by positioning a reference probe upstream of a disturbing body (a DISA stem, or small cylinders) and varying the orientation of the disturbing body and varying the distance of the disturbing body from the reference probe. The tests

show that the closer the disturbance to the probe, the greater its influence to the recorded velocity, with the higher perturbations occurring with the probe orientated perpendicular to the flow (i.e. $\beta = 90°$). A parallel-orientated disturbance increases the blockage effect and hence a reduction in velocity is observed. When the disturbing probe is perpendicular to the flow the velocity recoded by the reference probe increases in comparison to that recorded in the absence of the perturbing body. This can be explained by the flow having to accelerate around the body in question. It was found that a *neutral angle* existed for each case at $\beta = 45°$ where the blockage and acceleration effects were balanced (Comte-Bellot et al., 1971). This can be seen in Figure 2.10 which shows the perturbations from a stem, prongs and wire for a DISA 55A25 probe. Comparison of all the tests highlighted that the perturbation by the prongs is generally the larger, which agrees with the findings of Khan et al. (1987) discussed above. The findings show that the perturbation varies inversely to the prong spacing at $\beta = 90°$, and inversely to the square of the prong spacing at $\beta = 0°$. Perturbations from the probe stem were found to vary approximately to the square of the stem diameter and inversely to the square of the distance between the wire and stem at any orientation. Further, the perturbations of each component can be effectively added to find the total perturbating effect of the probe. As a final check, these authors performed an irrotational, inviscid flow solution over the prongs and stem at parallel and perpendicular orientations. Good agreement was found between the empirical and analytical results when temperature changes along the wire are taken into account.

In a similar study performed some time later, Adrian, Johnson, Jones & Tung (1984) investigated the pitch, yaw and combined pitch and yaw sensitivities of a number of probes, including some of the probes used by Comte-Bellot et al. (1971). Their aim was to develop a theory, based on slender-body theory, for pitch and yaw effects in terms of the aerodynamic disturbances and heat transfer effects on hot-wire probes. Their experimental procedure consisted of pure pitch and yaw rotation tests and a combined study, but with the inclusion of aerodynamic disturbances brought on by the probe itself. This is achieved through considering the actual velocity vector at the wire as

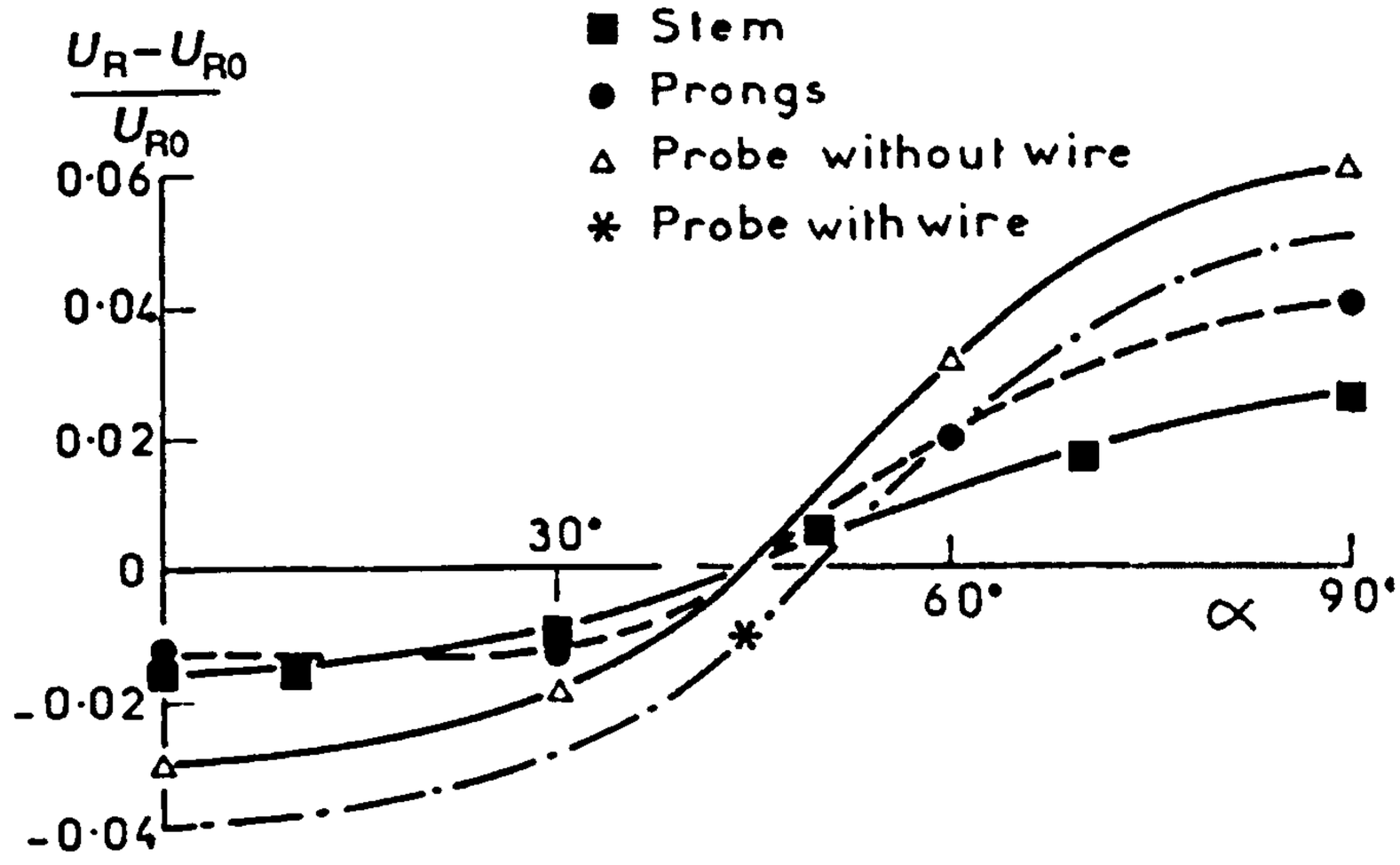

Figure 2.10: Perturbations from the individual components of a hot-wire probe, in relative order of magnitude, reproduced from Comte-Bellot et al. (1971). Here, U_R and U_{R0} are the velocities recorded by the reference probe with and without the perturbing body present; and α represents the yaw angle of the probe, i.e. β in the context of Figure 2.6.

opposed to the usual use of the free-stream velocity. The results of the pitching test agree well with those of Comte-Bellot et al. (1971) with a velocity increase at pitch angles $\beta \geq 0^o$. Each probe used in their investigation was scrutinised under a microscope to gauge its quality of construction. They found several probes with mis-positioned wires, others with bent sensor wires, and a few probes with differing prong tip diameter. Each of the non-perfect probes showed asymmetry in the recorded velocity in the pitch-rotation tests. It is suggested by Adrian et al. (1984) that many commercially available probes will suffer from such conditions and therefore this should be taken into account. The slender-body theory developed suggests a sine-squared relationship for pitching effect which matches the presented experimental results to a good degree. Comparisons of their theoretical and empirical results suggested that the pitching sensitivity was an artifact of aerodynamic disturbances alone, whereas the yawing sensitivity was an artifact of the aerodynamic disturbances, convective heat transfer due to flow parallel to the sensing wire, and conductive end losses (Adrian et al., 1984).

The experimental investigations of Adrian et al. (1984) were carried out over a veloc-

ity range of approximately 5 - 91 m s^{-1}, thus giving a much larger spread of results than the study of Comte-Bellot et al. (1971). Their findings show that the pitch sensitivity from a probe decreases with an increasing velocity, owing to a reduced thickness of the boundary layer over the prongs. These authors suggest that the boundary layer has significant effect below 9 m s^{-1}, i.e. below the velocity range studied by Comte-Bellot et al. (1971). The final part of their investigation briefly looked at the noise response of hot-wire probes and highlighted that periodic signals were being produced over the entire velocity, pitch, and yaw range. The frequencies were compared to the estimated vortex-shedding frequencies of the probe prongs; however, the observed frequencies were a factor of two greater than the estimated frequencies. Comte-Bellot (1976) also gives a brief account of previous work on aerodynamic perturbations of hot-wire probes.

Van Thinh (1969) has investigated hot-wire measurements in the vicinity of a solid wall and noted considerable difference in the recorded velocity depending on orientation and aspect ratio of the probe. In both measurements of mean velocity and of velocity fluctuations, it was observed that a probe orientated perpendicular to the flow over-predicted the magnitude of velocity. However, the measurement of turbulence intensity (u'/U) was under-predicted in this orientation. Mean velocity measurements were more affected by the aspect ratio of the probe wire. The lower the aspect ratio of the wire, the greater the dependence of mean velocity on the probe orientation. This effect is not observed with the velocity fluctuations. These differences are partly due to the cooling effect of the wall on the hot-wire probe (van Thinh, 1969). Lange, Durst & Breuer (1999) have investigated the effects of wall proximity on hot-wire readings using a numerical simulation of the probe wire. Their simulations showed that for a perfectly heat-conducting wall the temperature gradient in the vicinity of the wire is greatly affected owing to the additional heat losses to the wall, and hence the velocity measured is also over-predicted. With a perfectly insulating wall, the temperature gradient between the wall and the wire is reduced owing to heat accumulation in this region; this in turn reduces the measured velocity of the probe. It is clear from the studies that the type of wall material must be considered when making corrections to

velocity readings at the wall (Lange et al., 1999).

Perry & Morrison (1971) (and expanded on by Perry (1982)) have performed an investigation into the vibration of the hot-wire element and have shown that such phenomena should also be taken into consideration when using hot-wires. Such effects have also been reported by Collis & Williams (1959) who observed a change in the heat transfer from the wire as vortex shedding occurred from the wire. A hot-wire used in CT mode for the measurement of velocity fluctuations is generally operated at a high overheat ratio to ensure good velocity sensitivity. Operating at such an elevated temperature causes thermal expansion of the element and subsequently the element buckles (Perry & Morrison, 1971). In addition a hot-spot is generated in the buckle itself thus generating an asymmetric temperature distribution within the element (Perry, Smits & Chong, 1979; Perry, 1982).

The buckling of the element leads to further aerodynamic disturbance in addition to vortex shedding which can occur for Reynolds numbers (based on wire diameter) of 44 or more. Hot-wires have a low elastic resistance to lateral aerodynamic loads, and thus with a buckled probe the wire tends to rotate about its axis under aerodynamic loading (Perry et al., 1979). When vortex shedding occurs from the wire, Perry & Morrison (1971) have shown that the wire tends to oscillate with a circular motion with a frequency equivalent to the frequency of vortex shedding from the wire. This skipping of the wire leads to erroneous velocity readings as the wire is now moving relative to the flow. Perry & Morrison (1971) note that the error in velocity perturbation readings is evident with a vibrating wire, but is negligible with a purely bent wire. Bruun (1995) also notes several authors who have investigated the vibration effects of the prongs, noting specifically that the prongs tend to vibrate when the pitching angle is in the range, $60^{o} \leq \beta \leq 120^{o}$, owing to vortex shedding from the prongs. It is because of this phenomenon that hot-wire probes are often manufactured with some slack in the wire (Bruun, 1995). Such findings are confirmed by Widell (n.d.) who looked at the deformation of probe wires under aerodynamic loads, and under particle impacts.

Hot-Wire Measurements

Once data have been obtained using a hot-wire anemometer system, it is often necessary to perform some method of analysis to turn the data into useful information. This may be a simple case of filtering the signal to remove certain parts, or a simple frequency analysis to determine any periodicity in a signal. Typically, for many turbulent flows, a higher level of analysis is required in order to make sense of the flow. Bruun (1995) gives an excellent account of several methods of data analysis for turbulent flows, such as phase-locked-averaging techniques, determination of intermittency, conditional-sampling techniques, amplitude-domain analysis, and spectral-density functions.

When considering random flow phenomena (i.e. a flow that cannot be described by explicit mathematical relationships), it is necessary to know what form the random process is before any analysis may be carried out. Random processes can be divided into stationary and non-stationary processes and the former can be further split into weakly-stationary and strongly-stationary processes. This is discussed in chapter 5.

Chapter 3

Computational Predictions

3.1 Introduction

In this chapter the computational modelling of the throttle body is described and discussed. Section 3.2 describes the throttle body geometry itself before section 3.5 through section 3.7 describe the computational modelling techniques and model set-up used in the investigation. Finally, section 3.8 presents and discusses the findings of the computational investigation, with additional discussion and comparison of the predictions to experimental measurements made in chapter 6.

3.2 The Throttle Body Geometry

As previously described, the throttle body under investigation forms part of the intake system of a (port) fuel-injected engine. The fuel is delivered to the engine by spray injectors into the inlet port of each cylinder, and these are electronically controlled by the engine management system based on current operating conditions. Thus the primary role of the throttle body is to control the delivery of air entering the plenum chamber that is then fed via inlet runners to each cylinder, and hence the computational modelling is concerned with only one fluid medium, i.e. air. The throttle body is of standard configuration with a butterfly valve used to control the flow that is situated in the throat of the body. A schematic cross-section of the throttle is depicted in Figure 3.1 that shows the butterfly valve relative to the body, and indicates the flow direction from left to right. Note that the valve seals at approximately 6.9° and all throttle opening

angles quoted herein are relative to this closed position.

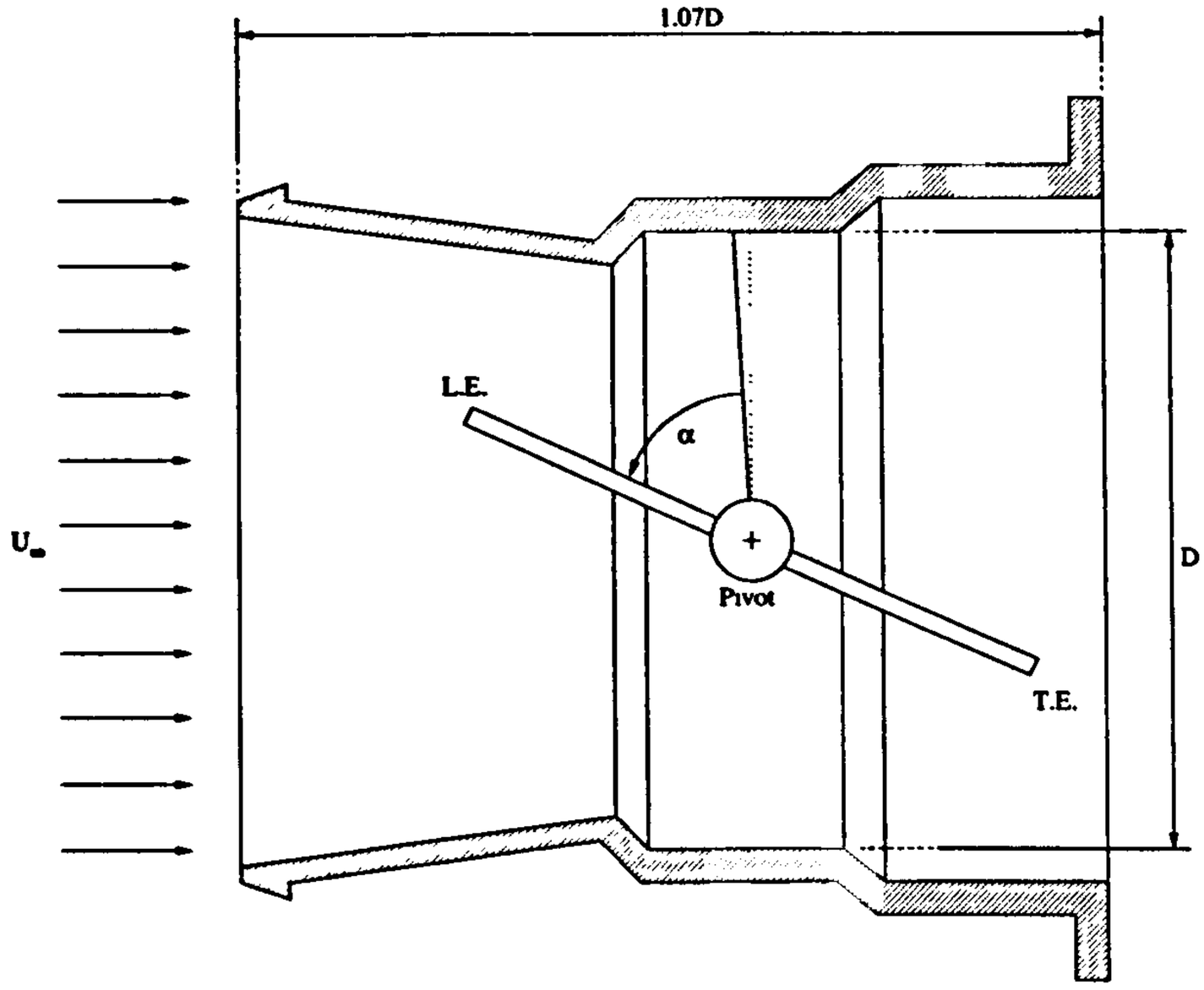

Figure 3.1: Schematic of the Jaguar throttle valve through the central cross-section.

For the remainder of this document, the throttle angle, α, will be regarded as the angle of the valve relative to its sealing position (as depicted). In addition, the upper left tip of the valve of Figure 3.1 (i.e. the edge facing the oncoming flow) will be termed the leading edge, whilst the lower right edge will be termed the trailing edge in a manner analogous to aerofoil theory.

When situated in the engine bay, a 90° elbow exists in the inlet tract upstream of the throttle body (owing to packaging) that has been shown in previous investigations to significantly affect the flow over a butterfly valve, Morris & Dutton (1991). However, the elbow has not been incorporated into the computational models in order to realise a simple investigation, and to maintain consistency with the experimental investigation. Although this omission leads to an unrealistic situation with regards to true engine simulation, a more practical investigation can be realised.

Similarly, under real conditions, the outlet of the throttle valve is attached to a short manifold which feeds air into the plenum chamber of the engine. As in the case

of the inlet, the manifold has been omitted from the investigation and been has been replaced by a straight circular tube. Work has previously been carried out into the flow through a plenum system by Lee, Shaw & Pierson (1997*a*), Lee, Shaw & Pierson (1997*b*), and Shaw et al. (2000), which may be of further interest. In their study the authors have investigated the flow through a plenum chamber of a V8 engine using computational and experimental methods. For the computational study these authors have investigated the effects of using various differencing schemes and turbulence models before using the unobtrusive advantage of CFD to investigate the shape of the plenum to inlet runner interface. The computational predictions were compared to experimental measurements made with a LDA system that indicated a good agreement between the two and suggests CFD is a practical tool for engine design.

Both the inlet and outlet manifolds of the throttle body additionally incorporate the breather-system nozzles, located so as to take advantage of the pressure differential generated across the valve. These have also been omitted from the computational models, and have been subsequently blocked in the experimental investigation in order to reduce the complexity of the investigation.

Here, the throttle-body geometry originates from a CAD model that represents the exact geometry of the throttle body. However, in order to generate a suitable CFD model the geometry has been modified to remove unnecessary components and to simplify some areas for improved spatial discretisation. The final CAD geometry consists of a fluid volume and valve with no external throttle components necessary. Details of the modelling assumptions will be discussed in section 3.5.

3.3 Fluid Properties

For accurate modelling of flows the computational model should reflect physical reality as well as possible, which includes the correct specification of geometry, boundary and initial conditions, and fluid properties. Often the choice of medium may be different to that used in the native environment, for example, for their studies Huang & Kim (1996) have used water as the working fluid through throttle valves, although in their native

operating environment this would be air. Such a change is permissible provided the flow is of the same Reynolds number. Ultimately, the availability of experimental facilities may prove to be more influential on the final decision of the fluid medium. It may be that only water-testing facilities are available, and hence the choice of the fluid medium would reflect this. Although this would be different to the native conditions, it can be argued that a closer comparison of the numerical and experimental results is possible, as a like-for-like comparison can be made. Here a bespoke experimental flow-rig has been constructed that uses an air compressor and hence the working medium for the CFD calculations is air as used in the native environment. Table 3.1 describes the main fluid properties used for the computational investigation.

Fluid Property	Value
Density, ρ	1.205 kg m^{-3}
Molecular viscosity, μ	1.81×10^{-5} kg m^{-1} s^{-1}
Molecular mass, M	28.96 kg mol^{-1}
Gas constant, R	287.1 J kg^{-1} K^{-1}
Thermal conductivity, k	0.024 W m^{-1} K^{-1}

Table 3.1: Thermo-physical properties of air at 20°C and 1 bar.

Given that local flow velocities exceed a Mach number of 0.3, the effects of compressibility need to be incorporated into the governing equations. For compressible flows, STAR-CD calculates the density of the flow using the equation of state, equation (2.6), expanded as below:

$$\rho = \frac{p}{R_o T \left(\sum_i \frac{m_i}{M_i} \right)}, \tag{3.1}$$

where, m_i is the mass fraction of a fluid (i) with molecular mass M_i; p is the fluid pressure and T is the fluid temperature. As only one medium is considered the equation simplifies to its most common form shown in equation (3.2) below,

$$\rho = \frac{pM}{R_o T} = \frac{p}{RT}. \tag{3.2}$$

The gas constant, R, has been calculated from the molecular mass of the fluid, M, and the Universal gas constant, $R_o = 8.3143$ kJ kg^{-1} K^{-1}, using $R = R_o\, M^{-1}$.

3.4 Boundary Conditions

In the process of setting up a CFD model the boundary conditions to the problem are normally applied after the mesh has been generated. However, through formulation of the problem the user should have in mind the boundary conditions that are required, or the possible combinations that exist. In addition the user will need to have knowledge of the flow, or a good appreciation of how the flow may behave in order to specify suitable boundary conditions to the problem and generate a suitable grid to model the flow.

Numerous types and combinations of boundary conditions are available within STAR-CD, their relevance depending on the flow in question. It is of vital importance that the correct boundary conditions are applied and that they are placed in the correct locations for the solution to be successful. For this particular case only a limited number of combinations are valid. In particular the use of prescribed in-flow velocity boundaries, prescribed pressure boundaries, and out-flow boundaries are permissible as the main flow boundaries. In addition, the use of wall, baffle, and symmetry plane boundaries are available for all flows. For the predictions presented here, a prescribed inlet-flow and a prescribed-pressure boundary have been used at the inlet and outlet of the domain respectively. Combinations of inflow-outflow, pressure-pressure, outflow-pressure, and pressure-outflow boundaries have additionally been evaluated; however, the combination of a prescribed inflow and prescribed pressure boundary has proved to be the most reliable combination for the investigation.

Throttle angle α (°)	Mass flow rate $\dot{m}$ (gs^{-1})	Velocity magnitude U_∞ ($m\,s^{-1}$)
3.5	8.43	1.82
5.8	13.50	2.91
8.3	17.36	3.74
12.5	20.65	4.45
19.0	80.00	17.25
30.0	147.00	31.70
47.0	267.00	57.58
60.0*	347.80	75.00

Table 3.2: Mass-flow data supplied by Jaguar Cars and the corresponding derived mean velocity applied at the inlet boundary of the computational models. * indicates extrapolated values.

3.4.1 Inlet Boundary

An inlet boundary condition has been applied to the inlet face of the computational domain, i.e. at the opening of the inlet runner, approximately 2D upstream of the true throttle-body inlet. Such a boundary condition applies fixed velocity components at the face in question, or a velocity profile that is specified by the user. Here a fixed velocity has been applied across the cell faces at the inlet ($\overline{u}$ = const), parallel to the axis of the domain. The velocity magnitude specified at the boundary has been derived from mass flow obtained from one-dimensional flow simulations and engine tests carried out at Jaguar Cars Ltd. (1999). Table 3.2 gives these values. For the smaller opening angles (3.5° to 12.5°) the data have been obtained from an instrumented supercharged engine, with the larger angle data (19° to 47°) generated through the 1D simulation code MANDY (Jaguar Cars Ltd., 1999). The value at 60° has been added to extend the range of the investigation, and is based on linear extrapolation of the higher-angle flows. Direct specification of the mass-flow rates through the domain was also considered through use of an outlet flow boundary condition; however, this proved to provide an unstable solution owing to the model being over-constrained.

In addition to the velocity at the inlet, the density is specified as given in Table 3.1, and, as the k-ε turbulence model is being used, the values of the turbulence kinetic energy, k, and dissipation rate, ε, must also be specified at the inlet. Ideally these values are derived from experimental measurements; however, the simulations were carried out before the experimental investigation and therefore the values have been approximated using standard methods and information from previous studies. The value of turbulence kinetic energy can be evaluated using the mean flow velocity and turbulence intensity through equation (3.3), and the associated dissipation rate via equations (3.4) and (3.5) below (Bruun, 1995; Computational Dynamics Ltd., 2001; Versteeg & Malalasekera, 1995; Wilcox, 1994),

$$k = \frac{3}{2}(U\ Ti)^2, \tag{3.3}$$

$$\varepsilon = \frac{C_\mu^{3/4} k^{1/2}}{l}, \tag{3.4}$$

$$l = 0.07L. \tag{3.5}$$

Here, U is the characteristic velocity of the flow; Ti is the turbulence intensity; C_μ is an empirical coefficient of the k-ε model; l is the mixing length; and L is characteristic length of the flow. For the current study, the characteristic length was set to the diameter of the throttle body, C_μ was left as the default value of 0.09, and the turbulence intensity was set at 10%.

3.4.2 Pressure Boundary

At the domain outlet, a prescribed pressure boundary has been applied to the cell faces with a constant pressure of 1 atmosphere (1.013×10^5 Pa); this reflects the experimental set-up. The outlet of the domain is sufficiently far downstream of the valve that the pressure can be assumed to be uniform and the flow steady and uni-directional thus reducing the risk of numerical instability (Computational Dynamics Ltd., 2001).

STAR-CD calculates the velocities at the cell faces using momentum equations linked to the local pressure gradients, together with the continuity constraint (Computational Dynamics Ltd., 2001). Variables at the boundary cell faces are extrapolated from upstream values assuming that zero gradient exists along mesh lines intersecting the boundary surface, i.e.

$$\frac{\partial u}{\partial n} = \frac{\partial v}{\partial n} = \frac{\partial w}{\partial n} = \frac{\partial T}{\partial n} = 0. \tag{3.6}$$

The method is therefore sensitive to the mesh topology at the pressure boundary and earlier versions of the solver required extrusion of cell layers adjacent to the boundary to ensure accuracy and stability. If the flow is orientated out of the domain then the boundary acts much like an outflow boundary with values extrapolated from upstream values.

Turbulence quantities have also been specified at the pressure outlet in a similar manner to the inlet. However, for the pressure boundary specification the values are defined in terms of the turbulence intensity, Ti, and a mixing length, l. These values have been calculated using equation (3.3) through equation (3.5) for each model and specified at the outlet accordingly.

3.4.3 Wall Boundaries

The remaining surfaces of the domain, i.e. the valve and throttle walls, have the default wall boundary applied that allows the specification of a roughness height, and a local velocity profile. For the simulations carried out here an impermeable wall is used (velocity normal to the wall is zero) and the no-slip condition has been applied that states the tangential velocity to the wall is zero (thus $u = v = w = 0$), and a smooth wall assumed throughout.

For the k-ϵ turbulence model, two different approaches are available for the treatment of near-wall conditions. For low-Reynolds number flows the transport equations are solved directly in the wall region, the same as for the bulk flow with the exception that the dissipation rate is fixed according to a function inversely proportional to the

distance from the wall; this is known as a wall damping function. Such a model requires that a fine mesh is generated in the immediate proximity of the wall to model the boundary layer. For high-Reynolds number flows the boundary layer is approximated by wall functions that stem from the well-known "law of the wall" (Computational Dynamics Ltd., 2001; Tritton, 1988).

It is well-known that the turbulent flow in the proximity of a wall differs greatly from the bulk free-stream flow away from the wall. As the flow approaches the wall, the inertia-driven bulk flow gives way to flows increasingly dominated by viscous action; this leads to distinct regions of the flow. These are observed experimentally and models have been formulated to account for these regions. In the region close to the wall the flow is no longer dominated by inertia but rather the flow velocity can be defined via the function,

$$U = f\left(y, u_\tau, \nu\right), \tag{3.7}$$

where y is the distance from the wall; $u_\tau = (\tau_w/\rho)^{1/2}$ is the velocity scale, or friction velocity; τ_w is the wall shear stress; and ν is the kinematic viscosity of the flow. Dimensional considerations thus give the law of the wall as (Tritton, 1988; Versteeg & Malalasekera, 1995),

$$u^+ = \frac{U}{u_\tau} = f\left(y, u_\tau, \nu\right) = f(y^+), \tag{3.8}$$

where the non-dimensional velocity and distance to the wall have been defined as u^+ and y^+ respectively.

In the immediate vicinity of the wall the flow is dominated solely by viscous effects such that the no-slip condition applies at the wall, $u = v = w = 0$. This region shows a linear variation of velocity, u^+, with the distance from the wall, y^+, in the region $y^+ < 30$ and is termed the viscous sub-layer. Moving slightly further from the wall, but not into the bulk flow, in the region $30 < y^+ < 200$, the viscosity no longer dominates and the flow can be described by a logarithmic law,

$$u^+ = \frac{U}{u_\tau} = \frac{1}{\kappa}\left[ln\left(\frac{yu_\tau}{\nu}\right) + A\right], \tag{3.9}$$

where κ is the Kármán constant that is empirically found to be 0.41, and A is a constant. This region of the boundary layer is termed the log-law layer owing to the logarithmic relationship between velocity, u^+, and distance from the wall, y^+. Equations (3.8) and (3.9) can be simplified by the following form, as adopted by STAR-CD,

$$u^+ = \begin{cases} y^+, & \text{for the viscous sub-layer,} \\ \frac{1}{\kappa} ln\,(Ey^+), & \text{for the log-law region,} \end{cases} \tag{3.10}$$

where E is the empirical constant of equation (3.9) brought within the natural logarithm.

The high-Reynolds number k-ε turbulence model utilises wall functions which account for the near-wall velocity, temperature, energy, and turbulence distributions (Launder & Spalding, 1974). In order to use these functions, STAR-CD requires that a single near-wall cell spans the boundary layer such that its centroid is located in the range $30 \leq y^+ \leq 100$, where they (Computational Dynamics Ltd., 2001) define

$$y^+ \equiv \rho C_\mu^{1/4} k^{1/2} y/\mu. \tag{3.11}$$

The wall functions also assume that velocity variations are predominantly normal to the wall; that pressure gradients and body forces are negligible; shear stress and velocity vectors are uni-directionally aligned; turbulence energy production is balanced by its dissipation; and that there is a linear variation of turbulence length scale (Computational Dynamics Ltd., 2001). A smooth wall has been modelled with the empirical coefficient, E, in equation (3.10) set to 9.0 that is the default value for a smooth wall. Generation of near-wall cells is discussed in the following section.

3.4.4 Modelling Approximation

Using the two main boundary conditions described above means that the computational model deviates considerably from the real flow conditions of the throttle body. Under normal operational conditions, the flow through the throttle valve is driven by the engine motion itself, i.e. the air is "sucked" through the valve. In addition, because of the reciprocating motion of the engine pistons, the air is not a constant stream, but rather a pulsating flow that varies depending on the engine load, engine speed and throttle position (Heywood, 1988). However, the experimental flow rig is designed to blow air through the throttle at a constant rate thus deviating considerably from the native engine conditions. In order to provide meaningful results, the CFD model must reflect the experimental set-up, justifying the assumptions made here. Although a more sophisticated experimental rig would have been preferred, the limitations of cost and time have to be taken into consideration, as well as available equipment. Therefore these assumptions are justified.

3.5 Mesh Generation

3.5.1 Meshing Preliminaries

In order to calculate the flow through the domain it first needs to be suitably discretised such that the governing partial differential equations can be solved for each discrete volume. Generating a suitable grid requires some knowledge of the flow concerned to enable an efficient solution to be obtained. Using a highly refined mesh will provide far greater resolution to the flow; however, this may not be a computationally efficient solution as unnecessary refinement is placed in regions of negligible flow gradient. By selectively refining the grid where flow gradients are high, a more efficient solution can be obtained.

One of the difficulties in generating a CFD model is the choice of mesh type to use; again this may depend on budget, resources and needs of the investigation. The most common grid types are hexahedral and tetrahedral grids, the latter normally com-

bined with prismatic cells on flow surfaces. One of the bottlenecks of CFD modelling is the grid-generation process and so in an environment with a fast turn-around, quick grid generation is a priority (Ferziger & Perić, 1999). This has led to the increased use of tetrahedral grids because of their ability to represent complex geometries easily whereas hexahedral gridding techniques are often more complicated. This too has led to increased research and development of automated, or semi-automated, unstructured gridding techniques such as advancing-front, Delaunay, octree, and other gridding methods (Mavriplis, 1997). However, it is known that tetrahedral cells tend to generate high levels of numerical diffusion compared to the equivalent hexahedral grid and many more cells are required to obtain a solution to the equivalent resolution of a hexahedral grid.

Generation of structured hexahedral grids for complex geometries is difficult owing to the restriction of the grid itself that requires structure to the grid that is often difficult or impossible to fit to a predefined geometry without modifications being made. Hexahedral grids, owing to the nature of their topology, generally offer a more efficient solution as each cell is implicitly linked to its nearest neighbours through the discretised equations. However, STAR-CD does not make use of this advantage owing to its ability to solve flows for structured and unstructured grids of multiple cell types that requires calculation of the cell neighbour positions for each cell (Computational Dynamics Ltd., 2001).

In this investigation, there has been some choice in the available gridding package and mesh type. The pre- and post-processing software accompanying STAR-CD, PROSTAR, allows for the generation of structured hexahedral grids, one avenue for mesh generation. The second choice for mesh generation is the automatic mesh-generation package, ICEM-Tetra (ICEM CFD Engineering, 1998), which generates unstructured tetrahedral grids using a variant of the octree method (Shaw, 1992). The software also caters for the generation of prismatic cells on the surfaces of a geometry in order to provide a more suitable mesh for wall-bounded flows. Here the choice of technique has been determined by the geometry of the throttle body. As the throttle

valve is to be modelled at several angles the use of tetrahedral grids provides a much quicker and simpler solution than bespoke hexahedral grids for each angle.

3.5.2 Geometric Definition

Before a grid can be built, the defining geometry must first be generated, which leads to several problems. Firstly the input data format of the geometry needs to be compatible with the chosen mesh-generation tool. When using a commercial package the user is limited to the input data formats specified by the software and it is sometimes necessary to use a third-party data translator to obtain a suitable format. This can often lead to poor data conversion with surfaces missing, or mis-represented; holes in the geometry; poor quality in general; or even complete failure to provide an adequate solution. However, data translation and communication between large software companies is improving, meaning that conversion of data is now far more reliable than in the past. Typically a capable mesh-generation package will have a direct interface for the most popular CAD packages used in industry (e.g. Catia, SDRC I-DEAS, Pro-Engineer, SolidWorks) whereby output can be sent directly from the CAD package to the meshing software with minimal user intervention thus leading to a quick turnaround. The translator is basically a front-end for a bespoke IGES translation for each package.

A second problem is the level of accuracy maintained in the conversion process. When using the direct interface methods, the level of accuracy is usually equivalent to that of the originating CAD geometry, hence no problems should be encountered. However, in some cases, as here, an intermediate format is required to bridge the gap between CAD package and meshing software, i.e. a standard format written by the CAD package that is readable by the meshing software. In some cases this means that an approximation of the geometry is actually passed on, and thus some accuracy is lost. The level of accuracy required for the computational domain therefore needs to be determined prior to the CAD export. Here, a surface mesh has been generated on the throttle body within the CAD software and exported as a Nastran file (a faceted surface definition file originally derived from the finite-element stress-analysis package

of the same name). Thus, in this case, the surface cells approximate the geometry and they have been made small enough to capture sufficient detail for the final volume mesh. The surface discretisation should be smaller than the required volume cells otherwise the computational domain will be a poor approximation of the actual geometry.

Often the originating geometry requires modification and approximation in order to make it suitable for CFD modelling; for example, through the addition or removal of surfaces or components and extensions to the domain. Here the extents of the computational domain are governed by the throttle body walls in the radial direction; however, the upstream and downstream limits are less clear. It is rare that a computational domain is limited to the geometry in question, rather the domain extends considerably in space, especially in the downstream direction, but also in the upstream direction, and in the case of external flow investigations, the cross-stream direction. By positioning the upstream and downstream boundaries sufficiently far from the area of interest, the flow is allowed to develop sufficiently to provide a more realistic solution. Specification of boundaries too close to the area of interest tends to over-constrain the model that can lead to non-physical flows being predicted, give unstable solutions, and as such failure of the computation is common (Abbott & Basco, 1989; Computational Dynamics Ltd., 2001; Versteeg & Malalasekera, 1995).

Each computational domain used in this investigation stems from a simplified three-dimensional CAD model of the throttle body. This CAD model incorporates the throttle body walls, valve and the valve pivot, but does not include the breather-system nozzles. As discussed previously, the inlet and outlet to the throttle body have been extended in order to allow the flow to develop before entering the valve and allow the flow structures to dissipate before leaving the domain outlet. Extensions of length approximately $2D$ and $8D$ (where D represents the throttle diameter) have been used for the inlet and outlet runners respectively, based on previous studies by the author (Alsemgeest, 1998) and work by Huang & Kim (1996). An outlet extension of this length was found to be the shortest length to allow the flow to return to settled conditions without compromising the remainder of the flow. However, in certain cases the outlet domain has had to be

shortened in order to obtain a suitable solution with adequate grid resolution, as will be discussed in subsequent sections.

In addition to the extension of the domain, a geometric simplification has been carried out to the throttle valve blade in order to improve the resulting mesh quality in this region. The nature of the throttle body topology is such that as the throttle valve opens a very fine crescent-shaped opening is formed between the throttle walls and the blade edge. This can be seen in Figure 3.2(a) which shows a schematic of the problem. When generating a mesh in this region, an unacceptable number of very fine cells were required to capture the topology of the gap with sufficient detail. Under such conditions the ratio of the sizes of adjacent cells was high and this is known to adversely affect the accuracy of a solution (especially in a region of high gradient) (Ferziger & Perić, 1999). Typically a CFD code will set its own limits on the ratio of successive cell sizes; however, no specific limitation has been found for STAR-CD. Although the cell sizes can be controlled by the adjustment of the meshing parameters, the decision was taken to slightly alter the geometry in order to relieve the problem.

The original CAD model was modified such that the valve blade diameter was slightly reduced thus creating a larger gap between the throttle wall and blade. This allows for larger cells to exist in the region, and also reduces the risk of cell warpage as the crescent shape is removed. Figure 3.2(b) shows a schematic of the geometry change. This increased gap allows several good quality cells to be placed in the region to adequately capture the flow detail. Although the model deviates from reality, evaluation of a results with and without the increased gap indicate little effect on the solution in terms of the flow structures produced whilst providing a much more robust solution.

3.5.3 Grid Generation

Grid generation using ICEM-Tetra requires that the imported geometry contain surfaces, curves and points, all of which are used to constrain the grid to the geometry. As a Nastran file was used as the import format only surface data was imported and hence curves and points were generated within ICEM. The use of curves and points must be

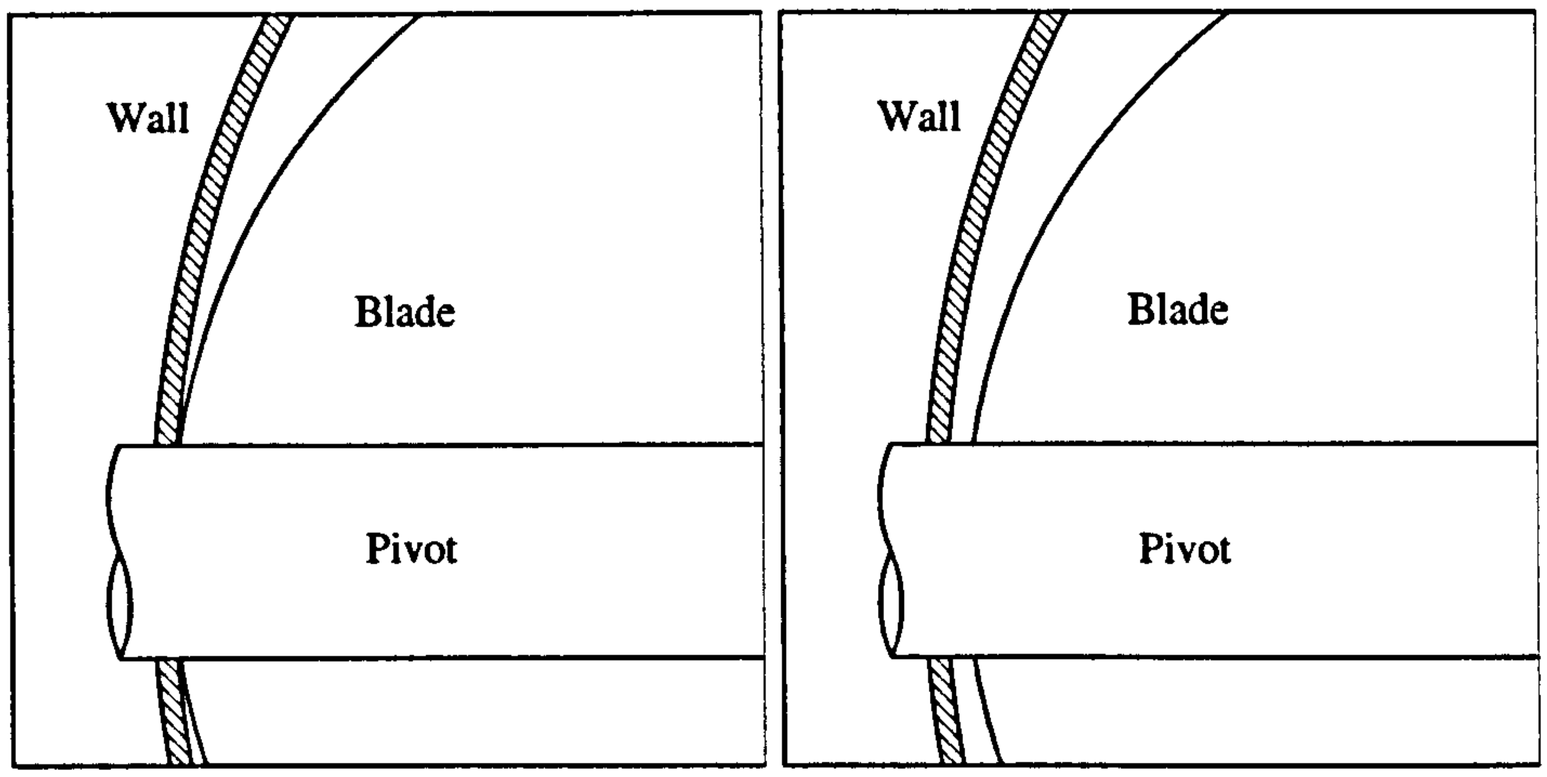

(a) Original geometry (b) Modified geometry

Figure 3.2: Schematic showing the modification made to the throttle body valve to reduce the crescent-shaped gap formed between throttle body walls and throttle valve. Both figures viewed in the plane of the valve blade, and not to scale.

carefully chosen as it is very easy to over-constrain the mesh. Generated cells are free to move on surfaces; however, a curve places the restriction that a cell edge must lie upon it, and a point restricts the mesh such that a cell corner must lie at the point. Thus curves have been limited to edges where a sharp geometric change exists, such as the valve edges, and points have only been specified at the intersection of the pivot with the blade faces and blade edges.

The overall mesh size is governed by a user-specified reference size to which all other assigned sizes are referenced. In addition to the reference size the user must also specify a maximum cell size for the entire model, and the level of refinement to be applied in complex geometric regions. Further the user is able to specify the cell sizes on the surfaces of the geometry, and also at the curves and points. Thus refinement of the entire grid is simplified to adjustment of the reference size alone. Once a suitable grid has been obtained, the cell count can be adjusted using the formula,

$$S_{new} = \sqrt[3]{\frac{N_{current}}{N_{required}}} S_{current}, \tag{3.12}$$

where S is the reference size, N is the tetrahedral cell count, and the subscripts refer to the current mesh and the required mesh. Thus within a few iterations a suitable grid can be generated whilst maintaining a consistent distribution of cells.

In order to uphold the y^+ restriction over the entire domain, the use of triangular prismatic cells is recommended. Prismatic cells are generated on the surface of the domain by extruding the existing tetrahedral cell faces and shrinking the entire tetrahedral domain (ICEM CFD Engineering, 1998). Here, the generation of prismatic cells proved unsuccessful owing to the close proximity of the throttle walls to the valve blade edge and pivot despite the modified geometry. Too many tetrahedral cells were present in these areas causing warpage, overlap, and negative volume cells to be generated. Hence for the investigation here, a carefully generated tetrahedral mesh with wall refinement has been used throughout. Although not ideal, this has provided a practical model with acceptable results produced. Each mesh consisted of approximately 270,000 cells, with increased grid density downstream of the valve, and also in proximity to the valve. Several meshes were also refined to approximately 700,000 cells, although this proved to be impractical for all cases in terms of computation time.

A typical mesh used in the investigation is depicted in Figure 3.3 where a clear distinction is present between the wall and core cells of the domain. Refinement is present over the entire wall surface, with increased cell density in the vicinity of the valve blade being necessary to ensure the correct range of y^+ in this region. The mesh shown in Figure 3.3 corresponds to a valve angle, $\alpha = 30°$, and contains approximately 650,000 tetrahedral cells.

In addition to the tetrahedral cell meshes, several hexahedral cell meshes were generated with the aim of comparing the flow predictions produced by the two cell types. These meshes were generated manually using a small self-written FORTRAN program and the pre-processing package PROSTAR. A basic raft of shell cells was defined using the FORTRAN code, and these shells were extruded to create volume cells within

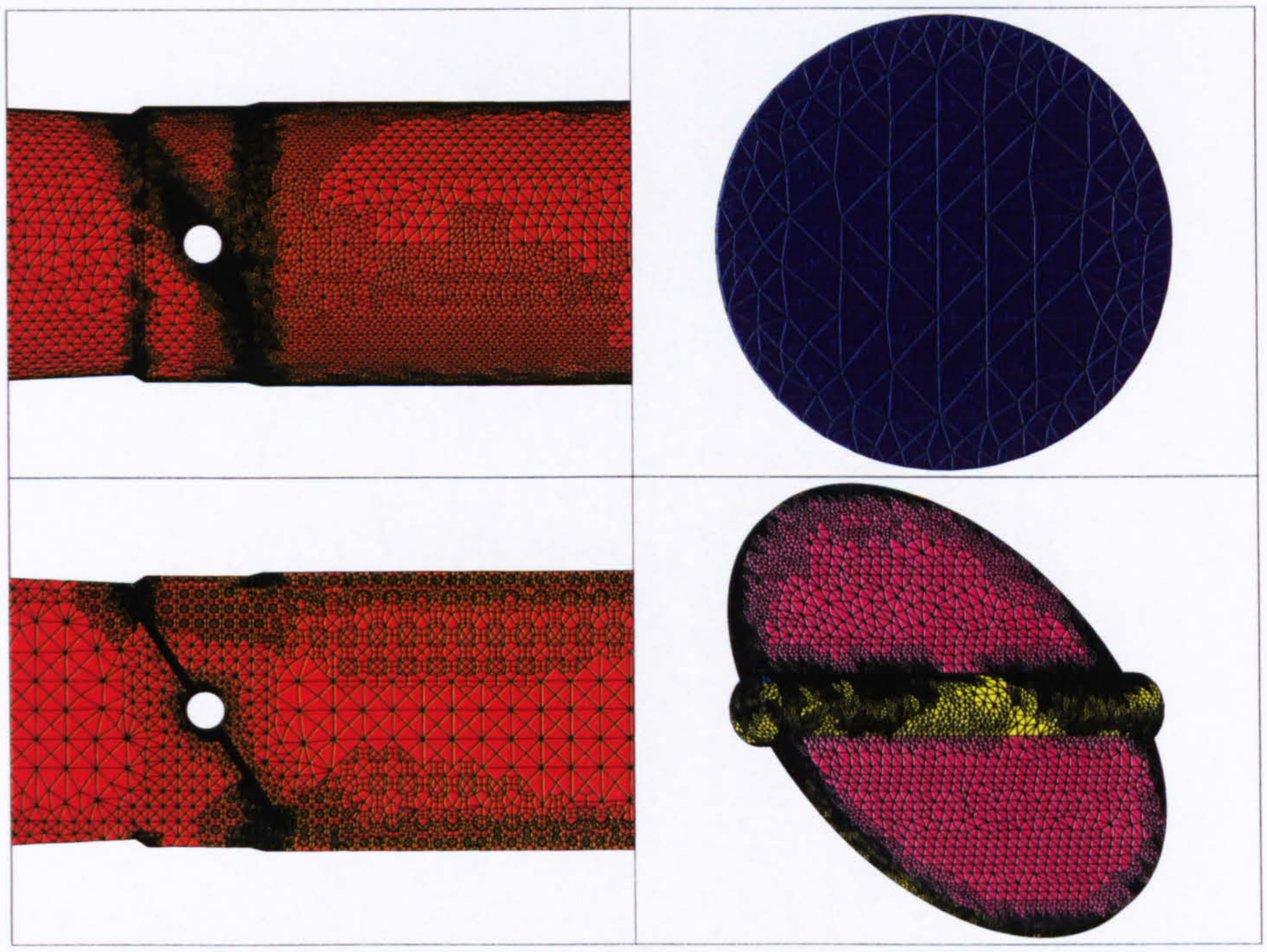

Figure 3.3: Typical computational mesh used for the investigation. A valve angle of 30° is shown, with adaptive mesh refinement leading to approximately 650,000 cells. From left to right, top to bottom: wall mesh around valve, outlet shells, section through fluid cells, and valve surface mesh.

PROSTAR. The meshes produced using this method are crude and hence they have seen little use throughout the investigation; however, further details are available in a previous publication (Alsemgeest, Shaw, Richardson & Pierson, 2000). Further development of the hexahedral cell meshes have not been carried out and, therefore, the remainder of this chapter is concerned with tetrahedral cell meshes alone.

3.5.4 Mesh Independence

Normally when conducting an investigation such as this, a study is performed into the level of grid refinement required to adequately capture a solution. This usually results in there being convergence of the solution where no further increase in grid resolution provides further gains. Thus the most computationally efficient grid can be found for a given solution. Such a task needs to be carried out for all the geometries under

investigation as significant differences in the flow field may exist and a grid tailored to one flow may not suit another.

This has been carried out here, but only to a limited degree. For a few of the throttle angles considered, grid refinement has been carried out using adaptive refinement whereby the cells of the original grid are refined in regions of high velocity and pressure gradient. Refining the grid in this way limits the overall refinement and should provide a more efficient solution in terms of cell count for solution resolution. The refinement procedure produced grids of approximately 700,000 cells with high levels of refinement around the valve where pressure gradients are highest, and also in the wake of the leading and trailing edges where high velocity gradients exist.

Further grid refinement was also investigated by generation of a new mesh from scratch that resulted in cell counts of over 1 million cells. The increase in cell count also increases the computational resources required to store the model and significantly increases the solution run time required to obtain a converged solution. Solutions using refined grids have thus been limited. Results from the models do, however, show improved resolution of the flow with the main flow features more clearly defined. In addition, more small-scale detail is captured by the refined grid, such as separation and recirculation behind the pivot and in the steps of the throttle body walls. Such features are typically smeared by the coarser grids.

Despite the increased resolution, the refined grids did not predict any significant differences to the dominant flow features to warrant their use throughout the investigation, thus the smaller-sized grids were used for the remaining investigation. However, in some instances the grids have been refined locally in order to improve the solution without significantly affecting performance.

3.6 Initial Conditions

The initial steady-state modelling of the valve flows proved inadequate to capture the flow and hence transient calculations were employed. Because of the more complex nature of the problem, the solution process had to be split into a series of stages in order

to obtain a stable solution. To initialise the solutions an enhanced-viscosity simulation has been carried out whereby the molecular viscosity of the fluid has been artificially enhanced in order to generate a stable starting flow. By increasing the viscosity in this way, the diffusive terms of the governing equations become more dominant with respect to the convective terms, hence leading to a more viscous flow solution. From experience it was found that increasing the viscosity by a factor of 100 provided suitable results for flow initialisation. The solution was stopped once the residual levels had reached steady levels.

The resulting flow is used as an initial field for the subsequent solution procedure where the turbulence model is employed and the molecular viscosity reduced to standard values. Application of the turbulence model adds diffusive terms to the equations through the *Boussinesq* approximation for the Reynolds stress terms (Tucker, 2001). In order to ensure not too great a step exists between the two flow regimes, the molecular viscosity may be gradually reduced to allow the flow to develop before application of the turbulence model. Again, the solution is allowed to progress before the transient and compressible terms are incorporated and the full solution procedure commences. Thus the model initial conditions and set-up procedure can be summarised as,

- Steady-state calculation,
  - Enhanced viscosity calculation,
  - Incompressible calculation;
- Initiate transient calculation (reducing the viscosity);
- Initiate k-ε turbulence model;
- Initiate compressible calculation.

In addition to the starting conditions, the only other initial conditions specified to initiate the solution are a uniform temperature of 20°C and uniform atmospheric pressure (1×10^5 Pa) throughout the domain. These are subsequently updated as the solution progresses.

3.7 Specification of the Computational Methodology

3.7.1 Solution Algorithms

All transient solutions have been solved using the transient PISO (Pressure Implicit with Splitting of Operators) algorithm (Issa, 1986), with the initial steady-state calculation performed using the SIMPLE (Semi-Implicit Method for Pressure-Linked Equations) algorithm (Patankar & Spalding, 1972). Both algorithms make use of an iterative predictor- and corrector-step strategy, with PISO including an additional corrector step. The first stages of both algorithms follow the same process of guessing an initial pressure field (p^*) which is used to solve the discretised momentum and continuity equations to find a new estimated velocity field (u^*, v^*, w^*). These values are then used to solve a pressure correction equation thus allowing for the correct pressure and hence velocity to be found (Shaw, 1992). To avoid unstable solutions, the pressure correction equation is subjected to under-relaxation which allows the user to control the fraction of corrected field to apply to the new field. That is,

$$p^{new} = p^* + \alpha_p p', \tag{3.13}$$

where p^* is the guessed pressure field, α_p is the pressure under-relaxation factor, and p' is the pressure correction factor (Shaw, 1992; Versteeg & Malalasekera, 1995). Thus should a solution become unstable, the under-relaxation factor can be reduced to minimise the change in solution between successive iterations. For the simulations carried out here, a pressure-correction under-relaxation factor of, $\alpha_p = 0.6$, has been used. Further under-relaxation factors for the individual velocity components are also present in both algorithms; however, no option to change these values when performing a transient analysis is given in the STAR-CD software.

The original PISO algorithms' second corrector step uses a second pressure-correction equation to calculate the pressure field, and hence the velocity field. Within STAR-CD, several secondary corrector stages are allowed, the number used depending on the level of internal error (Computational Dynamics Ltd., 2001). These can be used to gauge

the convergence of a solution.

For a fully transient calculation, the PISO algorithm incorporates all the time-dependent terms in the momentum and continuity equations. It has been shown (Issa, 1986) that the pressure and velocity fields obtained at the end of each PISO loop are accurate enough to proceed to the next time step immediately, and hence the algorithm can be considered as non-iterative. Versteeg & Malalasekera (1995) suggest that small time steps are necessary to gain accurate results when using the method. In addition, the use of higher-order temporal discretisation scheme is also recommended; this has been carried out here.

3.7.2 Completion Tests

In order to determine whether a satisfactory solution has been attained a number of completion tests are available within STAR-CD. These methods are used by the code to control the simulation and also allow the user to monitor the progress of the simulation. A monitoring function exists that outputs information from a given cell or set of cells for each iteration or time step of the simulation. This information is valuable to the user as it allows the flow to be monitored as the solution progresses. Here these monitor values are used to determine whether an oscillatory flow has developed and whether the oscillation experiences attenuation or amplification. For a steady-state simulation these values should show small variance; however, the monitored values do not provide convergence criteria and only offer the user information on the flow development (Computational Dynamics Ltd., 2001).

Control, for steady-state solutions, is achieved through use of residual error values which are in essence the difference in the transport equations from iteration to subsequent iteration. Discretisation of the Navier–Stokes equations leads to a set of simultaneous equations that need to be solved. For a small set of equations, a matrix equation can be generated in the traditional form $\mathbf{Ax} = \mathbf{b}$, and the solution found by finding the inverse matrix, $\mathbf{A}^{-1}$. Typically for small problems this is achieved through **LU** decomposition and is typically used for finite-element solvers (Zienkiewicz & Tay-

lor, 1989; Pozrikidis, 1997). For a large set of equations, however, this process becomes computationally expensive and thus iterative methods are used (Shaw, 1992). Iterative methods estimate the values of $\mathbf{x}$ and then successive iterations of the solver produces more accurate values of $\mathbf{x}$. After successive iterations an approximate solution ($\mathbf{x}^n$) exists, and this approximation leads to a non-zero residual, ϱ^n, that is the difference between the exact and approximate solution, $\mathbf{A}(\mathbf{x} - \mathbf{x}^n) = \varrho^n$ (Ferziger & Perić, 1999). The iterative procedure thus reduces the residual to a near-zero value. STAR-CD normalises this to provide an absolute residual which is summed over all cells in the computational domain. The normalisation factor is dynamically adjusted at each iteration by evaluating inflow and outflow fluxes across the domain boundaries. This is needed in the case of pressure boundaries (as used here) as the flow is free to enter and leave the domain through such a boundary.

For unsteady calculations, residual errors are not provided, as their meaning is lost in a time-dependent case. For such flows, global rates of change are used to monitor the solution progress. The global rate of change of each variable quantity is the change between the values for those variables at the new and old time-step; and again this is summed over each cell of the computational domain. Such values can be used to determine the state of a flow alongside the monitored quantities that are given for each time step.

As discussed above, the PISO algorithm within STAR-CD also provides information on the number of internal pressure sweeps that are performed per iteration. This information can be used to gauge the level of convergence of the solution, with a smaller number of sweeps representing a greater level of convergence. A limit can be set on the number of pressure sweeps performed per iteration before the solution advances to the next regardless of convergence. Here, the default value of 1000 pressure sweeps is used with the solutions here typically using between 50 and 100 sweeps per iteration. Monitoring of the Courant number is also used as a stability check on the solution and is discussed below.

3.7.3 Spatial Discretisation

Spatial discretisation of the finite-volume equations has been carried out using a multi-dimensional, second-order-accurate, differencing scheme known as MARS (Monotone Advection and Reconstruction Scheme) (Computational Dynamics Ltd., 2001). It is recommended to use this scheme when dealing with tetrahedral cell meshes within STAR-CD. Use of a second-order discretisation scheme can lead to errors in the form of numerical dispersion (i.e. spatial oscillations or wiggles); however, MARS is a monotonic scheme, hence eliminating the risk of numerical dispersion, especially when used in conjunction with good grid refinement (Hirsch, 1990). MARS is based on a total variation diminishing (TVD) scheme and incorporates a variable compression level that allows the user control over computational efficiency and resolution of the scheme. With a low compression level the scheme becomes more computationally efficient at the expense of resolution; i.e., it behaves more like an upwind scheme, resulting in numerical smearing. It is recommended to use a very low compression level when using tetrahedral meshes; however, the MARS scheme still provides a more stable and accurate solution than ordinary higher-order schemes and remains second-order-accurate (Computational Dynamics Ltd., 2001). Often the use of an upwind scheme is specified in order to initiate a solution, but given the variable compression scheme this allows the MARS scheme to be used throughout.

3.7.4 Temporal Discretisation

Temporal discretisation has been carried out using both a fully implicit first-order accurate scheme and the Crank-Nicolson second-order scheme. Both schemes are linked via the same discretised equation which contains a weighting parameter to enable blending of the schemes. Typically adjustment of the weighting parameter allows for an explicit scheme at one extreme (0) to the fully implicit scheme at the other extreme (1) with the Crank-Nicolson scheme resulting from a weighting factor of $^1/_2$. STAR-CD allows for the fully implicit and Crank-Nicholson schemes, both of which are unconditionally stable for all values of time step (Versteeg & Malalasekera, 1995), although too large

a time-step can result in temporal errors, or numerical dispersion in the case of the Crank-Nicolson scheme. For the cases here the Crank-Nicolson scheme offered no benefits despite its second-order accuracy, and thus for the main predictions the fully-implicit scheme has been used.

Several problems were encountered in obtaining a flow solution using transient calculations owing to the choice of time-step size. Despite the stability of the temporal schemes and the promise of using large time steps, it was found that very small time steps were needed in order to generate a converged and stable solution. To overcome the stability problem the time-step size was determined by the CFL (Courant-Friedrichs-Lewy) condition whereby the Courant number, C, is maintained at less than unity, $C < 1$ (Abbott & Basco, 1989; Tucker, 2001; Anderson, 2000; Wilcox, 1994). The Courant number is defined as,

$$C = \frac{u\Delta t}{\Delta x}, \tag{3.14}$$

thus representing the non-dimensional time step. By upholding the CFL condition the flow is restricted in travelling beyond one cell spacing per time step. Using this restriction does, however, remove the benefits of the implicit temporal discretisation schemes. The CFL condition has not been rigorously upheld, rather the Courant number was monitored throughout the simulations and maintained at values close to or approaching unity, particularly where convergence was an issue.

3.7.5 Turbulence Modelling

As the flow through the throttle valve is turbulent, a turbulence model has been used for the computational predictions. The k-ε turbulence model has been used owing to its availability, reasonable simplicity, small computational overhead, and perhaps most importantly because it has wide use, and hence validation, in the CFD industry. The latter means that there is a wealth of information about flows modelled using the model that highlights its strengths and shortcomings, and perhaps warrants its use, despite superior models being available.

The model has been used in standard form for high Reynolds number flows using wall functions to describe the local wall flows as discussed previously. Standard values of the empirical coefficients, as set out by Launder & Spalding (1974), have also been used with no modifications made through the experimental analysis. Of these, only those that have been used for the calculation of boundary conditions are presented, namely $C_\mu = 0.09$, used for the calculation of turbulent dissipation rate (equation (3.4)), and f_μ, a wall damping function used in the derivation of eddy viscosity (equation (2.19)), which for high Reynolds number flows is unity. As discussed, the values of k and ϵ are given at the inlet to the flow domain, and values of Ti and l at the outlet of the domain; see section 3.4.

3.8 Results of the Computational Predictions

One of the advantages of CFD modelling has over physical experiments is the ability to present the results in many ways and to evaluate the results at all locations within the flow domain. Here the results are presented in several formats and are initially shown for one instant in time before evaluation of the transient flow is considered. The presentation focuses on the velocity predictions that are initially presented as a series of in-plane velocity vectors and contours of velocity magnitude through the symmetry plane of the throttle body. This is followed by visualisation of the surface streamlines on the valve that indicate a three-dimensional flow and hence leads to further cross-sectional plots through the valve centre (perpendicular to the symmetry plane), and parallel to the outlet at locations downstream of the valve. Further surface streamlines are then presented of the throttle body walls.

To fully examine the three-dimensional flow structure a series of instantaneous velocity traces are then presented downstream of the valve. These traces have been used to highlight the vortex cores and the vortex paths, thus leading to a clearer indication of the overall structure of the flow. From here the full transient features of the flow structure are presented.

The final section briefly presents the results of the turbulence predictions through

use of cross-sectional plots of the turbulent kinetic energy and dissipation.

Simulations have been made for the valve open at 5.8°, 8.3°, 12.5°, 19°, 30°, 47°, and 60°; however, full results are not presented for each case owing to limitations of space and also owing to flow similarity between the cases.

3.8.1 Velocity Predictions

Symmetry Plane Cross-Sections

It is immediately apparent from the results that there is a distinct difference in the flow structure through the valve at small and large openings that stems not only from the change in geometry but also from the different boundary conditions used for each model that are summarised in Table 3.2 (see page 67). Despite the major differences between the characteristics of the flow, there remain underlying structures common to both small- and large-angle valve flows.

Flow upstream of the valve exhibits the typical characteristics of pipe flow with a steady and unidirectional flow developing. Only as the flow approaches the valve do significant changes in the flow patterns become apparent. One of the major differences between the small angle openings (5.8° to 12.5°) and the larger openings (19° to 60°) is the geometry of the throttle, or more correctly the change in flow area across the valve. At small throttle-opening angles the valve presents considerable blockage and hence only a small gap is available for the flow to pass through and hence flow passing through the gaps does not interact until further downstream of the valve. At larger throttle openings the flow area greatly increases and the valve acts more as a low-aspect-ratio aerofoil, thus the leading-edge and trailing-edge flows are linked through the vortex-shedding regime around the aerofoil.

Figures 3.4 and 3.5 show the flow through a valve at 5.8° and 47° as contours of velocity magnitude and vectors of the in-plane components of velocity through the symmetry plane of the valve. Note that the scaling is adjusted to account for each throttle angle and that the vectors are fixed in length to clarify the flow structures. It is immediately clear from the figures that at small angles the valve practically blocks

the throttle body. At the larger angle with the valve opened, which now appears more like a flat plate, the flow is able to negotiate the valve far more readily owing to the less abrupt geometric change.

For flow downstream of the valve greater differences between the two angles are apparent, but some similarities are also revealed. In both cases the flow is accelerated through the gap formed between the valve edges and the throttle walls leading to separation from both the leading and trailing edges of the valve. Separation is more abrupt for the smaller angles (Figure 3.4) where the geometry presents a sudden enlargement to the flow and a strong pressure gradient exists across the gap. Similarities to sudden enlargement flows allowed modelling of butterfly valves to be carried out in previous studies (Morris & Dutton, 1989*b*). At these smaller throttle angles the geometric presentation of the valve between upstream and downstream locations is practically symmetric when viewed side on and that leads to the similar leading- and trailing-edge flows. At the larger openings the valve breaks the near symmetry as the leading edge now significantly cants towards the oncoming flow. Under these conditions it is apparent that the flow passing over the upstream face of the valve is analogous to the flow through a convergent duct, and that flowing over the downstream face is analogous to the flow through a divergent duct (Figure 3.5). Of course, this holds true for the smaller-angle flows too; however, the analogy is more distinct at the larger openings. This analogy has been noted and examined in previous studies of throttle valves (Morris, 1987), although these tend to concentrate on two-dimensional flows and hence is not followed up here. The change in valve orientation produces a less severe separation and re-attachment of the flow on the upstream surface is also apparent and this leads to a different flow downstream of the valve.

For the small-angle flows the leading- and trailing-edge separation are similar with both forming a strong high-energy jet-like flow that remains attached to the wall downstream of the valve forming a free shear layer between the low-energy flow in the core of the domain. Flow past the trailing edge appears to have less energy leading to a reduced velocity magnitude and earlier dissipation of the flow. At the leading edge the

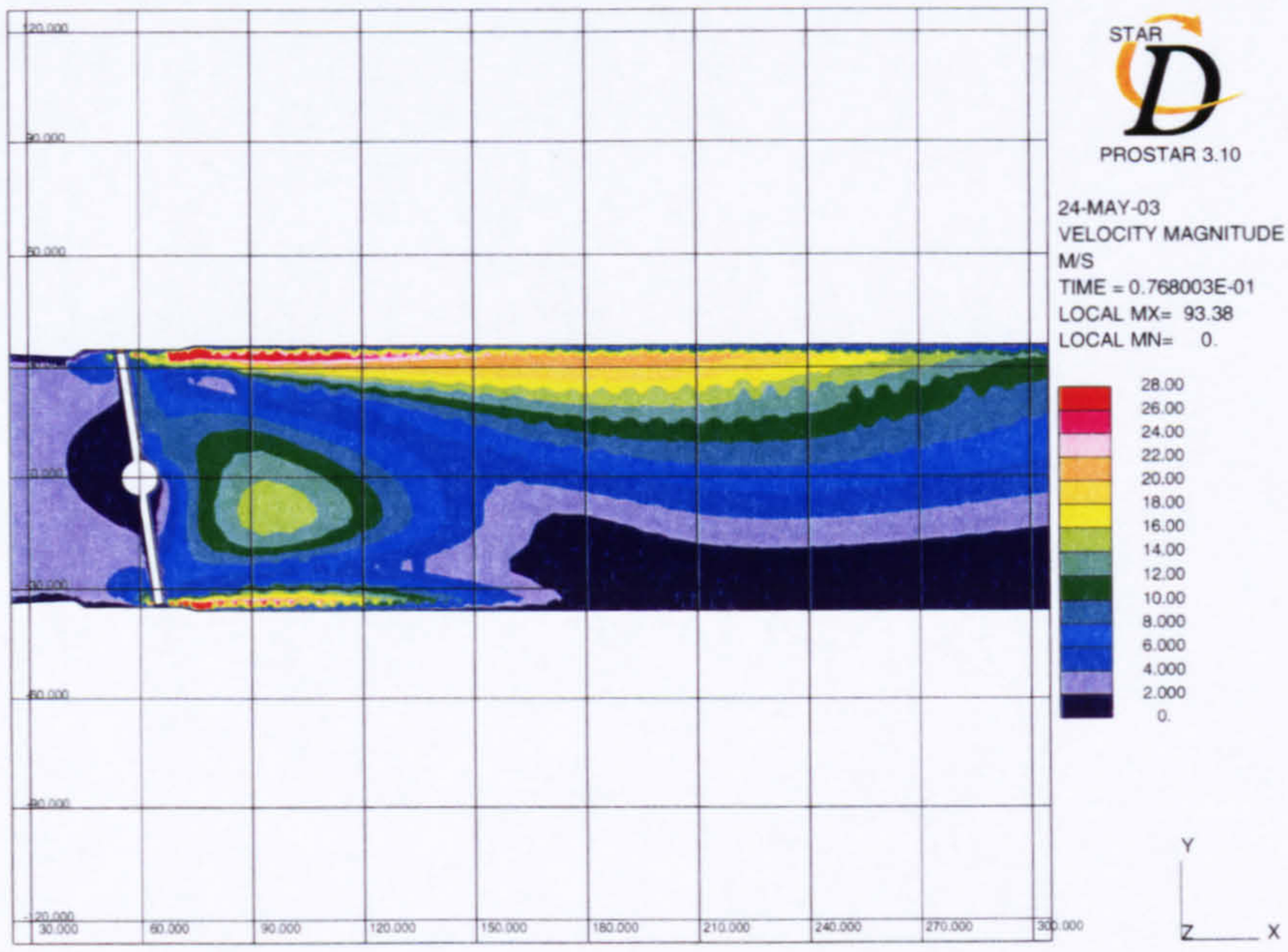

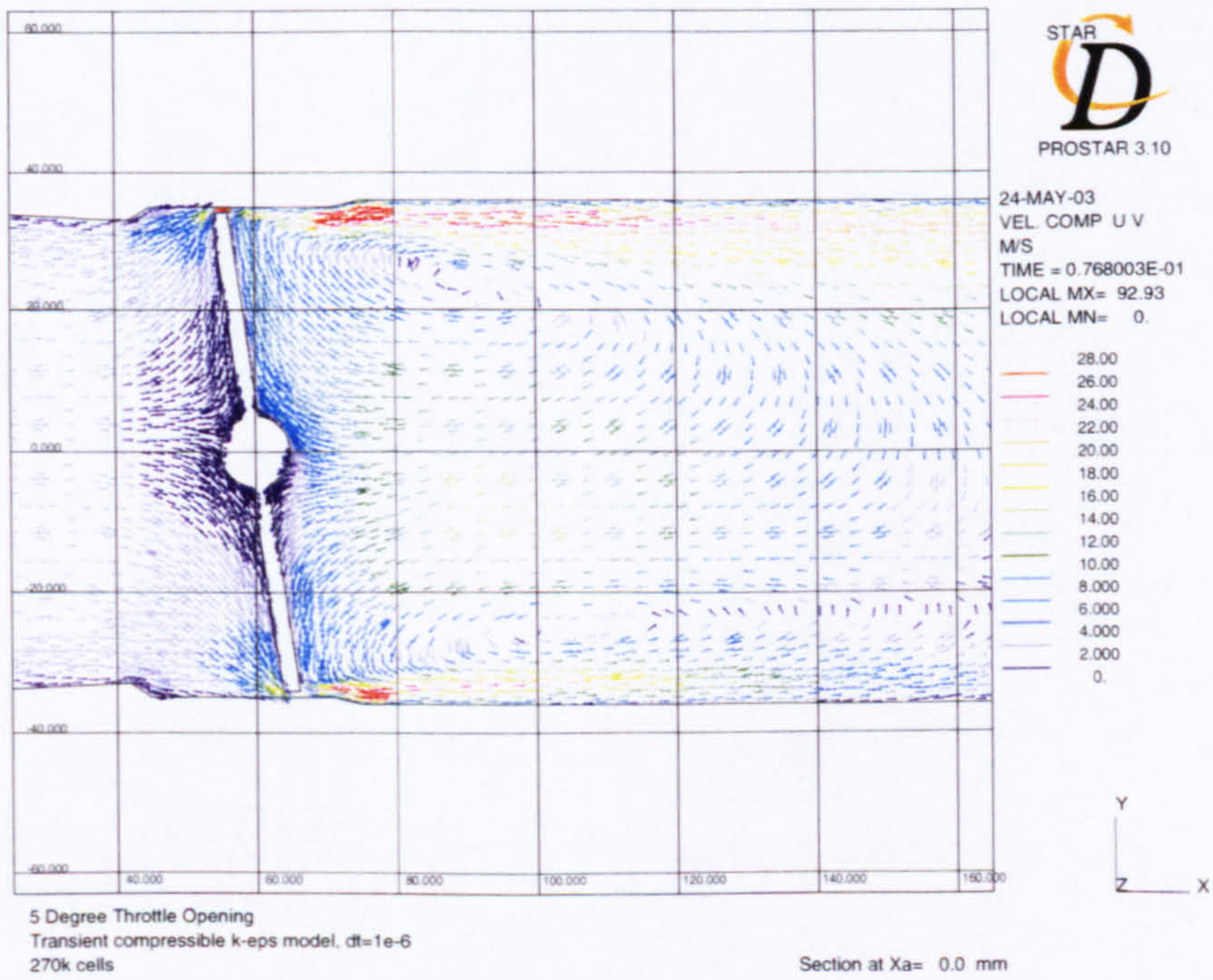

Figure 3.4: Prediction of the flow through a throttle valve opened at 5.8°. Section through symmetry plane showing contours of velocity magnitude, and vectors of the in-plane velocity component local to the valve. Vectors coloured by magnitude, fixed scaling.

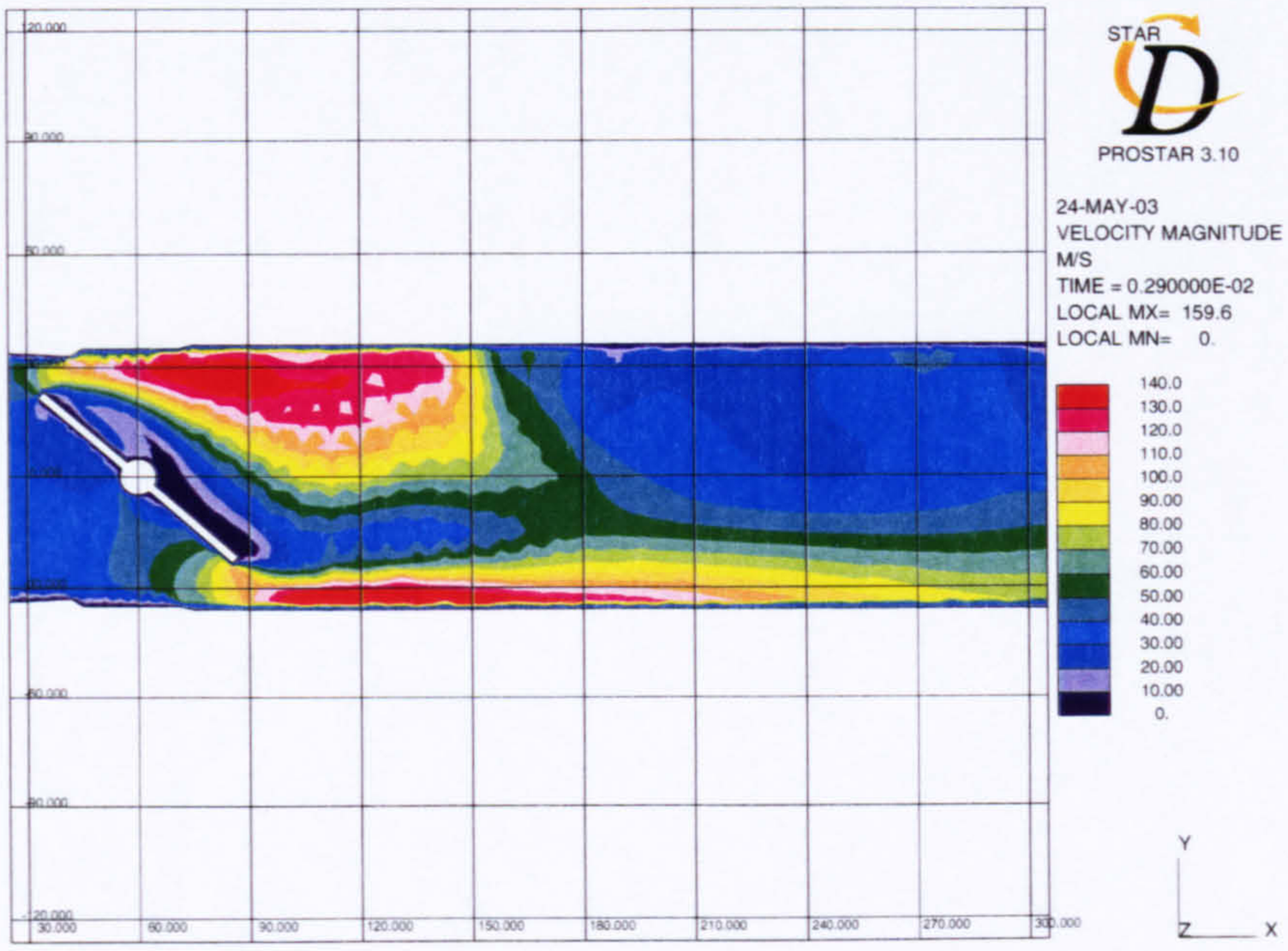

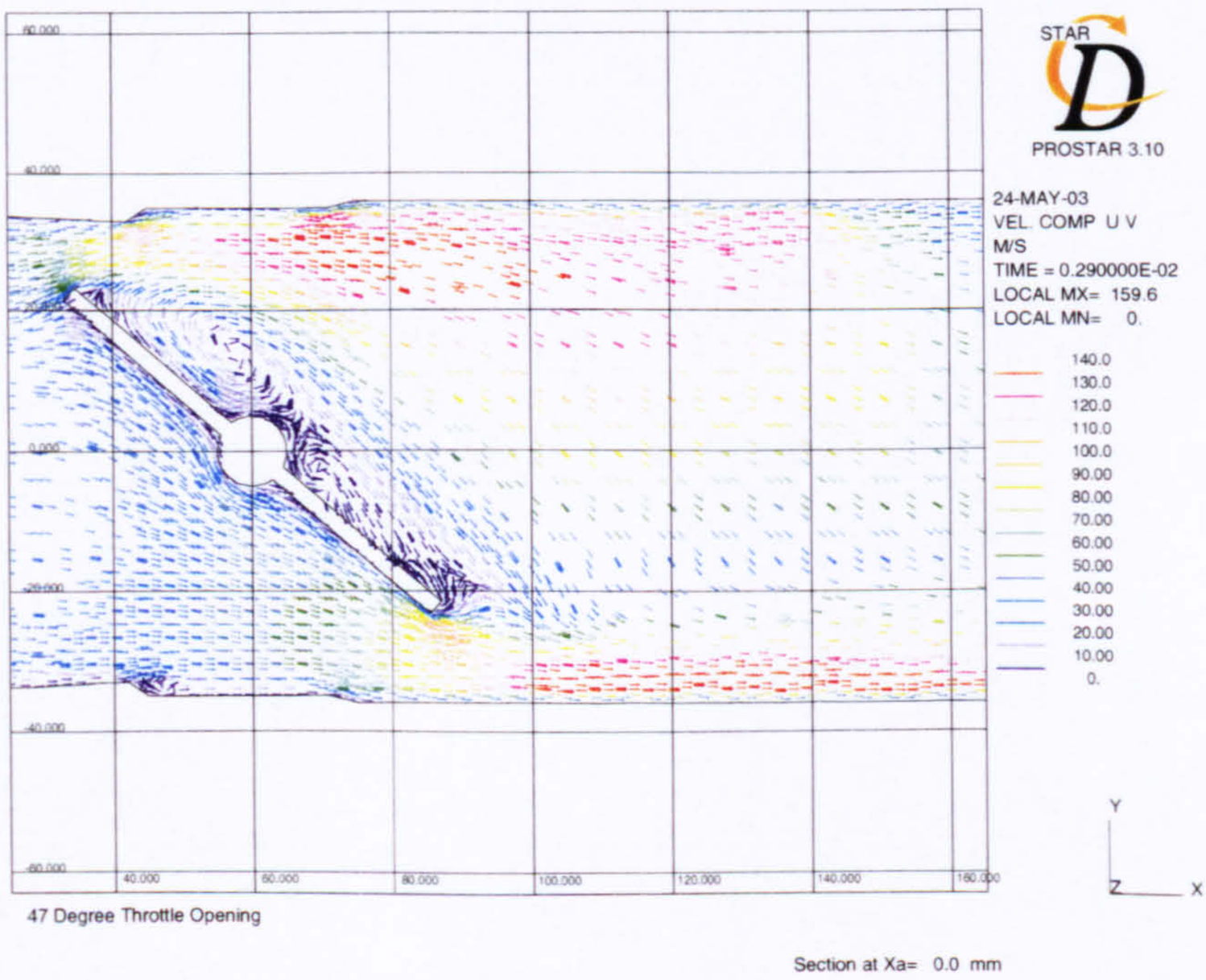

Figure 3.5: Prediction of the flow through a throttle valve opened at 47°. Section through symmetry plane showing contours of velocity magnitude, and vectors of the in-plane velocity component local to the valve. Vectors and contours coloured by velocity magnitude, with fixed vector sizes.

high-energy flow propagates downward into the domain losing energy through turbulent mixing and dissipation to the surrounding fluid.

Both separation zones lead to the formation of vortices just downstream of the valve, the combined action of which leads to a significant region of reversed flow forming in the centre of the domain that impinges on the downstream face of the valve. The upper vortex is the stronger of the two for all cases, owing to the increased downwash of the leading-edge flow, and it is also closer to the valve face and hence the action of the offset vortices is to produce downwash in the reverse-flow region also. Here downwash is defined as the negative vertical flow component of the velocity in the corresponding plots, and upwash as the positive vertical flow direction.

At the larger openings the leading-edge vortex becomes attached to the valve downstream face with separation from the edge no longer so extreme. Opening the valve reduces the pressure gradient at the tip of the valve that leads to a much smoother flow over the leading edge of the valve, and at higher incidence the flow re-attaches toward the trailing edge of the valve. The latter appears to produce reduced mixing downstream of the valve as the flow now remains predominantly orientated in the axial direction. At the larger opening angles the separation of the flow from the leading edge of the valve leads to local flow accelerations that form a *vena-contracta* between the separated region and the wall that is downstream of the physical *vena-contracta* defined by the valve tip and throttle wall (Figure 3.5). This has been shown in previous studies (Morris, 1987) and has the effect of further reducing the oncoming flow area.

Flow leaving the trailing edge of the valve at larger openings remains attached to the wall and does not dissipate as for the small-angle flows. The result is a strong shear layer that dominates the lower domain and entrains the flow from the leading edge some way downstream. The flow on the upstream valve face now resembles that of a convergent duct with smooth flow accelerating through the gap in a favourable pressure gradient. The action of both these flows appears to suppress the formation of the significant lower vortex predicted for the smaller valve openings.

Instantaneous Surface Streamlines

These findings are based on the symmetry plane sections alone, that represent a very two-dimensional picture of the flow. Several experimental studies have been performed for the flow over a valve using a two-dimensional configuration that obviously limits the true flow; however, such investigations do appear to pick out the significant features of the flow about the valve symmetry plane such as the separation and local vortices (Morris, 1987). Viewing the surface streamlines on the valve clearly shows the differences between the two angle extremes, but also shows a more three-dimensional nature to the flow. Figures 3.6 and 3.7 show the upstream and downstream surface streamlines corresponding to the flow through the valve at 5.8° and 47°. Here, the streamlines have been generated by extrapolation of the velocity from the near-wall cells to the surface.

The upstream face of the small-angle flow clearly shows the stagnation line along the valve pivot, with a predominantly symmetric flow above and below this. The appearance of a stagnation line (as opposed to point) indicates that the bulk of the flow is split between the leading and trailing edge; however, the radial distribution of the flow beyond the line hints at a three-dimensional flow. For the larger angle the stagnation line appears at the leading edge of the valve with the bulk of the flow traversing to the trailing edge of the valve. There are regions of flow entrained to the side of the valve about the upper face, but overall the flow appears more uni-directional than that at small angles. As the valve is opened the stagnation line moves toward the leading edge and the radial flow component reduces as the flow area increases at the leading and trailing edges of the valve.

The downstream face of the valve tells a different story, and it is immediately clear that the flow is considerably more three-dimensional than at first thought. At small opening angles the downstream face streamlines show that after stagnation, just below the pivot (cf Figure 3.4), the flow moves predominantly to the sides as opposed to the trailing edge as on the upstream face. The upper portion of the valve also shows a strong side component to the flow, although there is still significant upward flow owing

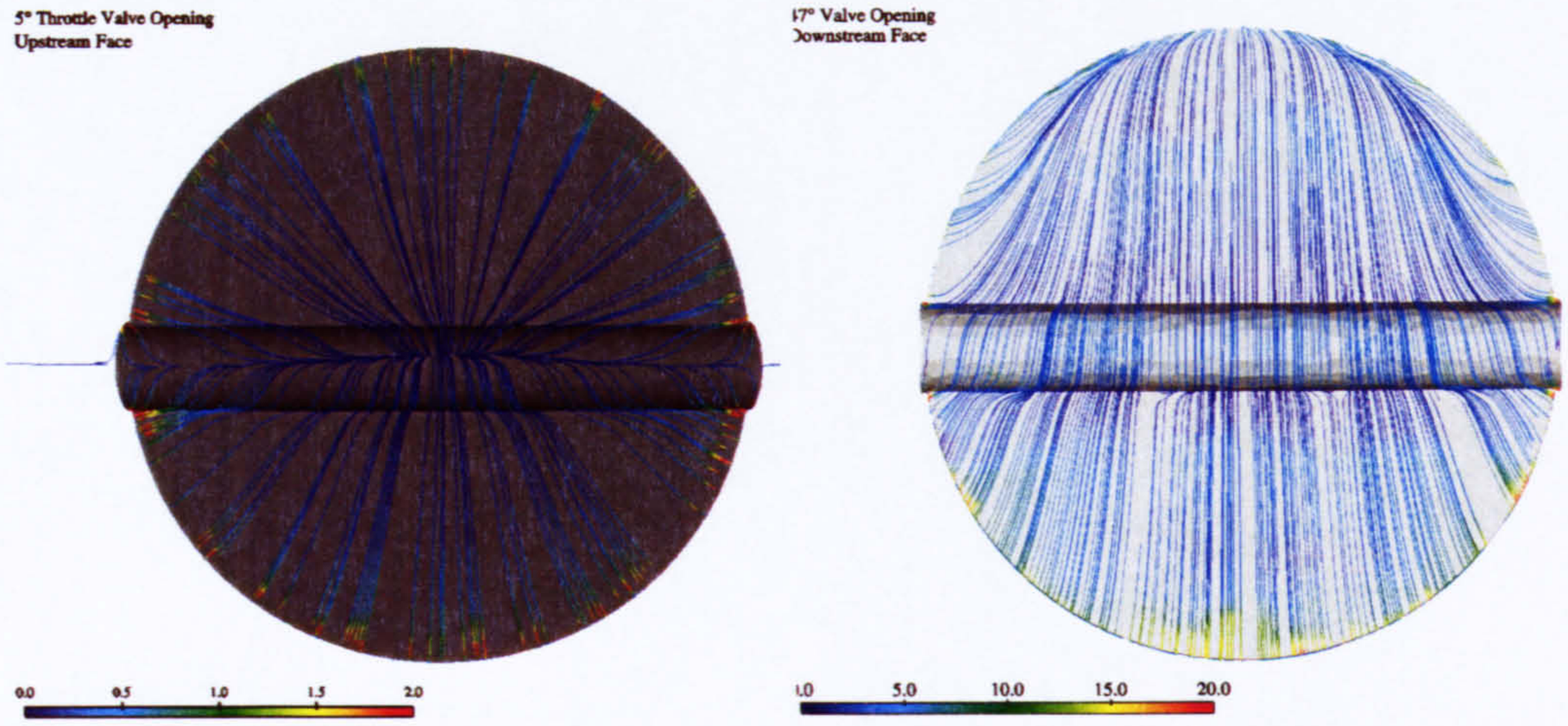

(a) 5.8° valve opening

(b) 47° valve opening

Figure 3.6: Instantaneous surface streamlines on the upstream face of the throttle valve corresponding to the flows of Figures 3.4 and 3.5. Views presented normal to the face of the valve, leading edge upward, with traces coloured by velocity magnitude.

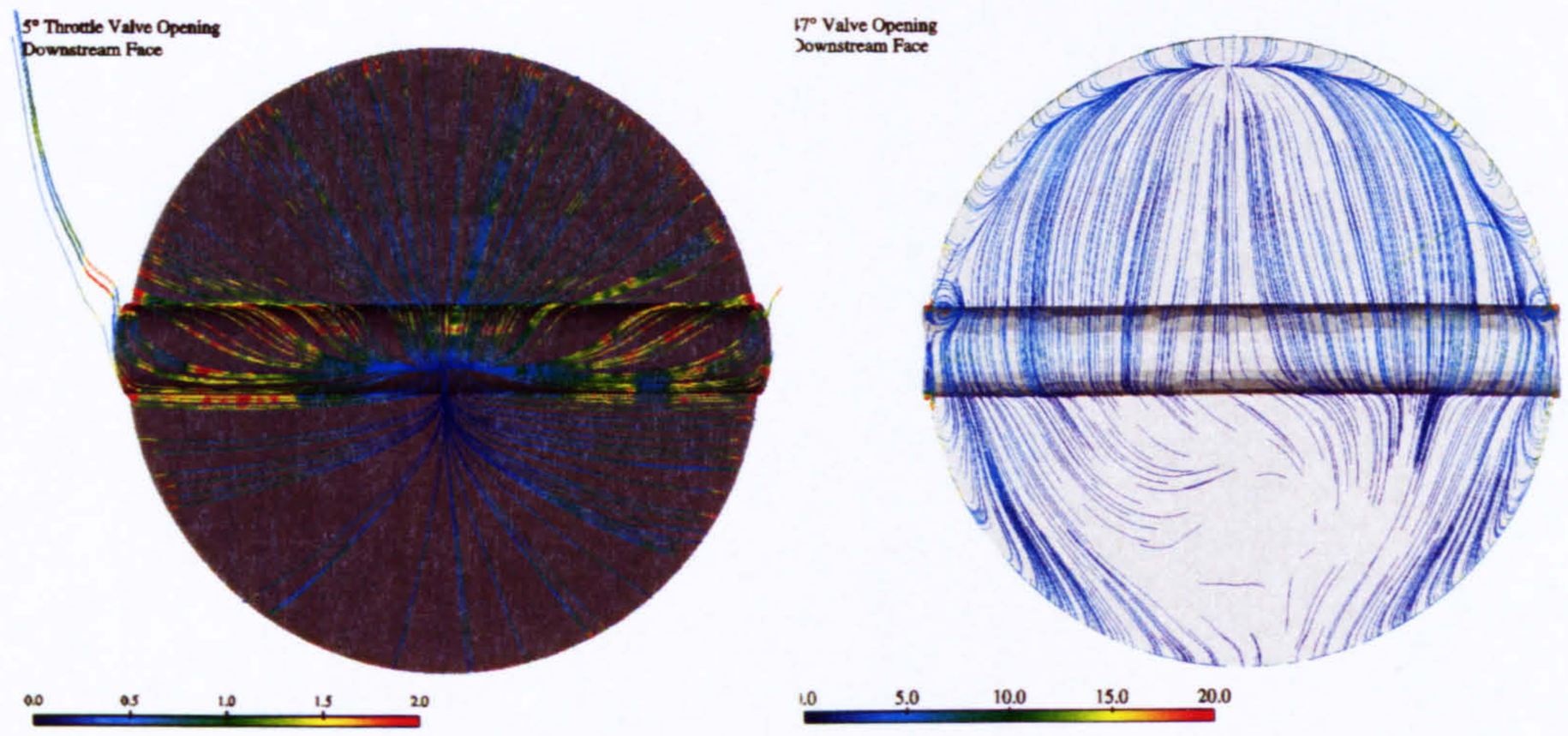

(a) 5.8° valve opening

(b) 47° valve opening

Figure 3.7: Instantaneous surface streamlines on the downstream face of the throttle valve corresponding to the flows of Figures 3.4, 3.5, and 3.6. Views presented normal to the face of the valve, leading edge upward, with traces coloured by velocity magnitude.

to the vortex downstream of this region.

Flow over the downstream face for large angles shows similar trends with the lower surface experiencing increased sideward flow in comparison to the upper region. The downstream vortex moves closer to the valve as it opens and, as depicted in Figure 3.5, becomes attached at the extremes. The curve of the stagnation line suggests the vortex follows the arc of the valve; this is discussed below. Of note from Figure 3.7(b) is the asymmetric streamlines present on the lower portion of the valve that are the first indication of transient features to the flow. This corresponds to the movement of vortices shed from the valve as will be discussed in following sections.

Central Valve Cross-Sections

It is useful now to evaluate the flow from a different angle as a three-dimensional and time-dependent flow structure is apparent. Thus, Figures 3.8 and 3.9 show section plots through the domain and pivot axes, corresponding to the flows presented previously.

Vortices are present at the valve sides at the smaller flow angle that appear to remain attached, but weaken, as the valve opens. These are a result of flow separating from the sides of the valve in a similar manner to the leading- and trailing-edge flows of the small-angle flows. Perhaps, the main difference between the plots is the reversed flow present at the valve for the small-angle flows which is no longer apparent at the larger openings. Noting that the plots show in-plane velocity components, it is clear that change between the forward- and reversed-flow region occurs approximately 1.5D downstream of the valve for the small openings. As the valve opens the point at which change occurs moves closer to the valve until only a small region of reversed flow exists. This corresponds to Figures 3.4 and 3.5 where the leading-edge vortex attaches to the valve, and the downstream flow shows less circulation.

A further point to note is that the line defining the boundary where change occurs is not straight but rather a "v" shaped boundary exists. This is a further indication of the three-dimensional nature to the flow, suggesting that the downwash is strongest at the symmetry plane, weakening as the flow moves away. As the valve is opened so the

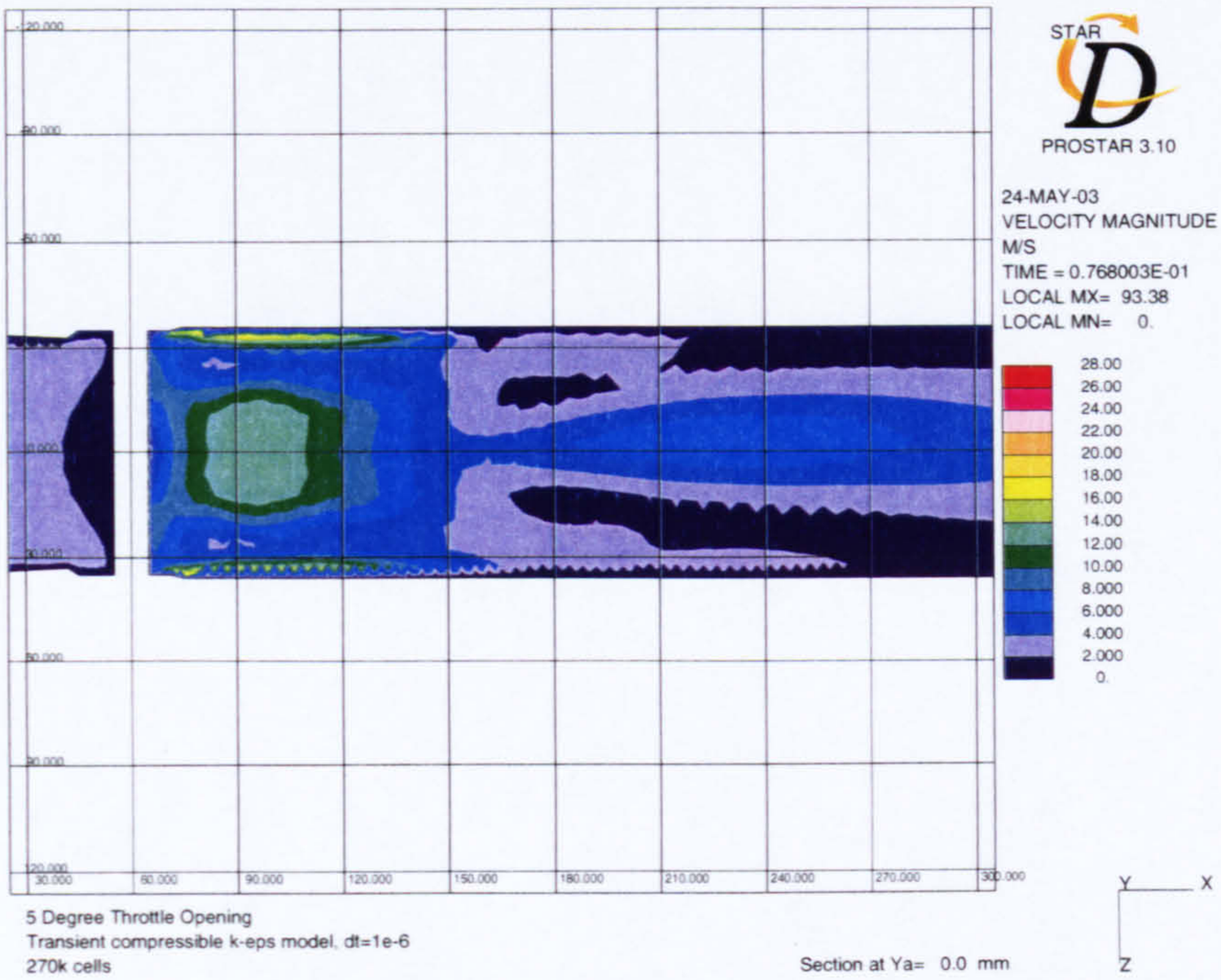

Figure 3.8: Prediction of the flow through a throttle valve opened at 5.8°. Section through pivot and domain axes showing contours of velocity magnitude, and vectors of the in-plane velocity component local to the valve. Vectors coloured by magnitude, fixed scaling.

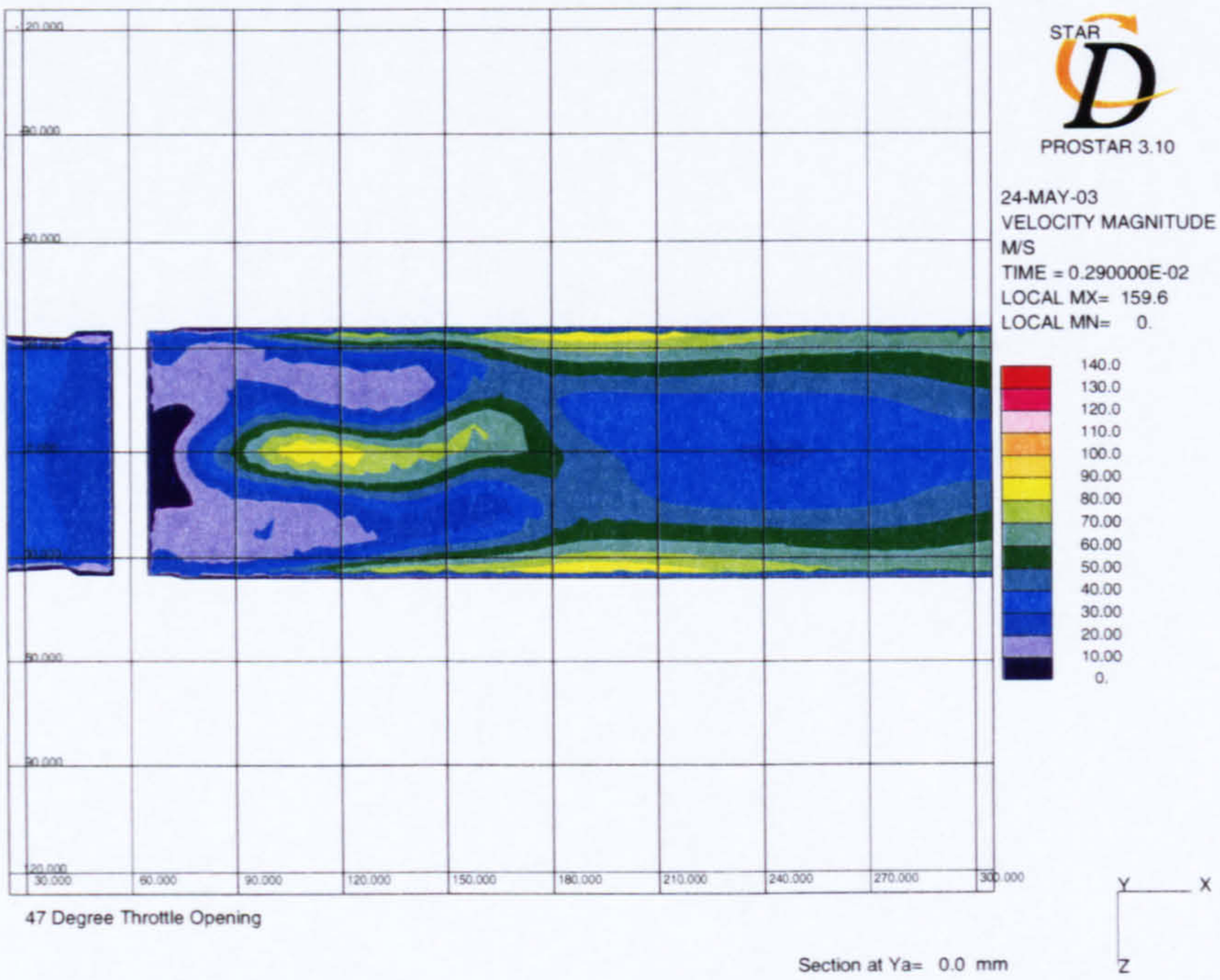

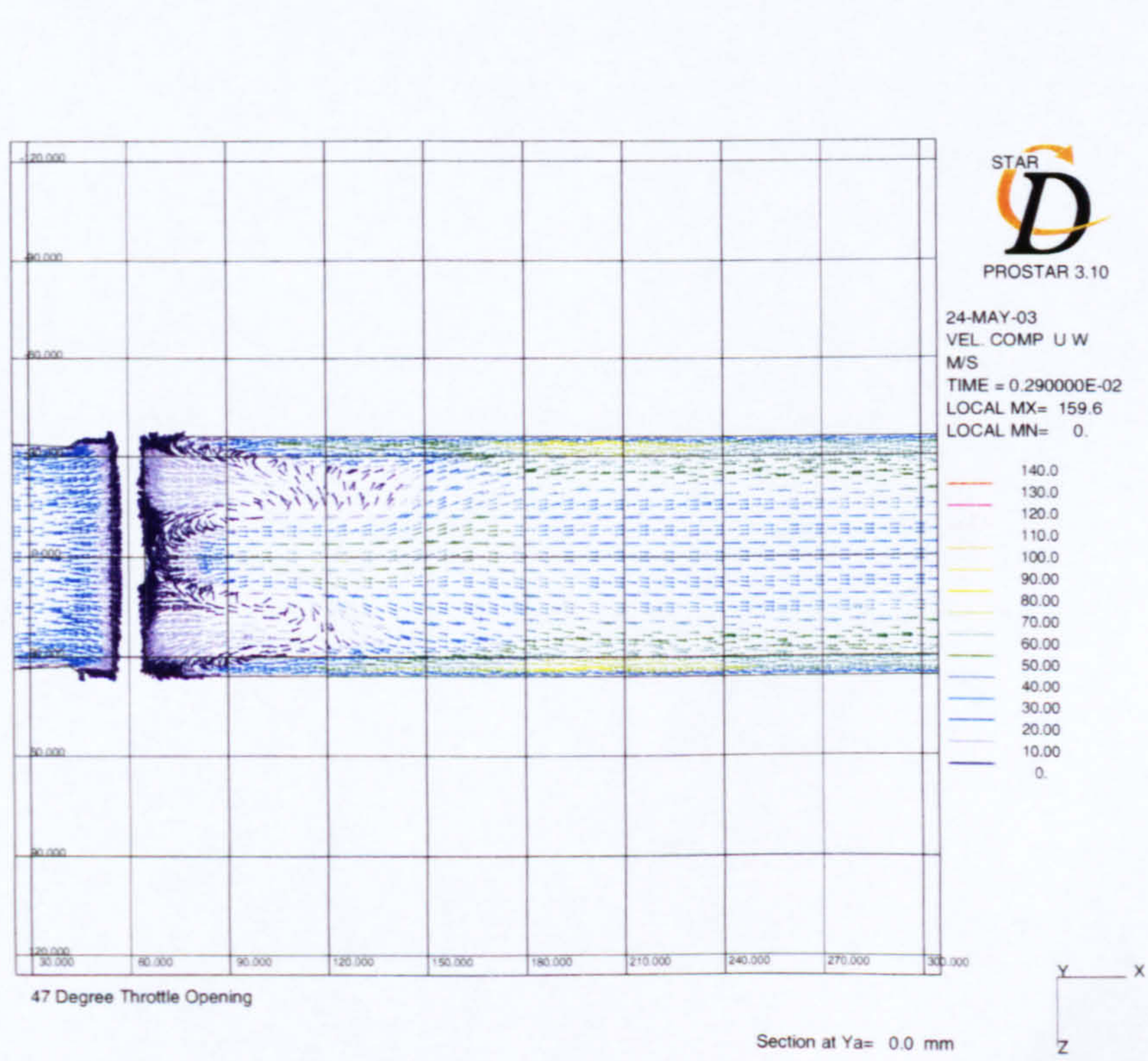

Figure 3.9: Prediction of the flow through a throttle valve opened at 47°. Section through pivot and domain axes showing contours of velocity magnitude, and vectors of the in-plane velocity component local to the valve. Vectors and contours coloured by velocity magnitude, with fixed vector sizes. Note the change in scale to Figure 3.8.

line is also stretched leading to two separated regions of reversed flow (this can be seen in Figure 3.9).

A final point from the latest plots is to note that the flow becomes far less symmetric away from the valve, in particular at the larger throttle openings. This is particularly obvious for the 47° opening where the flow clearly moves to one side of the domain away from the valve, and also the stretch in the reverse-flow boundary is asymmetric. A very symmetric flow exists for the smaller-angle plot up to the transition, but beyond this a secondary vortex is predicted on one side of the domain, breaking the symmetry of the flow and leading to time-dependent features forming. A small-scale vortex is present on the opposite side; however, this appears to be significantly smaller and under-developed by comparison.

The asymmetry of the flow in Figure 3.9 is a feature of the leading-edge wake, and the asymmetry becomes more apparent higher up in the domain. An example of this is shown in Figure 3.10, which shows the in-plane velocity vectors for a section 25 mm from the centre of the domain for the 5.8° and 47° flows. The obvious point from the two plots is that the small-angle flow shows practically no asymmetry while the larger angle flow indicates a high degree of asymmetry in the wake with distinct vortex structures present. This is not a universal trend as other small-angle cases predict similar, although weaker, asymmetry and vortices in the wake. Similar flows are observed for the large-angle flows, with slight asymmetry shown shown for the 19°, 30°, and 60° throttle openings. The flows below the centreline of the throttle do not appear to show any asymmetry.

Downstream Axial Cross-Sections

Figure 3.11 shows axial sections of the in-plane velocity vectors at stations 1D, 2D, and 3D downstream of the valve opened at 5.8°, and 47°. Both the small- and large-angle flows exhibit twin vortex structures that dominate the far downstream flow in the domain. Closer to the valve, at the 1D section, the section cuts through the regions of downwash and reversed flow found in the previous sections, and hence the flow appears

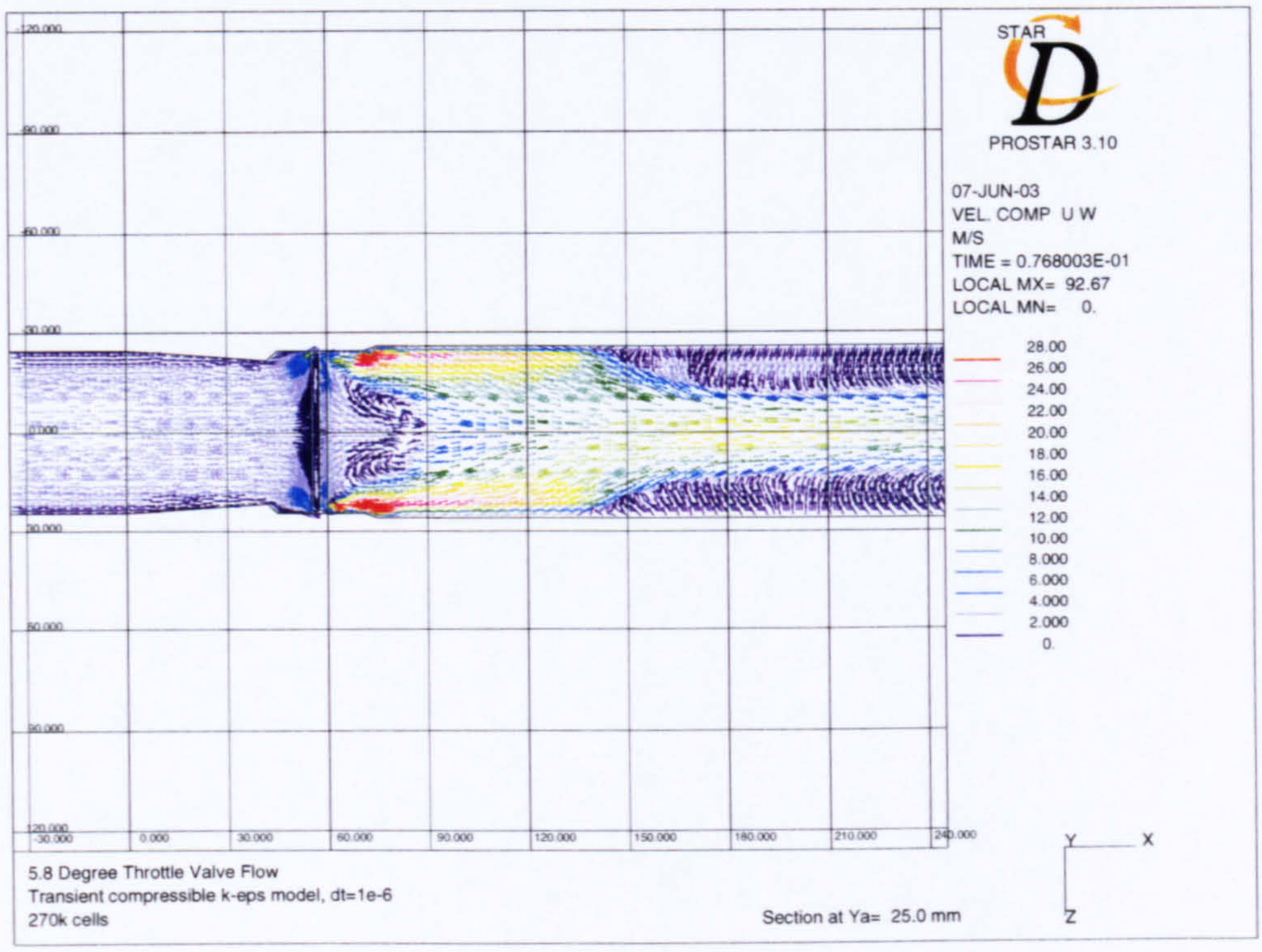

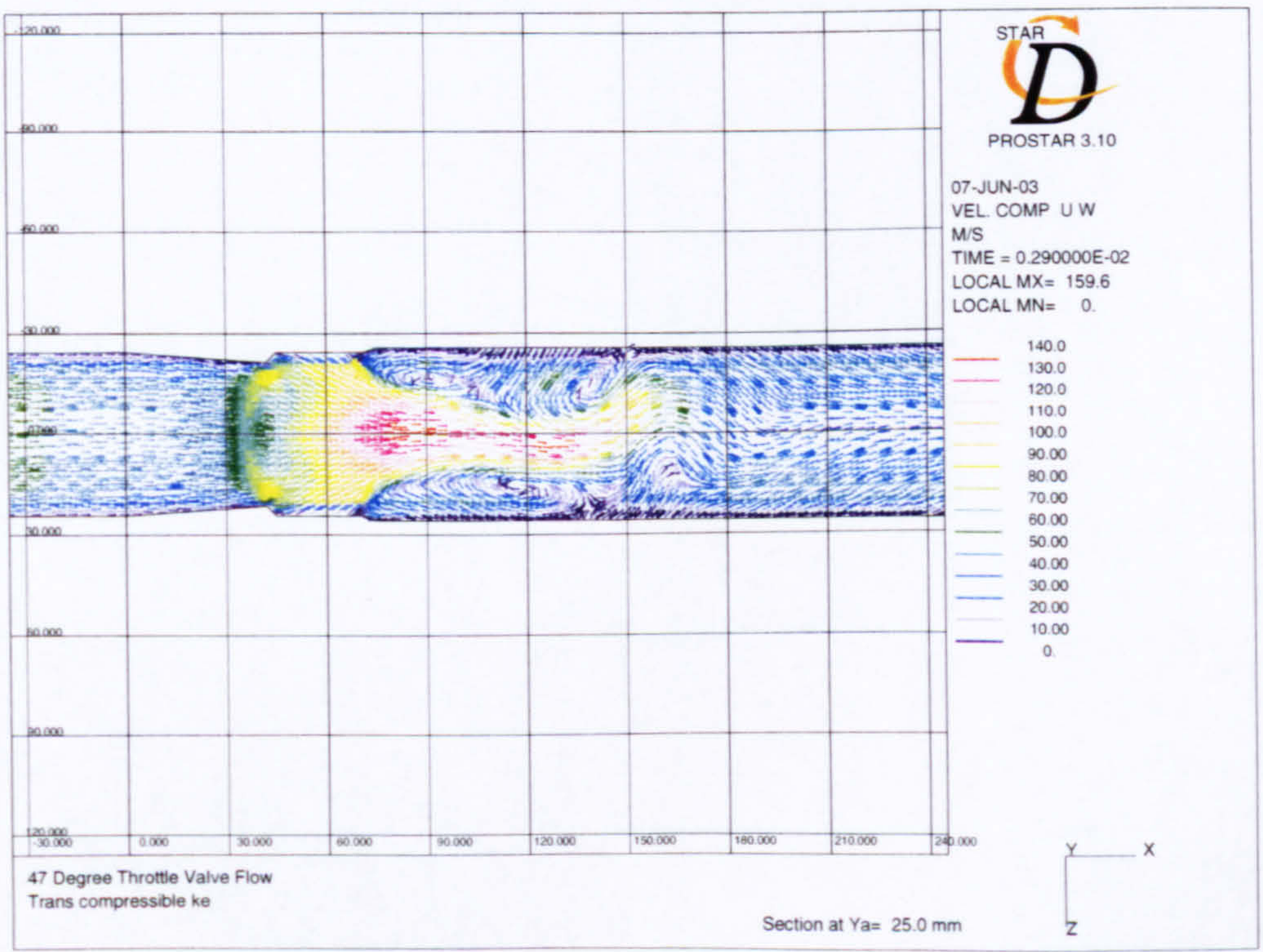

Figure 3.10: Section slice through upper domain of a valve open at 5.8° and 47°, showing in-plane velocity components with alternate vortices present in wake. Section lies 25 mm above centreline of the valve.

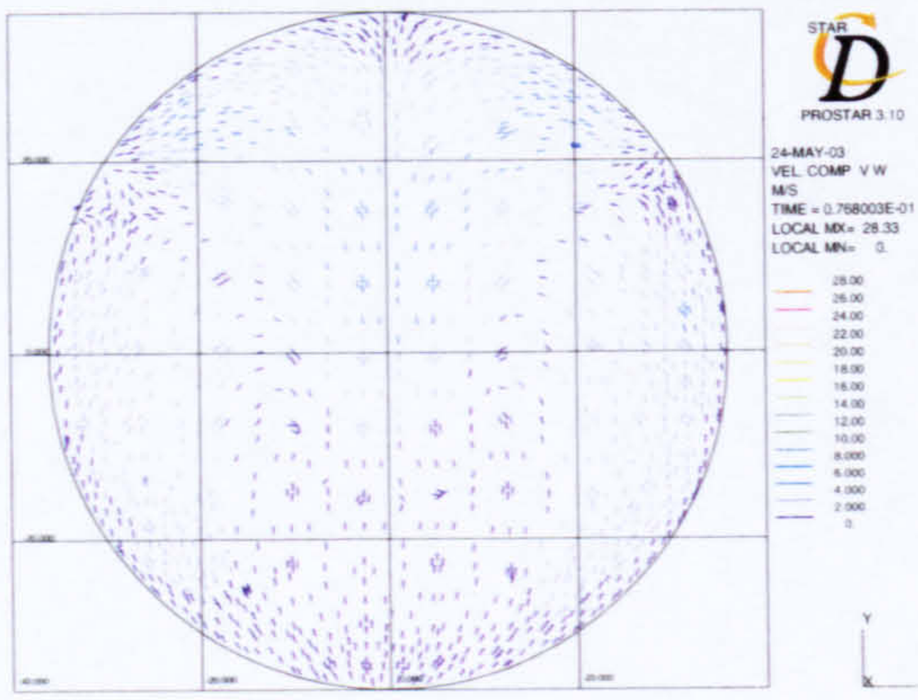

(a) 5.8° - 1D

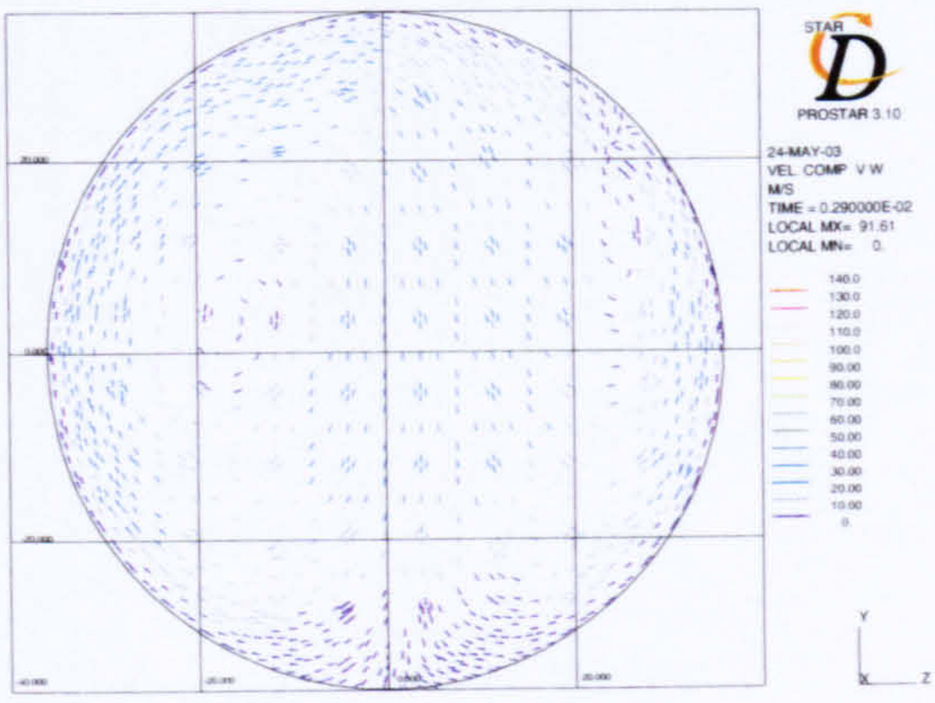

(b) 47° - 1D

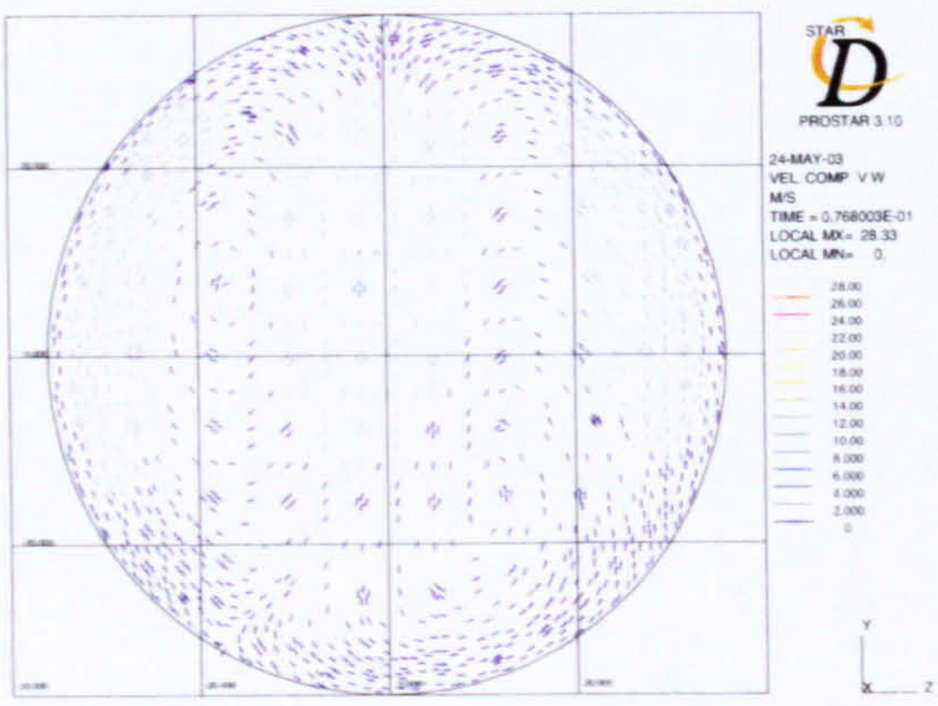

(c) 5.8° - 2D

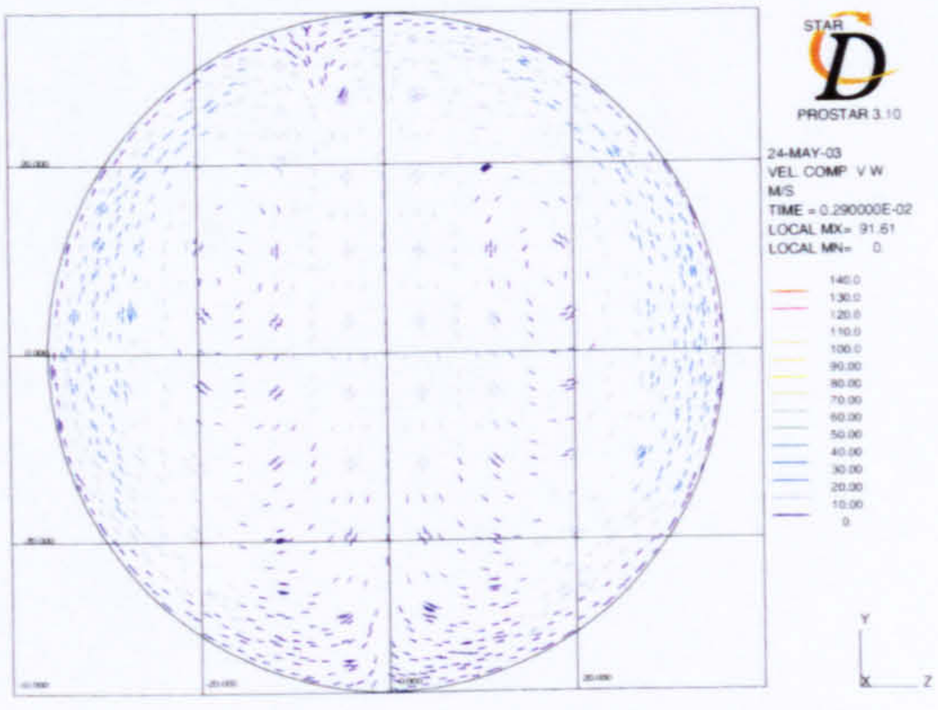

(d) 47° - 2D

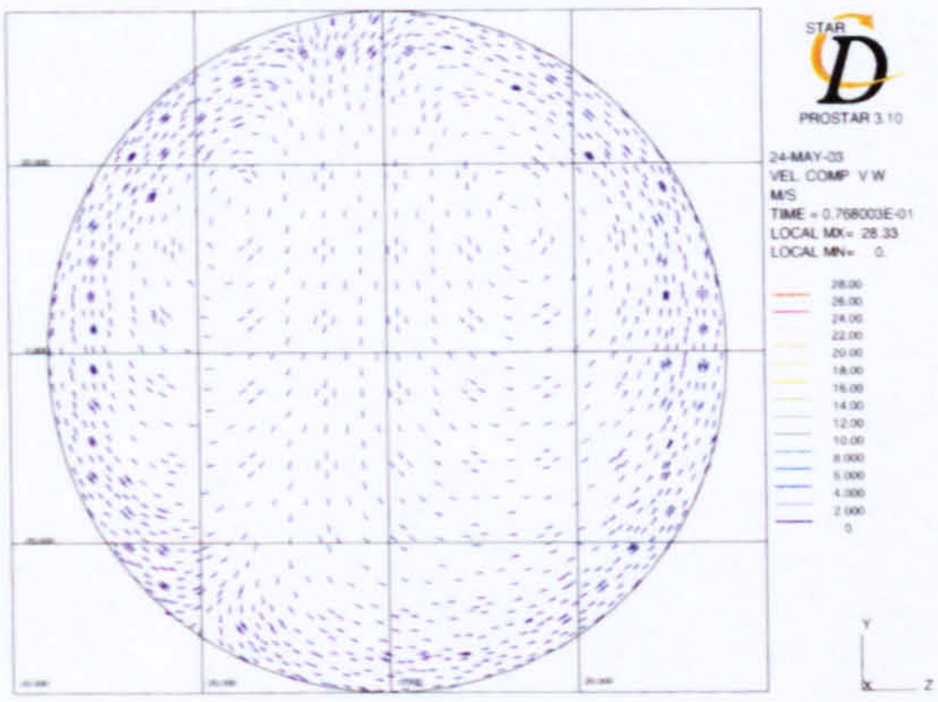

(e) 5.8° - 3D

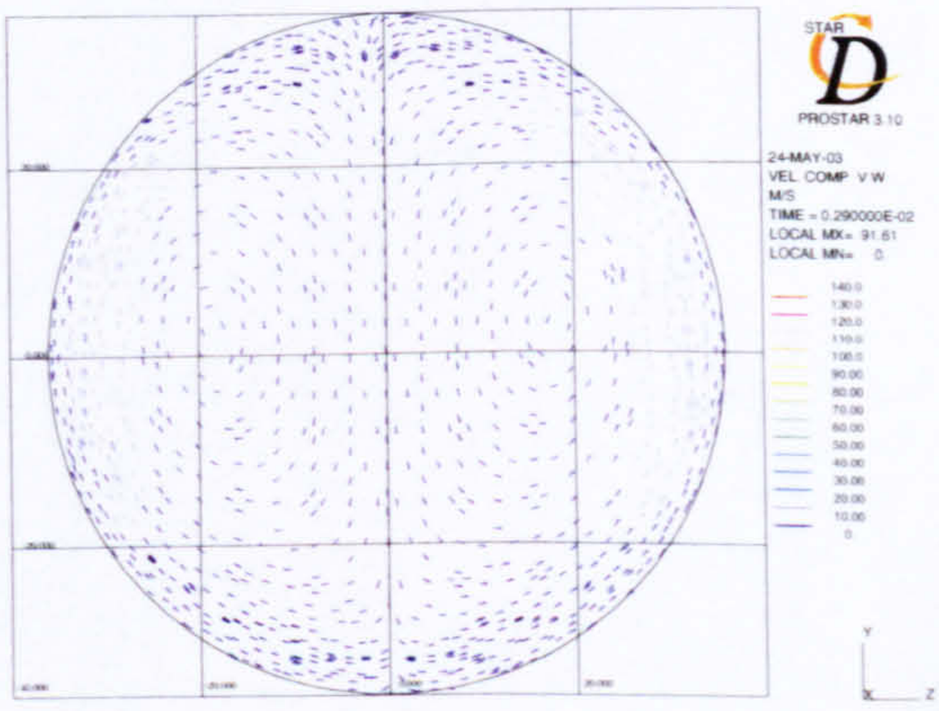

(f) 47° - 3D

Figure 3.11: Axial cross sections of the flow downstream of the valve showing in-plane velocity components. From top to bottom shows sections 1D, 2D, and 3D downstream; left 5.8° flow, right 47° flow. Vectors have fixed scaling and are coloured by velocity magnitude according to those of previous figures.

more untidy. Figure 3.11(a) reveals a change in flow direction from downwash to upwash as depicted in the earlier figures. By the time the flow has reached 2D downstream of the valve (Figures 3.11(c) and (d)) the main flow structures have developed that extend the remaining downstream domain without bursting. These are formed through separation of the flow from the leading edge of the valve that convects downward while the flow to the sides of the valve then also separates. The combined action of the gradual separation generates a net circulatory motion on either side of the domain leading to the vortices. These vortices are present for all the flows studied and have been picked up by previous studies of throttle and butterfly valves (Huang & Kim, 1996; Lacor & Hirsch, 1988). However, a degree of asymmetry exists in the structures that is missed when performing simulations using a half domain and symmetry plane.

The paired vortices appear stable, although a periodic oscillation exists where the vortices are swept from side to side in the domain. This is depicted in Figure 3.12 where a sequence of plots show the leading edge wake between the vortices sweeping across the domain and back again for a valve opened at 19°. Each plot shows the solution advanced 0.5 ms at an axial section 2D downstream from the valve pivot. The plots also show that the vortices alternately grow and shrink as the solution progresses. However, it is not clear from these plots as to what the method of oscillation is and further analysis yields that the vortices are in fact quasi-stable and fight for position in the domain. The structure is, however, maintained by the high-energy leading-edge flow that drives the vortices, and maintains the pairing and stability.

Instantaneous Wall Surface Streamlines

When this leading-edge flow reaches the lower wall it is swept up around the walls of the domain in order to maintain continuity. A second factor in generation of the vortices, generally only applicable to larger valve angles, is the flow passing between the valve edges and the throttle walls. This remains predominantly orientated normal to the valve face, and hence upwash is created along the wall by the flow that encourages the vortical motion of the flow. In addition, the side flows are partially driven by the

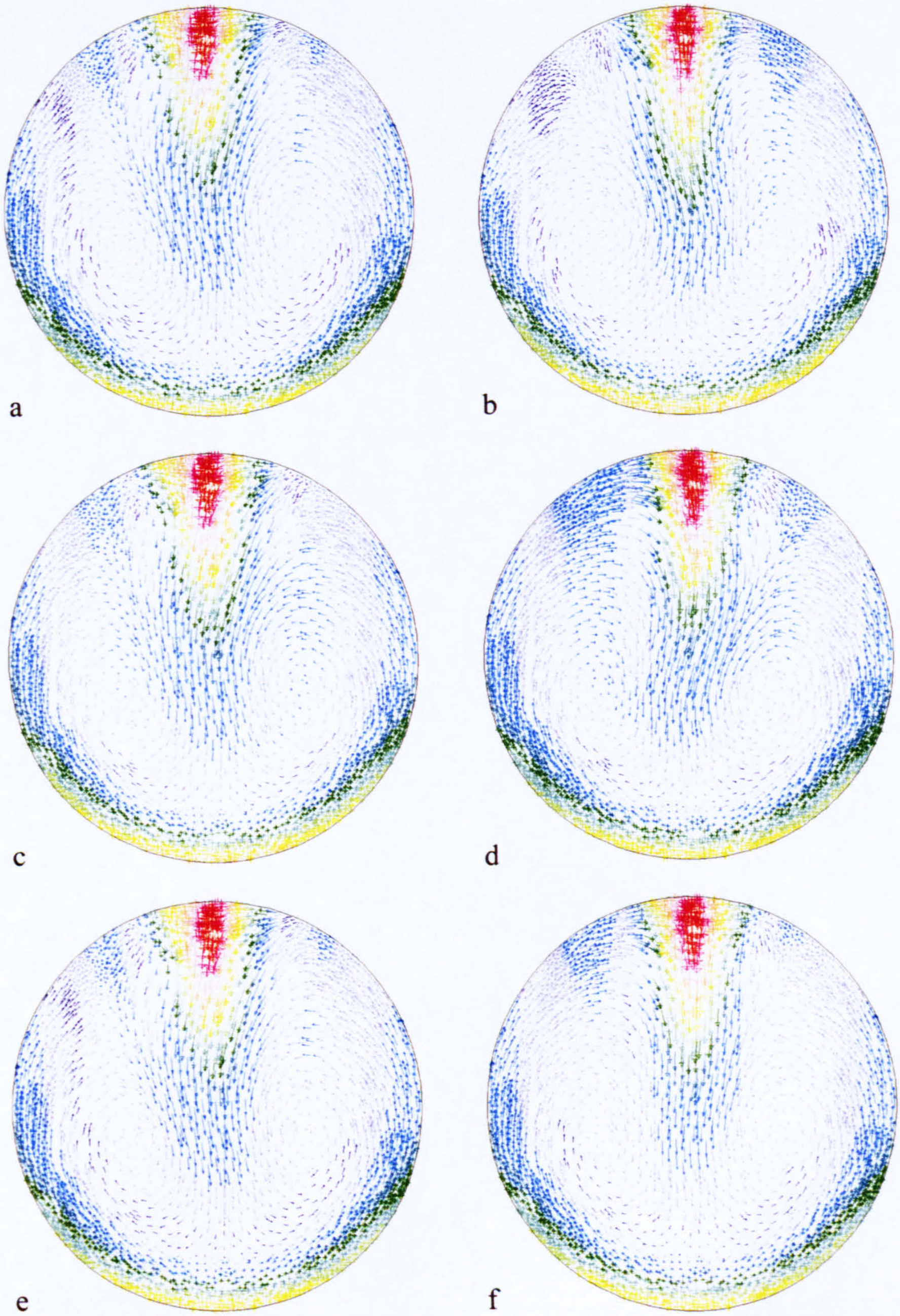

Figure 3.12: Velocity vectors plotted at 0.5 ms intervals in an axial cross section 2D downstream of valve for an opening of 19°.

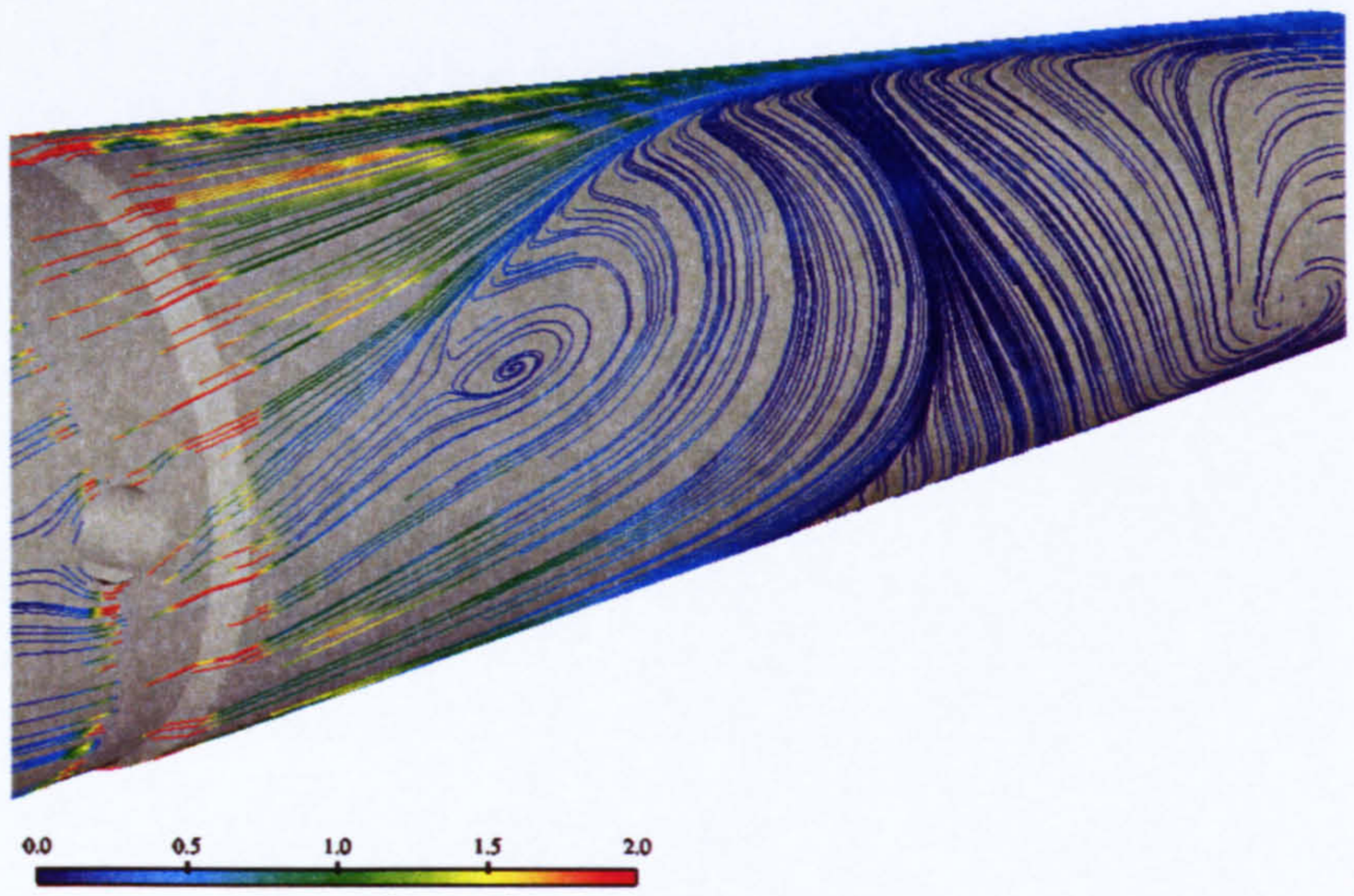

Figure 3.13: Instantaneous surface streamlines extrapolated from the near-wall cell projected onto the wall of the computational domain for the flow through the valve open at 5.8°.

locally attached vortices as found in the central section plots. Figure 3.13 shows the surface streamlines on the wall of the throttle body for a valve at 5.8° that shows locally generated upwash at the valve.

Figure 3.13 also highlights the low-energy region that exists in the lower downstream portion of the domain that is entrained upward by the high-energy flows surrounding this region. Once reaching the upper high-energy flow this low-energy upward flow is accelerated along the upper wall of the domain. A small vortical structure can also be seen on the surface of the wall which forms as a result of interaction of the low-energy flow in the lower region of the domain and the higher-energy flow of the upper domain. However, the vortex is intuitively counter-rotating, with rotation against the high-energy flow of the upper domain. It is thus likely that the vortex is quickly dissipated by the action of the flow. The vortex appears to form from the flow passing the valve side and pivot where a circular cylinder is effectively presented to the oncoming flow; however, there is insufficient evidence to verify this. Far downstream a further recirculation is evident; however, this may be the result of inadequately placed boundaries, as will be discussed.

In a similar manner the flow at the higher flow angle also shows upwash immediately downstream of the valve, which occurs close to the valve owing to the higher valve incidence, see Figure 3.14(a). The remaining flow structures are similar to the smaller-angle flow, with the high-energy leading-edge flow at the top of the domain; upwash along the walls; and a continuing flow downstream. However, in addition the large-angle flow depicts several vortical structures near the upper wall of the domain; these are more clearly shown in Figure 3.14(b) that shows the same flow from above. Intuitively one would expect these vortices to rotate with the flow, and the figure shows this to be the case with each vortex driven by the velocity gradient between the upwash and leading-edge flows. It is not immediately clear how these vortices interact with the other flow structures present in the domain, although they appear to coincide with the vortices predicted in the section plots through the upper domain (Figure 3.10).

Instantaneous Flow Streamlines

It appears as though the vortices present on the upper domain walls may be responsible for the periodic oscillation of the flow shown previously in Figures 3.10 and 3.12. Careful inspection of the axial flow sections (Figure 3.12) reveals that the pairing line of the main axial vortices actually initiates to one side of the main leading-edge flow, and that it is this position that moves from one side to the other of the central region as opposed to the core high-energy flow oscillating. The smaller vortices seen in the wall flows, and section cuts, exhibit periodic shedding patterns similar in formation to that of a von Kármán vortex street downstream of a circular cylinder or bluff body. It is the alternate passing of these vortices that leads to the periodic oscillation found in the downstream wake of the valve. However, it is not immediately clear how these small vortices have formed, whether they are induced by the flow, or whether they are as a result of shedding from part of the geometry. As discussed, this may be due to the shear layer formed between the high- and low-energy flow. A further possibility is a vortex being shed from the pivot exposed to the oncoming flow; however, the scale of the vortices suggest that this is unlikely. A further possibility, and, perhaps, the

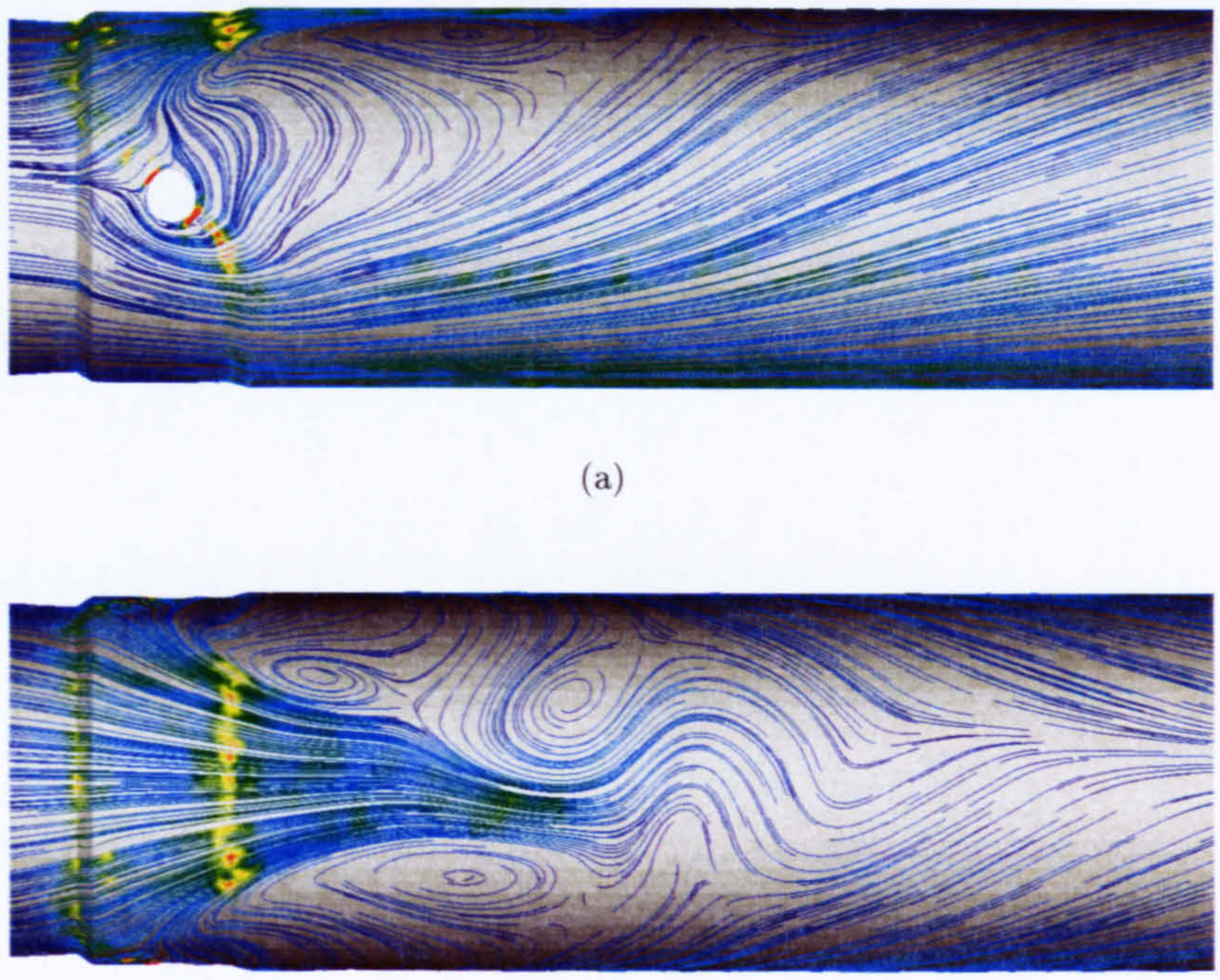

(a)

(b)

Figure 3.14: Instantaneous surface streamlines extrapolated from the near wall cell projected onto the wall of the computational domain for the flow through the valve open at 47°. (a) Side view, (b) top view.

most plausible in terms of the flow structure, is that the vortices are those depicted in the central section plots (Figures 3.8 and 3.9) which are periodically shed into the downstream flow. How these form is revealed below.

In order to fully understand the flow structure the results of the predictions have been analysed using alternative post-processing software, ENSIGHT (Computational Engineering International Inc., 2000), that specialises in flow visualisation. Although some of these capabilities are available in PROSTAR, their use is cumbersome and slow, and that limits the information that can be extracted from the results.

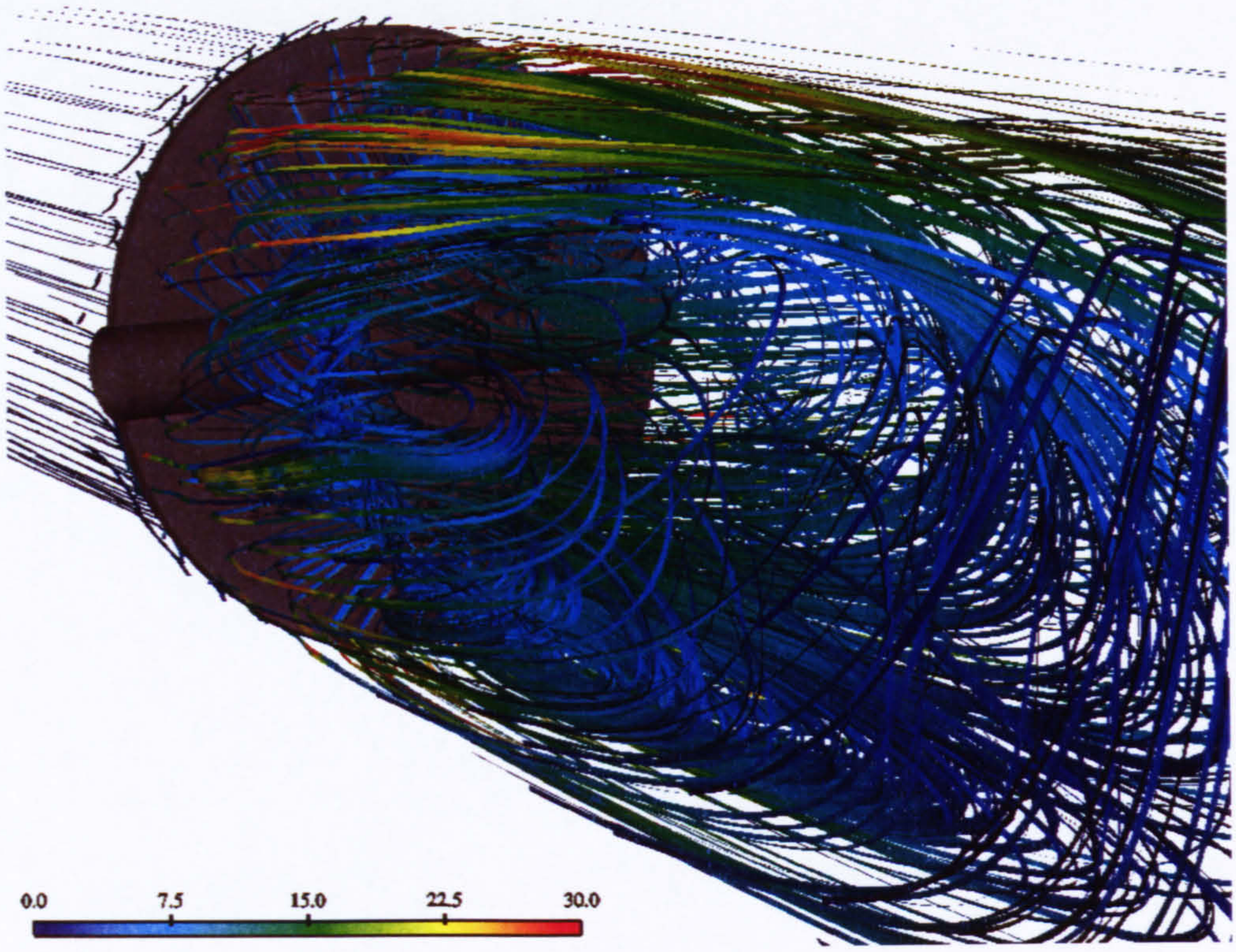

Figure 3.15: Streamlines (ribbons) in the wake of a valve open at 5.8° looking from downstream. Streamlines coloured by velocity magnitude.

Visualisation of the flows reveals that the same bulk structures exist in the flow for the range of flow angles studied; however, the methods by which the main axial vortices are generated differ from the small- to large-angle valve openings. Figure 3.15 shows the structure of the flow downstream of the valve open at 5.8° using instantaneous reverse-flow streamlines generated from the domain outlet. The streamlines reveal that the vortices of the previously presented sectional plots form a toroidal vortex that lies immediately downstream of the valve. The toroid has notably stronger vorticity at the leading and trailing edges where the flow is greatest past the valve. The leading-edge flow is pulled down into the domain and is subsequently split with some of this flow being entrained into the lower part of the toroid, and the remainder traversing downstream.

Flow leaving the trailing edge is entirely entrained into the lower vortex and hence a

low-energy region exists downstream of this, that has been shown in the wall streamlines and section plots. Flow from the side of the valve thus wraps up the side of the wall in this low-energy region, before it is pulled back into the leading- and trailing-edge vortices close to the valve, or further away, forms the main axial vortices as it is entrained by the downwash of the leading-edge flow. Detail of the vortex structures can be revealed by finding the vortex cores within the domain. This has been achieved by finding the connected points of zero flow that are present at the core of a vortex. By using these cores as seeding points, a further set of localised streamlines can be generated that show the vortex structures in the flow more clearly. Generating seeding points from the true core would result in no streamlines as the velocity at the core is zero; however, the core lines generated have a finite thickness and therefore the seeding locations are in regions of flow with non-zero velocity. Figure 3.16 depicts the vortex cores (as solid black lines) and the subsequent streamlines generated from these, corresponding to the flow of Figure 3.15.

The core structures are now much more apparent with the toroid vortex clearly defined just downstream of the valve. Downstream of the toroid the two main axial vortices are formed by the wrapping-up action described previously. There are, however, no notable vortex structures in the upper domain that are responsible for the oscillatory flow. Similar flow structure is found for the other small-angle flows; however, at these angles a few small vortices are present in the upper domain that form through the wrap-up of the flow up the walls. Again the toroid structure dominates the flow in the vicinity of the valve and the main vortices form downstream from this.

As the throttle valve is opened further, interesting changes occur in the flow structure that are not immediately apparent from the sectional plots shown previously. Opening the valve results in less severe separation and hence the leading-edge vortex becomes attached as has been shown. As this happens the trailing-edge vortex of the toroid becomes detached from the valve and moves further from the valve as the opening increases. At the same time the sides of the toroid are strengthened by the increased size of the gap at the valve sides, and the cores of these vortices become increasingly

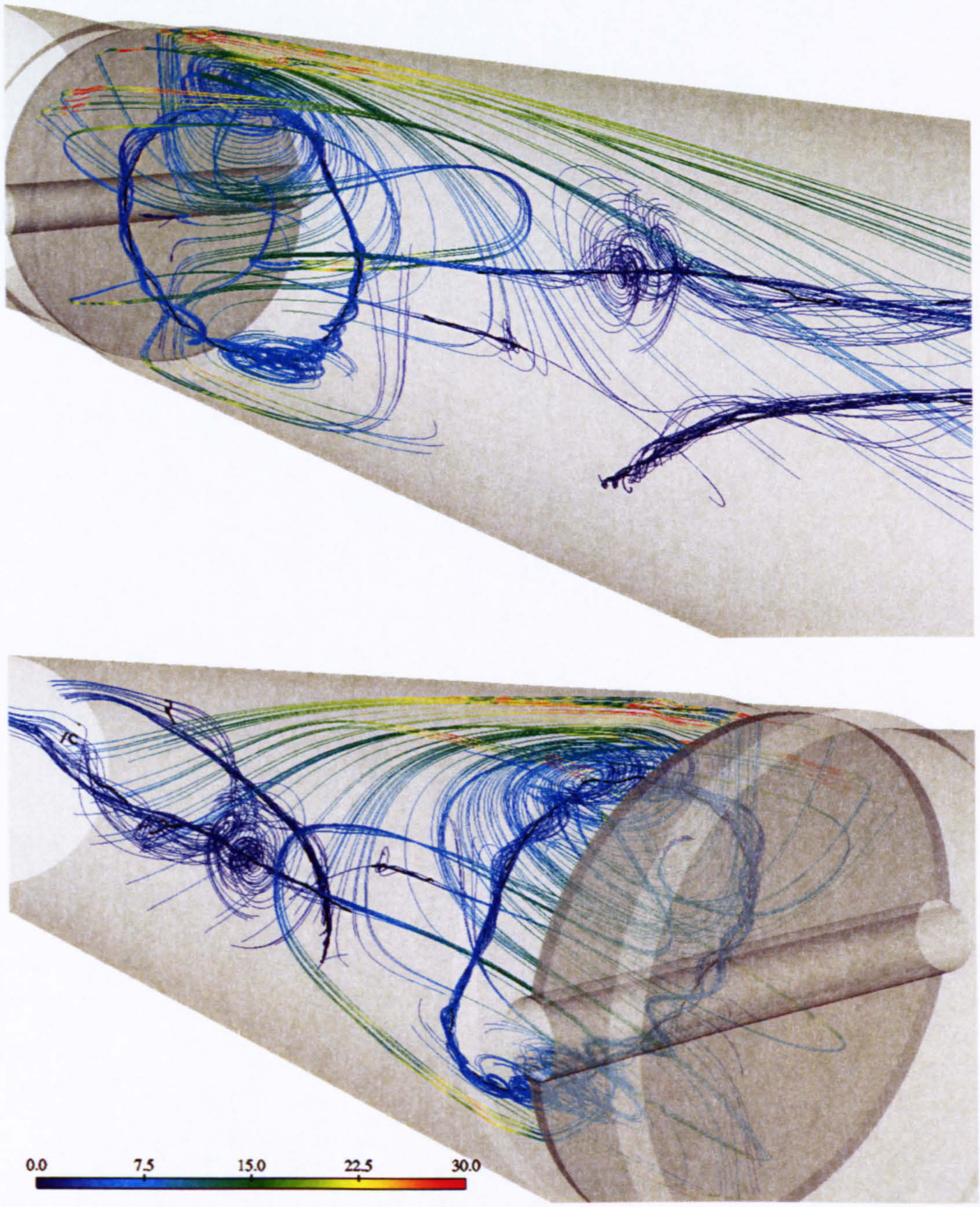

Figure 3.16: Instantaneous streamlines generated from the vortex cores (solid black lines) in the wake of a valve open at 5.8°. Views looking upstream and downstream with streamlines coloured by velocity magnitude.

aligned with the axial direction owing to the valve orientation. With the trailing-edge vortex detached, a horseshoe vortex is formed where the sides of the toroid vortex are stretched downstream forming the main vortical structures of the downstream wake. Figure 3.17 shows the vortex-core streamlines for the valve open at 30° that clearly shows this occurring.

For this case the leading-edge flow moves sharply down the rear face of the valve where interaction with the trailing-edge flow occurs. Flow passing around the side of the valve can clearly be seen wrapping up into the stretched side vortex that continues downstream. For the flow over the valve at 47° and 60°, the small-scale upper vortices become better defined allowing improved streamlines to be generated, as shown in Figure 3.18. Here the leading-edge vortex is still present and the side vortices are also stretched downstream in the manner described. However, the side vortices now appear to strongly curl upward to the upper wall of the domain with the flow further downstream curling up to form the main vortices in conjunction with the leading edge flows. Such vortex bending is reported by Rockwell (1998) for vortices interacting with bodies. These upwardly orientated vortices appear to form via the local separation around the valve sides at high incidence that combined with the local upwash orientates the separated vortex structure more vertically.

Unlike the main axial vortices, which are restricted in their movement by the walls of the domain, these smaller vortices have the freedom to move and given the unstable nature of the pairing, they alternately shed downstream from the valve. Downstream these vortices are dissipated by being entrained into the main vortices as the lower flows wrap up the sidewalls; however, a periodic oscillation to the flow remains. Dissipation of the axial vortices is apparent that is a result of the combined action of the flow and the dissipative nature of the k-ε turbulence model that is well-known for this. Unsteady RANS modelling using the k-ε model has previously been shown (Nishimura & Kimura, 2001; Tucker, 2001; Wilcox, 1994) to under-predict turbulence energy in stagnation regions resulting in dissipation of time-dependent processes, and hence these small-scale vortices may be a result of incorrectly applied turbulence quantities. The

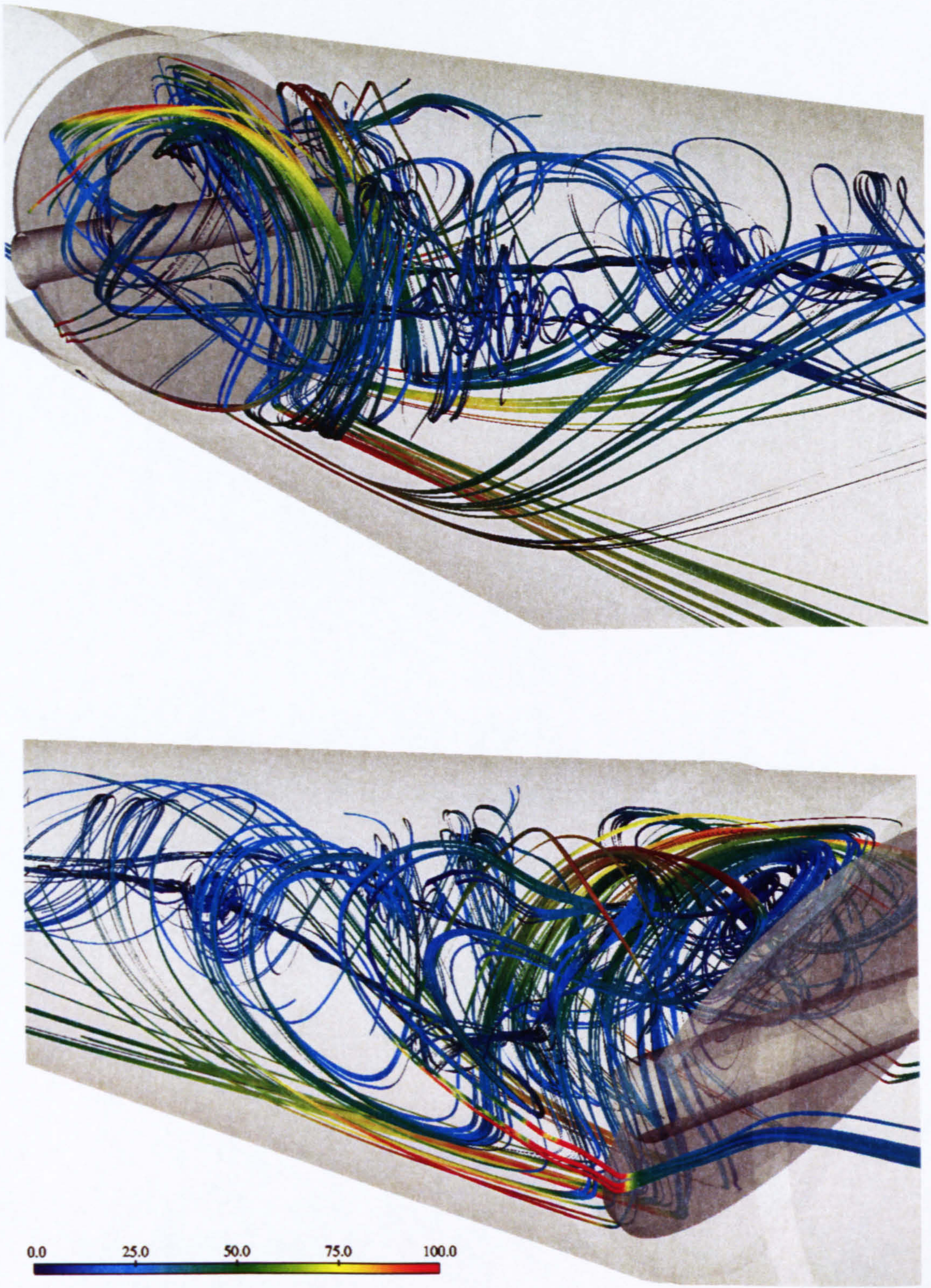

Figure 3.17: Instantaneous streamlines generated from the vortex cores (solid black lines) in the wake of a valve open at 30°. Detachment of the trailing edge is evident with stretching of the toroid structure to form an horseshoe vortex. Streamlines coloured by velocity magnitude.

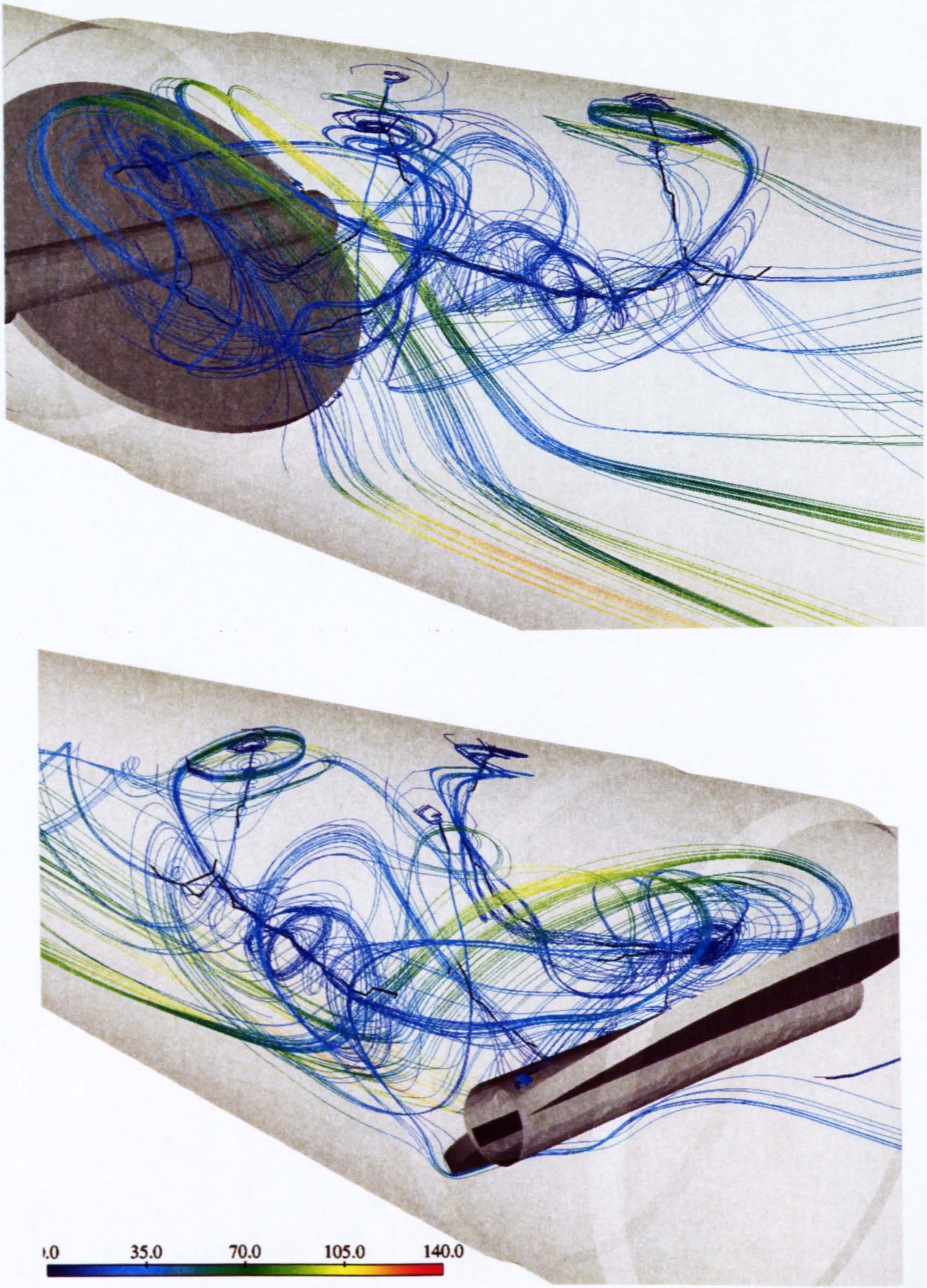

Figure 3.18: Instantaneous streamlines generated from the vortex cores (solid black lines) in the wake of a valve open at 47°. Detachment of the trailing edge is evident with stretching of the toroid structure to form an horseshoe vortex and upper domain vortices. Streamlines coloured by velocity magnitude.

over-prediction of turbulence generation at stagnation locations is a result of the wall-functions predicting the presence of a boundary layer where one would physically not exist, or be considerably thinner.

3.8.2 Time History

Evaluation of predictions over time reveals that the vortex shedding is indeed periodic and appears to remain stable for the duration of the prediction. The vortices shed alternately in a manner similar to a von Kármán vortex street at high Reynolds number (Williamson, 1996). However, growth of the wake and the individual vortices, as typically seen in the wake of bluff bodies in free flows (Matsumoto, 1999), is not observed owing to the restriction of the domain walls. The basic structure of the vortices remains the same for the cases considered, which reflects the Reynolds number invariance of turbulence, although considerable scatter in the latter has been found by Cantwell (1981).

Vortex shedding in this manner affects the torque loads on the valve that has been shown in previous studies to be sensitive to the pressure distribution on the valve (Solliec & Danbon, 1999; Danbon & Solliec, 2000; Morris, 1987; Morris & Dutton, 1989*a*). The vortex shedding leads to pressure fluctuations on the valve surface that in turn lead to a fluctuation in the torque on the valve (as the fluctuations occur predominantly on the downstream face) and hence flutter of the valve can occur (Hirt, Iten & Ziada, 1997; Danbon & Solliec, 2000) that can place additional load onto the throttle controlling mechanism. An oscillating valve in the flow stream generates further complexities to the flow where additional vortices are often formed as a result of valve movement (Matsumoto, 1999; Rockwell, 1998). The effects of torque load on the valve have not been evaluated in this study.

For each of the throttle flows investigated, the velocity in the wake of the valve has been monitored over the period of simulation, thus allowing a time-history of the downstream motion to be evaluated. Full transient flow histories have not been stored for the models owing to the exceptionally large size of the data files required for such analysis.

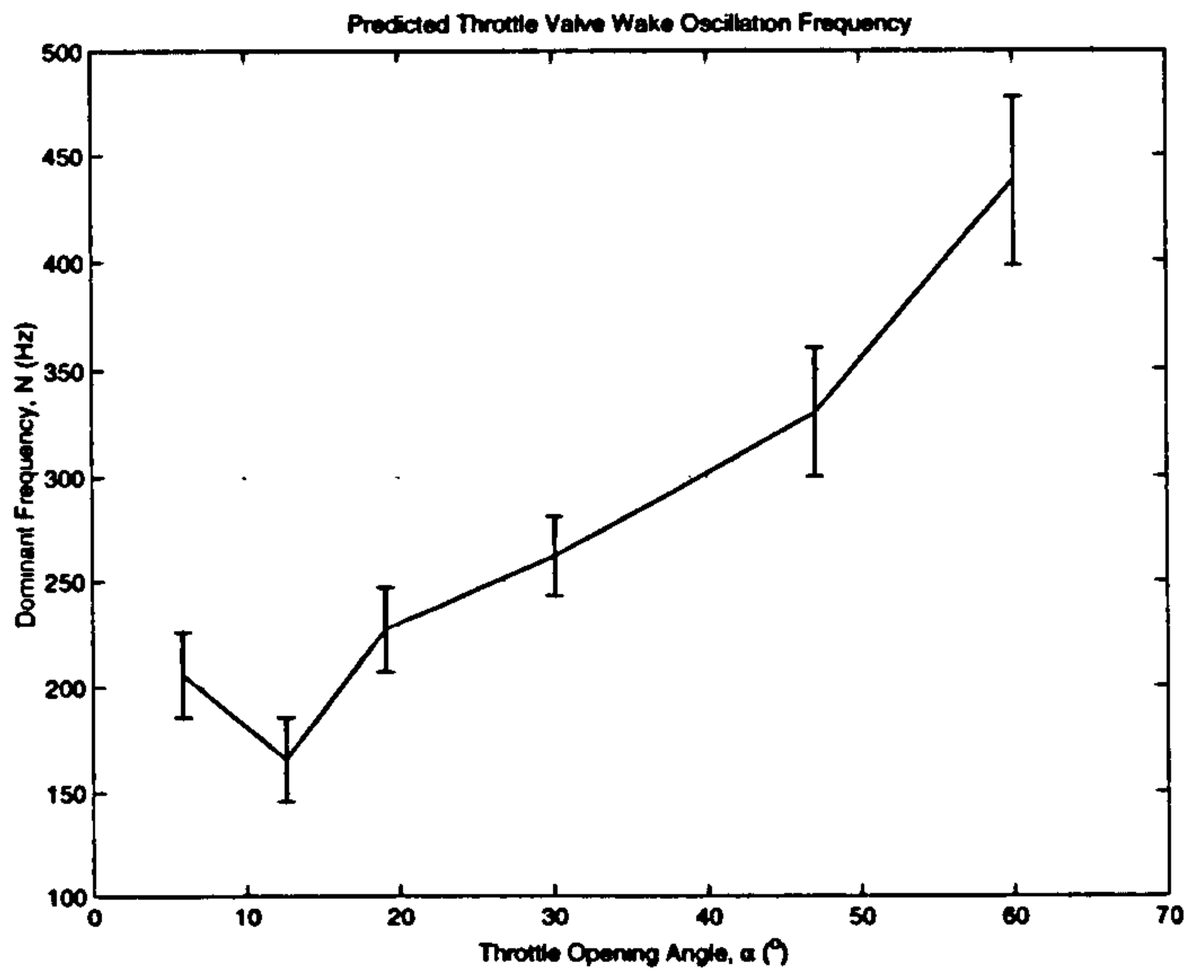

Figure 3.19: Prediction of flow oscillation frequency downstream of the valve leading edge for a range of throttle opening angles.

A monitor cell has been chosen that lies downstream of the leading edge of the valve such that it lies in the region of predicted oscillation. Evaluation of the velocity components in this region allows the frequency of the oscillation to be determined, alongside the amplitude of the oscillation in each of the component directions. Using these data also shows that small-scale oscillations exist where they have not been apparent in the plots, and they also reveal periodic flow for each of the flow angles considered. Figure 3.19 plots the frequency of oscillation of the flow against the throttle opening angle for the range of flows studied. Here the frequency has been evaluated using a Fast Fourier Transform (FFT) of the monitored signal.

Figure 3.19 shows that the frequency of flow oscillation is a function of the flow angle and that as the valve is opened so the frequency of oscillation also increases. At the lower valve openings the frequency is independent of angle and remains fairly constant at approximately 200 Hz. A near-linear increase in frequency is observed as the valve opens further. Evaluation of the velocity trace for the smaller-angle flows also shows that considerable damping of the oscillation is present, and that after sufficient time the flow tends to reach a predominantly steady-state solution. For the larger-angle flows,

the damping is considerably reduced and no longer apparent at the largest throttle angles considered (47° and 60°).

For each of the cases considered, an underlying high-frequency oscillation of the monitored values has also been found that oscillates about the mean velocity. This high-frequency component to the flow is considered to be an artifact of numerical dispersion that occurs when using the higher-order discretisation schemes.

Stability of the flow is maintained by ensuring that the Courant number for the flow remains low, as has been discussed previously. Monitoring of the Courant number over the duration of the simulation reveals that the flow undergoes an initialisation whereby the Courant number rises, either steadily or through a slight oscillation, before settling to a steady value that remains below a value of 100 for all flows. The initial settling of the Courant number coincides with the initial oscillations of the flows, and the damped flow oscillations corresponding to the steady Courant number. For the large-angle un-damped flows the Courant number also shows initial startup and subsequent settling.

Given that oscillations are predicted for the cases considered but that damping of the these oscillations is predicted for the small-angle flows, it is possible that for the larger angles that the flow will also eventually be damped and that the oscillation is nothing more than an artifact of the numerical dispersion of the models. However, the predicted flow fields appear to physically make sense and thus the oscillations can not be disregarded so readily. Previous studies have shows that the k-ϵ turbulence model, and unsteady RANS modelling in general, tend to damp oscillations in time-dependent flows. In particular, Nishimura & Kimura (2001) have shown that use of the k-ϵ model for URANS calculations of jet mixing severely under-predicts the level of mixing and severely damps the oscillation that is shown to exist by experiment, and is also predicted by LRSFM (low Reynolds number and heat flux equation) models. Where the flow is known to produce oscillations similar to those shown here, the k-ϵ model tends to smooth the flow to an almost steady state. Yao, Savill, Sandham & Dawes (2000) have highlighted the effect of grid density, and grid asymmetry on the prediction of transient flow features. In their study of trailing-edge separation using

URANS and LES simulations, they found that the URANS models were particularly sensitive to the symmetry of the grids, and use of a two-dimensional grid stemmed the transient effects completely. A strong possibility thus exists that the flow here is in fact transient, but over-damped by the turbulence model, coarse grid resolution, and limited domain.

In addition to the predicted vortex shedding, the time-dependent study also reveals the formation of some small-scale vortices, in particular from the leading edge of the valve. These form from the localised leading-edge separation zone and travel down the downstream face of the valve at the larger opening angles. Upon reaching the trailing edge the vortex is rapidly entrained into, and subsequently dissipated by, the free shear layer generated by the separated flow.

3.8.3 Turbulence Predictions

Predictions of the turbulent kinetic energy and turbulent dissipation rate are shown in Figures 3.20 and 3.21 for the valve open at 5.8° and 47° respectively. For both small and large valve openings, high kinetic-energy values exist downstream of the valve, with additional areas of high kinetic energy occurring in the valve-to-wall gap for the smaller-angle flows. High values of turbulent dissipation are predicted in approximately the same regions as turbulence production that stems from the proportional relationship between k and ε in the governing equations (2.20) and (2.21).

Typically, high levels of turbulence production are associated with areas of high Reynolds stress in a flow that in turn generally lie at regions of maximum velocity gradient in the flow (Tritton, 1988). Comparison of the plots with those showing the velocity vectors shows that high levels of turbulent production are indeed associated with regions of high velocity gradient such as the trailing-edge shear layer and edges of the large-scale vortices. Such large-scale structures are responsible for turbulence production and the classic energy-cascade theory suggests this is passed on to smaller-scale eddies in the flow (Bradshaw, 1970; Versteeg & Malalasekera, 1995). Predicted values of turbulence dissipation therefore seem qualitatively realistic.

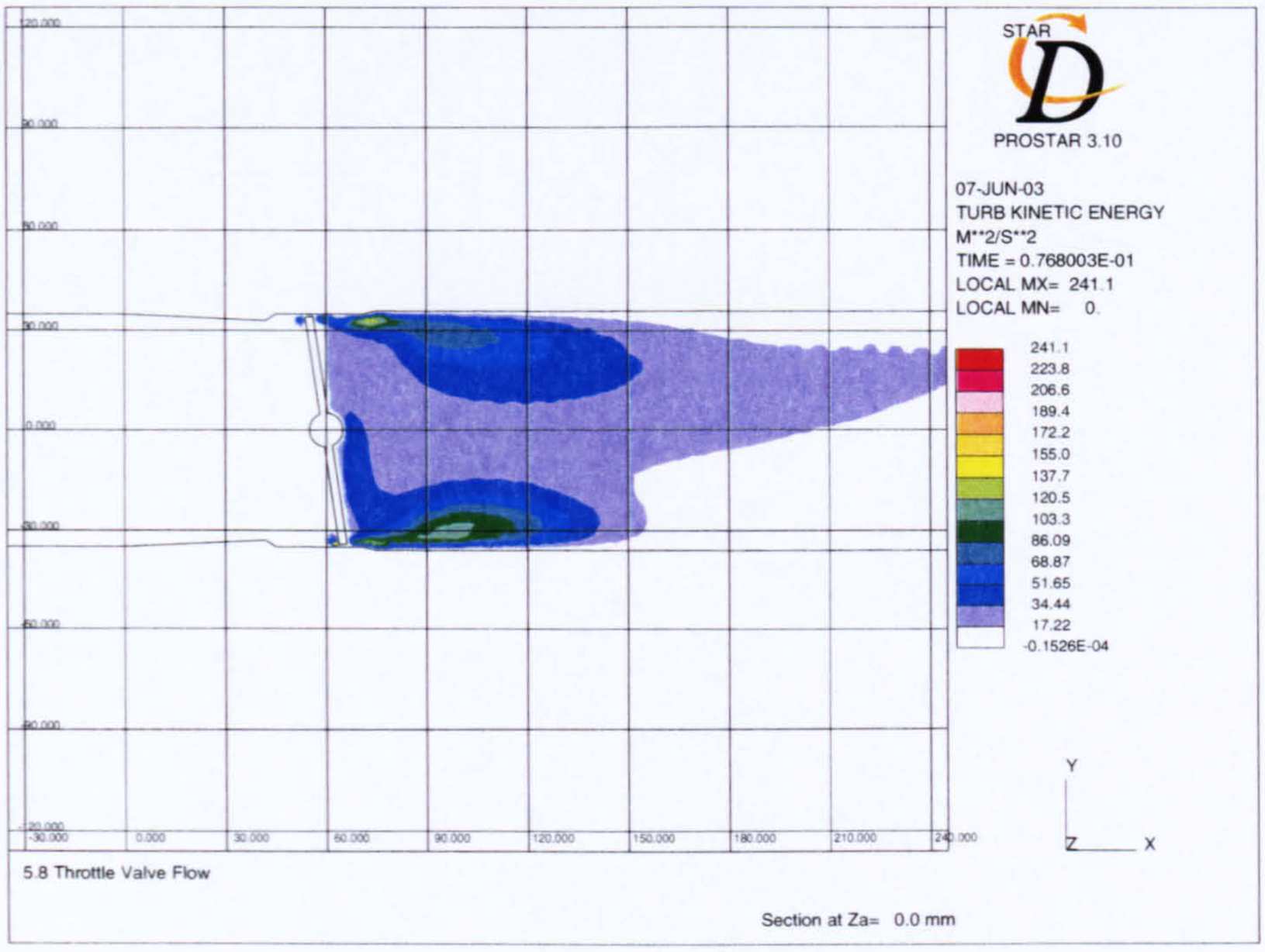

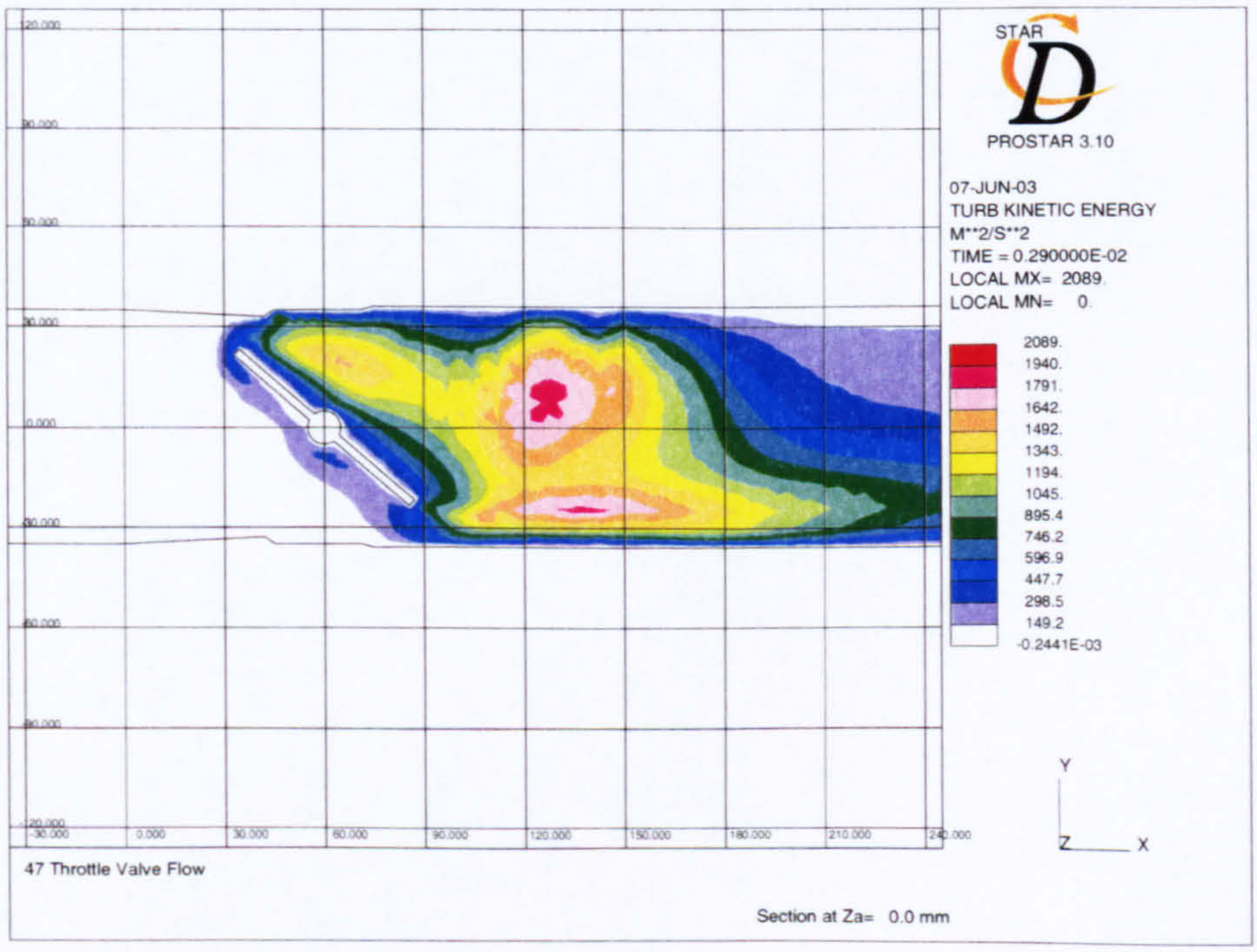

Figure 3.20: Predictions of the turbulent kinetic energy of the flow through a valve at 5.8° and 47° through the symmetry plane.

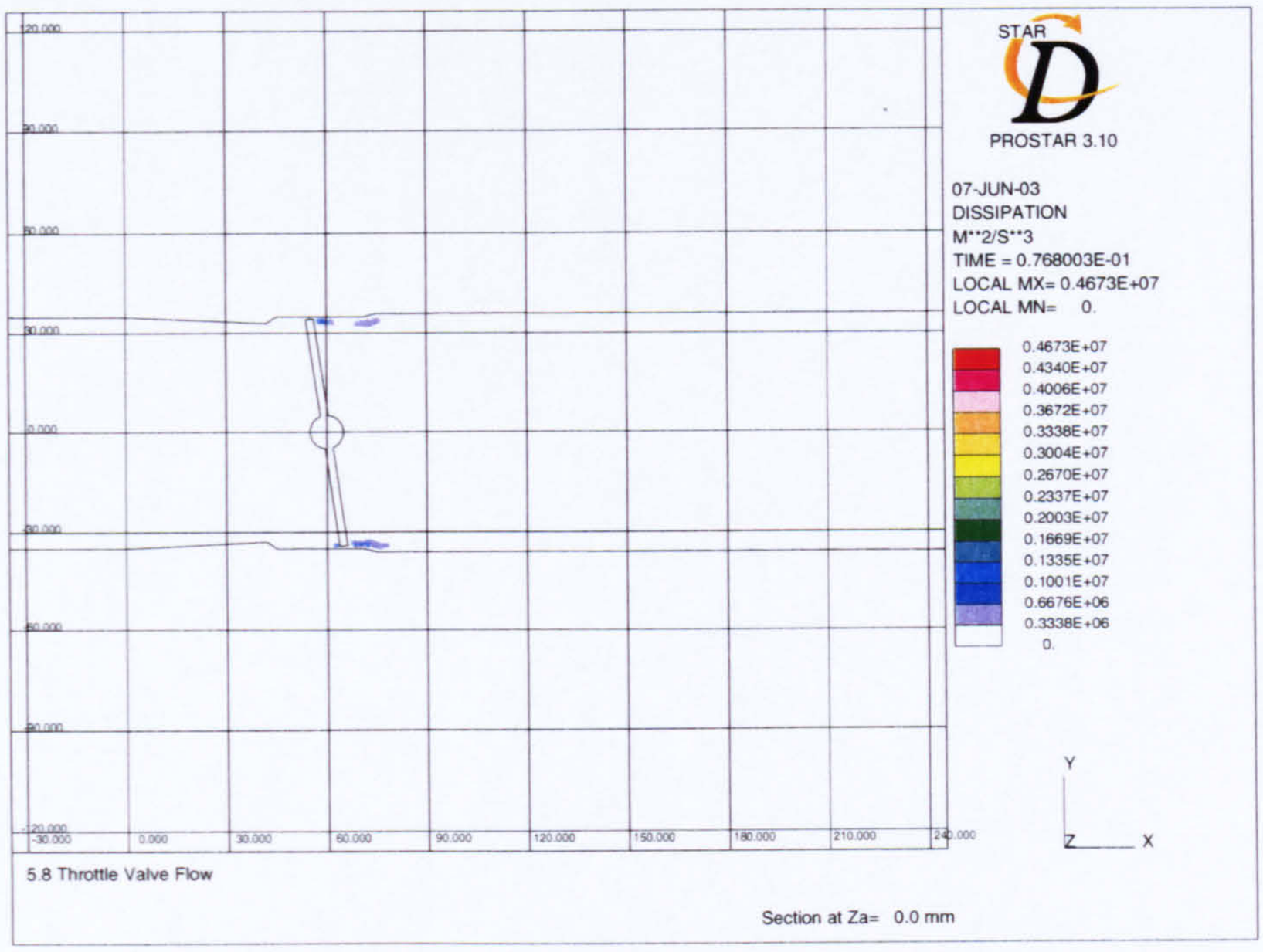

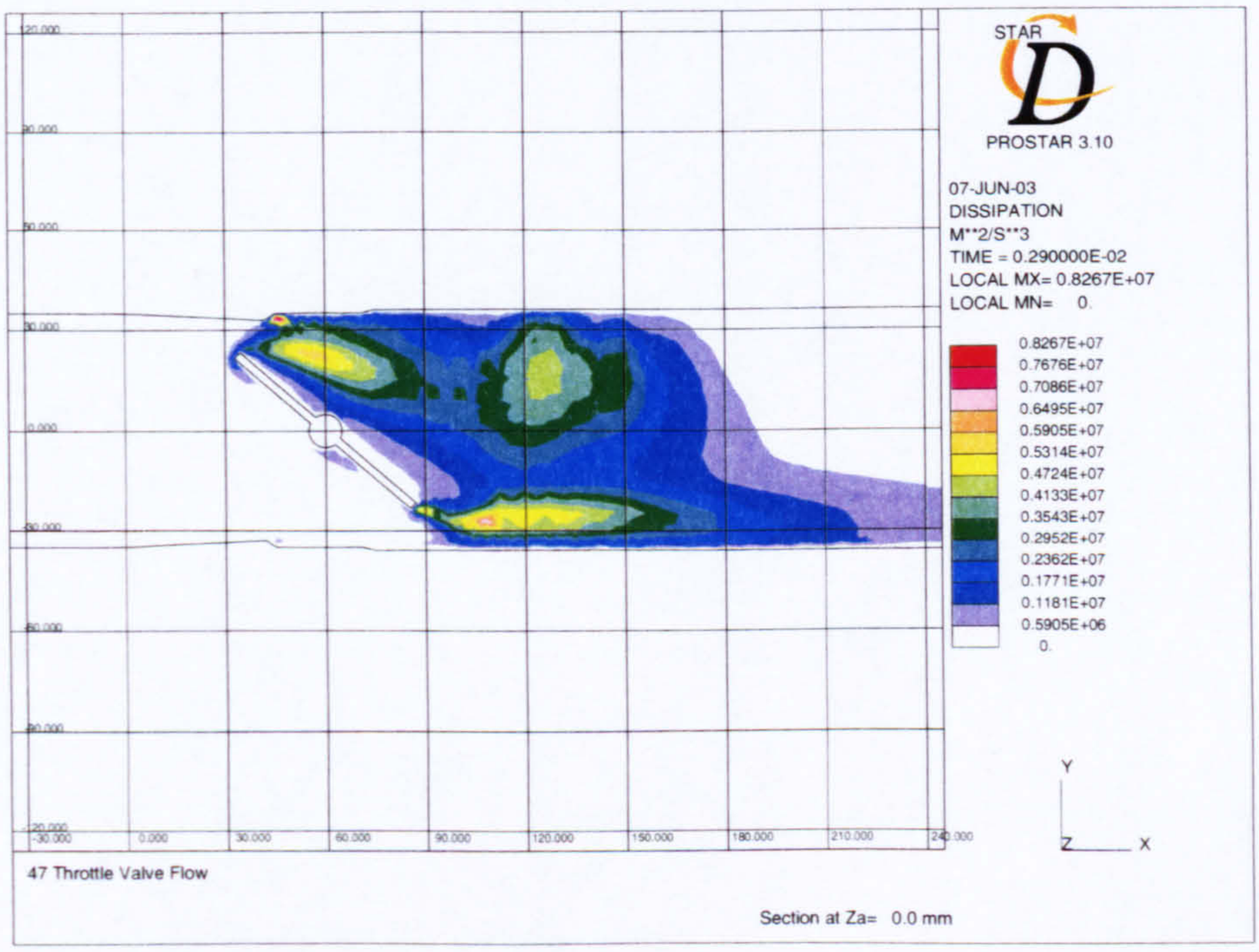

Figure 3.21: Predictions of the turbulent dissipation of the flow through a valve at 5.8° and 47° through the symmetry plane.

Dissipation levels are generally highest in the same regions although the peak values lie upstream to those of peak production, highlighting the k-ε relationship. High values can be also seen at the valve trailing edge in the flow at 47° as well as at the step in the upper throttle wall. These regions appear to correspond to regions of particularly high shear that, perhaps, stem from insufficient grid resolution. Such small-scale structures are known to be dissipative in nature and thus there regions of high dissipation are unsurprising. Further downstream the dissipation and production rate reduces considerably to levels of that found upstream of the throttle valve.

Quantitatively one notices that there is considerable difference in the levels of dissipation between the two flows shown. Turbulent kinetic energy for the flow at 47° is approximately one order of magnitude higher than that for the flow at 5.8°. Peak dissipation has doubled for the same cases. These values are specific to the cross-sectional plots shown, but the trend holds true for the entire flow field. This rise is perhaps unsurprising given the sharp rise in the velocity from the small- to large-angle flows, and that the turbulent boundary conditions are based on the square of velocity.

3.8.4 Compressible Calculations

Compressible flow calculations have been performed given that high-speed flows exist in the valve-to-wall gap where the flow is accelerated through the valve. For the flow solutions at 12.5° and above, the local Mach number has been found to reach 0.3 in the valve gap thus warranting the compressible flow calculation. A maximum Mach number of 0.6 has been found for the flow through a valve at 30° in the flow past the leading edge. The remaining flow also remains at subsonic speeds with no shock waves predicted that would suggest the onset of choked flow (Anderson, 1991). This is verified by there being no discontinuities in the static pressure or density fields within the domain that would suggest formation of a shock. The latter has been found by previous investigators when considering the compressible flow field through butterfly valves, although these studies were primarily targeted at transonic and supersonic flows and specifically interested in the onset of choked flows (Morris, 1987; Morris & Dutton,

1989*b*; Addy et al., 1985). The use of a slightly reduced valve diameter, so increasing the valve gap, is likely to have affected this as Chen & Chen (1995) have performed a similar study that shows an increase in Mach number for a larger gap. In their study the flow area is increased by approximately 100% at an opening of 0.5° that leads to an approximate 400% increase in mass flow-rate and 65% increase in Mach number. Correlating this to the current investigation, at an opening of 0.5° the increase in flow area is approximately 250% for the change in valve size, thus the change in mass flow rate and Mach number may be expected to be of a similar order of magnitude to that found by Chen & Chen (1995), and thus the localised Mach numbers are assumed to be over-predicted here.

The following chapter describes the layout and design of the experimental equipment used to investigate the physical flows, and the subsequent chapter presents the results of the investigation. These results are then compared and discussed to the predictions presented here in chapter 6.

Chapter 4

Experimental Design

4.1 Introduction

In order to validate the CFD simulations, and to gain a better understanding of the flows through throttle valves, a series of experiments have been carried out. For the work carried out here, the ideal experimental measurements would capture the entire flow field, or more realistically, capture a large number of locations in the flow to analyse the flow in sufficient detail. Unfortunately the flow field of interest is highly three-dimensional and rotational, thereby limiting the type of measurements that can be made successfully. Owing to the limitations of the available equipment and measuring techniques, the flow measurements were made on a smaller scale, but with enough detail to provide information suitable for validation of the computational predictions.

This chapter describes the design, manufacture, development and testing of the flow rig used to study the flow through the throttle valve. In addition, the methods of flow measurement and the equipment used are also described alongside the methods of data capture. The chapter thus begins with the initial design of the flow rig followed by detailed design of the individual components and ancillaries. The design of the measurement equipment and the associated data capture is then described and finally a description of the various tests that were performed on the rig and other components is presented. The results of basic flow tests and the measurements of the experimental investigation are then given in the following chapter.

4.2 Requirements and Assumptions of the Experimental Investigation

For the experiments to yield useful information some basic requirements need to be met. Firstly, the experiment must match the CFD model as accurately as possible. Accordingly, the flow entering the throttle body has to be smooth and steady with the smallest possible disturbances introduced. In addition, the inlet and outlet to the throttle need to reflect the extended length of the computational domain to enable the full flow features to develop and a uniform pressure gradient to exist at the outlet to the domain. Secondly, the measurements should be made at locations that exhibit flow characteristics of interest, such as the wake oscillation. Of course, it is also important that the measurement system does not introduce disturbances that alter the flow characteristics significantly. Thirdly, the measurements made should provide useful information for the validation of, and comparison with, the CFD predictions. Such quantities of interest are the measurement of oscillation frequency, peak velocity in the flow, the pressure drop across the valve, and flow temperature.

The main aim of the experimental investigation is therefore to study the flow through the throttle valve under controlled conditions. Of course, an investigation of the real situation would involve the flow in a throttle in an operating road vehicle, thus allowing the true flow characteristics to be studied. However, measurement under such circumstances is impractical because of constraints associated with the available equipment. The experimental investigation also has to revolve around the available resources and costs and thus simplifications have to be made to accommodate the study.

For the investigation here, we used a large blow-down rig with a compressor, and from this stems one of the main assumptions of the flow, i.e. that the flow is blown through the valve as opposed to sucked through as in the native environment. Further the flow is a uniform feed whereas the flow generated by a reciprocating engine is pulsed owing to the motion of the pistons. As such, the flow rig has been designed to provide flow over the valve and so uses a settling chamber and screens to ensure a

smooth flow. As described previously, the CFD and experiment must complement each other, and although a CFD model can be made very complex, the limitations are in the experiment, and thus a simple experimental rig has been designed. Generating a smooth flow through a straight domain is a fairly straight-forward achievement, and the CFD is easily able to model such a situation.

In a similar manner the measurement set-up is also often limited to available resources and equipment. Here a HWA system has been used to capture flow velocities and oscillation frequencies of the flow through the valve. HWA is particularly suited to such measurements as it is relatively easy to use, allows fluctuations up to 750 kHz to be measured, and provides fast and accurate results, although calibration is required to obtain velocity measurements and hence the overall quality of result is limited by the calibration accuracy. For frequency measurement, however, calibration is not required and thus the technique is well-suited for this purpose. One disadvantage is that the probe itself enters the flow thus causing some disturbance.

Temperature and pressure measurements have been made using commonly available transducers and a micro-manometer system. The measurement of throttle angle has been achieved through the use of a sensor built into the throttle valve. Signals from the equipment have been fed to a computer via a data-capture card and these raw data are then analysed in Matlab.

Before any full experimental data were obtained, a series of tests was carried out to verify that the rig performed safely and that the rig operated as expected without exceeding its limitations. With the rig assembled and tested the flow quality needed to be ascertained to establish any trends that may affect the results. To do this, several velocity sweeps of the system were made at different flow rates. From these samples a series of velocity profiles have been determined alongside the turbulence intensity for the flow. In addition, any noise in the system was noted to reduce the chances of erroneous signals being analysed in the final experiments. Finally a series of tests was performed to ensure that the HWA system correctly picked out flow oscillations.

4.3 Flow-Rig Design

From the CFD predictions and work of previous investigations it is possible to gauge which areas of the flow will yield the most interesting results. Ideally the entire flow field would be sampled and a wealth of information extracted from this; however, as always there are practical and cost limitations. Thus the rig has been designed to give access for a HWA probe and pressure tappings at distinct locations where computational predictions have shown the flow to be of most interest, in particular at locations downstream of the valve.

4.3.1 Flow Generation

For the experiments a flow-generation facility was required that could generate sufficient mass flow at the higher throttle openings whilst also providing the greatly reduced mass-flow rates at smaller opening angles. The air supply used for the experimental investigation forms part of a blow-down rig that consists of a large compressor and pressure vessel or reservoir with a controllable outlet. The compressor and reservoir happen to be situated adjacent to an anechoic chamber as a result of a previous experimental investigation and hence the experiments have been carried out within the chamber. Although not a necessary requirement, the use of the chamber reduces the sources of external noise that may otherwise influence the hot-wire measurements. The compressor feeds a large reservoir tank of volume 5.3 m^3 and an operational pressure range of approximately 6 through 26 bar. For the smallest throttle angle being considered, the mass-flow rate is approximately 0.008 kg s^{-1}, with the maximum flow rate reaching 0.27 kg s^{-1} for the largest of the valve openings (see Table 3.2 on page 67). Using simple analysis, an estimate of the time available for an individual experimental run can be calculated using the mass-flow requirements and the known operational reservoir pressure. Using the equation of state for a perfect gas (3.2) the approximate density of the compressed gas within the reservoir can be calculated at the two pressure extremes. Taking a value of $R = 287$ J kg^{-1} K^{-1}, and an average temperature of 293 K,

the following values for density are obtained,

$$\text{Low pressure (6 bar):} \quad \rho_6 = 7.14 \text{ kg m}^{-3},$$

$$\text{High pressure (26 bar):} \quad \rho_{26} = 30.92 \text{ kg m}^{-3}.$$

Note, that the assumption of constant temperature is not strictly valid but suffices for this simple calculation. Simple averaging of the density gives a mass of air of 126 kg available that, given the range of mass flow rates under investigation, yields a minimum run time of approximately 8 minutes, and a maximum run time of 4 hours, 22 minutes, respectively, for the largest and smallest throttle openings. These estimates indicate that the reservoir can provide sufficient flow over time in order for the experiments to be completed before needing to be recharged by the compressor.

Control of the flow rate is automated by a pressure regulator situated on the outlet of the reservoir that provides a constant pressure at the outlet; this would be very difficult to achieve manually. However, obtaining accurate and repeatable flow rates for the individual experiments proved difficult owing to the poor control of the valve. From the valve the flow is fed either directly through the flow rig, or via an optional air-dryer system that reduces the moisture content of the air. This has been used here owing to the initial compression of the gas raising its temperature such that this hot gas condensates within the cooler reservoir.

4.3.2 Experimental Layout

Figure 4.1 shows a basic schematic of the flow-facility components used for the investigation. A plenum chamber has been used that is fitted with internal screens and honeycomb in order to settle the flow and provide smooth flow within the chamber and particularly at its outlet that itself incorporates a convergent duct. The remainder of the rig consists of the throttle body positioned between straight-walled tubes all of which are connected via specially manufactured coupling flanges. In addition a series of stands have been used to support the unit and on which are mounted the traverse system for the hot-wire probe. The plenum chamber is fed from the reservoir air supply

and outlet of the flow rig vents directly to atmosphere far downstream of the throttle valve mimicking the computational layout.

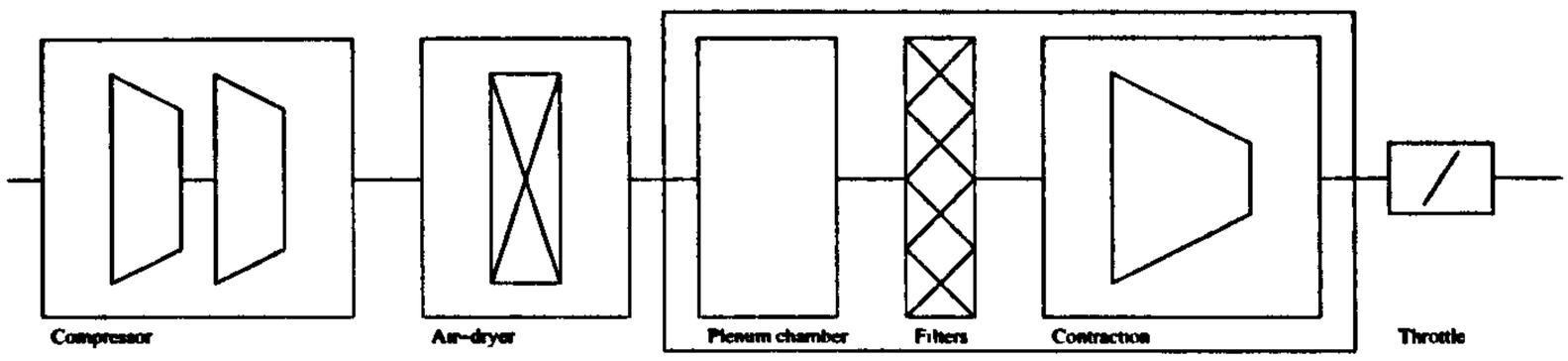

Figure 4.1: Schematic showing the basic layout of the experimental test components.

The nature of the experimental set-up is such that the flow is driven in a different way to that of the normal throttle operating conditions, i.e. a high inlet pressure is generated by the upstream air supply that drives the flow through the throttle, whereas normally the engine generates a low-pressure region downstream of the throttle that effectively sucks the air through the throttle. The two methods, however, generate the same overall pressure drop across the valve, and this is the governing condition for the flow. Measurements have been made of the upstream and downstream pressure in order to verify that the correct pressure differential exists, alongside mean flow measurements, and together these should ensure that the correct operating conditions exist. When the throttle body is in its native environment, the engine generates an unsteady suction brought about by the reciprocating nature of the engine. The level of variation in the flow is determined predominantly by the size and shape of both the engine inlet plenum and inlet runners, that are known to have a significant effect on the pressure waves propagating through the inlet system (Heywood, 1988; Heisler, 1995). Here, the inlet is assumed to be a uniform constant flow that remains consistent with the CFD model.

It is essential that the flow rig has as smooth a wetted surface as possible to ensure minimal flow disturbance, especially upstream of the throttle body. Although in the real operating environment the connections to the throttle body are somewhat crude, the CFD model has assumed smooth undisturbed flow at the inlet to the throttle and thus this must be ensured here to maintain consistency. This has proved a little difficult

to achieve owing to several manufacturing problems that will be subsequently discussed.

Ideally the flowrig would be orientated horizontally to mimic the native environment of the throttle; however, space restrictions required that the unit be mounted vertically (the final unit being over 2 m in length). This change in orientation can be modelled in the CFD; however, the orientation change has negligible effect on the flow through the throttle.

Although this further deviates from the ideal conditions, the effect on the resulting flow is negligible and any effects could be incorporated into the CFD models, and hence the change only brings additional complexity to the design of the rig.

4.3.3 Initial Contraction Designs

A contraction has been used to smoothly accelerate the flow from the plenum chamber to the smaller-diameter throttle body and outlet tubes. As this forms a crucial part of the experimental flow rig, the profile of the contraction needed careful consideration and several designs were investigated before a final design was chosen and manufactured. Initial designs were very simple with a separate circular plenum chamber and convergent section, with a radiused exit to the plenum and external flow-conditioning devices proposed downstream. This simple approach is based on the design principles for venturi meters (ISO, 1991; Linford, 1961), thus the contraction would consist of a straight-walled conical section with an included angle of 21°, as recommended by the ISO. Another vital consideration is the ratio of the upstream and downstream diameters of the convergent section, which given the included angle, also stipulates the length of the contraction. Again using information taken from the ISO, the ratio of upstream to downstream diameter should be in the range $0.4 \leq D_1/D_2 \leq 0.75$, with no radiusing between the interface of the straight pipes and the convergent section.

This preliminary design was not used for several reasons. Firstly, due to the low flow rates that are required at small throttle opening angles, there is a severe risk of separation occurring at the interface between the conical wall and the downstream straight pipe of the contraction. This is observed in venturi meters when the Reynolds

number (based on throat diameter) falls below approximately 1×10^4. A separation bubble occurs at the interface, the presence of which severely affects the operation of the venturi (Linford, 1961; ISO, 1991; Ward-Smith, 1980). Although the Reynolds number (based on outlet diameter) is higher than this value for the most part, the low flow rates generated at small throttle openings give a Reynolds number below this value. Secondly, the design of the contraction is such that the flow-conditioning device is placed at an inappropriate position owing to the lack of sufficient upstream and downstream pipe length. By placing any flow conditioners within the plenum chamber a much smoother flow can be achieved. Finally, the design itself was fairly crude and basic, and with some effort a much more appropriate design has been achieved.

Further design iterations combined the contraction and plenum chamber in a similar manner to the contraction of a wind-tunnel. Such designs provide a much smoother flow path and are more commonly used in these situations. The plenum chamber again consisted of a large circular chamber, although the flow-conditioning device (such as honeycomb, or gauze) was incorporated within the chamber. The contraction thus had an inlet diameter equal to the plenum-chamber diameter and an exit diameter equal to the diameter of the throttle-body inlet. Flow passes through the flow conditioner, before passing directly into the contraction where it accelerates to the required downstream velocity. The previous schematic of Figure 4.1 reflects such a design.

The contraction was designed by the traditional 'what looks good' approach, which is a common method of designing contractions (Morel, 1975; Pope & Goin, 1965). The contraction is created by two arcs of equal arbitrary radius joined to produce an S-shaped curve with an arbitrary choice of curve positioning, and cone length made in the design. This design lead to further research into the design of contractions to ensure that the curvature of the contraction is adequately defined in order to maintain a high flow quality through the section.

There have been numerous previous studies into the analysis and design of contractions, the majority of the literature concentrating on the analysis of the flow through a contraction, and a smaller number of sources dealing with practical design issues.

In addition, much of the literature are concerned with two-dimensional contractions or contractions with a non-circular cross-section and these topics, although not directly applicable to the problem at hand, are of value for determining of a suitable contraction and evaluating methods of design and analysis.

Previous Analysis and Design of Contractions

Research into the design and analysis of contractions was popular in the 1940s and 1950s with several authors presenting work on the subject. Later, with the advent of widespread digital computing, a greater range of analysis was possible, and in the present day the use of CFD also plays a role in the design of contractions. Previous studies have looked at several different types of contraction, including square cross-sections, octagonal cross-sections, axi-symmetric and two-dimensional contractions. Although an axi-symmetric contraction is required here, the previous work on other types of contraction still provides useful information.

For a contraction of infinite length, the velocity is able to increase monotonically throughout the entire contraction owing to the lack of adverse pressure gradients in the system. By truncating the contraction and adding straight sections upstream and downstream of the contraction, adverse pressure gradients are introduced which leads to growth of the boundary layer, a change in the velocity distribution, and risk of separation. In addition, the local velocity at the walls of the contraction experiences 'undershoot' and 'overshoot' at the inlet and exit respectively. These terms refer to the velocity at the wall being below or above the centre-line velocity. Figure 4.2 shows how the velocity and pressure distributions change as flow passes through a contraction of straight sides. The figure is reproduced from Ward-Smith (1980) and is also applicable to contractions with curved walls (Morel, 1975; Downie, Jordinson & Barnes, 1984). Infinite-length contractions obviously do not exist and in designing a contraction certain allowances have to be made to take into account the truncation of the ideal contraction. The effects of truncating the contraction to a finite length are well-documented and commented on by many authors (Cohen & Ritchie, 1962; Downie et al., 1984; Jordinson

& Rodger, 1981; Morel, 1975; Su, 1991; Whitehead, Wu & Waters, 1951).

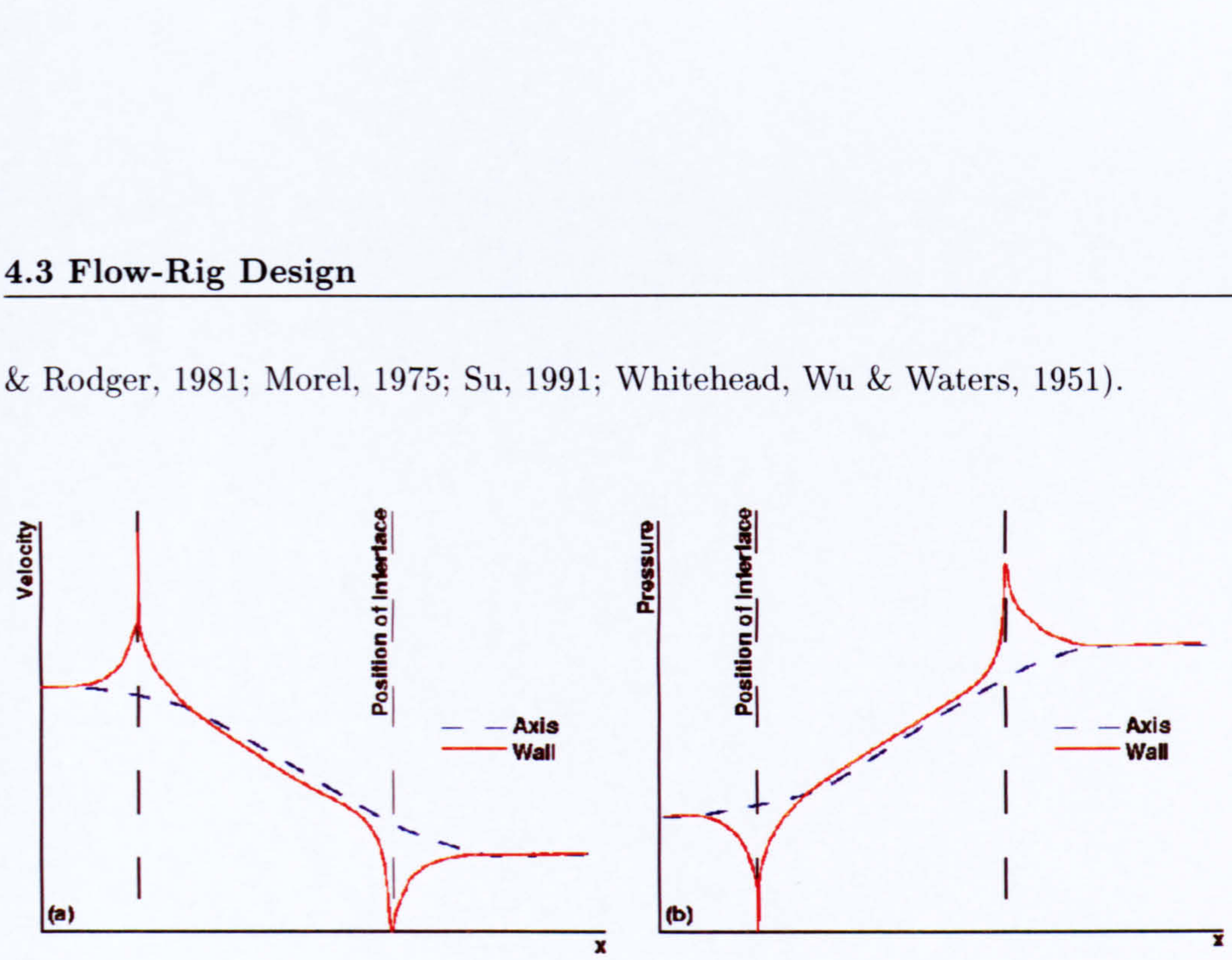

Figure 4.2: Velocity and pressure distributions of a flow passing through a contraction with straight walls. Flow is from left to right, with the dashed vertical lines representing the interface between the straight and conical sections. Reproduced from Ward-Smith (1980).

Many authors have made use of conformal transformations and the hodograph method in their analysis of contractions owing to the suitability of the geometry and the technique. Both methods are similar, and enable the flow around, or through, bodies to be analysed by a transformation of the real plane into a complex plane. Once in the complex plane the flow can be represented by simple flows using solutions to Laplace's equation that simplifies the analysis. This is made possible through the use of stream-functions and velocity potentials, and the fact that the Cauchy-Riemann relations ensure that all analytic functions form a solution to the two-dimensional Laplace equation (Prandtl & Tietjens, 1934).

The methods rely on the fact that an analytic function $F(z) = F(x + iy)$ can be split into its real and imaginary components, which is written in terms of the (real) velocity potential and (real) stream function, as shown below,

$$F(z) = F(x + iy) = \phi(x, y) + i\psi(x, y), \tag{4.1}$$

where ϕ is therefore the velocity potential, and ψ is the stream function. Taking second

derivatives of equation (4.1) and equating the real and imaginary parts leads to solutions of the Laplace equation (the working is not shown here),

$$\frac{\partial \phi}{\partial x} + \frac{\partial \phi}{\partial y} = 0, \qquad \frac{\partial \psi}{\partial x} + \frac{\partial \psi}{\partial y} = 0. \tag{4.2}$$

Thus, when an appropriate function describes a flow, it can be transformed into its complex equivalent and solved for. The advantage of these methods is that complex flows can be easily be represented within the complex plane by variation of certain terms. For example, a function $F(z) = az^n/n$ can be used to describe the flow in a corner, over a wedge, over a step and the flow round the edge of a flat plate simply by changing the the value of n (Prandtl & Tietjens, 1934). In the real plane, the stream functions show the stream lines of the flow, and lines of velocity potential are perpendicular to these lines. When transformed conformally into the complex plane, the flow is plotted on axes of ϕ and ψ, so a Cartesian grid with lines of constant ϕ and ψ is formed. On this grid the points of equal x and y coordinate are plotted as a series of curves and hence for a real flow, e.g. flow over a cylinder, the conformally transformed equivalent flow is a flow parallel to the axis which is far easier to analyse.

The hodograph method has been used by a number of authors to analyse the flow through various types of contraction (Cohen & Ritchie, 1962; Downie et al., 1984; Gay, Spettel, Jeandel & Mathieu, 1973; Gibbings, 1964; Jordinson & Rodger, 1981; Libby & Reiss, 1951; Su, 1991; Whitehead et al., 1951). Many of these authors have used the method to aid in the design of a particular contraction, rather than producing a general design methodology. Whitehead et al. (1951) have used the method to design a two-dimensional contraction and then used the stream function and velocity potential of the model to initiate modelling of a three-dimensional contraction. The shape of the contraction was designed to minimise the adverse pressure gradients at the entrance and exit of the contraction whilst maintaining a rapid change of cross-section. This was achieved by considering the upstream and downstream portions of the contraction separately.

Jordinson & Rodger (1981) have also used this method of splitting the contraction

where each half is solved for in the hodograph plane to provide a constant velocity in the curved parts. The results predict undershoot and overshoot of the local wall velocities as found by other authors (Downie et al., 1984; Gay et al., 1973; Jordinson & Rodger, 1981; Morel, 1975; Su, 1991; Ward-Smith, 1980). However, comparison with experimental work showed that the overshoot seen near the exit did not exist; this is explained by the lack of viscous effects in the numerical calculation. Viscous effects in the real flow lead to growth of the boundary layer throughout the contraction thereby reducing the effective outlet diameter seen by the flow. This reduction in diameter leads to the overshoot being displaced downstream of the theoretical point forming a vena contracta (Jordinson & Rodger, 1981).

In a study of flow through S-shaped ducts, Bansod & Bradshaw (1972) have made analogies to the flow through two-dimensional contractions, in particular to the thickening of the boundary layer through the contraction. As the flow passes through the contraction so the boundary layer grows owing to pressure gradients causing the flow to converge. However, counteracting this, the acceleration of the flow through the contraction reduces the boundary layer thickness. For two-dimensional contractions the rate of growth owing to convergence is balanced by the rate of thinning owing to acceleration, whilst for three-dimensional contractions, the acceleration has a dominant effect and so the growth of the boundary layer is reduced.

By designing contractions as two separate upstream and downstream sections, the designer is able to have far more control over the flow within the contraction. The curves defining the upstream and downstream sections can be modified to give the smallest adverse pressure gradient, and the curve-matching position can also be moved to aid in the design. Morel has used a method of matching cubic curves for the design of axi-symmetric contractions (Morel, 1975), and also for the design of two-dimensional contractions (Morel, 1977). Both of these papers give a substantial account of the design of contractions for wind-tunnels, based on the need for a non-separated flow through the contraction and a uniform exit flow. Thus, the papers can be used to determine the shape of a contraction knowing the required contraction ratio (CR, the ratio of inlet

to outlet area), and the coefficients of pressure at the inlet and exit. These coefficients are closely related to the pressure gradients in the contraction and give an indication of the risk of separation occurring at the inlet and exit. The choice of cubic curves was justified by an analysis of a family of curves of the form x^n which showed that $n = 3$ gave the smallest pressure gradients in the system and smooth exit flow. Using a finite-difference scheme to solve the Euler equations, Morel carried out a thorough numerical investigation of contraction shapes with a total of 124 combinations being analysed. Variations were made on the contraction ratio, the curve-matching location and the ratio of length to inlet diameter.

In a similar manner to Morel, Downie et al. (1984) have used a pair of matched elliptic arcs to form the profile of their contraction. The hodograph method has again been used to analyse the flow in the contraction, which is of rectangular cross-section. Both Morel (1975, 1977) and Downie et al. (1984) note that the length of the contraction is also of importance. By increasing the length of a contraction the boundary-layer growth becomes more apparent and this needs to be kept to a minimum to avoid separation and unsteady exit flow. Keeping the length of the contraction short requires a steep maximum slope within the contraction to reduce the effects of undershoot and overshoot which are amplified with a shortened length (Downie et al., 1984). Morel (1975) notes that an increase of contraction ratio allows for a reduction in length of the contraction (when non-dimensionalised with the inlet diameter). This is advantageous here owing to the limited amount of available space for the experimental rig. Morel also notes that the total length of the contraction should include the addition of straight sections upstream and downstream of the contraction to ensure smooth flow (Morel, 1975; Morel, 1976). Both Downie and Morel make use of Stratford's separation criterion (Stratford, 1959) in determination of pressure coefficients, and hence the pressure gradients within and exit uniformity of the contraction.

Su (1991) has adopted the methods of Morel for the design of three-dimensional rectangular contractions. He uses similar coefficients of pressure but applies them to the walls and to the roof of the contraction to allow for more accurate modelling.

He notes that there are considerable cross-flow effects that are not observed in axi-symmetric contractions. His numerical investigation also revealed areas of undershoot and overshoot, both at the side walls, and the floor and roof. The most noticeable regions of undershoot and overshoot were found in the corner regions and it is these that are likely to lead to flow separation and unsteadiness. Su (1991) also notes that the use of curves of a higher order than cubic are beneficial in providing a uniform exit flow despite causing larger pressure gradients. The same is not true for the inlet where a cubic curve was found to give the best flow. Thus, Su suggests matching a cubic curve to a higher power curve for the profile of a contraction.

Cohen & Ritchie (1962) have used the hodograph method to solve Laplace's equation for the flow through a three-dimensional octagonal contraction forming part of a closed-return wind-tunnel. This has been achieved by approximating the contraction to the equivalent axi-symmetric contraction based on cross-sectional area. One of the design criteria being a total axial length of no more than 126 inches whilst maintaining low turbulence in the working section. In their analysis, the authors have truncated an infinite contraction at appropriate positions so as to maintain the desired contraction ratio and velocity ratio.

More recent studies on the flow through contractions have made use of CFD thus allowing for easier design optimization to be performed, and to allow more complex flows to be analysed, for example, through the inclusion of turbulence models (Gordon & Imbabi, 1998; Wang, Tortorelli & Dantzig, 1996). Wang et al. (1996) have used a Newton-Raphson algorithm with finite elements to solve for a coupled thermal and flow problem within a contraction. The contraction has been analysed for both laminar and turbulent flows (using the k-ε model) and an optimized shape found. In both cases, considerable changes occur to the original straight-walled conical contraction. For laminar flows, a short contraction is suggested with large maximum slope. For the turbulent flow, the contraction has a gradual change in diameter from inlet to exit with a reduced maximum slope. The authors performed numerous analyses allowing them to create an optimized contraction shape for flows at specific Reynolds numbers.

Gordon & Imbabi (1998) have used a commercial CFD code to analyse and design a closed-circuit wind/water tunnel. The contraction of the tunnel was based on the work of Downie et al. (1984); hence it had two matched elliptic curves. The authors note the good performance of a contraction designed by such methods.

4.3.4 Final Contraction Design

There are generally three ways to design a contraction, firstly is to use an existing design, secondly is to design a contraction that looks correct, and finally a design based on extensive analysis. For the contraction used here, a combination of the latter two methods has been utilized based the work by Morel.

Morel (1975) used two matched cubic curves to define the wall shape of an axi-symmetric contraction and carried out an extensive design study based upon this. The methods outlined in the paper are based on wind-tunnel contraction design and he highlights that the most important factors in the design criteria are a lack of separation at the inlet, and a uniform exit flow. Design parameters are thus narrowed down to the maximum wall-pressure coefficients at the inlet and exit to the contraction that prove to be the dominant influence in the design. The methods described thus assumes suitable values for the wall-pressure coefficients have been chosen and using design charts, suitable contraction shape and length can be determined. The wall-pressure coefficients defined by Morel in his two papers are based on the non-dimensionalised (with respect to velocity far upstream and far downstream) wall-velocity minima and maxima that occur at the inlet and exit to the contraction respectively. Their definition is given as,

$$C_{pe} = 1 - \left(\frac{U_{c2,\infty}}{U_{we}}\right)^2, \tag{4.3}$$

$$C_{pi} = 1 - \left(\frac{U_{wi}}{U_{c1,\infty}}\right)^2, \tag{4.4}$$

where U_c is the centre-line velocity, U_w is the wall velocity; subscripts 1 and 2 refer to the inlet and exit plane of the contraction, and e and i to the points of wall-velocity

maximum and minimum respectively, and ∞ represents a measurement far upstream or downstream. Morel's investigation revealed that for designs based on matched cubic curves the wall-pressure gradients were predominantly a function of the wall-pressure coefficients and that exit-flow uniformity was largely independent of geometry, and also proportional to C_{pe}. Thus with suitable values of the coefficients chosen the next stage of the design process is to determine the matching point of the two cubic curves, i.e. the intersection point of the curves. This is found in non-dimensional form from the implicit equation given in (4.5) below,

$$X^{1/2}(1-X)^{-2/3} = F_e^{1/3} G_i^{-1/2} m^{1/2}(m-1)^{1/6} = \xi m^{1/2}(m-1)^{1/6}, \qquad (4.5)$$

where, X is the non-dimensional match point (with respect to nozzle length), m is the ratio of upstream to downstream diameters (D_1/D_2), F_e & G_i are functions of the wall curvature that are found by graphical interpretation (Morel, 1975). Thus, the left hand side of (4.5) is found by using a heuristic (or graphical) approach and the curve match point determined. With the value of X known, the length of the contraction can be found from equations (4.6) and (4.7) below.

$$L = \left\{ \frac{D_1^3(m-1)}{m(1-X)^2 F_e} \right\}^{1/3}, \qquad (4.6)$$

$$L = \left\{ \frac{D_1^2(m-1)}{mXG_i} \right\}^{1/2}. \qquad (4.7)$$

Finally, the shape of the contraction is determined using the length, match point, and the functions of pressure; each as a function of x/L, the non-dimensional distance along the contraction. Equation (4.8) below describes the two sections of the contraction as a function of (x/L).

$$f(x/L) = \begin{cases} 1 - \dfrac{1}{X^2}\left(\dfrac{x}{L}\right)^3 & x/L \le X, \\ \dfrac{1}{(1-X)^2}\left(1 - \dfrac{x}{L}\right)^3 & x/L > X. \end{cases} \qquad (4.8)$$

And therefore, the diameter at any point of the contraction can be found from,

$$D(x/L) = f(D_1 - D_2) + D_2, \tag{4.9}$$

with the inlet and outlet diameters, D_1 and D_2, being predetermined by the contraction ratio and outlet requirements. These simplified equations apply to the design of cubic-matched curves alone and are not applicable to other design methods.

In order to evaluate possible contraction designs and evaluate the work of Morel, equations (4.5) through (4.9) have been parametrically evaluated to find a suitable design solution for the flow requirements here. This approach enabled the effects of changing parameters to be seen on the shape of the contraction, and allow for a suitable shape to be selected. This method confirmed the results of Morel (1975) indicating an increase in the exit wall-pressure coefficient (Cp_e) causes the wall shape to become steeper and more abrupt by reducing the curvature at the exit. Also, an increase in the inlet wall-pressure coefficient (Cp_i) reduces the length of the contraction, and moves the curve-matching point further downstream. An example of a family of curves is shown in Figure 4.3 where variations in both Cp_i and Cp_e are plotted.

Selection of an appropriate curve shape was achieved by evaluation of the flow rates expected through the plenum system, and hence, the risk of flow separation within the contraction. Stratford's separation criterion assumes knowledge of boundary-layer growth, and the location of separation. As these quantities are not known, the suggested values based on the Re of the flow have been used. The design methodology of Morel (1975) is based on wind-tunnel contraction design and assumes that the majority of flows will have a turbulent boundary layer present. However, there is a chance that a laminar boundary layer will exist in the experiments here, especially at the low flow rates. A subsequent discussion (Morel, 1976) of Morel's original paper (Morel, 1975) highlights that there may be laminar boundary layers present and suggests reducing the pressure coefficients to account for this. Suitable values for contractions with laminar boundary layers were given.

For a range of contraction ratios, $1.7 \leq \mathrm{CR} \leq 27$, and throttle angles, $3.5^{\circ} \leq \alpha \leq 60^{\circ}$,

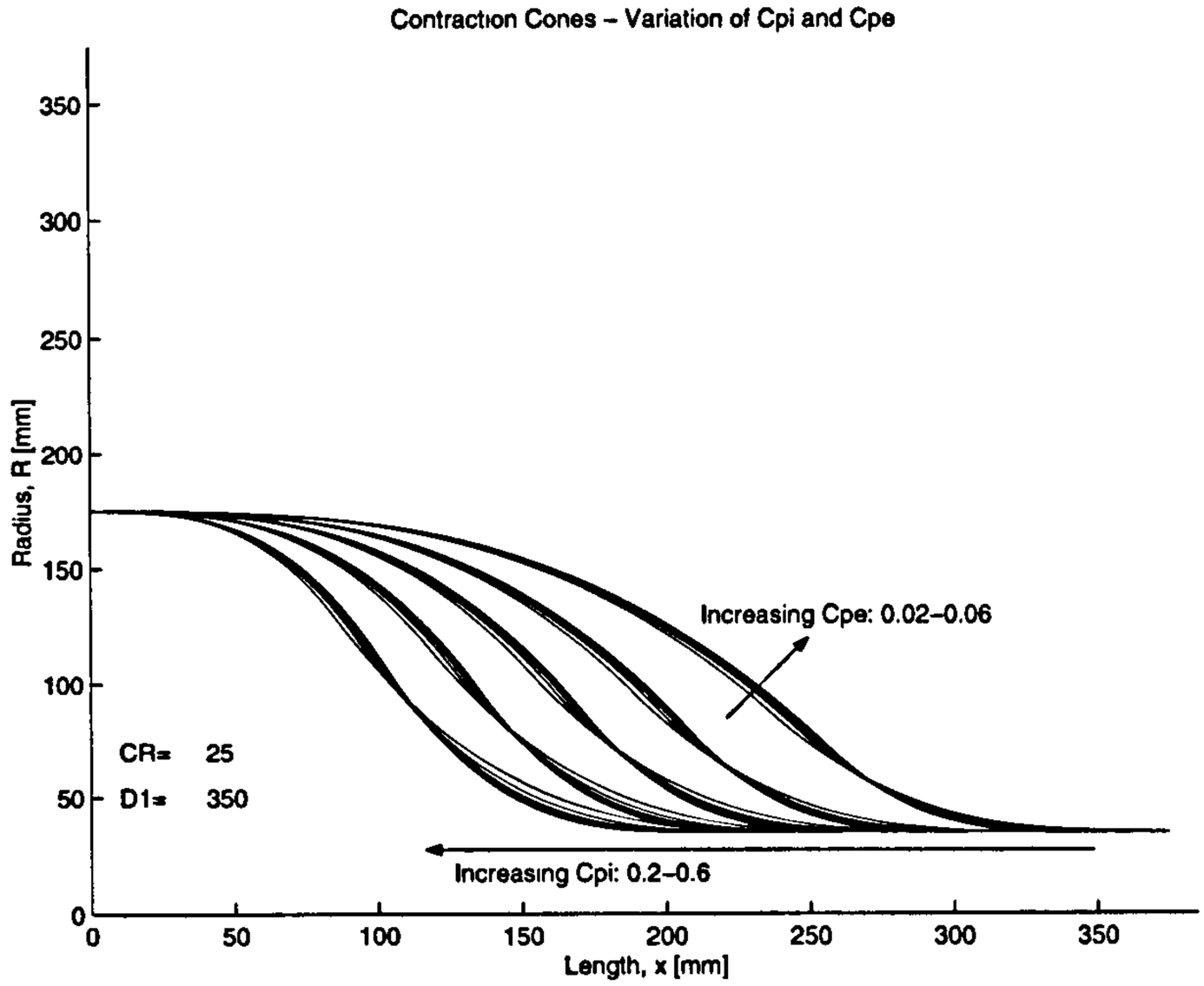

Figure 4.3: Variation of Cp_i and Cp_e on the shape of an axi-symmetric contraction. Each group of curves represents a fixed Cp_i with varying Cp_e, hence, moving to the left shows an increase in Cp_i. An increase in Cp_e causes the curve to become steeper. Plots are for a CR of approximately 20, with an outlet diameter of 70 mm, with axis centre line on the absissca.

the Reynolds number was calculated and suitable values of Cp_i found. An exit pressure coefficient range of $0.04 \leq Cp_e \leq 0.06$ is suggested where the presence of a laminar boundary layer is probable.

The final design parameters for the contraction are now presented. Inlet and outlet diameters of $D_1 = 350$ mm and $D_2 = 70$ mm respectively have been used giving a contraction ratio of CR = 25 and a contraction length of $L = 332$ mm. Wall-pressure coefficients calculated at inlet and exit are $Cp_i = 0.25$, and $Cp_e = 0.04$ respectively. This combination of coefficients leads to a contraction shape that is suitable for both the lower and higher flow rates. Using equations (4.5) to (4.9) the information given in Table 4.1 has been obtained and is the final specification of the contraction cone with the final contraction profile is shown in Figure 4.4.

The final stage of the contraction design involved the physical representation of the mathematical curve of the contraction profile and incorporating the contraction into

Property	Value
Inlet diameter, D_1	350 mm
Outlet diameter, D_2	70 mm
Contraction ratio, CR	25
Match point, X	0.68
Length of contraction, L	332 mm
Min Reynolds number, Re_{min}	2000
Max Reynolds number, Re_{max}	70700
Inlet wall-pressure coefficient, C_{pi}	0.25
Exit wall-pressure coefficient, C_{pe}	0.04

Table 4.1: Contraction design properties, based on design methodology given in Morel (1975).

the remaining flow rig. In this case the physical design of the contraction is governed by the manufacturing techniques and materials used in its construction, given the size and shape of the contraction. A wide range of materials and manufacturing techniques were considered before the final manufacturing method and material choice were decided upon. For the most part these methods were discounted owing to excess cost, impractical manufacture, poor internal surface quality, or excess waste in manufacture. Through collaboration with Jaguar Cars Ltd, the contraction was manufactured using a rapid-prototyping technique at their engineering centre. Although not initially considered, the method offers a fast and effective turnaround with the additional benefit of no external manufacturing costs.

Thus the basic requirements of the final design were to ensure sufficient wall thickness, and a suitable method of attachment to the remaining flow rig. A wall thickness of 5 mm has been used and to ensure strength in the design, additional strengthening vanes have been incorporated into the tube walls to prevent axial and radial distortion of the contraction. Owing to the size of the contraction, and the limited capacity of the rapid-prototyping equipment, the unit had to be designed in two halves with a split

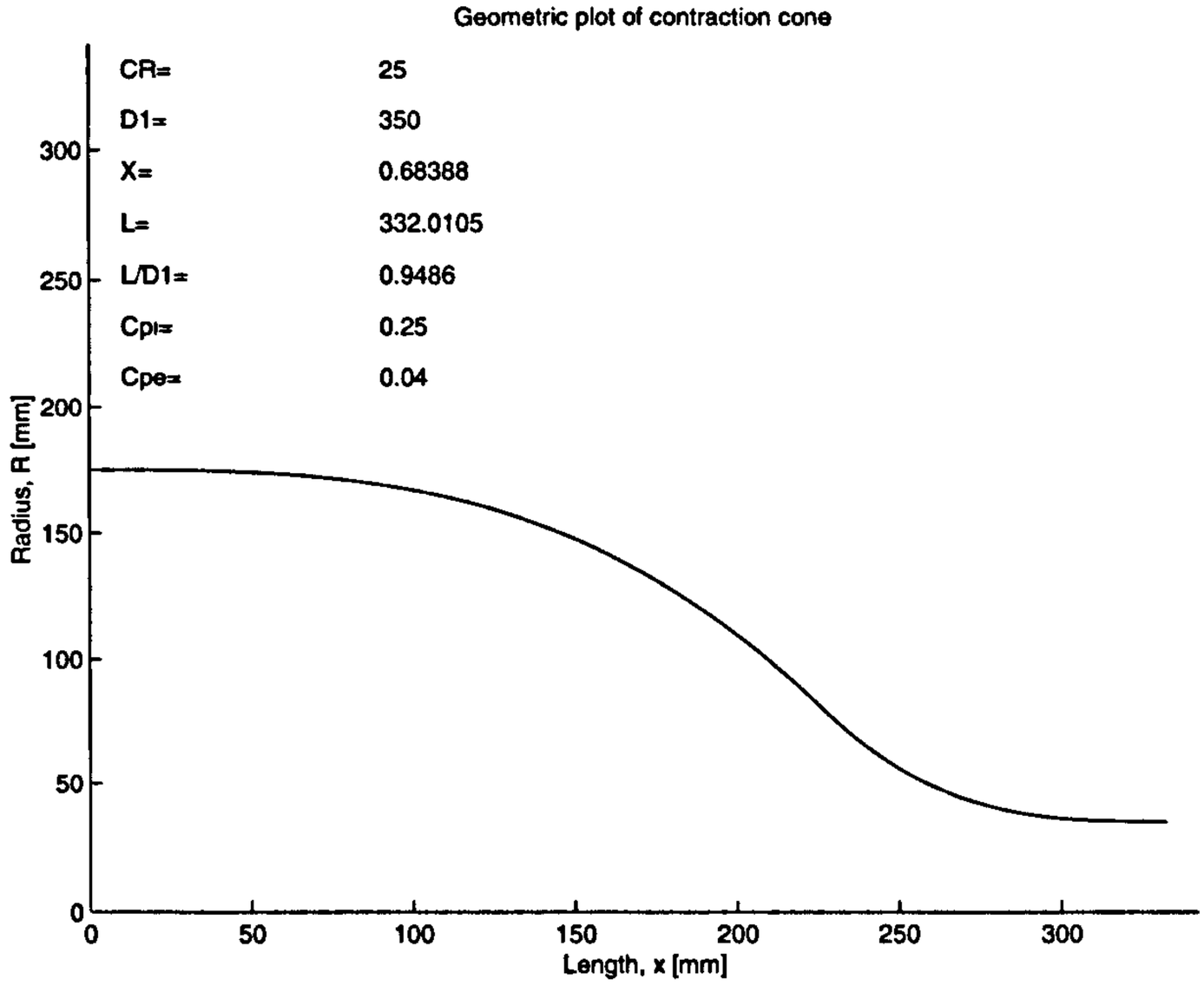

Figure 4.4: Final axi-symmetric contraction profile used in the investigation. Inlet diameter 350 mm, outlet diameter 70 mm, and a length of 332 mm.

running along its length. As the two halves could be made identical this was deemed an acceptable solution as adequate sealing and surface preparation could be performed. Unfortunately, the contraction was finally manufactured in four quarter sections, which should not have presented a problem; however, the variation of the sections meant that severe problems were encountered in sealing the contraction and attempting to achieve the original shape.

Attachment of the contraction to the plenum chamber and inlet runners has been achieved through use of flanges incorporated into the inlet and outlet of the contraction. Each has a 5 mm thickness and forms part of the main structure as opposed to being attached as separate items. At the inlet a 450 mm flange has been used with 12 $\times$ 8 mm holes spaced equi-distantly on a 420 mm PCD (pitch circle diameter), whilst the outlet flange is of 126 mm diameter with 8$\times$6 mm holes on a 110 mm diameter spaced 15° from the joints of the cone. Flanges have also been used on the cone sections in order to allow the unit to be bolted together using 5 $\times$ 6 mm holes positioned between each of

the vanes. Figure 4.5 shows the design concept for the contraction.

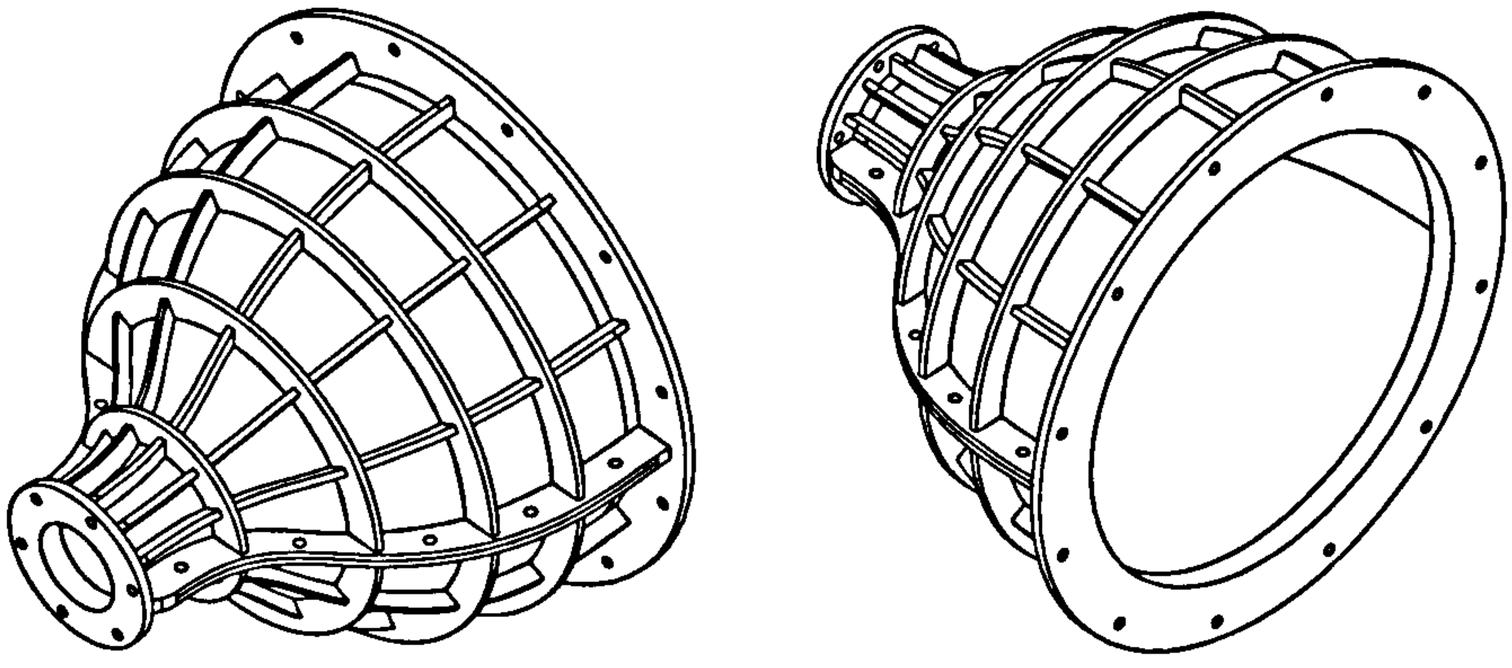

Figure 4.5: CAD model of the contraction design incorporating axial and radial strengthening vanes and inlet and outlet flanges.

4.3.5 Plenum Chamber Design

In order for the contraction to operate efficiently the flow entering it must be steady and smooth and this is the job of the plenum chamber, which effectively acts as a flow-settling chamber for the downstream flow-rig. A series of flow-conditioning screens have been incorporated into the the plenum chamber in order to provide a low turbulence intensity and smooth flow though the contraction. The plenum chamber consists of a cylindrical volume with an inlet at one end and the contraction at the other, i.e. a sudden expansion exists at the inlet to the unit. The inlet is fed by the compressor via a standard 1.5 inch pipe, which equates to an inlet diameter of 38 mm, and the plenum internal diameter matches that of the contraction at 350 mm, thus giving an expansion ratio of approximately 9 at the inlet. Flows through sudden expansions has been the topic of previous studies (Plint & Böswirth, 1978; Ward-Smith, 1980), including some used to predict the flow through throttle valves (Addy et al., 1985); however, full evaluation of such flows is not undertaken here. In addition the expansion ratio here is typically larger than those found in such studies.

Pressure losses occur as the flow passes through the sudden expansion and hence some preliminary investigations looked into smoothing the inlet junction to reduce the

loss. However, Benedict (1980) suggests that the non-dimensionalised pressure loss coefficient remains unchanged regardless of the topology of the inlet interface and hence the sharp interface has been retained in the design.

With such a design the flow entering the plenum chamber is essentially a jet structure and hence at the higher flow-rates the flow has sufficient momentum to allow it to pass directly through the chamber with minimal diffusion or settling. As such, a deflector assembly has been incorporated into the inlet to suppress the jet formation and encourage mixing of the flow. The deflector consisted of a flat plate orientated normal to the flow direction a little way into the plenum, thus the flow is forced through a rapid direction change from an axial to radial direction upon entering the plenum. This modification provides a suitable level of mixing despite the crude nature of the design, and the additional blockage offered by the deflector further enforces the lack of smoothing at the inlet junction.

Between the inlet and contraction lie the flow-conditioning devices that consist of a honeycomb section positioned between two gauze screens. These are necessary to generate a smooth steady uni-directional flow with low turbulence intensity that is fed via the contraction to the test section, i.e. to the downstream throttle body. The honeycomb structure produces smooth flow via local small-scale accelerations that have a tendency to absorb energy and swamp any larger accelerations in the flow (Batchelor, 1970; Tritton, 1988). On exiting the honeycomb, small-scale eddies are formed that rapidly decay providing a uniform flow field. The ISO recommends fitment of a flow-conditioning device between two long straight pipes to ensure correct and efficient operation of the device (ISO, 1991). Using a long pipe length upstream of the flow conditioner allows the flow to fully develop and minimizes other effects such as swirl that may be detrimental to the flow. Plint & Böswirth (1978) suggest that a pipe entry length between $10D$ and $40D$ for turbulent pipe flow is required before the flow reaches a fully developed state, a distance that far exceeds the proposed distance from the plenum inlet to the flow conditioner. Ward-Smith (1980) also notes that a fully turbulent wall boundary layer at a pipe inlet allows the flow to reach a fully developed

state far sooner than for an initially laminar flow that undergoes transition. Studies by Barbin & Jones (1963) have shown that pressure gradient and wall shear stress reached fully developed states after approximately 10 to 15 pipe diameters for a smooth pipe, whilst the velocity distribution only reached its fully developed state after 60 to 70 pipe diameters. Wang & Tullis (1974) carried out a similar investigation for rough pipes and found that the pressure gradient and wall shear-stress reached their fully developed state in the same distance as for smooth pipes; however, the velocity distribution reached a fully developed state in a shorter length of 50 pipe diameters. Their studies used a relative roughness, h/D, of 0.00038 and 0.0002 (where h is the pipe roughness) and they note that an associated increase in wall friction exists that assumes normal conditions after approximately 15 pipe diameters. Thus, under ideal conditions, it may be necessary to have the additional length to ensure perfect flow conditions; however, this is impossible here owing to space restrictions, and the lengths mentioned are impractical for many applications. Shaw et al. (2000) have made use of a straw bundle to reduce turbulence levels in a similar scenario and found that a 50% reduction could be achieved even though a short upstream pipe length had been used. Further, the flow rates through the plenum are reasonably low and hence the conditioning device should work more effectively at reducing energy levels in the flow.

In order to fit the screens, the plenum chamber has been designed with a removable section of larger diameter that contains the honeycomb. Thus three sections make up the plenum with the inlet portion being approximately 150 mm in length, the honeycomb section 50 mm, and the outlet a further 50 mm before the contraction is attached at the end. The plenum chamber incorporates a flange at its outlet to the same specification as that of the contraction inlet to allow the two to be bolted together, and a slightly narrower flange is used to bolt the individual sections of the plenum chamber together. The plenum inlet is attached via a standard pipe connector and hence no specific design is required. Stainless steel is used for the manufacture of the chamber sections and thus the flanges have been designed as separate components that are welded onto the chamber sections and then machined down to provide a smooth and flat mating surface. Figure

4.6 shows the detail of the design.

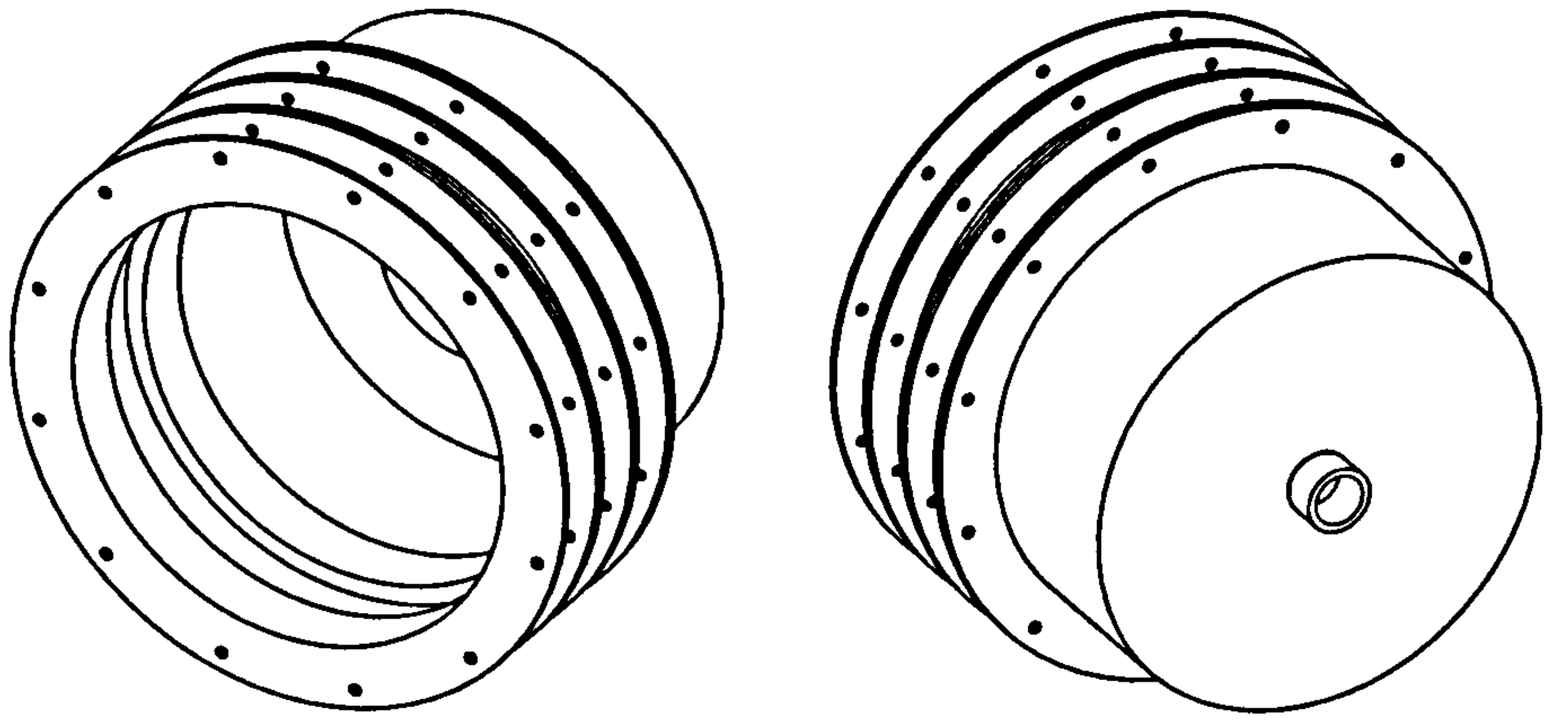

Figure 4.6: CAD model of the plenum chamber and deflector used in the investigation.

4.3.6 Main Flow Domain

The remaining part of the flow rig is the main flow domain that encompasses the throttle body and any measuring equipment used. Here, owing to the cylindrical throttle body, the main domain consists of inlet and outlet runners positioned upstream and downstream of the throttle body. The lengths of the inlet and outlet runners have partly been based on information found in the literature, although normal design rules have had to be modified in this case owing to space restrictions. As velocity measurements are to be made by Pitot tube, a shorter upstream pipe length is possible than required for other measurement techniques. For example, venturi meters require approximately a 20-pipe-diameters length of pipe upstream of the meter for successful measurement (ISO, 1991). No specific values of suitable upstream pipe length have been found for using a Pitot tube, hence an upstream length of 4 pipe diameters has been used with measurements being made approximately 3/4 of the way along the runner tube, so an overall pipe length of 5 diameters has been used (approximately 350 mm). This length should be adequate for successful measurements, considering that Pitot tubes produce negligible head loss in a system (Ward-Smith, 1980). Again to ensure a fully developed profile a longer pipe length should be used as discussed previously.

As with the inlet runner, the outlet to the domain has been designed in accordance with the CFD modelling; the tube allows the flow to return to a fully developed state before exiting to atmosphere. To allow for this given the space restrictions imposed on the rig, the length of the outlet runner used is 8 pipe diameters based on CFD modelling and previous studies (Huang & Kim, 1996). Both runners have been made from standard lengths of clear acrylic tubing to provide optical access, and hence also to allow for basic flow visualization to be performed, although PIV or high-quality flow visualization would require a tube of much better optical quality, such as quartz.

The inlet runner has been mated to the contraction through a separate flange matching that on the cone. A tight fit, but not an interference fit, has been specified to attach the flange to the tube, with the addition of a number of grub screws to ensure a good fixing. Attachment of the inlet runner to the throttle body required a coupling part to be made that gripped the tubing in a similar manner to the flange, and also clamped onto the throttle body. In order to give a good fit, the external walls of the throttle body have been machined down to provide a parallel-walled surface on which to clamp the coupling. The latter thus comprises a circular slotted sleeve that clamps tight to the throttle, but allows for loosening so that the throttle may be rotated for the experiments. Figure 4.7 depicts a CAD model of the coupling part.

4.3.7 Support Design

A basic support unit has been designed and manufactured that holds the entire flow rig such that the flow domain is vertically orientated and includes mountings for the measurement equipment and traverse system. The plenum chamber is gripped around its diameter by a clamp that is supported by four legs leading to a floor mounted "H-frame". This forms the basis for the support system and ensures that the heaviest parts of the rig, i.e. the plenum chamber and cone, are mounted low to the floor for additional stability. Bolted to this main structure (for alignment) is a table-top support that holds the traverse system. As the traverse itself is of heavy construction the table structure is also floor-mounted to take the weight so as not to overload the main supports. The

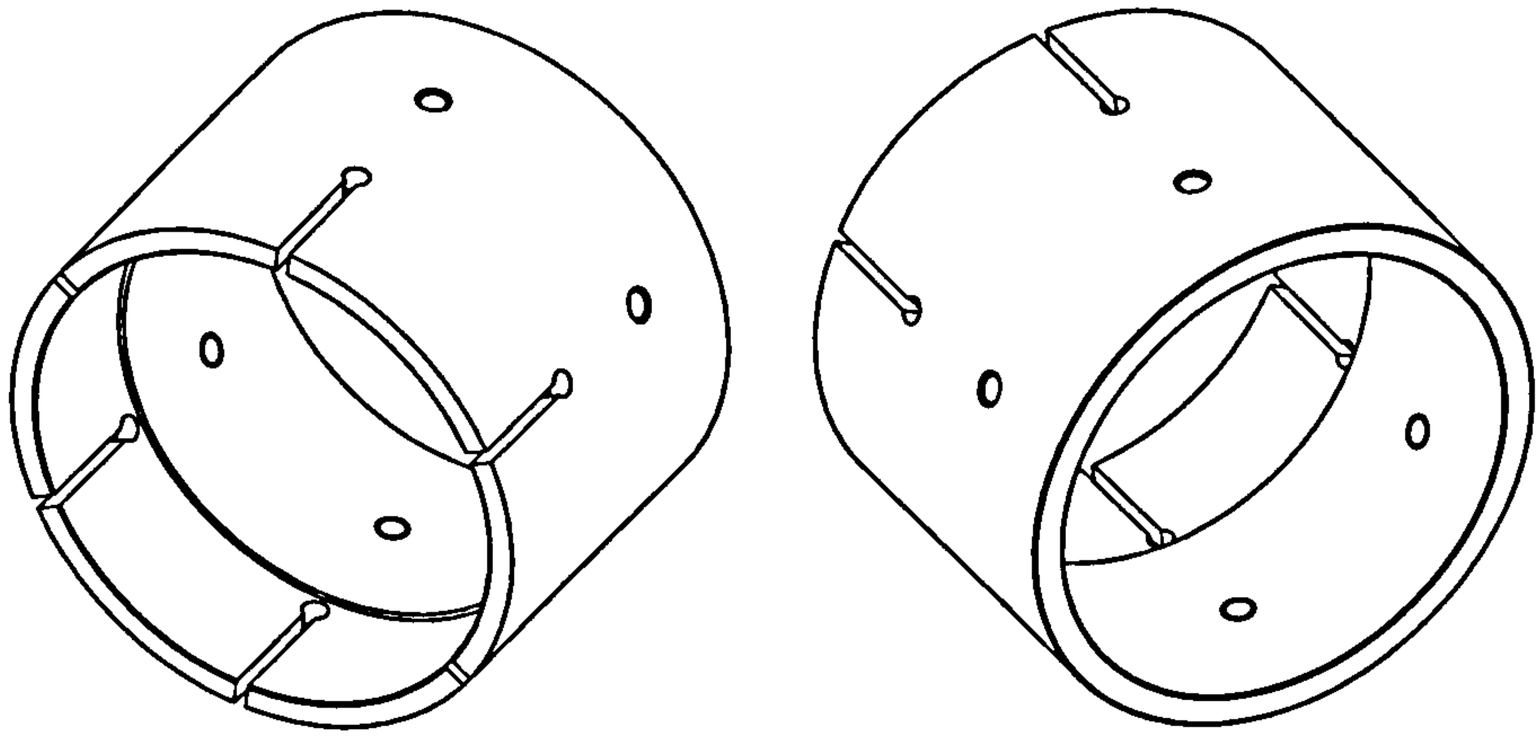

Figure 4.7: CAD model of the throttle body coupling. The slotted end allows the throttle to be gripped and released easily thus allowing for rotation.

top surface of the table incorporates a number of mounting holes and slots to allow for positioning of the traverse system, thus ensuring the vertical axis of the traverse is aligned with the vertical axis of the throttle outlet runner. Figure 4.8 shows the design concept of the support system in conjunction with the the plenum chamber and traverse system.

4.3.8 Traverse System Design

A simple traverse system has been designed and built with the sole purpose of allowing a hot-wire probe to be swept across the flow domain at various downstream locations. Given the limited number of proposed measurement locations the traverse has been simplified with manual control of the traverse and a fine adjustment in one direction alone. The traverse is designed to mount the hot-wire probe perpendicularly to the flow direction, i.e. through the wall of the outlet runner, although normal practice is to mount the probe such that its body is aligned with the mean flow direction in order to minimise flow disturbance. The latter approach can not be used here owing to the length of the outlet runner preventing access for the probe without use of an extended probe mount that would be susceptible to disturbance, and may also add excess blockage to

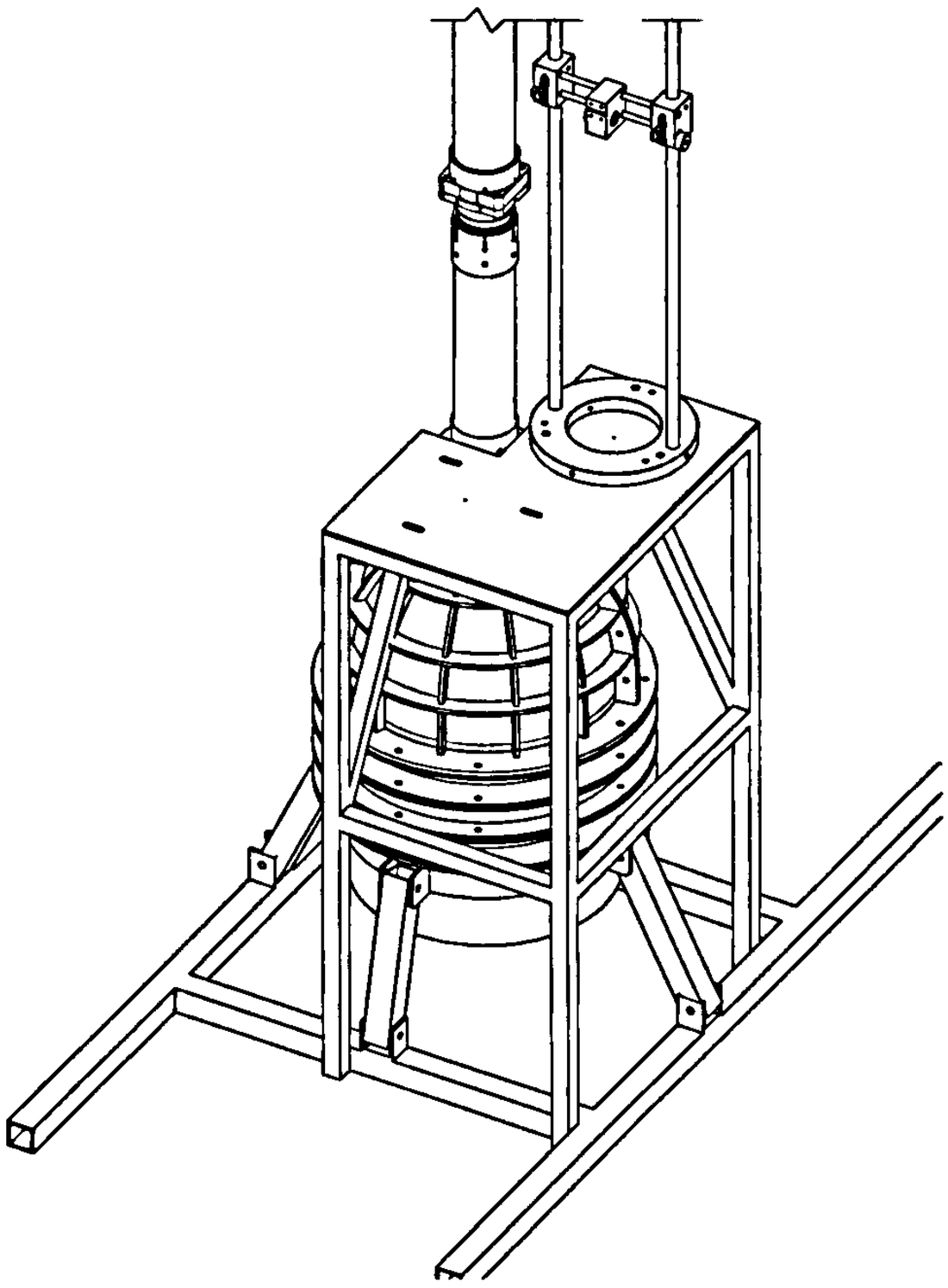

Figure 4.8: CAD model showing the main flow rig support and the traverse tabletop.

the flow. The traverse has an fine adjustment across the domain that is controlled by a lead screw therefore providing infinite adjustment. A coarse adjustment is used for the axial direction that requires the entire traverse system to be manually slid along the upright runners. As this is a fairly crude method of adjustment, care is required to ensure correct alignment of the probe with each adjustment; however, this adjustment has only been performed a few times as the measurements at one downstream location were made in one session before moving to the next station.

The probe itself is clamped in a block that is moved along sliders by the lead screw arrangement. Each slide shaft passes through lubricated brass inserts in the block to ensure smooth motion of the probe. A further clamp is incorporated on one of the slide shafts in order to prevent the block being slid too far and thus preventing the probe

from contacting the far wall of the domain.

To ensure that the traverse was correctly positioned the rig incorporates an adjustable base that allows the whole traverse system to be levelled. In addition a further clamp is present at the top of the traverse that attaches to the outlet tube thus giving further stability to the outlet and ensuring alignment of the traverse and flow rig. Probe positioning is calculated through use of a rule attached to the side of the traverse and a pointer on the probe block. A somewhat crude approach, this method is prone to human error in reading the values; however, care has been taken to ensure the system is used in an identical manner each time, and the scale read from the same position. Further, the exact location of the probe is not deemed to be of the greatest importance for such measurements. Figure 4.9 shows a model of the traverse system described.

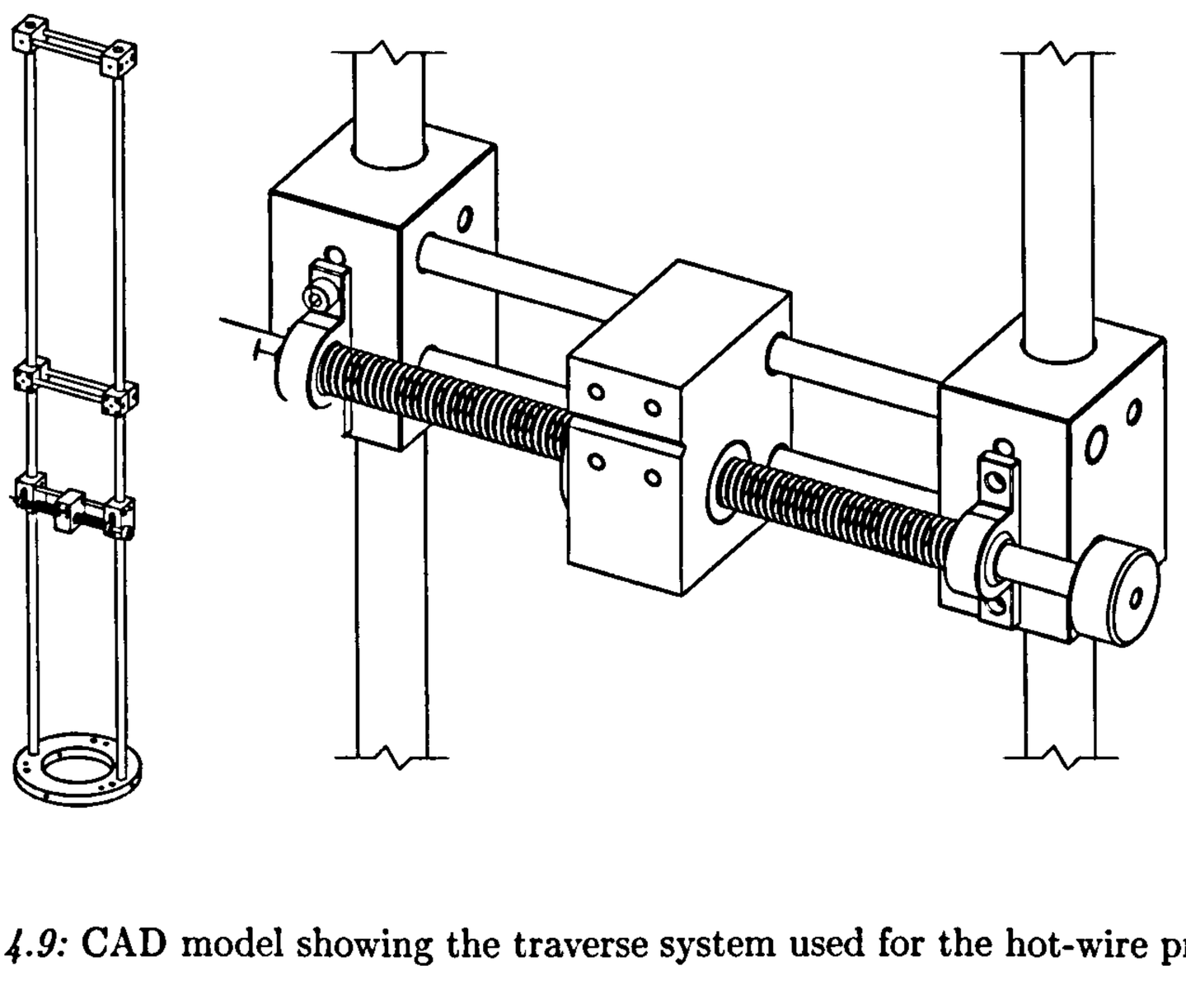

Figure 4.9: CAD model showing the traverse system used for the hot-wire probe.

4.4 Methods of Measurement

4.4.1 Requirements of the Measurement Equipment

Alongside the flow rig the measurement equipment design needs to be considered and this is now briefly presented. The main requirement of the equipment is to allow measurement of the flow quantities of interest, i.e. wake oscillation frequency, point velocity measurements, turbulence values, flow temperature, flow rate, throttle position, and both absolute and differential pressures. As well as being able to measure these quantities a suitable means of recording and capturing the data is required and for this purpose a data-acquisition card has been used to digitally sample the data. Such a card was installed in a standard, IBM-compatible, personal computer and a suitable signal-conditioning board designed and built to feed the raw data signals to the data-acquisition card. The signal-conditioning unit modifies the raw data to a suitable format for the acquisition card and to fully exploit the data-capture range of the card. Sampled data have been stored digitally as ASCII data files and post processing has been subsequently carried out using Matlab and other tools.

4.4.2 HWA System

Perhaps the most important measuring device is the hot-wire anemometry system as this has been used to record the time-history of the flow, and the signals analysed to calculate mean velocities, turbulence quantities and oscillation frequency of the flow. A DISA 55m constant-temperature hot-wire anemometry system has been used, as such a system was readily available at the University, and although somewhat dated, the unit is easily capable of giving accurate flow measurements.

Measurements were made using a DANTEC 55P11 miniature parallel probe with a probe length of 30 mm, probe diameter of 1.9 mm, prong length of 5 mm, wire length of 1.25 mm and a wire diameter of 5 μm. This was in turn mounted in a 4 mm diameter DANTEC 55H21 probe mount. Owing to the short length of the probe, the mount itself also needed to enter the flow domain in order to obtain a full traverse. Thus, the outlet runner of the domain incorporates a number of 4 mm diameter holes to allow access;

that are sealed when not used. When taking measurements the probe is traversed across the half of the domain away from the access point in order to minimise the risk of flow disturbance due to the access hole.

Probe traverses were made in planes located one, two and three diameters downstream from the throttle-valve pivot. To avoid unnecessary movement of the traverse and hot-wire components the throttle body was rotated about 180° to allow a full traverse to be made over the domain, and also rotated by 90° to allow measurements to be made in the axial plane of the pivot. The design of the traverse allows the probe body to be rotated by 90°, providing an additional set of readings sensitive to different velocity components.

Output from the HWA system is in the form of a continuous (bridge) voltage which is fed to the data capture card via the signal-conditioning device. In addition, the signal is also fed to an oscilloscope to allow real-time evaluation of the signals to be performed.

4.4.3 Pressure Measurement

Static pressure measurements were made at the outlet to the plenum chamber, and at locations upstream and downstream of the throttle valve. Pressure tappings have been used in order to achieve this, which are suited here, as the flow is expected to be uniform. Tappings were placed in the plenum and at locations 1D and 2D upstream and downstream of the throttle body respectively. The tappings consisted of a brass insert with a 1 mm internal diameter, mounted flush with the internal walls of the plenum and throttle runners. The tappings are connected to the measurement equipment through flexible pressure tubing cut to a short length in order to reduce the response time of the system. Surface-mounted pressure transducers could also have been used at each location, but the use of static tappings and a remote sensor suits the application best and allows a single transducer to be used for all measurements.

Fraden (1993) gives details on many pressure-measurement devices including piezoresistive, capacitive, VRP (variable reluctance pressure), and optoelectronic sensors. Piezoresistive and capacitive sensors use a diaphragm that moves under the influence

of a differential pressure. The movement of the diaphragm causes a change in the resistance or capacitance of the device which is manifested as a change in the output signal of the device. Capacitive sensors are more suited to low-pressure applications where large pressure pulses are likely to occur owing to their ability to handle large over-pressures before diaphragm breakage. VRP sensors are suited to low pressures where silicon-based devices do not give good response owing to the small displacements involved. Such a device works by using a magnetic field to induce a current is a circuit by movement of a small diaphragm. From the details that Fraden gives it seems that piezoresistive or capacitive sensors are applicable here. As these sensors are silicon-based they may require temperature compensation; typically the sensor is calibrated to operate within a given temperature range to ensure accuracy in readings. Temperature measurement should ensure that this can be achieved if necessary.

Measurements have been made using a Kulite capacitive pressure transducer of vented gauge type thus allowing differential pressure measurements over a diaphragm. Absolute pressure measurements are thus not possible using this transducer, rather any direct measurements are made against the local atmospheric conditions which must be determined by other means. Calibration of the sensor is not required as each sensor is custom built and calibrated with temperature compensation included at the time of manufacture. A linear output is provided by the sensor in the approximate range of 0–100 mV, the exact range being specified by the ambient temperature. Pressure in the range of 0–3 bar is safely measurable by the sensor with a proof pressure of 6 bar. Output from the sensor is fed to the signal-conditioning board that converts the signal to a suitable format for the data-acquisition card.

In order to calibrate the hot-wire probe it is necessary to make pressure measurements where the pressure variation is of the order of 100 mbar. Given the relatively large pressure range of the Kulite transducer (0 to 3 bar) it is insensitive to such small changes in pressure and hence its use for hot-wire calibration proved unsuccessful. As such, a Furness Controls FC012 micro-manometer system has also been used for pressure measurements in conjunction with the Kulite transducer. This system was used

for the calibration of the probes, but also for the mean velocity measurements with the Pitot-static tube as described below.

4.4.4 Throttle Angle Measurement

The throttle body used in the investigation is used as part of a fuel-injected engine and therefore incorporates a throttle position sensor for the purposes of fuel mapping. This sensor has been utilized to establish the angle of the throttle blade throughout the experiment. The sensor consists of a potentiometer that provides a linear output signal proportional to the angle of throttle opening, in the range of 0-5 V. This was verified by measurement of the throttle angle and recording the voltage output of the sensor, thus the actual range of output was found to be 1.002 V to 4.69 V for an opening range of 6.85° (sealed position) to 85.35° (maximum opening) with an approximate error of ±0.2°.

4.4.5 Temperature Measurement

In order to correctly set up the hot-wire probe, and to allow for its calibration, the air temperature must be known. In order to measure this, three different devices have been used; a standard mercury-filled thermometer, a TSI hand-held hot-wire device, and a LM35DZ transistor. The thermometer gives an indication of the mean air temperature to within 0.5° C for calibration and probe set up, with the hot-wire unit being used as a backup. Both devices were used to measure ambient temperature at the same moment with both providing the same reading. The TSI unit offers considerably faster response times than the mercury thermometer and hence the unit has been used to record the ambient flow temperature where possible, although owing to the large probe size of the unit it cannot be used in proximity to the throttle body.

A transistor device was used as a further temperature probe owing to its small size, low costs, and improved accuracy over the other devices. Such devices are typically mounted on an electronic circuit board to monitor system temperatures; however, they can be readily applied to other applications with due care. Here the unit has been

soldered to a length of wire to allow it to be positioned directly in the airflow as necessary. The unit has been calibrated by exposing it to known temperatures and has a linear output in the range 0 mV to 100 mV for the temperature range 0 to 100 °C.

Owing to its small size, the transducer can be inserted into the flow domain through one of the tube side walls thus allowing the temperature of the local flow field to be measured. However, simultaneous measurements with the hot-wire probe are not viable in an upstream location as the temperature transducer is intrusive and therefore generates a flow disturbance that will affect the hot-wire signal. Temperature measurements were performed infrequently as the flow temperature varies slowly; thus this was an acceptable compromise.

4.4.6 Mean Velocity Measurements

Measurement of the mean flow velocity is required in order to establish the correct operating conditions of the experiment and thus match the inlet conditions of the CFD. A Pitot-static tube placed upstream of the throttle body has been used to measure the velocity, and as the probe only makes one measurement at a fixed location per run, the need for a complicated traverse system has been eliminated. Owing to the small dimensions of the inlet a small Pitot tube has to be used to minimise the blockage produced, despite the Pitot tube being a very "clean" measurement device that produces small losses. Bryer & Pankhurst (1971) give detail on the design and construction of Pitot tubes and other pressure probes and note that calibration of individual probes is required to ensure that the static pressure holes are correctly positioned for accurate measurements. However, probes, which have been carefully designed and calibrated, are readily available in a variety of sizes and configurations, and hence these considerations have not been dealt with here. The Pitot-static tube used is a hemispherical-head type, with single static hole and a main body diameter of 4 mm. Such probes are particularly insensitive to yaw effects (Linford, 1961), allowing up to 20° of mis-alignment with minimal effect on the velocity reading obtained. Rae & Pope (1984) suggest that for a deviation of 5° the error in pressure measurement is -0.2% for total pressure, and

+0.4% for static pressure. To measure the difference in total and static pressure the unit is attached via pressure tubing to the micro-manometer; this allows direct velocity measurement.

The Pitot-static tube measures the mean component of velocity at its measurement location and not the overall mean velocity of the fluid. To measure the actual mean of the flow the Pitot-static tube should be positioned at a set location determined by the velocity profile or it must be calibrated appropriately. The former method assumes knowledge of the fully-developed velocity profile of the flow. For standard hydraulic conditions within circular pipes the velocity distribution is a function of Re and is well-known and documented. For long pipes the velocity can be measured at a distance of 0.762 times the pipe radius from the centre to give the velocity to within 0.5% of the mean velocity of the pipe for a wide range of flows (Linford, 1961). Ratios of the mean-to-central velocity (U/U_c) can also be used for this purpose. By measuring the central velocity a smaller error is introduced due to the flatness of the velocity profile in this region.

The latter method has been used here as positioning of the probe is thereby less problematic, and the velocity profile can easily be measured using the HWA system thus allowing calculation of the mean velocity magnitude. Owing to the short inlet pipe used throughout the investigation the Pitot-static tube measurements have been calibrated against the HWA measurements to ensure that the correct velocity profile is read by the tube. Comparisons of the profiles revealed that the Pitot-tube accurately measured the velocity with a maximum deviation from the HWA signal of 2%. Thus for the experiments carried out the maximum centreline velocity has been measured and this has been appropriately scaled to obtain the mean velocity.

4.4.7 Data Acquisition

All the signals were recorded using a data-acquisition (DAQ) card mounted into a standard, IBM-compatible, personal computer running a version of Microsoft Windows. The DAQ card is a PCI-6023E multi-function I/O board supplied by National Instruments.

The unit uses the PCI bus of the PC to transfer data and an external SCSII connector to receive data. The board provides 12 analogue or 8 digital inputs, a sampling rate of 200 kSamples/sec at a resolution of 12 bits, and a signal input range of 0 to 10 V. Thus the board is sufficient for the needs of the investigation, with the 12 bit resolution giving 2^{12} (4096) discrete voltage steps of approximately 2.44 mV. Further the maximum Nyquist frequency is 100 kHz which is easily sufficient for frequency analysis of the hot-wire signals.

A signal-conditioning unit has been designed and built within the University to convert the signals from all the measuring equipment to a suitable format for the DAQ card. Power for the sensors is provided by the board and the signals returned are suitably scaled and offset to provide the DAQ card with a 0–10 V input voltage for each channel with each sensor using a separate channel. Ensuring that the input voltage lies in the 0–10 V range ensures that the captured signal is of the highest accuracy as the full range of the input is being used. Measurements are made using differential mode whereby the difference between two inputs is actually measured, thus reducing the likelihood of noise entering the system.

For the HWA system the conditioning is a little more complicated. As interest lies in the frequency of the hot-wire signals as well as the raw signal, the unit splits the signal into AC and DC components and feeds these to the DAQ under separate channels. By splitting the signal in this way, the signal-conditioning board is able to amplify each signal independently thus maintaining high resolution of the signal. By using a single combined signal there is a risk of the AC signal suffering from resolution errors where the DC component takes up the majority of the bandwidth of the DAQ card (Bruun, 1995; National Instruments Corporation., 2000). Both parts of the signal are amplified and modified such that the full input range of the DAQ channels are used and the signals are then recombined. Thus the input to the DAQ can be written as, $E(t) = G_1(E_{DC}(t) - E_{off}) + G_2 E_{AC}(t)$, where E_{AC} and E_{AC} represent the raw HWA signal, E_{off} represents the offset voltage, and G_1 and G_2 represent the gain applied to the signals. Knowing the gain for each component allows the signal to be reconstructed

once sampled and stored without loss of resolution.

Continuous sampling of the throttle angle is not required as the value does not change and hence this is only required as a check at the start and end of each experimental run. Temperature and pressure vary slowly over time and thus these were initially sampled at an appropriate rate for the runs, typically once every 30 seconds. Although pressure variations are predicted, the pressure sensors have a low response time and hence mean values are recorded for each run. Examination of the results shows that the variation was small enough to reduce the samples to one at the start and end of the run.

Transient measurements of the velocity using the hot-wire probe are the main measurements of interest and thus emphasis has been placed on these readings. Based on the results from the CFD investigation, the frequency of the throttle-valve-wake oscillation is expected to reach 500 Hz at most, and hence a sample rate of 10 kHz has been used thus allowing for frequencies up to 5 kHz to be accurately recorded by the system. Checks were made using the system to ensure that the signal could be downloaded quickly without the DAQ card memory becoming full as this would require buffering of the signals before writing to disk. The tests showed that the transfer speed of the system was sufficient to allow the signals to be written directly to disk.

Sample length is dictated by the available run-time of the flow rig and the ability to perform one complete set of measurements using one charge of air from the reservoir. As such, a sample time of 5 seconds has been used for each measurement; this allows a full traverse to be carried out for the highest flow rates. Under ideal circumstances longer run times would be used, and several such runs would also be made to improve measurement quality and accuracy.

4.5 Flow-Rig Assembly

4.5.1 Plenum Chamber and Contraction

Owing to the poor quality of manufacture of the plenum chamber and contraction, assembly of the units proved difficult, and required several attempts before the unit

was finally ready for testing. Assembly began with the lower plenum sections, followed by the mating of the contraction to the final plenum section and then a finally assembly of the two main parts. Sealing of the units was achieved using cork and rubber seals that were manually cut to shape as required. The seals had a guaranteed pressure rating of 15 bar that easily satisfied the needs of the plenum chamber.

The base unit was first modified to accept the deflector unit which was bolted into place, and the unit was then inserted into the main supports to allow the remainder of the rig to be built upon this. Before further assembly, the gauze, honeycomb and seals were cut and dry assembled to ensure correct fitting and to eliminate any internal flow obstructions. Seals were thus applied to the base unit along with a liberal coating of silicone sealant, the first gauze laid on top before a second seal, and then the first spacer was added. The units were bolted together such that the load was evenly distributed around the diameter, and the unit again checked for flow obstruction. Use of the silicone sealant proved beneficial as this acted as a lubricant and allowed the gauze to slip between the seals as the units were bolted together, thus pulling the gauze tight. Further seals were added to the unit and then the secondary (larger diameter) spacer was bolted to the unit, again with additional sealant. The honeycomb was then inserted into the secondary spacer and the second layer of gauze added. Figure 4.10 shows the fitment of the honeycomb to the plenum chamber before the second mesh and remaining flow rig is bolted down.

As the contraction was liable to breakage on assembly, it was first bolted to the final spacer before the mated units were then added to the main plenum assembly. The contraction itself required several attempts at sealing before the unit was successfully installed. Owing to the differing sizes and levels of warpage, seals had to be specifically cut in order to space the unit to match the plenum spacer, although the outlet of the contraction was correctly proportioned. With a dry assembly successfully completed the unit was assembled with additional silicone sealant and finally bolted to the final plenum spacer. Owing to the sealing process, the internal surfaces of the contraction were no longer smooth and required smoothing in order to remain useful. A hard drying

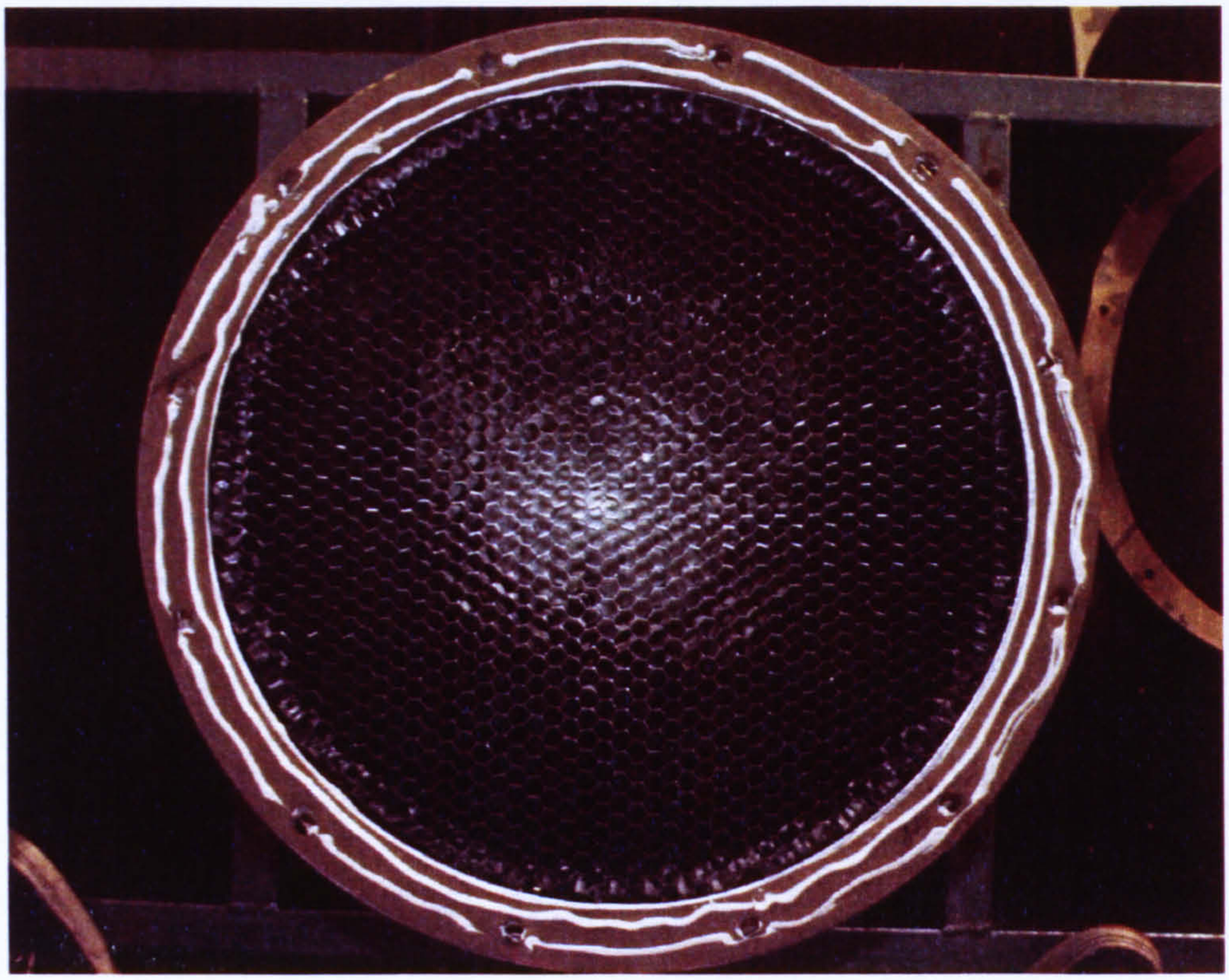

Figure 4.10: Fitment of the honeycomb flow conditioner within the plenum chamber. The photograph also shows the cork seal and silicone sealant used to mate the sections of the plenum.

putty was thus used to fill the gaps of the contraction and to smooth the transition from the contraction to the plenum spacer. This putty could be shaped and smoothed when wet, thus allowing a clean transition between the contraction sections and the plenum spacer to be created. Once dry the internal surfaces were sanded to give a consistent flow surface. Figure 4.11 shows the contraction cone mated to the plenum spacer before final assembly of the components.

With the contraction cone assembled, the contraction and spacer were bolted to the base of the plenum, again with additional sealant. In order to evaluate the success of the internal sealing of the contraction, a small CCD camera was lowered into the plenum to allow the internal surfaces to be viewed. This highlighted that some of the putty had cracked upon bolting the unit together, and although the cracks were small, approximately of the order of 0.5 mm, they were deemed unacceptable and the

Figure 4.11: Assembly of the contraction sections and plenum spacer using cork seals, silicone sealant, and modelling putty. The photograph shows the four sections of the contraction with the seams filled by putty.

unit was disassembled, resealed and then reassembled with care to ensure no further cracking occurred.

4.5.2 Remaining Flow-Rig Components

In a similar manner to mating the plenum to the contraction, the outlet to the cone required additional seals and spacers to be cut to provide an adequate sealing surface to which the inlet runner could be mounted. The spacers and seals were cut to allow the runner to snugly fit against the contraction with a smooth internal transition. These spacers and seals were applied to the contraction with additional silicone sealant with

the outlet flange then bolted in place and the seals allowed to set. With the seals dry, the flange was removed and the inlet runner re-fitted to ensure a smooth flow path existed and any residual sealant removed. The elastic nature of the set silicone sealant provided a very good mating surface for the tube, and ensured an excellent seal was provided between it and the contraction.

With the inlet runner in place, the throttle body was then added to the unit using the coupling device. A small amount of PTFE plumbing tape was applied to the surfaces to allow for an improved seal with the throttle, whilst still allowing the throttle body to be easily rotated for the measurements. The throttle outlet tube was bolted to the throttle body and sealed using standard inlet manifold seals that are used for the throttle under normal conditions.

The traverse supports and stand were bolted to the main stand and the table top then bolted to this. The traverse unit was mounted on the table top and carefully aligned such that the vertical axis of the traverse matched that of the flow domain. The top of the traverse unit incorporated a clamp that held the outlet tube in place thus stabilizing the structure and reducing the risks of hot-wire probe damage through movement of the tube walls relative to the domain. The traverse axes were aligned with the tube, clearances were checked to ensure the probe would not foul the walls of the tube, and a safety stop adjusted to ensure the probe would not contact the opposite tube wall. This procedure needed to be carried out each time a new measurement position was investigated. Figure 4.12 shows the traverse system with hot-wire probe attached being checked for clearance and clean operation, and Figure 4.13 shows the final fully-assembled flow rig.

4.6 Flow-Rig Testing

4.6.1 Plenum Chamber Pressure Testing

Before the final assembly of the plenum chamber and contraction as described above, a number of tests were performed on the unit to ensure that it would function safely. As the plenum chamber operates under pressure there were concerns that a certified

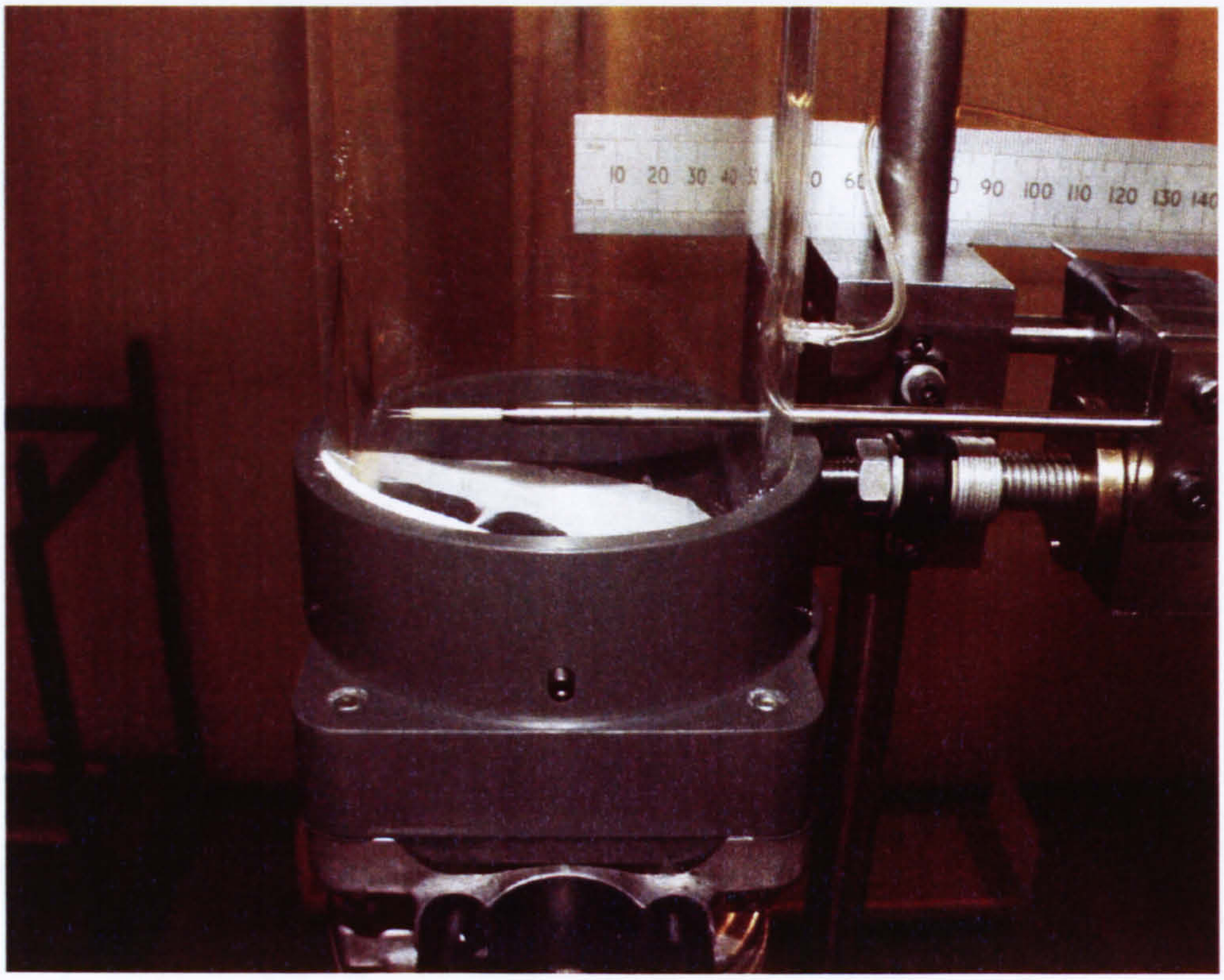

Figure 4.12: Testing the hot-wire probe traverse system. Photograph shows the hot-wire probe (white) inserted into the probe mount that in turn is held by the traverse system.

pressure test would be required by law as the unit was effectively a pressure vessel. On further investigation, a pressure vessel is formally described as one that has a *barlitres* rating over 250 (ISO, 1991; Reese & Kawahara, 1993). That is, the product of the volume and pressures in the unit must be greater than 250 bar-ltr. From the CFD, and previous studies it was known that the pressure in the plenum chamber would at most reach 3 bar. The volume of the unit can easily be calculated as the profile of the contraction is known, and the plenum is a simple cylinder. A calculation shows that the entire volume of the plenum and contraction is 0.044m^3, thus the product of volume and pressure for the system is 130.6 bar-ltr, and a maximum allowable pressure of 5.74 bar can be used without the unit being considered a pressure vessel, thus providing an adequate safety margin.

Although the unit does not qualify as a pressure vessel, a pressure test was still

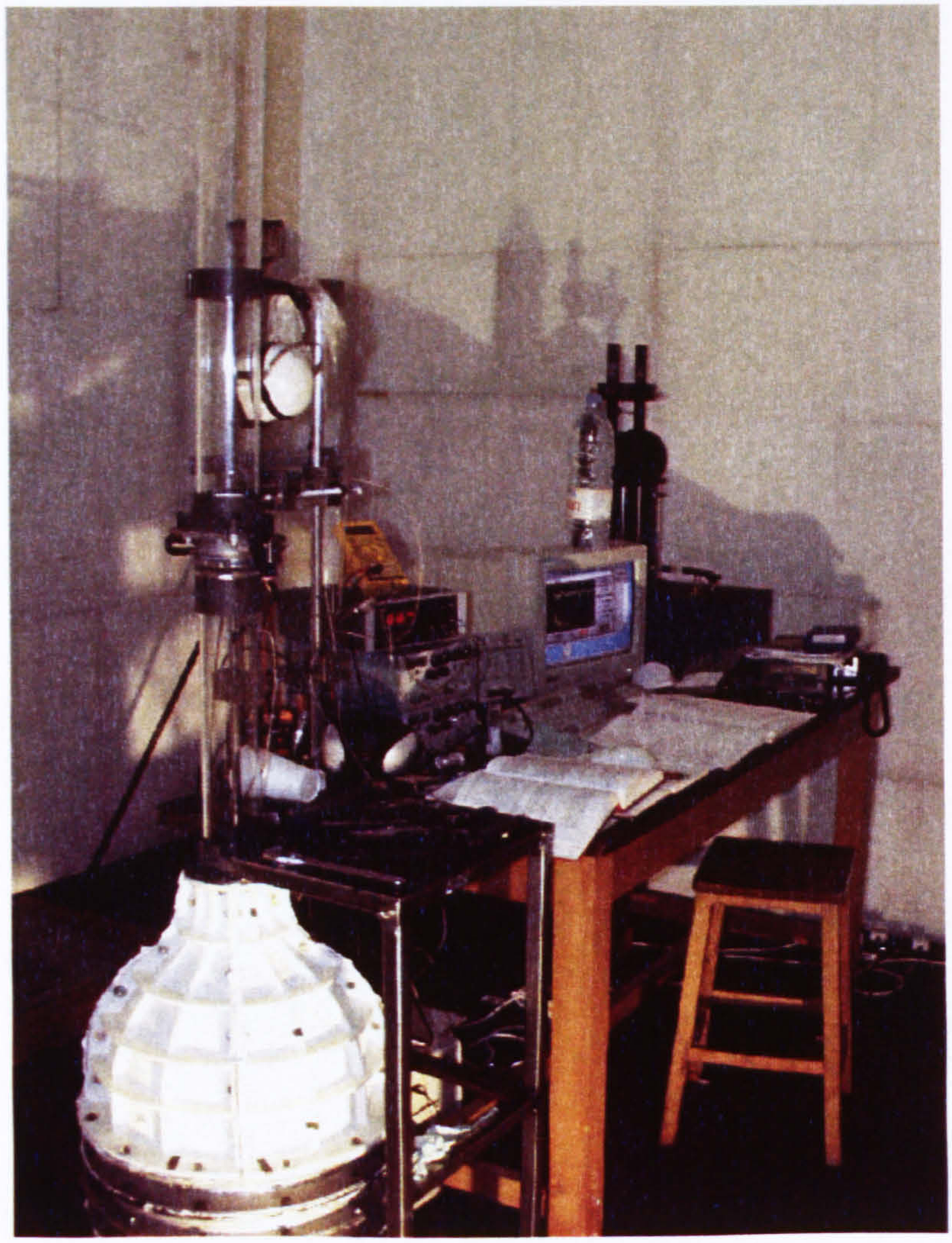

Figure 4.13: Full assembly of the flow-rig with traverse and measuring equipment installed.

performed in order to ensure the unit could be safely operated and in order to test the seals. Firstly the plenum was assembled without the contraction and sealed using a metal plate and a number of clamps. The pressure was then steadily increased to a maximum of 4 bar with observations recorded. Several leaks were discovered on the initial runs and these were eliminated with the addition of larger seals in the plenum. A second pressure test proved successful with no leaks present from the plenum chamber.

Pressure tests were then performed with the contraction fitted to the plenum chamber although only to a pressure of 3 bar. Upon testing some minor leaks were found that prompted the use of additional sealant in the relevant areas to eliminate the leaks.

4.6.2 Vibration Testing

During the pressure-testing phase the gauze screens in the plenum were examined for signs of vibration. With the honeycomb, second spacer, and contraction initially removed, the air supply was activated into the plenum unit, the flow rate gradually increased, and the first gauze screen observed for signs of vibration. The initial tests revealed small-scale vibrations present with intermittent large-scale vibrations becoming apparent at larger flow rates. This was deemed undesirable because of flow disturbance that would be created and convected downstream.

Re-assembly of the plenum using the silicone sealant as described above pulled the gauze taut and a repeat of the tests revealed that the large-scale vibrations were completely eliminated and the small-scale vibrations were negligible. A further test with the addition of the spacers, honeycomb and second layer of gauze showed no vibrations in the upper gauze. A final check with the contraction in place revealed no change in the level of vibration of the upper gauze screen, as could be ascertained using the CCD camera. Further analysis of the air flow thought the domain showed no signs of large-scale fluctuations.

4.6.3 Final Checks

With the main sections of the flow rig fully assembled and the initial testing successful, the remaining parts of the rig were assembled and some basic tests carried out to ensure leaks were minimised or eliminated, and that no vibrations occurred in the system. The traverse system was positioned and the hot-wire probe mount aligned and the unit checked for operation to ensure no fouling and smooth movement. Basic flow measurements were then performed in order to establish the background noise levels within the system. These and other tests are discussed in the following chapter, where the full measurements are also presented.

Chapter 5

Experimental Investigation

5.1 Introduction

In order to validate the CFD simulations, and to gain a better understanding of the flows through throttle valves, a series of flow experiments have been carried out. These have been performed using the flow rig described in the previous chapter that accommodates the throttle body and provides a controlled flow environment in which to take measurements. Measurements of velocity, pressure, and flow oscillation frequency have been made at specific locations that coincide with the computational predictions. These data have then been analysed to provide useful information on the flow through the throttle valve and to provide validation for the computational study.

5.2 Needs of the Investigation

The main requirement of the investigation here is to validate the computational predictions; this has been achieved through measurements of the flow field through the throttle valve using the flow-rig and measuring equipment described in chapter 4. In order to validate the computational predictions the following information has been gained from the experimental investigation:

- Determination of free-stream conditions;
- Mean streamwise velocity components at locations upstream and downstream of the throttle valve;

- Turbulence intensity of the flow;
- Determination of the oscillation frequencies of the wake behind the throttle valve;
- Measurements of the pressure drop across the valve using static-pressure measurements.

This information has been determined for each of the throttle-valve angles considered in addition to free-flow conditions with the throttle body absent from the flow. These measurements and their procurement are described in the following sections.

5.3 Experimental Procedure

The experimental investigation has been carried out in stages, involving initial testing; determination of operating parameters; error analysis; and finally the main set of measurements. Tests on the system were carried out during the flow-rig assembly process and the installation of the measurement equipment to ensure that the system was operating as expected according to the design specification, and to allow the levels of base noise and error to be ascertained. With operation of the flow rig found to be satisfactory the main flow measurements were then carried out. Flow measurements downstream of the throttle valve were made at locations 1D, 2D, and 3D downstream of the valve pivot axis. These locations were chosen based on the results of the CFD predictions and from previous studies (Alsemgeest, 1998) as these have shown to be the locations of most interest for the range of angles considered, and it also allows for the progression of the flow to be evaluated as it moves downstream. At each downstream location the HWA system has been used to record the time-history of the flow at discrete points across the domain with two probe-element orientations and three probe-body orientations. The three probe-body orientations are defined below as:

- Leading Edge - The probe *body* is aligned perpendicular to the valve pivot with the sensing element downstream of the valve leading edge, i.e. measurements behind the leading edge in the symmetry plane of the valve.

- Trailing Edge - The probe *body* is aligned perpendicular to the valve pivot with the element downstream of the valve trailing edge, i.e. measurements behind the trailing edge in the symmetry plane of the valve.

- Parallel Pivot - The probe *body* is aligned parallel to the axis of the valve pivot, i.e. the measurements are made normal to the symmetry plane of the valve along the axis of the pivot.

These orientations can be realised with the traverse system maintained in position and the throttle body rotated to suit. In each case the probe is traversed between the tube centreline and the tube wall *opposite* the probe entry point, i.e. across the radius of the tube. The combination of the leading-edge and trailing-edge traverses provides a profile of the flow across the entire domain. For the measurements presented here, the traverse distance is shown in millimetres, with the zero value corresponding to the centre of the domain and a maximum radial distance of $r = D/2 = 35$ mm at the domain wall. Convention for the presentation is that a positive radial value corresponds to the leading edge of the valve and a negative value to the trailing edge. Figure 5.1 depicts a simple schematic of the measurement locations relative to the valve and the axis system used for the symmetry plane measurements.

Traversing the domain in two halves considerably reduces the risk of flow disturbance from the probe body, and from any inadequacies in the sealing of the probe body at the wall of the domain. For each individual measurement location, readings have been made with the probe element orientated parallel and perpendicular to the free-stream flow direction, thus allowing two components of the velocity to be recorded. By allowing the throttle body to rotate, the number of probe entrance holes drilled into the side of the outlet tube has been minimised to the three required for measurements in the downstream planes. These have been sealed when not in use to ensure no excess flow disturbance is introduced.

For each flow traverse, a series of discrete measurement locations have been used (Figure 5.1). These have been staggered such that an increased number of readings

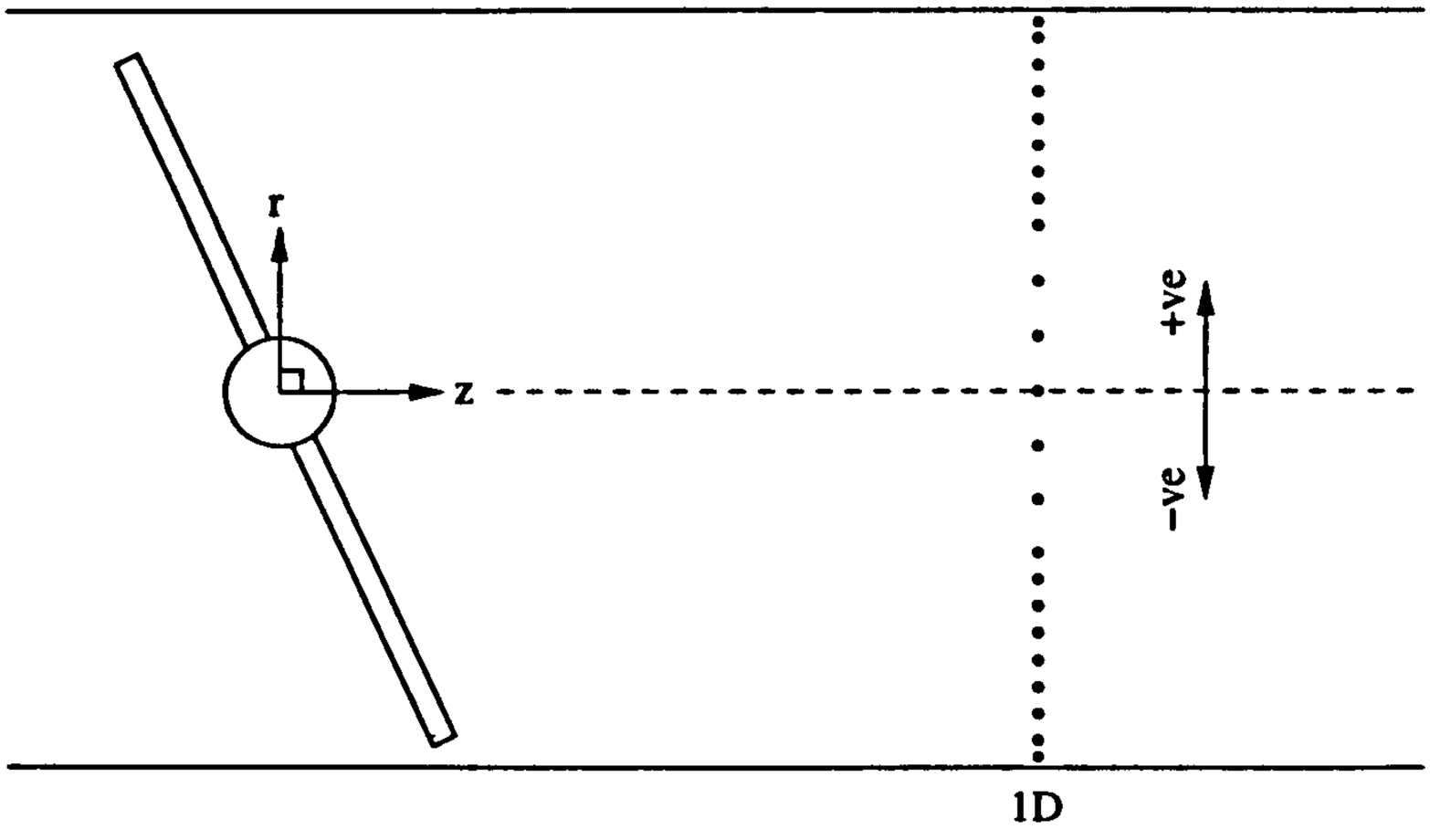

Figure 5.1: Schematic showing the how-wire measurement points relative to the valve position and the coordinate system defined for the measurements. The figure shows locations at the 1D plane only, and these are repeated at the 2D and 3D planes. Not to scale.

has been made towards the wall where flow changes are more frequent, and a reduced number towards the centre of the domain where the flow is more steady. Twelve discrete locations have been used per half of the domain with the first at the domain centreline ($r = 0$), and the last located 1 mm from the wall ($r = 34$ mm). Measurements made in the near-wall region have been investigated by Lange et al. (1999) using computational methods and their results indicate that measurements at this distance from the wall will not suffer from adverse affects through heat conduction to the wall, hence this does not need to be taken into account. Analysis of the time-history signals was carried out in real time using the software used to control the DAQ card, Labview, and has subsequently been analysed further using Matlab.

In order to fully validate the computational predictions, each of the throttle opening angles studied computationally needs to be investigated experimentally. The angles of interest and corresponding inlet flow rates have been provided by Jaguar Cars Ltd. and are given in Table 3.2 (p67). Approximately 276 measurement points have been used for each throttle angle and velocity combination investigated giving a fairly detailed measurement field of the throttle wake flow. As an aside, a few additional measurements

were made with the large valve openings at reduced flow rates.

In addition to the hot-wire velocity time-history measurements, measurements of the static pressure upstream and downstream of the valve were made in order to establish the pressure drop across the valve at the various opening angles and flow rates. These measurements were made using pressure tappings inserted at locations 1D upstream and 1D downstream of the valve, located at points in the tube walls in line with the pivot axis. Each tapping has been carefully inserted into the centre of the tube with a flush fit to the inner tube walls.

Temperature measurements were made in the flow at the contraction outlet and downstream of the throttle valve, in addition to measuring atmospheric conditions. Inflow temperature measurements were made at different instances to the hot-wire and pressure readings to ensure that the sensor did not influence the readings of the latter.

With the data recorded, the HWA time-history signals were analysed for their frequency content in order to establish the oscillation frequencies of the wake. Mean velocity readings were also ascertained along with turbulence data. The results of the measurements are presented below.

5.4 Preliminary Results and Testing

5.4.1 Signal and Flow Noise Analysis (Flow Quality)

With the assembly of the flow rig completed the first measurements performed were to establish the base flow quality generated by the unit. This was achieved by running the flow rig without the throttle-body and throttle outlet runner in place, thus no blockage exists to the flow. Initial tests were performed to verify the operation of the hot-wire probe, to validate its output using readings from the pitot-static tube, and to establish the background noise levels of the flow; the latter of which was highlighted though these initial tests.

With the hot-wire probe aligned with its sensing element and body perpendicular to the flow, point velocity readings were taken for a number of flow rates at arbitrary points in the plane of the throttle inlet without the throttle body present. Evaluation

of the recorded signals revealed that considerable noise was present in the readings; however, the origins of the noise were unclear. Analysis of the flow using the pitot-tube revealed a steady velocity reading; however, this is to be expected as the response of this system is very slow. Likewise, the small hand-held hot-wire sensor also proved to have too slow a response to provide further information. Thus the flow rig and all equipment were carefully checked to establish any effects on the signals produced.

Analysis of the frequency content of the recorded hot-wire signal revealed clear spikes in the frequency domain that were too clean and dominant to be considered a flow feature, but more likely a source of electrical noise. Further investigations revealed this to be the case and the source traced to positioning of the hot-wire unit with respect to the other electrical equipment. It was found that the hot-wire system was picking up interference from the computer monitor and also from the oscilloscope. Thus the HWA unit was relocated such that it remained remote to all other electrical equipment, and its power source was shielded from the remaining equipment to reduce any further noise. Examination of the system plus a series of trial and error investigations with equipment positioning, allowed the electrical noise of the system to be eliminated.

However, on running more tests, further noise was found to be affecting the signals. In this case the noise was clearly an electrical signal as a sharp spike in the frequency domain at 50 Hz was present. This was traced to the compressor, so the unit was switched off during the remaining flow investigations, thus the reservoir had to be fully charged before any runs took place.

A final source of noise at low flow rates was observed in the recorded hot-wire signal, and also observed on the real-time oscilloscope trace. This was attributed to flow disturbance and it was found that, at low flow rates, the flow rig was sensitive to physical vibrations of the system and surrounding apparatus. At these lower flow rates, a small disturbance such as knocking the main stand or unit, produced clear disruption to the signal, thus every effort was made to isolate the unit from external sources of vibration in order to minimise the risk of disturbance. This included mounting the flow-rig on a cushioned floor; making measurements in the evenings or weekends to limit

background noise; ensuring the compressor was switched off; and closing the anechoic chamber during the measurements.

5.4.2 Velocity Profiles

Once the background noise was eliminated a series of measurements was made to establish the velocity profile across the outlet of the plenum. This was carried out for a traverse across the outlet, aligned with the pivot axis, and a further traverse at 90° to this. Both the hot-wire and the Pitot tube were used to generate a velocity profile, thus allowing comparison of the values and to allow the Pitot tube to be calibrated. The final profiles were then used to establish correction factors for the mean velocity measurements during the investigation. Measurements were made over a range of flow rates that included those used for the main investigation, hence giving a range of values for the mean-flow correction factor, and indicating the level of flow asymmetry over the range.

A small degree of asymmetry exists in the plenum outlet flow with a maximum variation in velocity across the developed core of the domain reaching 10%. These initial measurements used only a small number of measurement points and hence the resolution of the velocity profiles is poor and a full analysis of the data could not be performed.

5.4.3 Determination of Turbulence Intensity

The turbulence intensity (Ti) has been determined at various locations in the flow using the measurements made with the hot-wire anemometry system. Instantaneous velocity data have been sampled over a five-second period at a sample rate of 10 kHz in order to achieve this and the values used to calculate Ti from equation 5.1 below,

$$Ti = \frac{\sigma_u}{U} \times 100 = \sqrt{\frac{\sum_{i=1}^{n}(u_i - U)^2}{N}} \times \frac{100}{U}, \tag{5.1}$$

where, σ_u is the standard deviation of the signal, U is the mean velocity, u_i is the instantaneous velocity component at sample i of total sample size, N. In a similar

Mean Flow Rate U, (m s^{-1})	Turbulence Intensity Max (%)	Mean (%)
2.8	1.5	0.4
3.5	2.1	0.6
5.8	8.5	3.0
9.0	8.5	3.1
13.3	13.0	4.0
15.7	9.2	4.5
20.0	6.0	3.0

Table 5.1: Turbulence intensities measured at contraction outlet.

manner to the velocity profiles, the turbulence intensity has been determined across the domain. Table 5.1 gives the mean and maximum turbulence intensities measured at the contraction outlet with no throttle body present in the flow. The maximum values of turbulence intensity reported in the table are found in proximity to the domain walls owing to the reduced mean velocity in this region. It is also apparent from Table 5.1, as expected, that as the flow rate increases, so the turbulence intensity of the flow also increases. However, the levels are small thus indicating the contraction provides suitably clean flow for the experiments.

5.4.4 Frequency Analysis from a Circular Cylinder

In order to ensure that the hot-wire system could adequately capture flow oscillations, a simple experiment was devised where the flow behind a circular cylinder was measured using the HWA system and the signals analysed for their frequency content. The flow behind a circular cylinder at Reynolds numbers larger than approximately 40 becomes unsteady and exhibits a flow field known as a von Kármán vortex street whereby vortices are periodically shed from alternate sides of the cylinder (Tritton, 1988). Hence measurement of such a flow provides a simple test for the HWA system to capture the known flow oscillation, and to give an indication of the accuracy of the readings. The frequency of the signal can be evaluated using the Strouhal number, St, a non-dimensional number that may be considered to be the non-dimensionalised frequency

of a flow. This is defined as,

$$\mathrm{St} = \frac{nd}{U_\infty}, \tag{5.2}$$

where n is the frequency of the flow measured in Hz, d is the cylinder diameter and U_∞ is the free-stream velocity. Although the Strouhal number is a function of Reynolds number, the variation of St with Re is so small that a value of St=0.2 is typical for such flows (Tritton, 1988). Thus, by using this known flow field, the flow behind the cylinder can be evaluated and experimental measurements verified.

To achieve this, the flow rig was used with the inlet and outlet runners and throttle body removed such that the flow from the contraction exited to atmosphere as a jet. At the exit to the contraction a cylinder was mounted so that its axis lay across the flow through the centre of the generated flow jet. The hot-wire traverse was mounted such that readings could be made downstream of the cylinder about the central axis of the jet (to ensure clean flow). A cylinder of diameter 3 mm has been used, with measurements made at locations $x/d = 0.5$, 1, 2.33, 3.33, 6, 8.33, 12.7, 15.33, 18.7, and 24.33; where x is the distance downstream of the cylinder. The flow rate was adjusted so that measurements were made at Reynolds numbers of 85, 160, 240, 380, 600, and 1250; based on the cylinder diameter. Readings were made at the centreline thus capturing vortices shed from both sides of the cylinder, and to one side of the centreline thus capturing only one set of vortices.

A typical velocity trace takes slightly off-centre of the domain is given in Figure 5.2(a), with a corresponding trace at approximately the same non-dimensional distance from the cylinder and same Reynolds number, from the work of Tritton (1988) given in Figure 5.2(b). Each plot shows the velocity trace at a distance $x/d = 8.33$ and $x/d = 8$ respectively for a flow at Re=85, over a period of 0.5 seconds. Very similar characteristics can be seen in the two traces, showing a clear periodic signal that has a frequency of 34 Hz. Using equation 5.2, the Strouhal number for the flow can be evaluated, and this gives a value of St=0.23, thus agreeing with the previous accepted value. Figure 5.3 plots the Strouhal number for all the flow cases considered. It is clear from the plot that there is a fair degree of scatter in the points, but all lie in the range

$0.19 \leq \mathrm{St} \leq 0.29$ and an overall mean of all points is approximately 0.24. The scatter in the data is indicative of the poor experimental set-up and restricted flow domain as opposed to a direct indication of the accuracy of frequency measurements. Given the lack of quality data, no definite level of uncertainty has been defined for the frequency measurement. However, the results are consistent with the correct operation of the HWA system, and also of the real-time and post-processing frequency analysis.

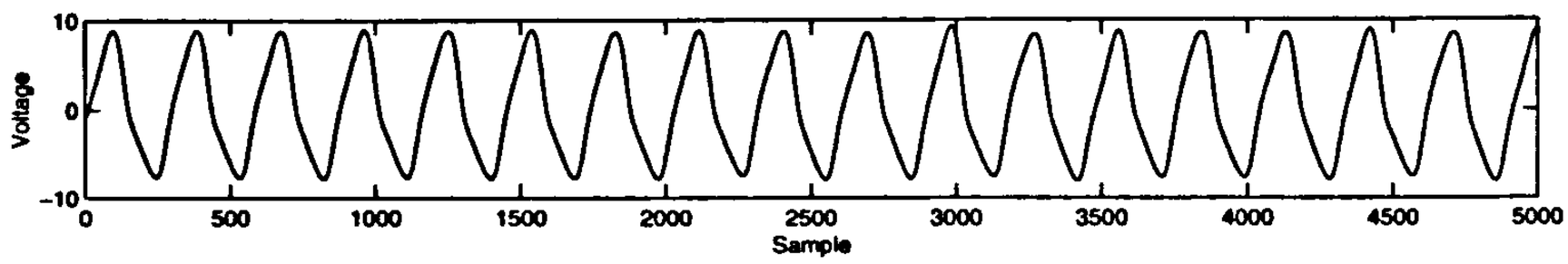

(a)

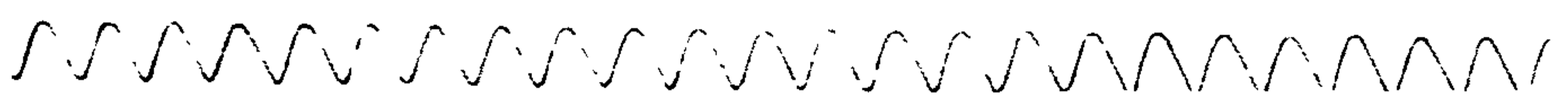

(b)

Figure 5.2: Plots of the measured velocity in the wake of a circular cylinder. (a) Current investigation, $x/d = 6$, Re = 85. (b) The work of Tritton (1988), $x/d = 8$, Re = 85. Both measurements made off the centreline to predominantly capture vortex history from one side of cylinder.

5.5 Experimental Uncertainty Analysis

It is appropriate to briefly discuss the experimental uncertainty before the presentation of the results of the investigation. Each measurement performed will have associated with it an error, i.e. the deviation of the measured value from the true value of the measurand. Generally, the true value of the measurand is not known, hence neither is the true error in the measurement and therefore an estimate of the probable error in the measurement must be made. Only where a strict calibration has been carried out does the measured value represent the true value; however, even calibration includes sources or error that must be accounted for. The combination of individual measurement errors

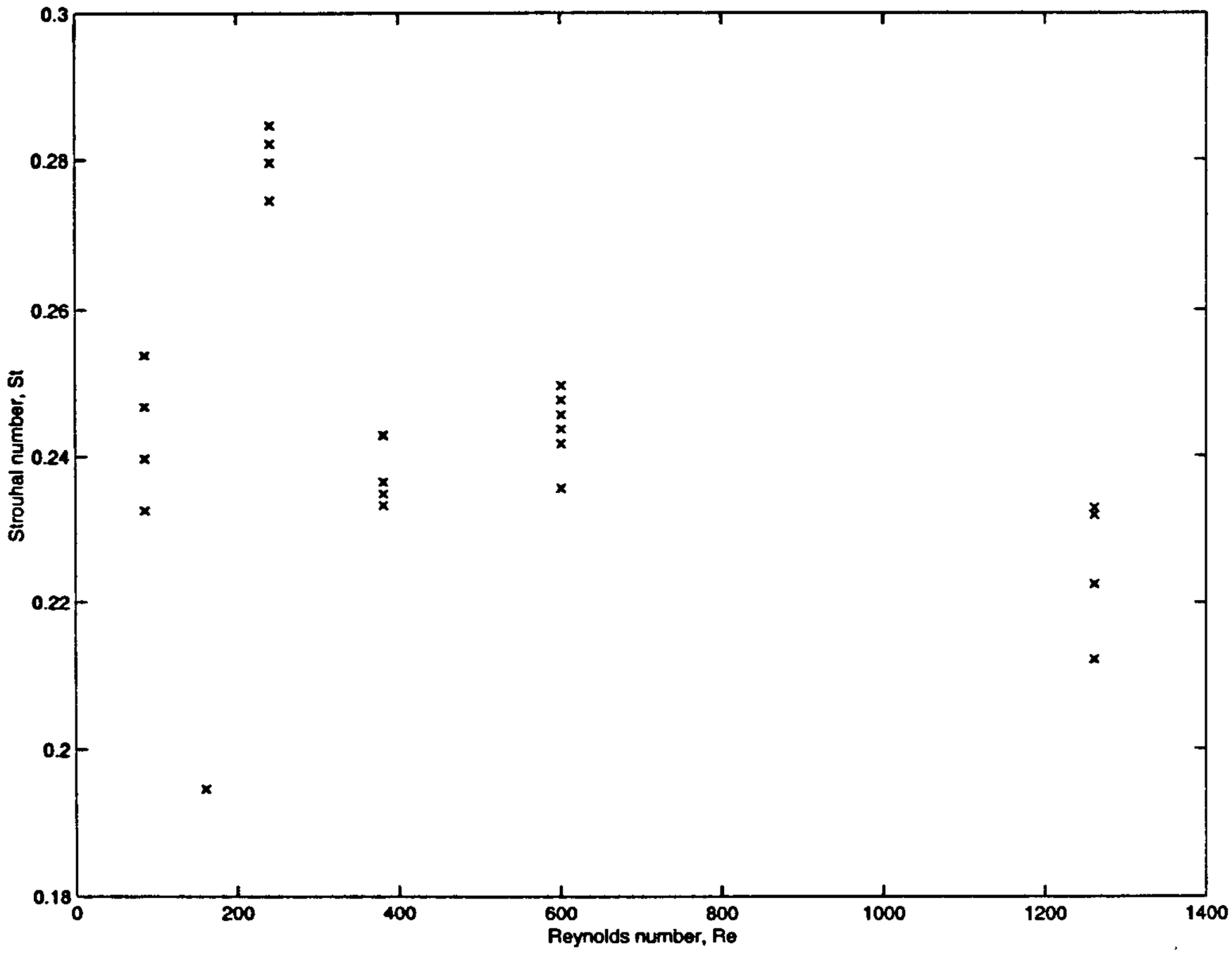

Figure 5.3: Variation of Strouhal number with Reynolds number for the flow behind a circular cylinder.

and error estimates leads to an overall estimate of the probable error of a reported value, i.e. the uncertainty in the result.

The experimental measurements made are limited in number owing to time restraints of the investigation and also the initial underestimate of their importance. Therefore, measurements of flow temperature, pressure and ambient conditions have only a small sample set from which to evaluate their uncertainty. Given this, the uncertainty in these measurements is based on design-stage and single-measurement uncertainty analysis. The individual errors for each measurement are then propagated through to the final result using the root-sum-squares (RSS) method to give the overall uncertainty (Figliola & Beasley, 1995).

For example, measurements of the flow temperature have been made using an LM35DZ transducer mounted in the flow. For these measurements only a limited num-

ber of samples are available and hence only a basic uncertainty analysis is performed. The specifications for this device are a resolution of ±0.6°C, a range of 0°C to 100°C, linearity of ±0.2°C over the range, and a repeatability of ±0.08°C over the range. Using the RSS method the design stage uncertainty can be given as, $v_d = \sqrt{v_c^2 + v_o^2}$, where, v_o is the zero-order uncertainty (typically half the resolution of the device), and v_c is the instrument error (Figliola & Beasley, 1995). The latter can be estimated from the linearity error and repeatability error of the device, ϵ_1 and ϵ_2 respectively, as $v_c = \sqrt{\epsilon_1^2 + \epsilon_2^2}$. Thus the design-stage uncertainty of the temperature measurement is ±0.37°C. The measurements find a mean flow temperature of 20°C, with a spread of 1°C. Thus, combining the errors using the RSS method gives a mean flow temperature of 20 ± 1.06°C (95%). Similar methods are used to give a basic uncertainty estimate for ambient conditions and for pressure measurements.

For the main hot-wire measurements, calibration has been performed that significantly reduces the error in measurement. However, calibration involves individual measurements and the errors associated with these measurements (such as those described above) are carried through to the overall uncertainty of the measurement. Additionally, finite statistical methods have been used to evaluate the uncertainty in each of the readings owing to the large sample size available. From the individual samples, the sample mean and sample variance have been calculated and using the assumption that the measured values fall within a normal distribution about the sample mean, the uncertainty in the measurement can be estimated using a t-distribution (Figliola & Beasley, 1995). Estimates using this method have been calculated with a 95% confidence level and have been presented as error bars on some of the results. The uncertainty in the measurements is greatest for flows with high turbulence intensity and is therefore not constant across the flow domain. This will be highlighted in subsequent discussions.

5.6 Experimental Results

This section presents the results obtained using the experimental procedures described previously in this, and the preceding chapter. As the parameters for the experiments

have been chosen on the basis of two alternative data sources, the velocity-based results are presented accordingly. For the smaller throttle-valve openings, 3.5° to 12.5°, the data source is an instrumented super-charged engine and is presented as "small valve openings." For the larger openings, 19° to 47°, the information has been obtained from the 1D engine simulation code, MANDY (see chapter 2), for a normally aspirated engine and these results are presented as "large valve openings."

Figure 5.4 shows the inlet velocity magnitude derived from mass-flow data as three curves labelled as *low*, *medium*, and *high*. The data provided by Jaguar that forms the basis for this investigation is labelled as *high* and shows the distinct step between the smaller and larger throttle-valve openings that corresponds to the different data sources. As an aside, linear extrapolation of the small-angle data (supercharged engine, 3.5° to 12.5°) produces the curve labelled *low* and these values have been used to evaluate low flow rates and the larger throttle openings. An intermediate set of data values has also been investigated and these are represented by the curve labelled *medium* that represents the median point between the two extremes. Note that comparisons to the computational predictions are only made of the high flow rates.

5.6.1 Pressure and Mean Flow-Rate Measurement

Static-pressure measurements have been made upstream and downstream of the throttle valve for each combination of throttle angle and flow velocity considered. These are presented as a pressure drop across the valve as well as in the form of the static-pressure loss coefficient; the latter allows clearer comparisons to be made to previous studies as the pressure drop is non-dimensionalised. In addition, the mean flow rate has been measured at the inlet in order to ensure that the experiment mirrors the conditions of the computational predictions and tallies with the given data. Table 5.2 shows the ideal and measured inlet velocities, the pressure drop, and the corresponding pressure loss coefficient for the investigation. There exists a discrepancy between the actual and desired flow rates owing to the poor control of the flow rate through the rig at low velocities. However, the maximum deviation of the measured flow rate from the ideal

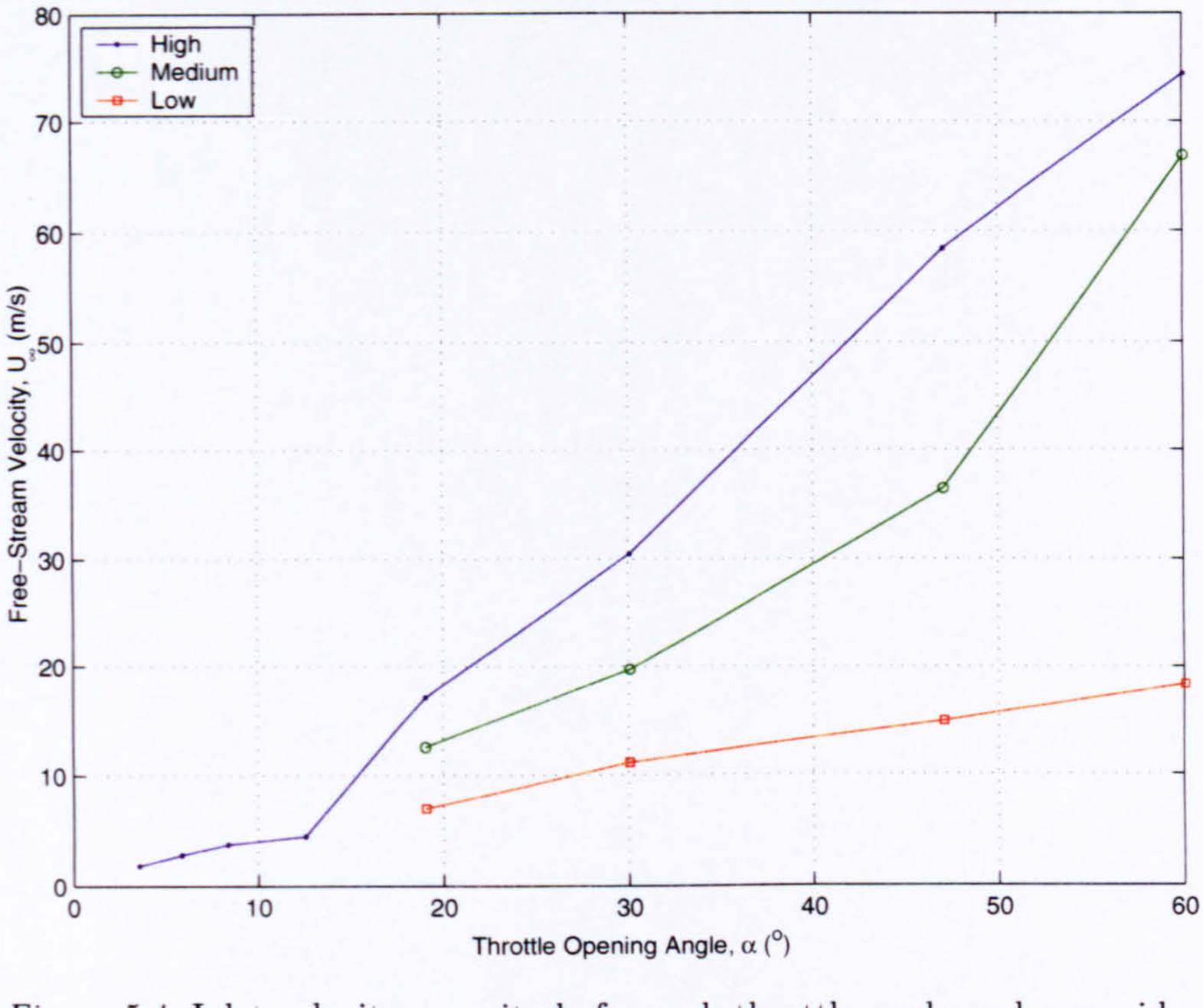

Figure 5.4: Inlet velocity magnitude for each throttle angle under consideration derived from the given mass-flow data and throttle inlet area. "High" represents the given data, "low", the linear extrapolation of the small angle flows, and "medium" the intermediate of these two extremes.

is less than 5% except for the slightly high reading at 3.5°; hence this is acceptable. Further, small changes in the flow velocity have been found to produce little change in the structure of the flow for a specific throttle angle, the change merely altering the magnitude of the measured quantities. Given the small change in velocities, no significant effect on the results has been observed.

Using the static-pressure drop across the valve, the static-pressure-loss coefficient (or pressure-drop coefficient) has been calculated as,

$$C_p = \frac{\Delta p}{\frac{1}{2}\rho U_\infty^2}. \tag{5.3}$$

The coefficient, C_p, represents the non-dimensional pressure drop across the valve and has been used in previous studies to evaluate butterfly-valve performance. Table 5.2 clearly shows a considerable difference in the pressure drop over the range of throttle

Throttle angle α (°)	Ideal velocity U_{ideal} (m s^{-1})	Measured velocity U_∞ (m s^{-1})	Pressure drop Δp (kPa)	Pressure coefficient C_p
3.5	1.8	1.83	31.51	15617.7
5.8	2.9	2.81	38.60	8114.7
8.3	3.7	3.76	19.76	2319.6
12.5	4.5	4.47	8.46	702.80
19.0*	7.5	7.0	7.09	240.25
19.0*	12.5	12.5	23.41	248.63
19.0	17.3	17.1	52.49	297.92
30.0*	10.1	11.1	2.00	26.89
30.0*	20.0	19.7	12.77	54.60
30.0	31.7	30.5	35.16	64.84
47.0*	15.3	14.9	0.00	0.00
47.0*	36.1	36.4	5.67	7.11
47.0	57.6	58.4	18.75	9.12
60.0*	18.0	18.3	0.00	0.00
60.0*	65.0	66.8	4.26	2.58
60.0*	75.0	74.4	7.80	2.34

Table 5.2: Pressure drop across the throttle valve for a range of angles and flow-rates. *-indicates measurements made at extrapolated flow rates.

angles investigated, with very large values of C_p for the small angle openings owing to the inversely proportional relationship between C_p and U_∞^2. This variation of C_p with throttle angle is plotted in Figure 5.5 that highlights the large losses at small angles and the subsequent asymptotic reduction at larger throttle openings. In this non-dimensionalised format the pressure drop over the valve can be readily compared to the results of previous studies, for example the work of Kimura et al. (1995), who investigated pressure losses through butterfly valves comparing computational predictions and experiments in a water tunnel. Although their work concentrates on cavitation prediction for a given valve shape, they also present data for the pressure drop through the valve with no cavitation. The trends predicted here match those of Kimura et al. (1995) well, with a considerable reduction in C_p as the valve is opened and values of C_p within 20% of those reported for angles in the range 30° through 60° (smaller angles were not presented). The authors do, however, describe a considerable increase in the value of C_p at the smaller angles owing to the reduced flow areas and the increased separation, and hence losses downstream of the valve. Similar agreement is also found with the work of Eom (1988) who evaluates the closed-valve blockage ratio for throttling control. A fair comparison can only be made with the smallest blockage ratio used and this again gives fair qualitative agreement for the larger opening angles. Quantitatively the results are not so well matched with values of C_p here reaching 400% of those reported by Eom (1988) over the limited comparison range. Despite the large percentage error, the values are still within an order of magnitude. For the smaller valve openings there is considerable disagreement with the work of Eom (1988) with predicted C_p approximately one order of magnitude higher. This large difference is brought about by the smaller blockage ratio of the valve used by Eom allowing considerable flow to pass at near closed positions. Similar results have been discussed in chapter 3.

Thus the results presented here appear qualitatively correct with the correct trends predicted; however qualitative agreement is worse as has been discussed. These differences stem from the dissimilar valve geometries and configurations used in previous studies, the influence of which can have considerable effect on the flow passing through

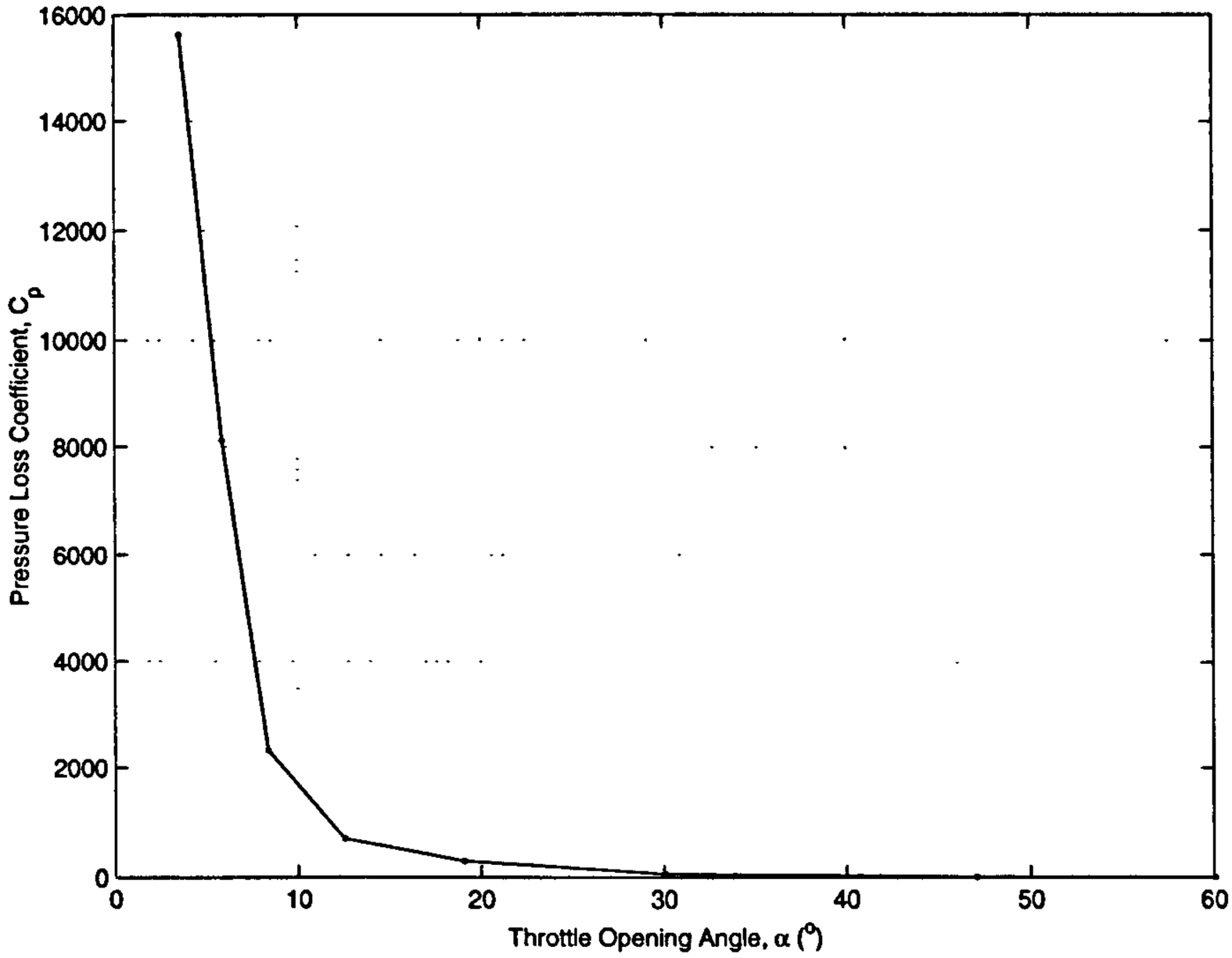

Figure 5.5: Measured static pressure-loss coefficient, C_p, for each throttle opening angle considered at the standard (high) flow-rate.

the valve (Cohn, 1951). In particular, the large discrepancy at small angles is a result of the valve of Eom (1988) having a smaller blockage ratio that the valve considered here. A full evaluation of trends is not possible here as the experiments have been restricted to the given flow rates and opening angles specified. To gauge a true representation of the flow, a range of flow rates needs to be considered for each throttle angle, the range of which would also need to be increased. Given the time required to perform an individual analysis, the measurements have been restricted to those presented in Table 5.2 above.

5.6.2 Hot-Wire Measurements

The remaining presentation of the experimental results concerns the measurements made with the hot-wire anemometry system, and these measurements are briefly outlined before the presentation of the results. Measurements have been made at the locations described previously, i.e. at the three measurement planes for two perpendicularly

aligned traverses, and two wire orientations. Measurements of the raw bridge voltage have been recorded over a five-second period and have subsequently been converted to meaningful information by calibration of the data using Kings Law (2.27). Initially the system was intended to capture only frequency content, thus requiring no calibration; however, the point velocity measurements have proved valuable to the investigation and hence a basic calibration has been carried out.

Calibration of the hot-wire probe has been performed using a TSI air-velocity calibration unit that consists of a nozzle with a probe mount situated downstream, thus providing a known controllable uniform jet of air in which to calibrate the probe. The unit provides the ability for calibration of multiple velocity components up to a maximum velocity of 150 m s^{-1}. In order to mirror the conditions of the experiment, the hot-wire probe and the sensing element were both orientated perpendicular to the flow direction for calibration. Although the probe stem presents increased blockage in this orientation, as discussed in chapter 2, the effects have not been accounted for here. The flow velocity at the sensing element is determined by measurement of the pressure drop across the nozzle and subsequent calculation of Mach number and the local speed of sound. These are found through the usual compressible flow equations described in equations (5.4) through (5.7) below. Note that STAR-CD uses a rearrangement of equation (5.5) for the calculation of pressure in compressible flow fields.

$$a_o = \left[\gamma R(T + 273.15)\right]^{1/2}, \tag{5.4}$$

$$\mathrm{M} = \left[2\,\frac{\left(\frac{p+\Delta p}{p}\right)^{\frac{\gamma-1}{\gamma}} - 1}{\gamma - 1}\right]^{1/2}, \tag{5.5}$$

$$a = \left[\frac{a_o^2}{1 + \left(\frac{\gamma-1}{2}\mathrm{M}^2\right)}\right]^{1/2}, \tag{5.6}$$

$$U = \mathrm{M}a. \tag{5.7}$$

Here, a_o is the speed of sound at stagnation conditions; a is the speed of sound at the measurement location; M is the Mach number; p is ambient pressure; Δp is the pressure drop across the nozzle; γ is the ratio of specific heats for air (1.4); and U is the mean jet velocity. For the average ambient conditions here, the speed of sound was found to be 343.3 ± 0.6 m s^{-1}(95%).

Calibration involves taking hot-wire measurements in the jet for a range of flow velocities, $0 \leq U < 150$ m s^{-1}. Measurements are made of the pressure drop using the manometer for small readings, and the Kulite transducer for the larger pressure readings, with the overlap adjusted for. Kings Law (equation (2.27)) has then been used to calibrate the data and the calibration coefficients have been found using the sum-of-error-squared method described in chapter 2 and the calculated values correspond closely to those suggested in the literature.

Using the calibrated probe, measurements have then been made in the flow domain and the signals analysed to extract the mean velocity magnitude; the turbulence intensity; the skew of the reading; the kurtosis (flatness) of the readings; and the frequency content of the flow. An estimate into the uncertainty has also been calculated using finite statistical methods, and these are presented with the results. These results are now presented for the small and large angle flow regimes respectively.

As the descriptions of the probe positions and orientations can be a little confusing they have been presented schematically in Figure 5.6. The figure shows the positioning for the symmetry plane measurements on the left, and the normal plane measurements to the right. In each case the hot-wire probe *body* is orientated perpendicular to the flow direction while the probe *sensing element*, or *wire*, is either orientated parallel or perpendicular to the mean flow direction.

5.6.3 Velocity Measurements at Small Throttle Valve Openings

Measurements in the Symmetry Plane

Time averages of the hot-wire signals have been made and these have been used to generate time-averaged velocity magnitude profiles across the domain. Evaluation of

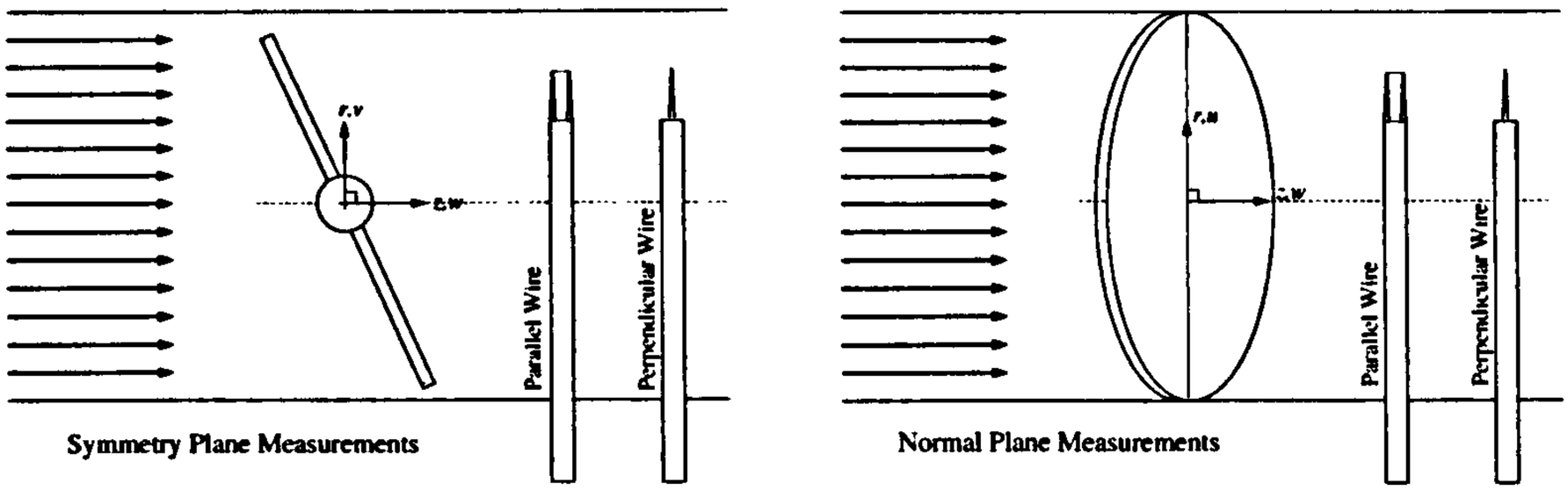

Figure 5.6: Schematic showing the orientation of the hot-wire probe and sensing element relative to the throttle body and mean flow direction. Symmetry plane measurements are represented to the left, and normal plane measurements to the right.

the profiles through the symmetry plane of the throttle valve (i.e. trailing edge to leading edge) show the basic structure of the flow is similar for each throttle angle investigated and the flow decays as it moves downstream of the valve. The profiles are shown in Figure 5.7 for a sensing element orientated perpendicular to the mean flow direction. Included in the figure are error bars that represent the uncertainty in the measurements for a 95% confidence level. This has been calculated based on individual instrument errors, calibration errors, and statistical analysis of each set of measured data. Note that error bars have not been shown for the position of the probe to aid clarity. The positional uncertainty is ± 0.46 mm across the span of the traverse for all flows.

The profiles indicate that high-energy jet-like flows exist downstream of the leading and trailing edges of the valve with a high axial-velocity gradient, $\partial w/\partial z$, generated between these high-energy flows and the surrounding low-energy flow to the centre of the domain. These free shear layers form as a result of separation from the valve tips and are found for each of the throttle openings considered. As the throttle valve is opened, the peak velocity magnitude at the leading-edge flow rises and this region becomes the dominant flow regime. In contrast, the flow originating from the trailing edge reveals little change in velocity magnitude over the range of throttle openings. The figure also reveals that the high-energy regions are diffused as the flow convects downstream, resulting in reduced velocity magnitude and thickening of the shear layers into the central domain.

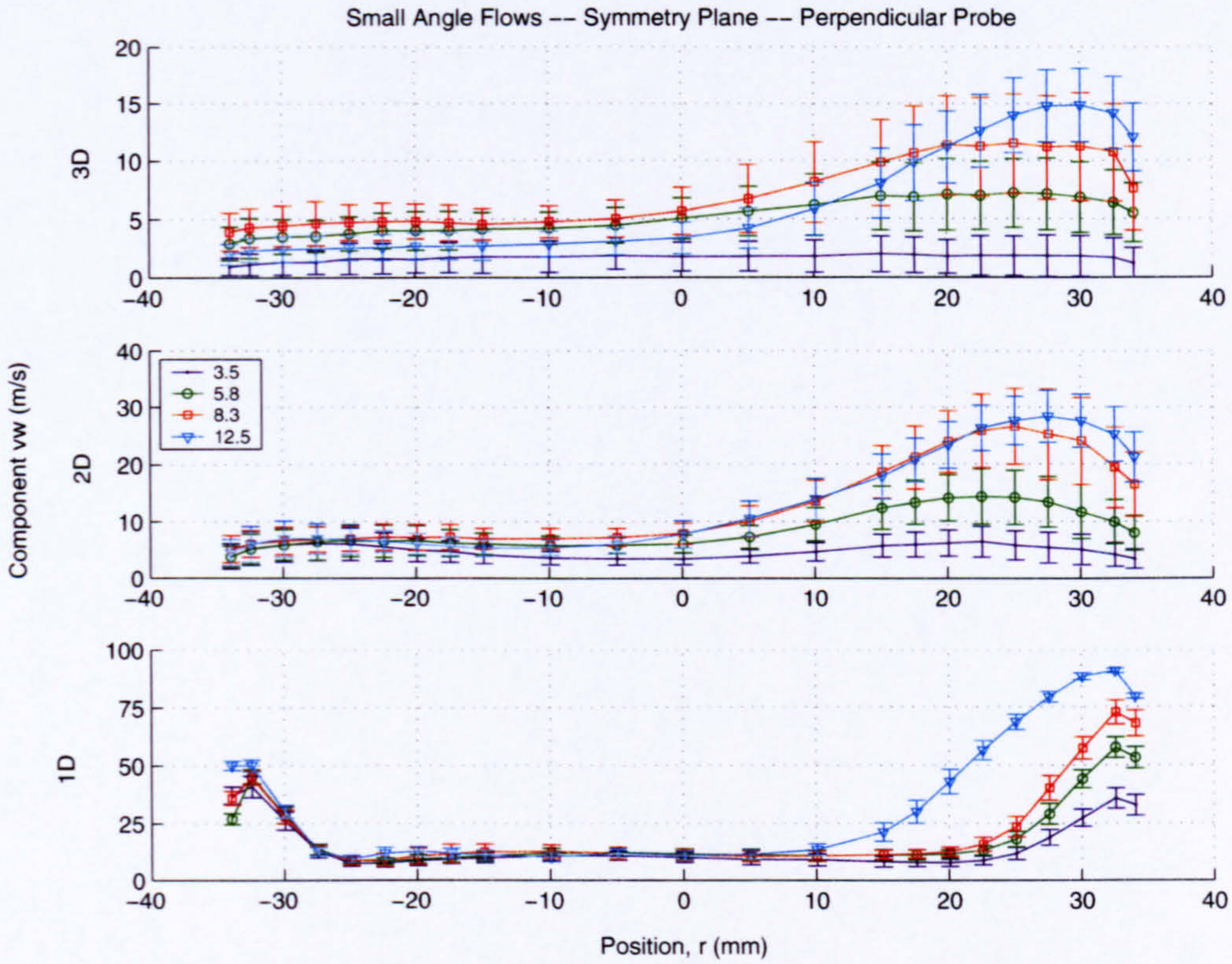

Figure 5.7: Velocity magnitude profiles for small throttle valve openings obtained with the HWA element aligned perpendicular to the mean flow direction, and a traverse through the valve symmetry plane. The profiles thus represent the combined components of the mean axial flow direction and the downwash over the valve. Positive values of position represent the leading edge side of the valve, and the plots represent from bottom, 1D, 2D, and 3D planes downstream from valve. Note the change in scale for the individual plots.

The trends are similar for each flow except that at a throttle angle of 12.5°, for which the leading-edge flow maintains its distinctive peak as it moves downstream and reduced diffusion into the surrounding flow is observed in comparison to the other angles. For the smallest throttle opening, 3.5°, an almost symmetric profile is observed stemming from the near-symmetric geometry of the valve at this angle. For this case, the flow passing the leading edge is quickly dissipated such that by the time the flow reaches the 3D measurement plane it is no longer distinguishable from the low-energy flow in the centre of the domain. Over this distance, the peak velocity is observed to reduce to approximately 6% of that at the 1D measurement plane, in comparison to values of 13%, 16%, and 17% for the remaining flows at 5.8°, 8.3°, and 12.5°. Even by the 2D

measurement plane the flow is noticeably dissipated with a reduction in peak velocity to 17% of that at the 1D plane, while the remaining flows show reduced loss with peak magnitudes of 27%, 37%, and 31% of their value at the 1D plane.

Over the same range of throttle opening angles, the rate of diffusion of the leading-edge flows also varies. For the smallest angles, where the initial energy is reduced, diffusion is more apparent with the shear layer showing considerable thickening leading to the flat profiles found at the 3D measurement plane. For the largest openings, the level of dissipation is reduced with the bulk leading-edge flow still apparent at the far (3D) plane. At this point the sharp leading-edge profile of the 1D plane is observed to have increase in width by approximately 250%.

In contrast, flow passing the trailing edge of the valve shows less variation between the different opening angles with similar structure maintained as the flow moves downstream. Diffusion of the flow into the surrounding flow is, however, still apparent with a 90% reduction in velocity magnitude at the 2D plane and considerable spread of the flow such that by the 3D measurement plane is no longer distinguishable from that of the central domain.

Comparison to the CFD predictions of velocity-magnitude contours and velocity vectors on the symmetry plane (Figure 3.4) reveals that the flow remains predominantly uni-directional in the vicinity of the wall. Thus with the probe element orientated perpendicular to the flow, the dominant velocity component being recorded is the axial component. Hence the peak velocity magnitude readings should give a fairly good indication of the peak velocity near to the walls of the domain. As the probe is moved away from the wall, an increasing component of downwash is experienced by the sensing element and thus the readings become more ambiguous. CFD predicts that for the smaller flow angles an increased level of reversed flow exists downstream of the valve and at the 1D plane there exists a high component of downwash over the probe element. This has also been predicted by previous numerical simulations (Chen & Chen, 1995; Launder & Spalding, 1974), and observed in previous experimental investigations (Addy et al., 1985; Heywood, 1988; Morris, 1987). Here, evaluation of Figure 5.7 reveals a very

slight increase in velocity magnitude just central of the trailing edge that arguably corresponds to regions of reversed flow as predicted by the CFD. This is reflected by the marginal increase in measurement uncertainty in this region compared to that of the central domain.

Overall, the measurement uncertainty is similar for each throttle angle considered, and each flow shows a similar trend with increased uncertainty in the higher-energy flow toward the leading-edge side of the domain. The range of uncertainty for each measurement is similar at each location for each angle, and reduces marginally downstream. However, the relative uncertainty when taking into account the mean velocity shows greater variation and is more significant at small throttle openings. For the smallest angles, close to the valve, the uncertainty in measurement varies between 10% and 25% depending on position, whilst further from the valve, these values rise significantly to 60% and 80%. For the largest angle shown in Figure 5.7 (12.5°) this reduces to between 30% and 40% far from the valve.

In order to gain further understanding of the flow it is useful to present the measurements made with the probe element aligned parallel to the flow direction. These profiles are presented in Figure 5.8.

With the sensing element orientated parallel to the flow direction the measurements should theoretically be most sensitive to the cross-flow (out of plane) and downwash components of the flow with the axial component having an insignificant effect. Note, however, that the measurements record velocity magnitude and do not discriminate between velocity components and therefore the measurements give no indication of the relative level of downwash or cross-flow. Given that the measurements are made in the symmetry plane of the valve and are time-averaged values, the cross-flow component of the flow should average out to zero (assuming the flow behaves as predicted) and thus theoretically the measurements give an indication of downwash alone.

Comparing the profiles of Figure 5.8 to those of Figure 5.7 reveals similar trends. Shear layers are observed originating from the valve tips that have a high velocity gradient at the 1D measurement plane and subsequently diffuse further downstream.

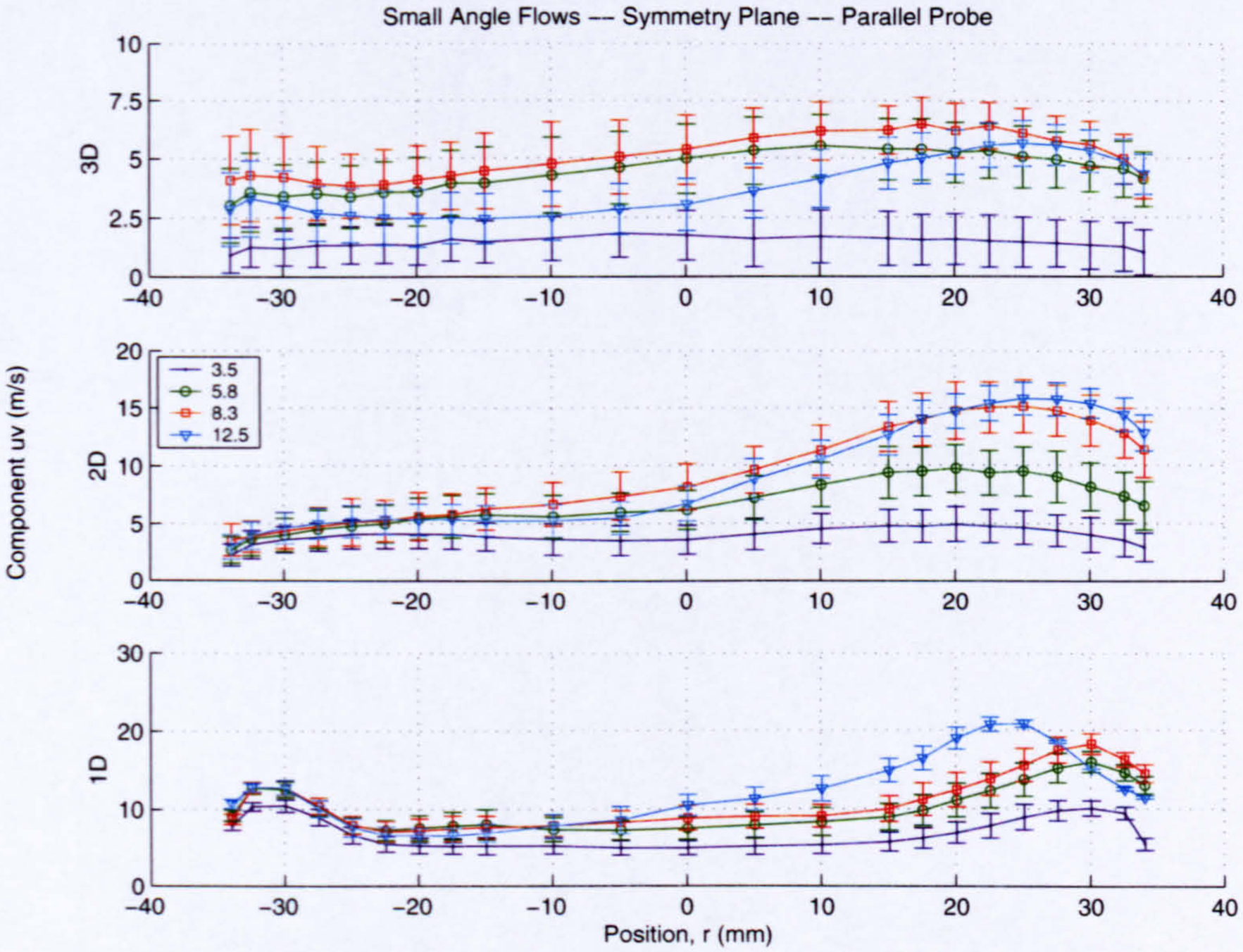

Figure 5.8: Velocity magnitude profiles for small throttle valve openings obtained with the HWA element aligned parallel to the mean flow direction, through the valve symmetry plane, for the flows of Figure 5.7.

Other similarities include the dominant leading-edge flow structure close to the valve, highly symmetry flows for the 3.5° throttle opening, and a greater level of asymmetry for the 12.5° opening. The latter imbalance of the leading edge and trailing edge wakes is brought about by the large change in flow geometry of the valve at the larger angle.

The fairly strong leading and trailing edge flows are unexpected with the hot-wire probe in this orientation as this suggests a strong component of downwash exists in immediate proximity to the wall where is would be expected at the centre of the domain. Comparisons indicate that the peak velocity magnitudes recorded with the parallel probe (Figure 5.8) are more central in the domain than those recorded with the perpendicular probe (Figure 5.7), suggesting there is increased downwash at the edge of the shear layers.

Comparison of the experimental measurements to the computational predictions

of in-plane velocity vectors through axial planes downstream of the valve (Figure 3.11) reveals that the maximum predicted downwash lies central to the domain. This therefore suggests that either the CFD is over-predicting the level of downwash, perhaps through increased diffusion of the flow, or that the hot-wire probe is mis-aligned. Given the fairly inaccurate methods of the experimental set-up, the latter is believed to be the main cause of the discrepancy although increased diffusion of the computational model will also play a role. These findings will be discussed in more detail in chapter 6.

Measurements Normal to the Symmetry Plane

Flows in the plane normal to the symmetry plane at the level of the valve pivot have a considerably reduced velocity magnitude, owing to the reduced influence of the high-energy flows passing the leading and trailing edges of the valve. Trends are similar to the results presented previously with the flow through the valve open at 3.5° having a very flat profile in comparison to the other flows, and the flow at 12.5° showing significant deviation of the velocity profile from those at smaller valve openings. Figure 5.9 shows the profiles for a sensing element aligned perpendicular to the mean flow direction for each of the small throttle angles investigated. Note that for these profiles, the measurements have been made for one half of the domain alone and these have been mirrored to generate the full profile. This is partially justified as any asymmetric flow features should be removed from the recorded measurements by the time-averaging process. The number of measurement locations across the domain is reduced in comparison to those made across the symmetry plane presented previously.

At the 1D measurement plane each of the velocity profiles remains fairly flat with the exception of the profile for the 12.5° opening that exhibits particularly high velocity magnitude toward the wall of the domain. This suggests a considerable increase in the energy of the flow in comparison to the smaller-angle flows where the flows are more readily dissipated by the viscous dominated wall flows. The profiles for the three smaller angle flows are all very similar with little change in profile shape or velocity magnitude.

As the flow moves downstream the profiles change more noticeably, with the two

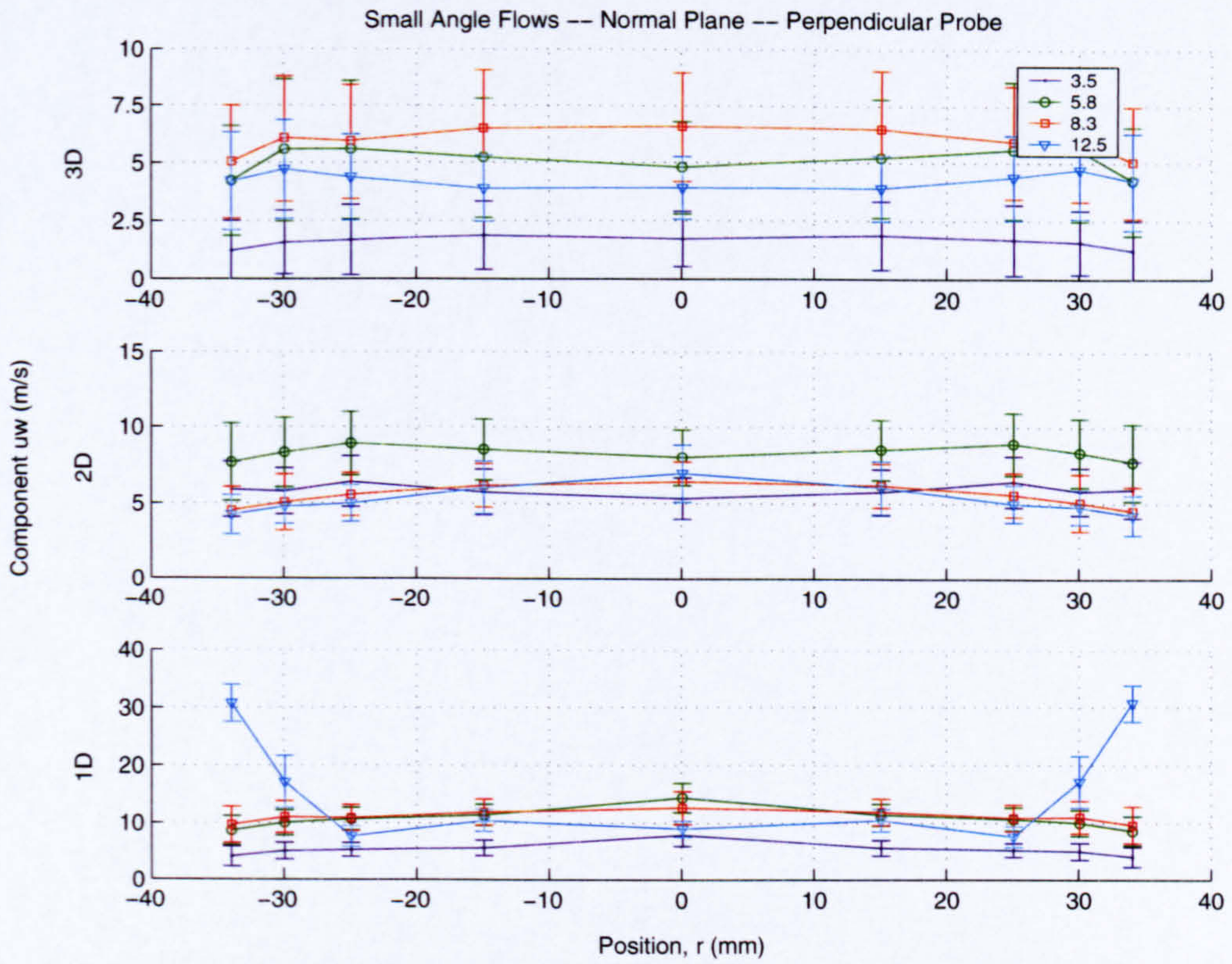

Figure 5.9: Velocity magnitude profiles for small throttle valve openings obtained with the HWA element aligned perpendicular to the mean flow direction, and a traverse normal to the symmetry plane at the level of the valve pivot. From bottom: 1D, 2D, and 3D planes downstream from valve. Note change in scale.

smallest angle flows (3.5° and 5.8°) exhibiting a drop in velocity magnitude in the centre of the domain whilst the profiles for the two larger valve openings (8.3° and 12.5°) maintain an elliptic profile with central peak. The high-energy "jetting" of the flow around the valve sides observed for the 12.5° opening at the 1D measurement plane is rapidly dissipated and is no longer apparent by the 2D measurement plane. CFD predictions also show this high-energy flow is generated downstream of the valve and then subsequently dissipated as it moves downstream. The elliptic profiles indicate a uni-directionally aligned flow structure downstream of the valve because for a reversed flow a dip in the profile would be observed that corresponds to traversal of the probe through a region of reversed flow.

Uncertainty in the readings remains fairly consistent across the domain and for each

of the flows, but again the relative uncertainty is much greater far from the valve where mean velocities are much smaller. At the 3D plane the uncertainty reaches 90% for the 3.5° opening and lies between 40% and 50% for the remaining flows. Such high levels of uncertainty brings into question the quality of the low-velocity measurements.

Velocity profiles for a sensing element aligned parallel to the mean flow direction are depicted in Figure 5.10, again for a traverse normal to the symmetry plane. The hot-wire is now most sensitive to the downwash and cross-flow components of velocity and provided the CFD prediction of the large-scale axial vortices is correct, the velocity profiles should be well defined with clear maxima and minima present in the traces.

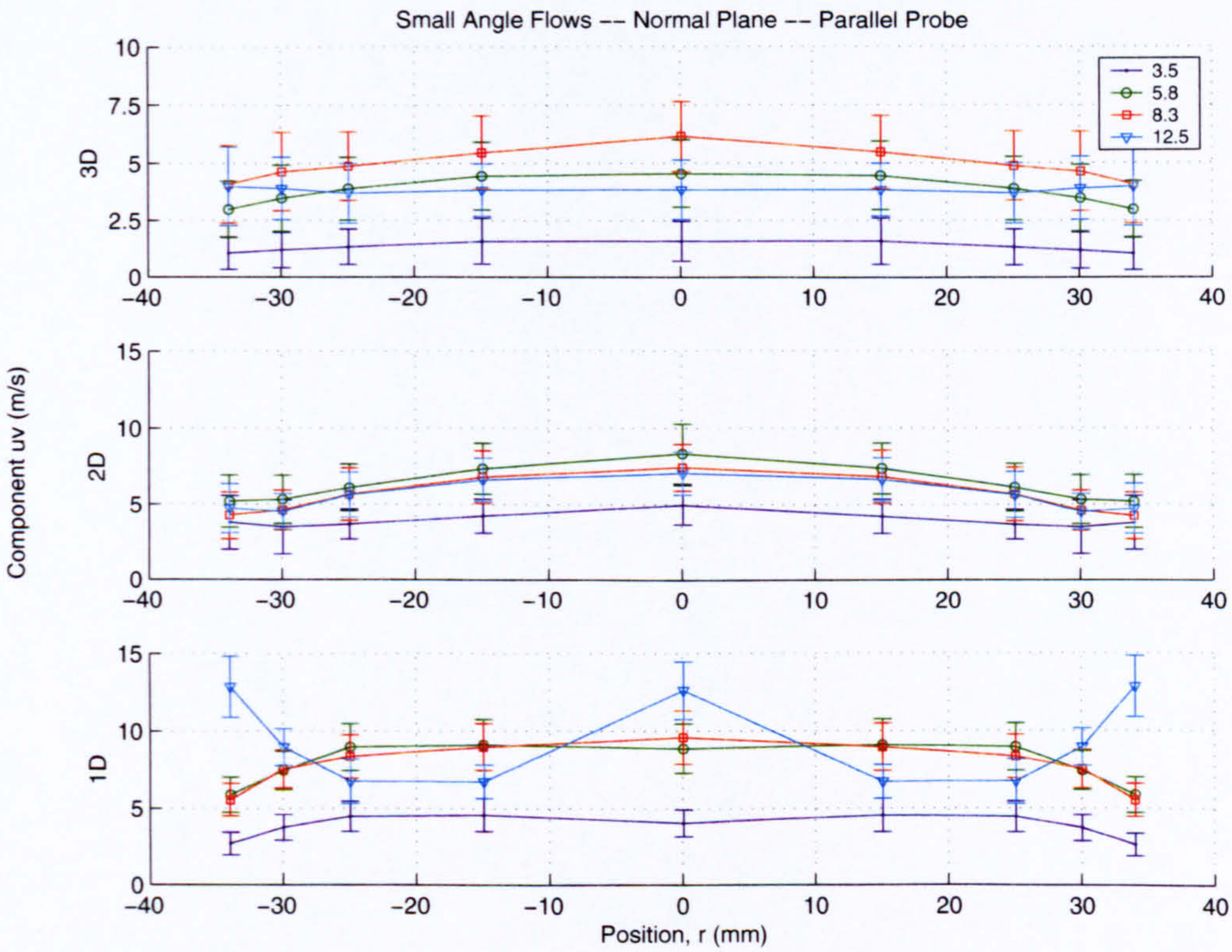

Figure 5.10: Velocity magnitude profiles for small throttle valve openings obtained with the HWA element aligned parallel to the mean flow direction, and a traverse normal to the symmetry plane at the level of the valve pivot. Flows correspond to those of Figure 5.9.

However, the figure shows fairly similar profiles to those for the perpendicular orientation with only slight differences. At the 1D measurement plane the 12.5° flow again

shows considerably higher velocity magnitude at the walls that is associated with the jetting of the flow as it passes from between the valve and throttle walls. The velocity magnitude then reduces away from the wall before rising again at the centre of the domain that agrees well with the computationally predicted flows. The latter profile is an indication of a classic twin-vortex system with the vortex cores represented by the low-velocity regions to either side of the central domain. Towards the walls, the measurements show high velocities corresponding to the outer, high-speed, vortex structure, with the central rise in velocity magnitude corresponding to the upwash generated by the action of the vortices.

Examination of the other small-angle profiles at the 1D measurement plane (Figure 5.10) reveals profiles that differ from that found at the 12.5° opening. A gradual rise in the velocity magnitude from the wall is observed with very flat or slightly elliptic profiles formed. Close examination shows that a slight reduction of magnitude is found at the centre of the domain for the flows through the valve open at 3.5° and 5.8°, while a slight rise is observed at 8.3°. Thus the velocity profiles of the flow at smaller openings reveal little in the way of flow structure, nor do they show evidence of a classic vortex structure. The figure also shows that the levels of uncertainty are similar to those for perpendicular wire measurements.

Measurements made further downstream show reduced velocity magnitude, and the profiles become more similar with the elliptic form dominating that suggests a steady, predominantly uni-directional flow is present. No evidence exists of a vortex structure at these locations. This may again be down to mis-alignment of the probe causing the axial component of the flow to drown out the cross-flow and downwash components of the flow. CFD predictions have shown that the axial component of the flow in the far wake of the valve is far greater then the in-plane components and hence only a small influence may be necessary to mask the signals.

5.6.4 Large Throttle Valve Openings

Measurements in the Symmetry Plane

The velocity profiles for the flows through the valve at larger throttle angles are now presented and discussed. Figures 5.11 and 5.12 show the velocity-magnitude profiles for the flow through throttle openings of 19°, 30°, 47°, and 60°, for a sensing element aligned perpendicular and parallel to the mean flow direction respectively. The error bars in the figures again represent the uncertainty in the measurements with 95% confidence.

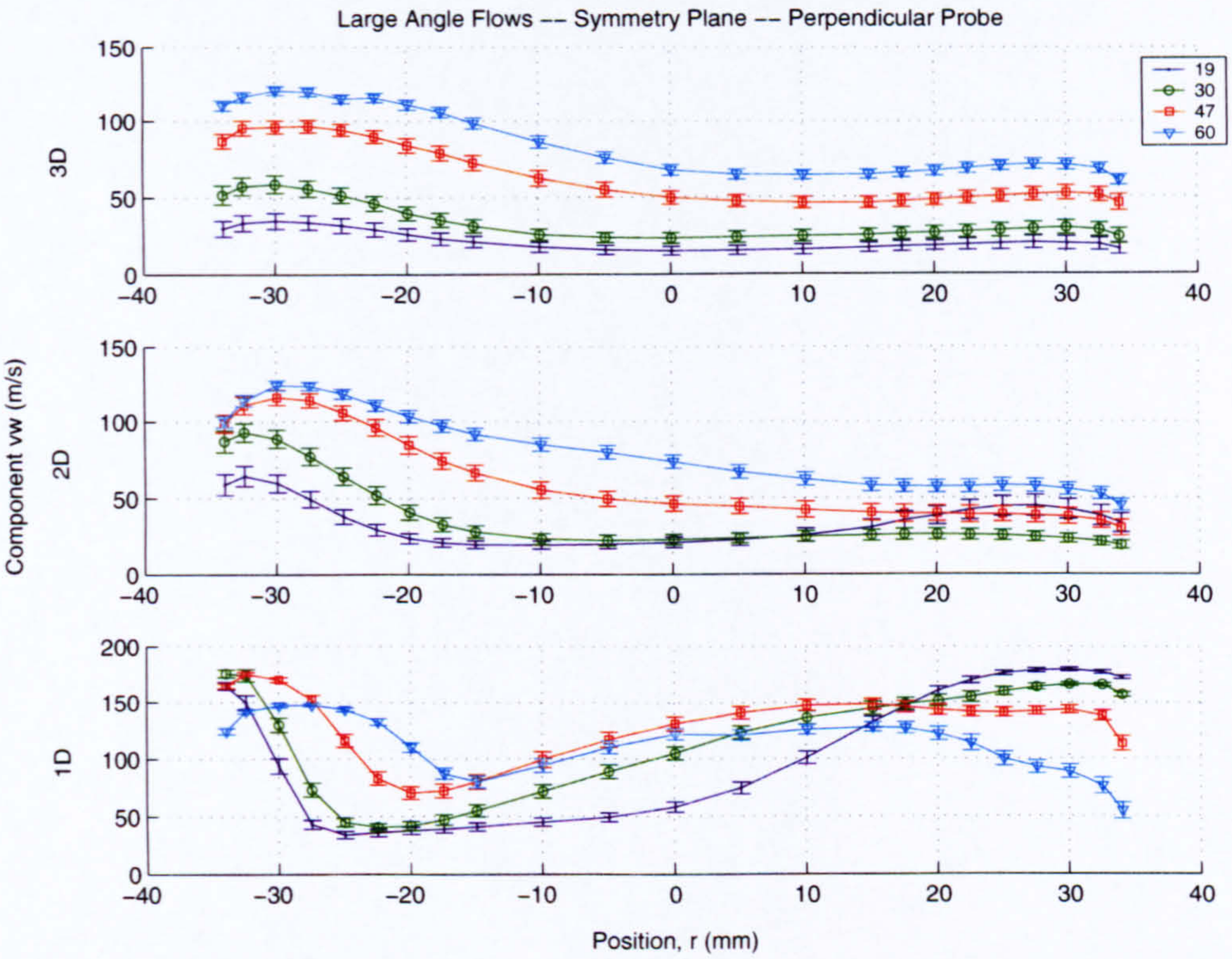

Figure 5.11: Velocity magnitude profiles for large throttle valve openings obtained with the HWA element aligned perpendicular to the mean flow direction, and a traverse through the symmetry plane of the valve. From bottom: 1D, 2D, and 3D planes downstream from valve. Note change in scale.

On evaluation of the perpendicular profiles of Figure 5.11 it is immediately apparent that the flows show marked differences to those at the smaller valve openings with a the dominant flow features reversed. The dominant flow feature is now the trailing-edge flow that now appears similar to the leading-edge flows of the smaller valve openings

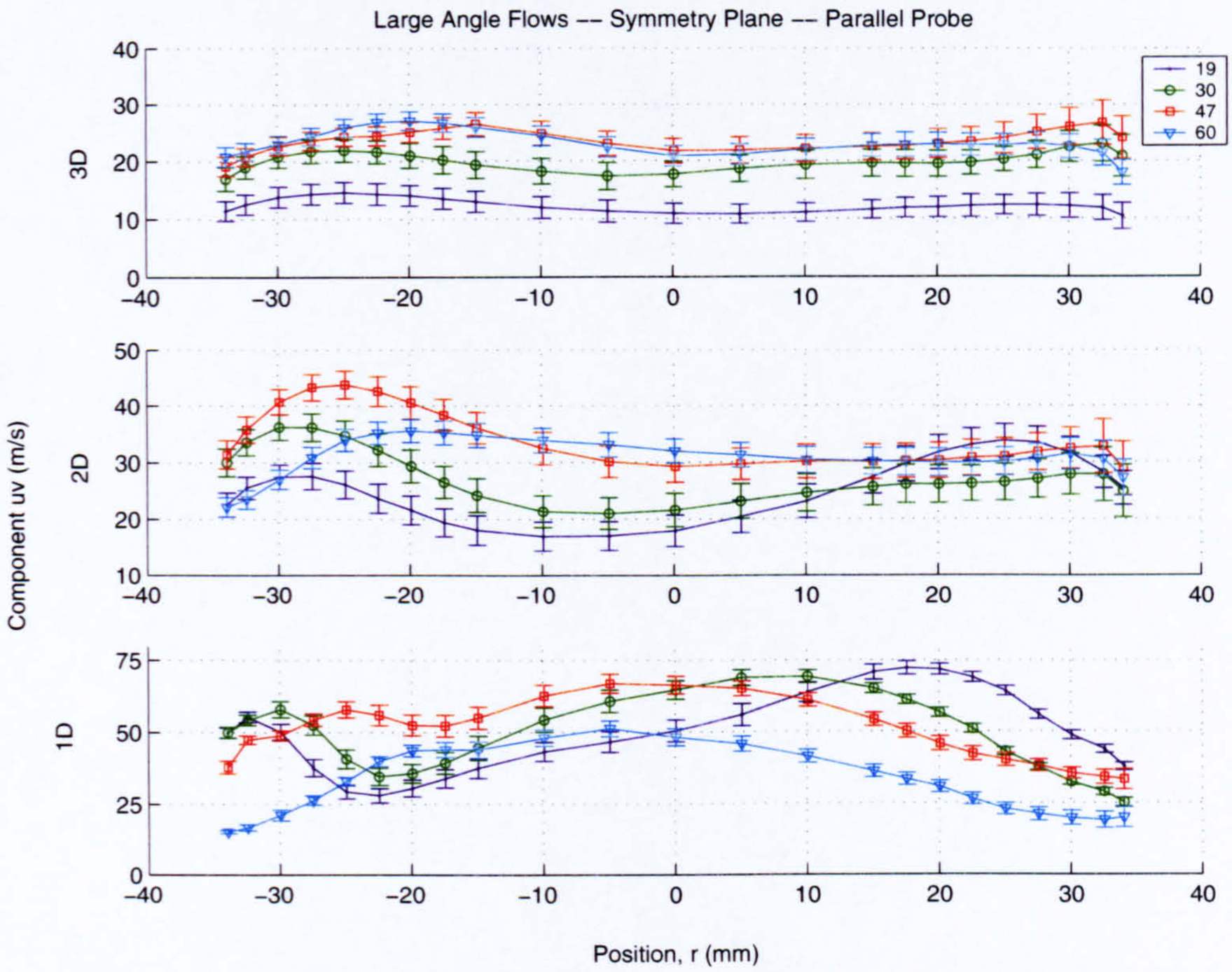

Figure 5.12: As Figure 5.11 with the sensing element parallel to the flow direction.

with a high-energy jet-like flow present close to the wall forming a shear layer to the flow in the central domain. Flow past the valve leading edge is less distinct with a much flatter profile and considerable diffusion of the flow apparent downstream. CFD predictions show that at these larger openings the leading-edge flow is swept down into the central domain, which leads to rapid diffusion of the high-energy flow. This corresponds well to the increased thickness and reduced magnitude of the leading-edge velocity profiles.

Of further note is that the leading-edge profiles swap their order of peak velocity magnitude moving downstream. At the 1D measurement station closest to the valve, the flow through an opening of 19° exhibits the largest velocity magnitude with a somewhat more distinctive peaked region toward the wall. The remaining flows are ranked in reverse order, thus the flow at the largest opening (60°) shows the lowest velocity magnitude and a flatter profile. Moving downstream the flow order now reverses with

the 19° angle flow showing the smallest velocity magnitude and the flow through a valve at 60° the highest. This reflects the geometric differences between the throttle at these angles that undergo considerable change. At 19° the valve still presents considerable blockage to the flow with only 9% of the cross-section available for the flow to pass though, in contrast to the 60% area available at an opening of 60°. The smaller opening angle presents a more aggressive geometry to the flow and hence separation is more severe and resembles the smaller-angle throttle opening flows shown previously. The reduced area accelerates the flow through the gap leading to the formation of the high-energy separated jet and subsequent expansion downstream.

The geometric change is also apparent in the trailing-edge flow where the convergent nature to the geometry gently accelerates the flow and a smooth separation exists at the trailing edge. Peaks in the trailing-edge velocity profile reflect the extent of the opening with the 19° flow exhibiting a much narrower high-energy region than that of the larger openings that typically show a wider velocity profile with a less peaky magnitude. Note that the peak velocity magnitudes vary little at the 1D measurement plane, and this is a consequence of the change in flow rate for each case balancing out the change is flow area. Moving downstream reflects on the reduced energy of the system with the reduction of the velocity magnitude.

Differences are also found in the levels of uncertainty at the larger throttle openings with a greater absolute range of uncertainty but significant reduction in the relative uncertainty. At the 2D and 3D measurement planes the level of uncertainty remains consistent across the domain for each throttle angle with the relative uncertainty approximately 20% at 30°, and 5% at 60°. This proves considerably lower than the levels found at the small throttle openings. At the 1D plane, greater differences in the level of uncertainty are observed, however, the general trend is a reduction in uncertainty toward the wall where the flows appear more uniform.

Measurements made with the element orientated parallel to the mean flow direction (Figure 5.12) reveal similar, but less distinct, trends in the flows, again suggesting influence of the axial-velocity component on the measurements, perhaps through mis-

alignment of the probe. The flows indicate a fair degree of downwash close to the leading edge of the valve and a much smoother flow further downstream where the dominant flow features are less apparent. Further conclusions are not drawn at this stage owing to the ambiguity of the readings.

Measurements Normal to the Symmetry Plane

Measurements across the valve for the large angle flows show much more distinct flow profiles than those of the smaller-angle flows presented previously. Figures 5.13 and 5.14 show the measured profiles for a cross-flow traverse using perpendicular- and parallel-aligned sensing elements respectively. The plots show that the two orientations capture very similar profile shapes and that the profiles for each flow angle are also found to be similar at each measurement location.

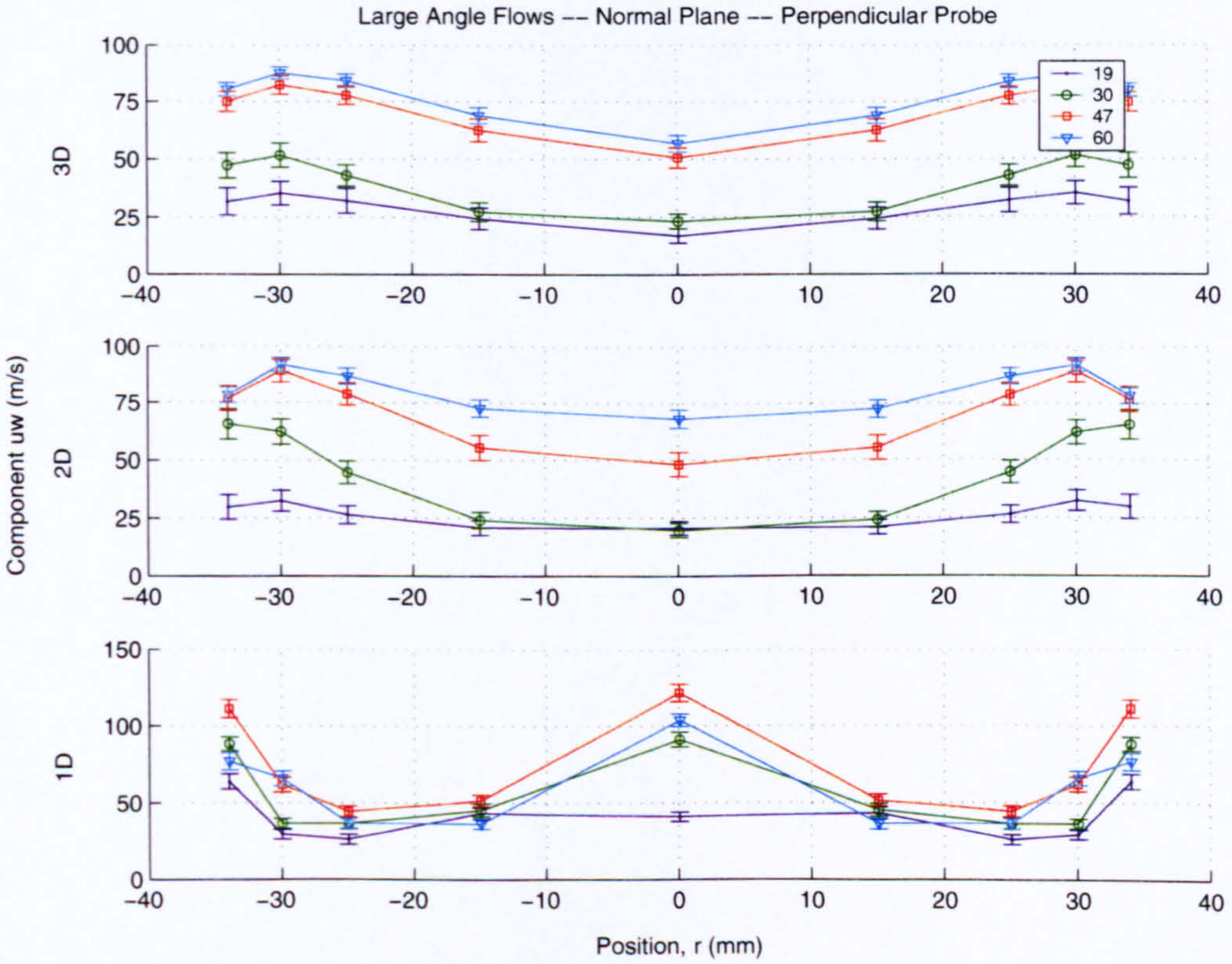

Figure 5.13: Velocity magnitude profiles for large throttle-valve openings obtained with the HWA element aligned perpendicular to the mean flow direction, and a traverse normal to the symmetry plane at the level of the valve pivot. From bottom: 1D, 2D, and 3D planes downstream from valve. Note change in scale.

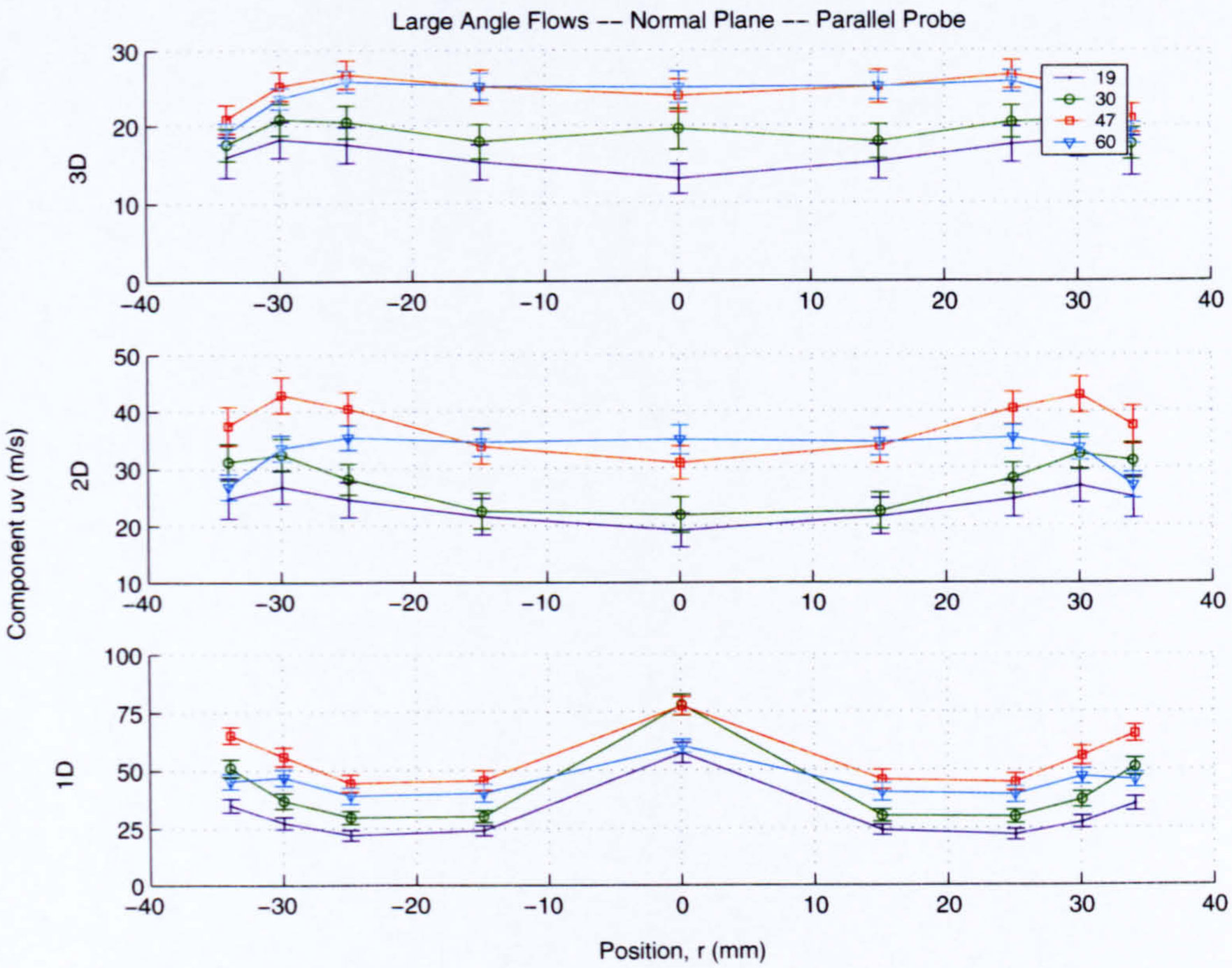

Figure 5.14: Velocity magnitude profiles for large throttle valve openings obtained with the HWA element aligned parallel to the mean flow direction, and a traverse normal to the symmetry plane at the level of the valve pivot. Labels and flows correspond to those of Figure 5.13.

At the 1D measurement plane, for each of the flows considered, both element orientations show a high velocity magnitude at the walls and the centre of the domain that corresponds to the classic vortex structure discussed previously. However, the readings indicate that the central high-energy region is dissipated for all flows by the 2D measurement plane. Comparison to the plots of the CFD predictions reveals that the velocity gradient across the vortices is considerably reduced as the flow moves downstream, with the axial flow being the dominant component. Thus the reduction in central peak and flattening of the profiles correspond well with this. Higher velocities are also predicted at the walls than in the central domain by the computation as a result of the vortices creating a smaller flow area close to the walls that accelerates the flow. This is reflected in the profiles shown in the figures. Further discussion and comparison of the results is

presented in the following chapter.

5.6.5 Turbulence Intensity Measurements

Measurement of the turbulence intensity, Ti, (equation (5.1)) downstream of the throttle valve shows variation of Ti with downstream location, position across the domain, throttle opening angle and mean flow velocity. Values of Ti vary mostly with the position downstream of the valve where increased intensity is observed as the flow moves downstream. It is noted that the large-angle throttle flows have reduced turbulence intensity compared with the smaller-angle flows throughout the downstream wake and a significant step is observed between the two regimes. The measurements are therefore presented separately.

Figure 5.15 shows the turbulence intensity measurements measured across the domain at the 1D, 2D and 3D measurement planes for the small-angle flows. With the throttle body present, the levels of Ti close to the valve are similar to the maximum values recorded with no throttle body present (see Table 5.1). Close to the valve the flows shows increased three-dimensional structure and mixing, giving rise to variations in turbulence intensity across the domain and less variation downstream where the flow is more settled. Despite the variation across the domain, the overall values of Ti at any one point are fairly similar and the general shape of the profiles is also similar.

Further downstream, the levels of Ti are again similar and the recorded profiles are more similar than those close to the valve. Of note is that the elliptic shape of the profiles at the 1D plane is reversed at the 2D plane with the central core showing reduced levels of Ti. At the 3D plane the distributions of Ti across the domain have flattened out considerably although overall levels of turbulence have increased. Values for the 3.5° flow show unusually large values at this station when compared to the other angles. The results suggest there is a trend for the higher throttle openings to generate reduced levels of turbulence; however, the latter high values seem excessive.

Typical of a wall-bounded flow is an increase in turbulence intensity toward the wall with a sharp drop in the immediate vicinity of the wall owing to the viscous action of

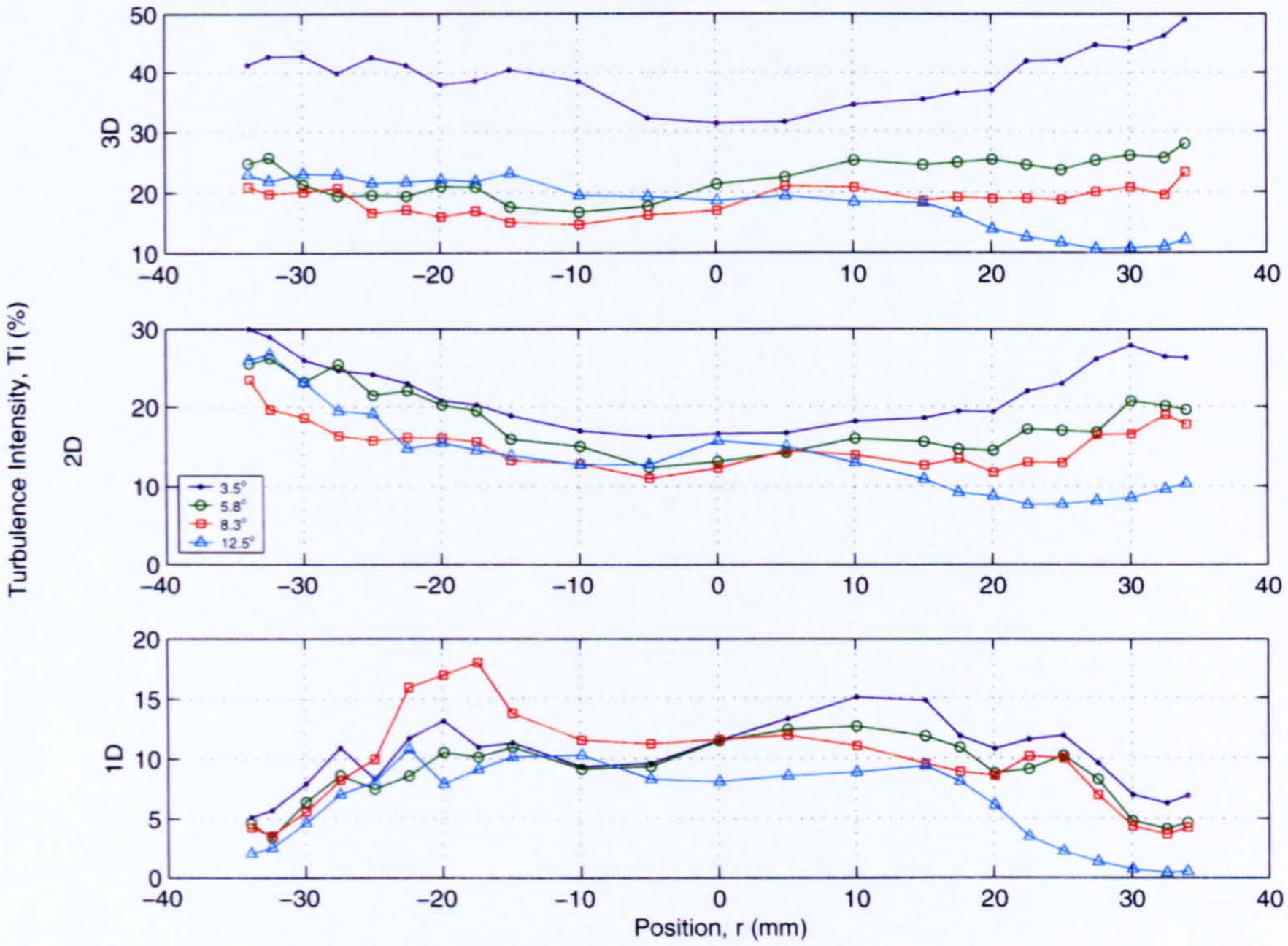

Figure 5.15: Variation of the turbulence intensity downstream of the throttle valve for small-angle flows. Values are shown as a percentage and the plots show from bottom to top the measurements at the 1D, 2D and 3D planes.

the boundary layer damping the flow fluctuations (Tritton, 1988). This phenomenon is, perhaps, indicated by a slight rise in Ti at the wall being observed for some of the flows. However, there are insufficient measurement points close to the wall to fully resolve the flow profile and hence confirm this. In addition, the near-wall measurement lies 1 mm from the wall and therefore the attenuation of the velocity fluctuations would not be fully captured.

For the large-angle flows the trends are a little different although similarities still exist as is shown in Figure 5.16. At the 1D measurement plane there is again a larger variation in the level of Ti than found further downstream, and the values here are found to be the lowest overall. For these flows there appears to be a biasing of the values towards the trailing-edge side of the domain that corresponds to the regions of low velocity adjacent to the shear layer shed from the valve. Absolute values of turbulence

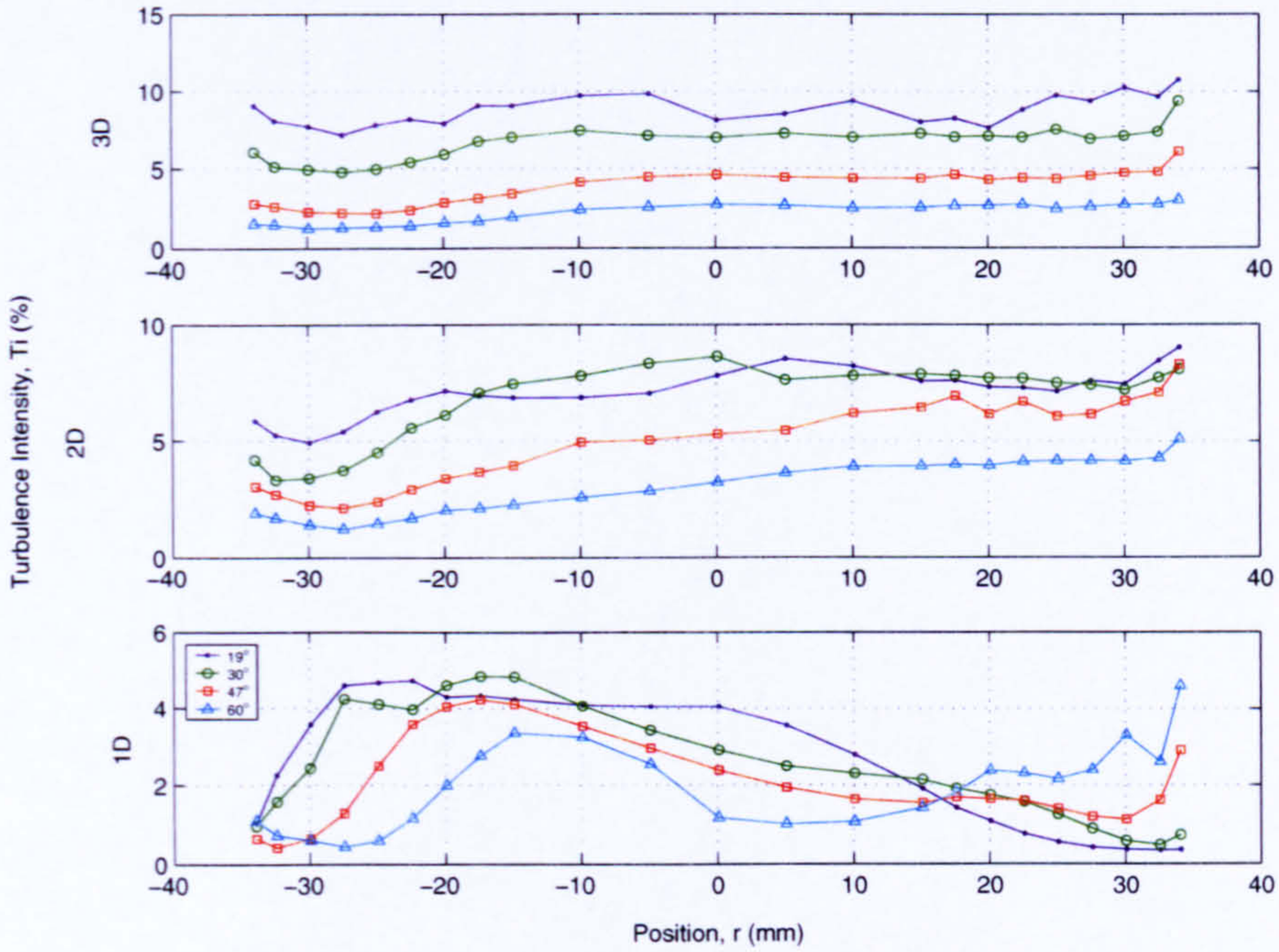

Figure 5.16: Variation of the turbulence intensity downstream of the throttle valve for large-angle flows. Values are shown as a percentage and the plots show from bottom to top the measurements at the 1D, 2D and 3D planes.

intensity are again similar across the domain despite the variation. As the flow moves further downstream the level of turbulence intensity increases and the distributions flatten out. These trends are partially reflected by the levels of uncertainty shown in the measurements. The large-angle flows show a larger variation in the measurements and increased overlap in comparison to those made for the smaller-angle flows.

The measurements of the small- and large-angle flows suggest that the mean flow rate is the main contributor to the levels of Ti in the flow. Equation 5.1 shows an inversely proportional relationship between Ti and U, the mean velocity, and hence this hypothesis holds true. Examination of the Ti distributions show that an increased local velocity, stemming from the local flow accelerations around the valve, corresponds to reduced levels of turbulence intensity at the same location. This is more noticeable close to the valve and the increased turbulence intensity downstream is a consequence of the reduced local velocity. Thus the observed increase in Ti for a reduced flow angle is a reflection of the mean flow-rate through the valve as opposed to a direct consequence

of the change in flow geometry. The limited number of additional flow rates considered here (see Figure 5.4, and Table 3.2) show that for a fixed throttle angle, an increase in flow rate coincides with a reduction in turbulence intensity. Hence this leads to the hypothesis that the flow rate is the governing contributor to turbulence-intensity levels in the flow. This is confirmed by evaluation of two cases of different throttle angle where similar flow rates exist. Levels of turbulence intensity were found to be similar in such a case with little change in profile shape brought about by the differences in flow geometry.

Quantitatively the mean values of turbulence intensity also reflect these findings, and these values are presented in Figure 5.17. The distinction between the small- and large-angle flows becomes immediately apparent with the smaller-angle flows having a considerably greater level of turbulence intensity. A near-linear variation of Ti with opening angle is observed at the larger throttle openings although this is owing to the scale of the plot and an asymptotic distribution is actually observed with values of Ti reaching levels close to the background levels found in the system as the valve is opened further. The plot also reveals the increase in turbulence as the flow moves downstream, with only the flows at 47° and 60° showing dissipation of turbulence levels at the 3D measurement plane.

The experimental measurements have shown that a fair spread exists in the level of turbulence intensity in the wake downstream of the throttle valve for the throttle angles considered. For the CFD to fully reflect this, each case would need to be set up based on the levels of intensity found for each flow thus leading to a large variation in the boundary conditions used. The level of Ti is, however, fairly similar for each flow therefore reducing the variation in mean values. This, and the fact that the CFD reflects the Ti levels found in the base system, which have been shown to be similar to those close to the valve, justifies the boundary conditions used.

The variation in the recorded values of Ti suggests that the mean velocity measurements may be adversely affected by the change in flow quality. This is briefly considered in the following section that investigates the statistical bias of the signals.

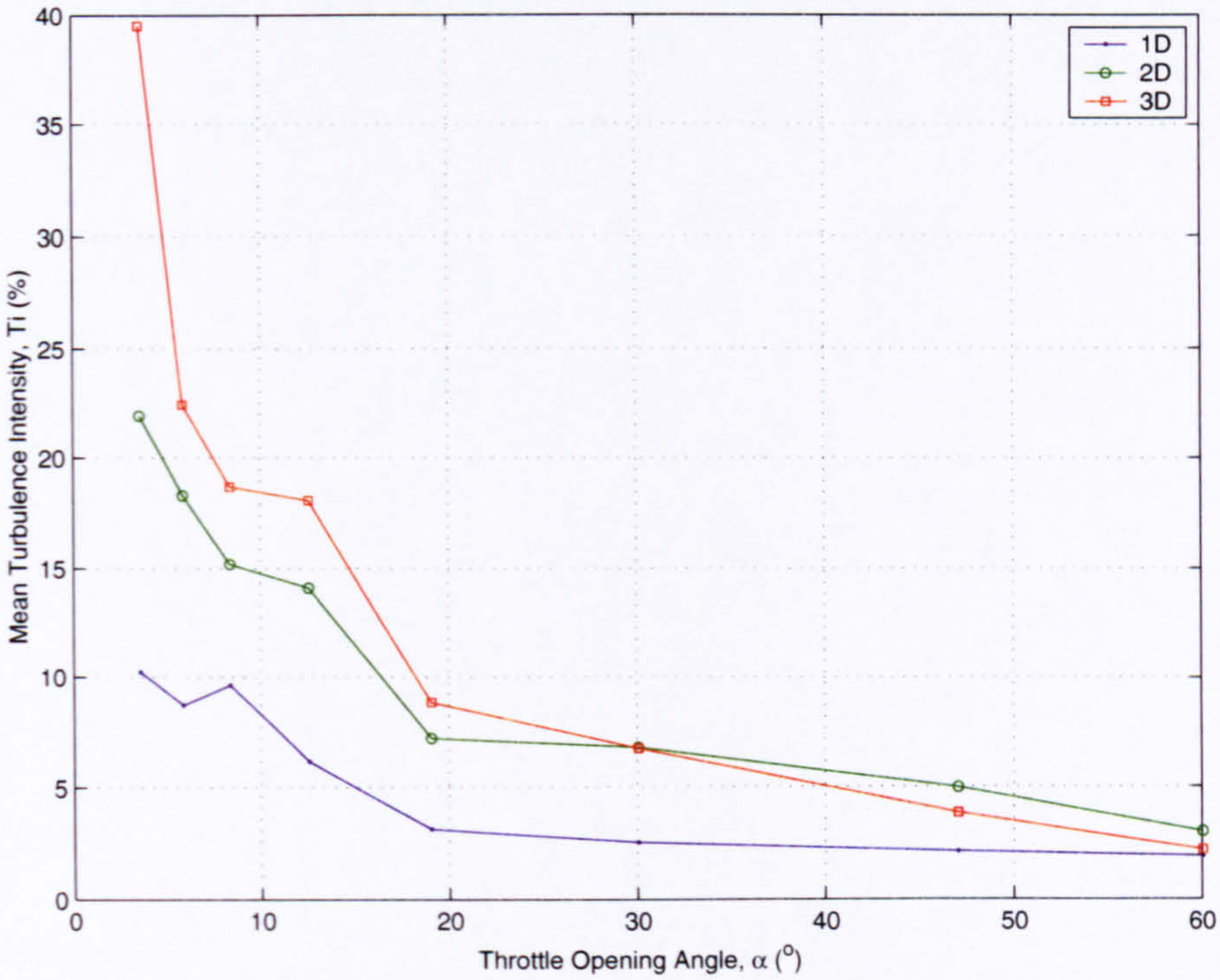

Figure 5.17: Variation of mean turbulence intensity, Ti, with throttle angle and downstream measurement location.

5.6.6 Statistical Bias of the Measurements

A brief analysis of the statistical bias is now considered in light of the variation of turbulence intensity within the flow and the uncertainties given in the previous sections. Figures 5.18 and 5.19 depict histograms of the velocity measurements corresponding to Ti levels of approximately 2% and 35% that represent the typical extremes found within the range of measurements.

It is clear from the figures that for high turbulence-intensity levels there is increased asymmetry in the velocity measurements. A quantitative value can be placed on the level of asymmetry in the measurements using the value of skew, S, that is defined as the 3rd moment of the signal,

$$S = \frac{\overline{u'^3}}{\sigma_u^3}, \tag{5.8}$$

where u' is the fluctuating component of the signal. Using equation (5.8), the value of

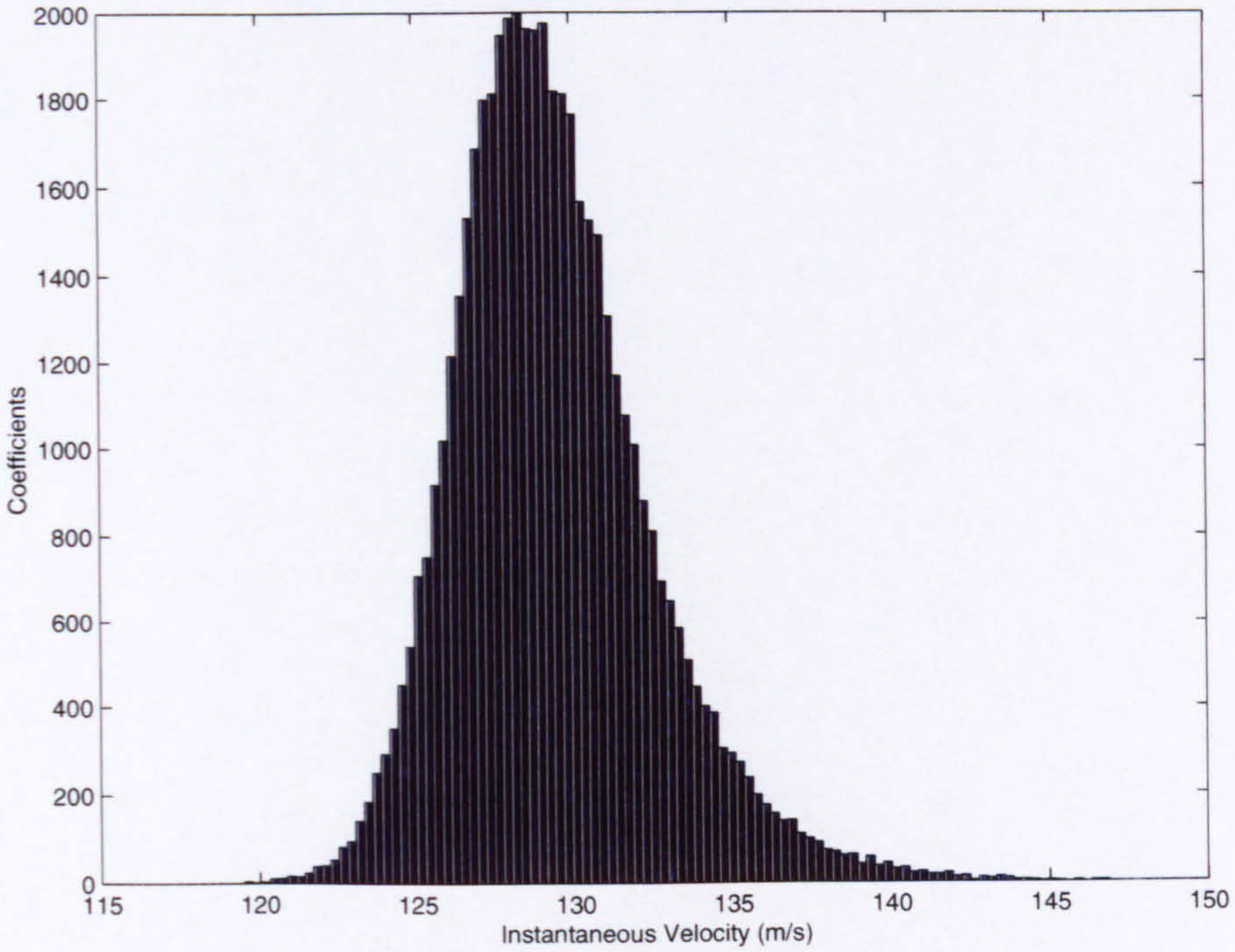

Figure 5.18: Histogram of the velocity signal for a flow of low turbulence intensity ($Ti \sim 2\%$).

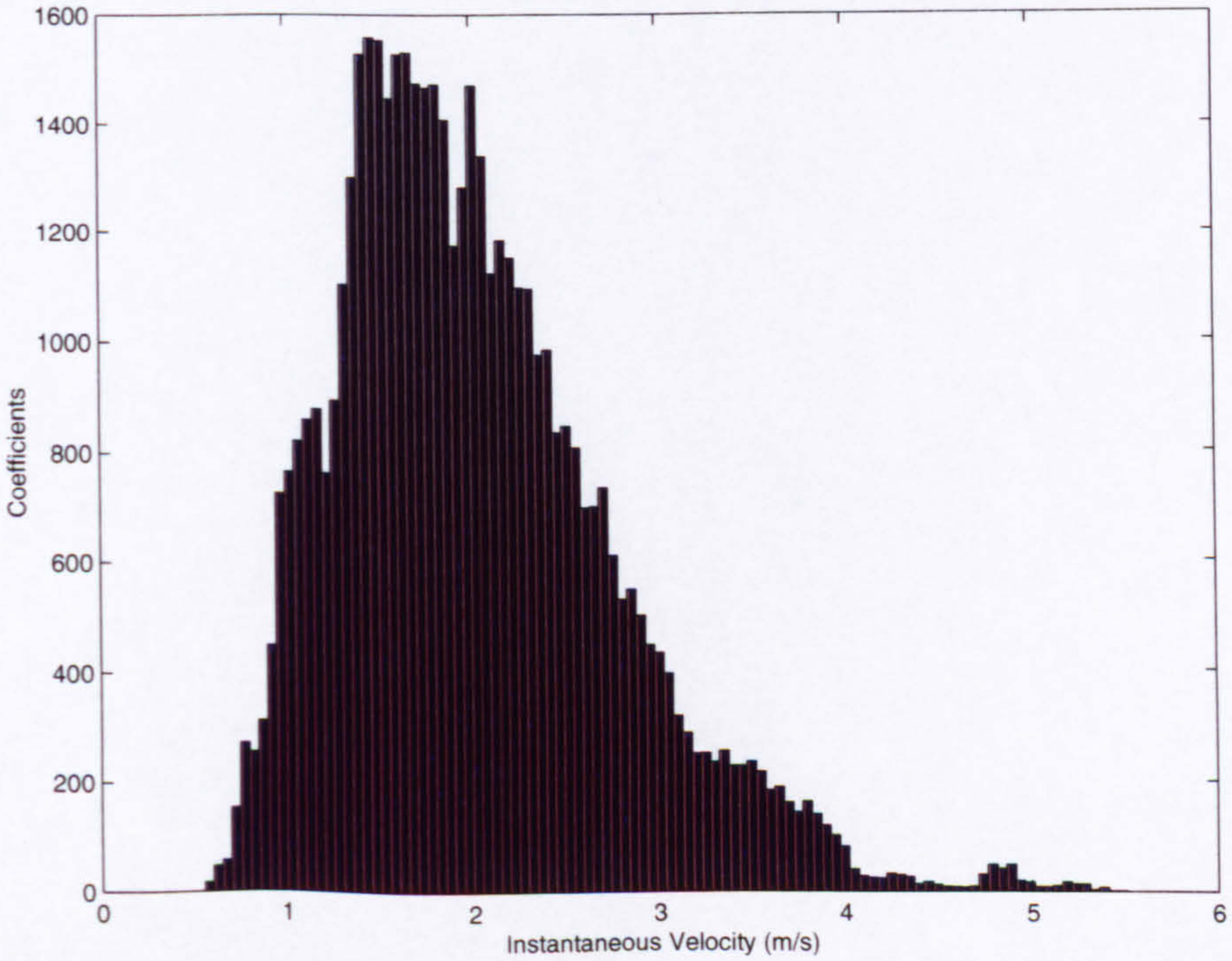

Figure 5.19: Histogram of the velocity signal for a flow of high turbulence intensity ($Ti \sim 35\%$).

skew for the signals plotted in Figures 5.18 and 5.19 have been calculated to be 0.025 and 2.23 respectively. High level of measurement skew are observed for flows with a high turbulence intensity, which are limited to the smaller throttle-valve openings and generally found further downstream. Therefore the level of skew shows some variation with downstream position and throttle opening angle. Average values of skew have been calculated for the each case and are plotted in Figure 5.20 against throttle opening angle.

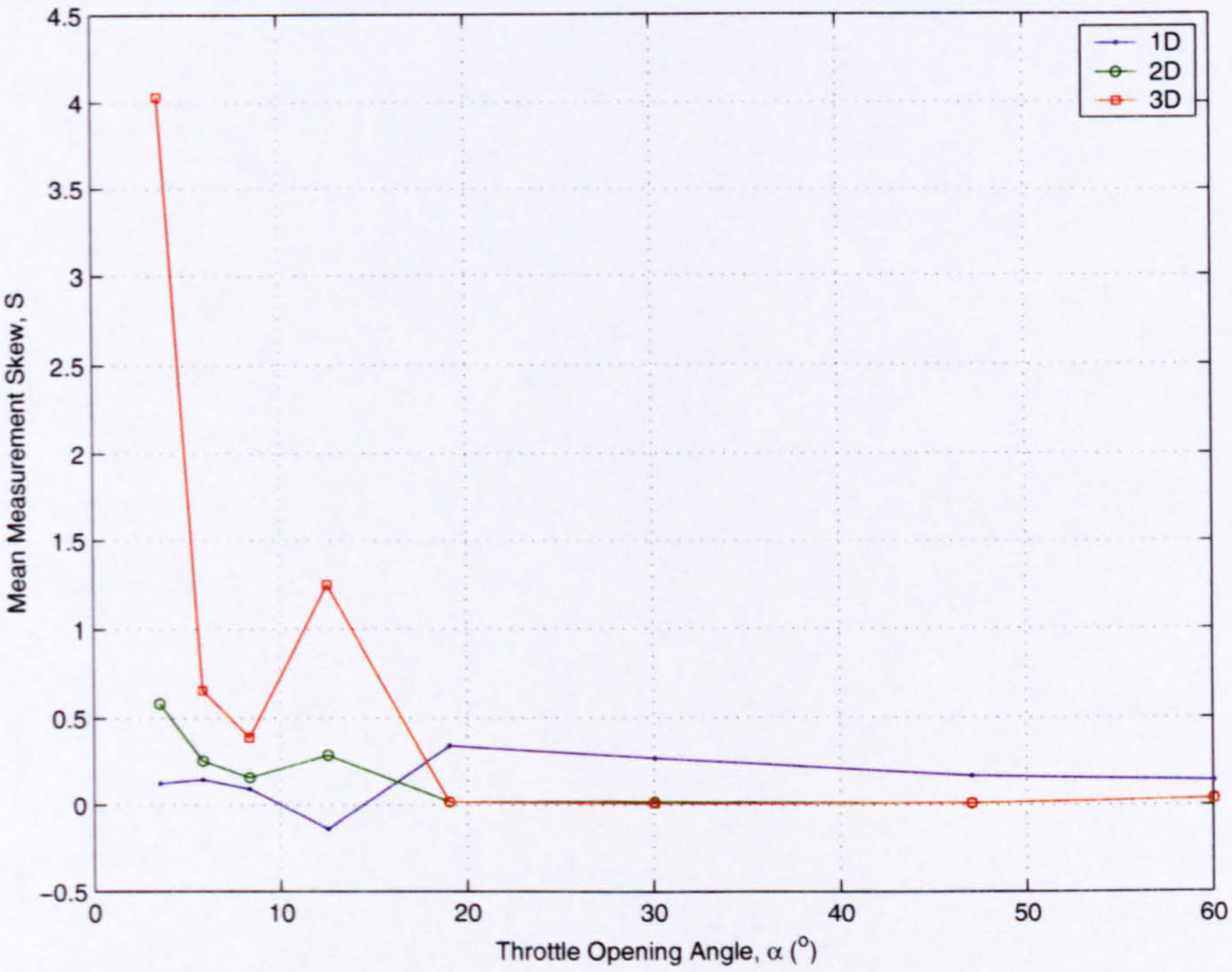

Figure 5.20: Variation of mean measurement skew with throttle angle.

Comparison of Figure 5.20 and Figure 5.17 shows the unusually high value of skew found for the 3.5° flow at the 3D measurement plane corresponds to an equally unusually high value of turbulence intensity. Values of skew are, however, not proportional to the level of turbulence intensity of a flow, but the measurements show a general trend of higher skew for higher turbulence intensity. High levels of skew will add uncertainty to the measurements as the calculation of uncertainty assumes the measurements fall within a normal distribution about the mean. Deviations from this, such as for the 3.5° throttle opening, will tend to add a bias to the resulting measurements.

Measurements at the larger angles show virtually no skew in the readings made at the 2D and 3D measurement planes and although values are slightly higher at the 1D measurement plane than elsewhere, the values are similar overall. In contrast, the measurements made at the smaller throttle openings have increased scatter in the level of skew and show higher values at the 2D and 3D measurement planes.

High values of skew in a reading has the effect of offsetting the calculated mean velocity value from its true mean value as more of the velocity fluctuations are captured to either the positive or negative of the mean signal (Bruun, 1995; Tennekes & Lumley, 1999). This is apparent from the histogram shown in Figure 5.19 where a calculated mean of 2.2 m s^{-1} is found, although the true mean of the signal lies closer to 1.9 m s^{-1}. This deviation remains fairly small and only becomes significant for high values of skew. Here the majority of cases show low skew, with the exception of one case, and hence the offsets in velocity reading have not been accounted for.

A second method of basic statistical analysis can be carried out by evaluation of the 4th moment of the measured signals that gives an indication into the flatness of the signal. This is termed the kurtosis of the signal and is found through equation (5.9) below,

$$K = \frac{\overline{u'^4}}{\sigma_u^4}. \tag{5.9}$$

Figure 5.21 plots the variation in signal kurtosis with throttle angle derived through equation (5.9). Similar trends are found to the skew of the signal with high values of kurtosis, accompanied with increased scatter, for the small valve openings, and reduced values and scatter for the measurements made for the large throttle openings. The increased kurtosis (i.e. reduced flatness) of the signals at the smaller openings again coincides to large turbulence-intensity values, and also to large values of skew, although greater overlap of the kurtosis values is found at the smaller throttle openings.

A large value of kurtosis indicates that the signal experiences large sharp fluctuations about the mean that has leads to a thinned out distribution of values with long thin tails present on the distribution curve (Bruun, 1995; Tennekes & Lumley, 1999). Smaller

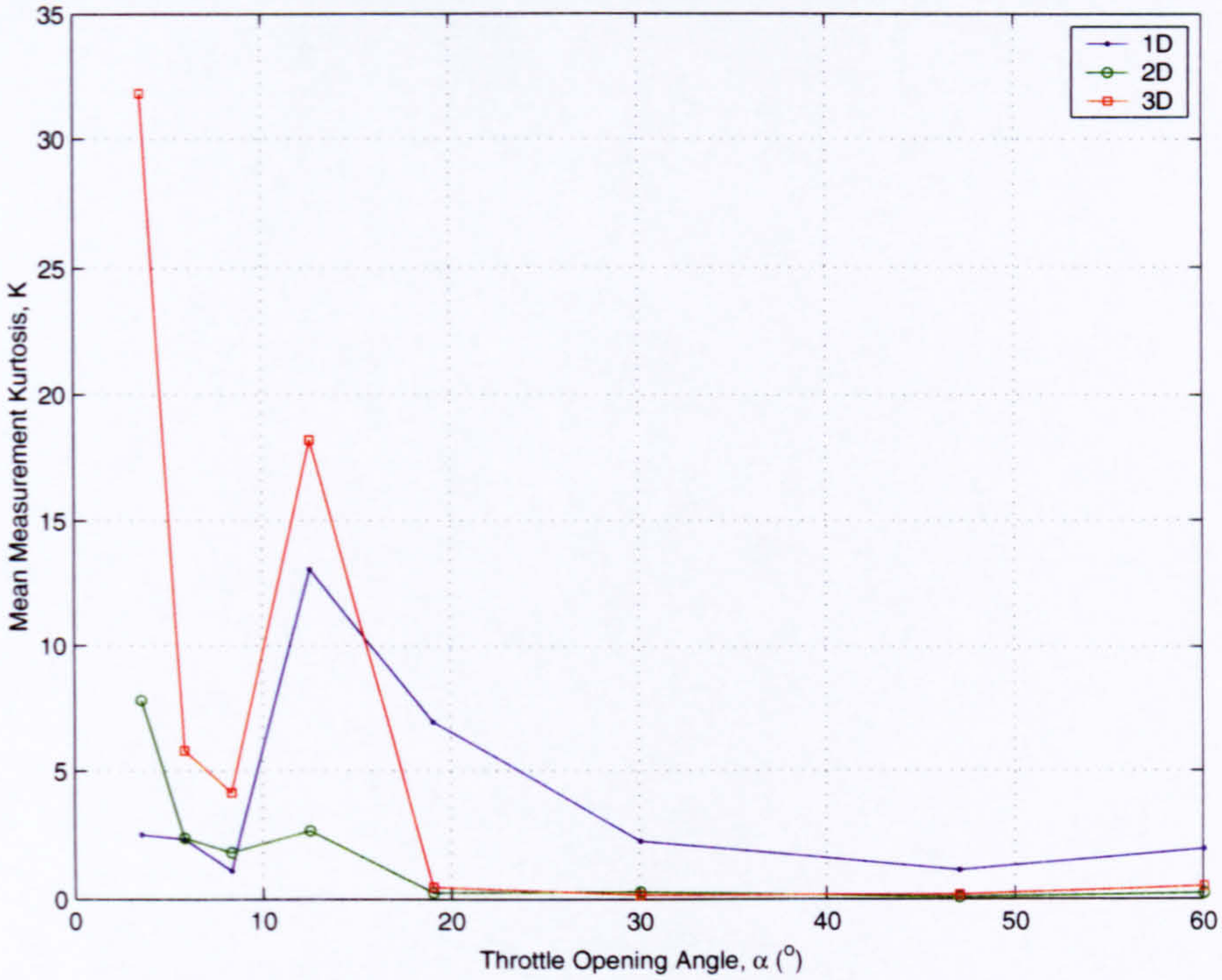

Figure 5.21: Variation of mean kurtosis of the velocity measurements with throttle angle.

values of kurtosis represent a signal with smaller fluctuations about the mean value and hence leading to a fuller and well-defined distribution curve.

The analysis of the skew and kurtosis of the measurements made indicate that for the majority of cases the signals are of good quality. The smaller-angle flows tend to have a greater variation in the levels of skew and kurtosis and hence the level of error associated with these signals will be higher, although for the most part this is still small. For the flow at 3.5°, the measurements appear poor, in particular at the 3D measurement plane and hence these values should be treated with caution.

Autocorrelation, Ensemble, and Time-Averages

Results presented so far have been based on the time-averaged measurement signals, thus providing no insight into any transient or periodic flow phenomena. In order to determine whether the computational study has correctly predicted the flow oscillations within the flow, the time-history of the measurements are now considered, followed by

evaluation of the frequency content of the signals.

Here a brief evaluation of the signals is carried out in order to classify the flow and give an initial indication into the flow structure. For this purpose the ensemble average of the signals has been determined alongside the autocorrelation function that shows the dependence of the flow at one instant to another instant. The ensemble average, μ_u, and autocorrelation function, R_u, for a digital (i.e. discretised signal) are calculated as (Bruun, 1995),

$$\mu_u(t_1) = \lim_{N\to\infty} \frac{1}{N} \sum_{i=1}^{N} u_i(t_1), \tag{5.10}$$

$$R_u(t_1, t_1 + \Delta t) = \lim_{N\to\infty} \frac{1}{N} \sum_{i=1}^{N} u_i(t_1) u_i(t_1 + \Delta t), \tag{5.11}$$

where N is the number of time-history records over which the average is made; t_1 is the time at which the average is made; Δt is the offset in time for the autocorrelation; and u_i is the instantaneous signal. Here, the number of records over which to make the time average is limited as a result of the time required to make the measurements. For the majority of cases only one time-history record has been recorded and in order to calculate an ensemble average the rather unorthodox approach of splitting this into a series of shorter sample sets has been carried out, thus simulating a series of shorter measurements. Given the already short length of the signals, this approach can lead to a reduced quality of the signal, but has sufficed here for providing information about the flows.

Bruun (1995) classifies physical flows as either deterministic or random, and the latter is further split into stationary and non-stationary processes. It is assumed here that the flow is a random process, i.e. it can not be mathematically represented, thus an ensemble average and autocorrelation function are used to further classify the flow. A non-stationary flow is classified by varying values of μ_u and R_u in time, while a *weakly* stationary process is one where these are time invariant, and with the latter true for all time, i.e. $\mu_u(t_1) = \mu_u$ and $R_u(t_1 + \Delta t) = R_u$ for all t, then the process is termed

strongly stationary. For the flows here the ensemble average has been found to remain time invariant for each measurement, and the autocorrelation determined for several offsets also remains time invariant; thus the flows can be considered to be a strongly stationary process.

Further analysis is made through the time-average of the data that has been used for the presentation of the results so far. In a similar light to the ensemble analysis, the time-average analysis can be used to classify the flow as stationary if the values of time-average, μ_u and corresponding autocorrelation, R_u are time-invariant. Further, if the time-averaged values are equivalent to the ensemble-averaged ones then the process is said to be *ergodic*. The time-average and autocorrelation for a digitised signal are calculated through equations (5.12) and (5.13), below,

$$\mu_u(i) = \lim_{T\to\infty} \frac{1}{T} \int_0^T u_i(t)\mathrm{d}t, \tag{5.12}$$

$$R_u(\Delta t, i) = \lim_{T\to\infty} \frac{1}{T} \int_0^T u_i(t)u_i(t+\Delta t)\mathrm{d}t, \tag{5.13}$$

where i represents the i^{th} time-history record; t is the instantaneous time, and Δt is the offset in time for the autocorrelation as before. Again, given the limited data available a full comparison of the time-averages for a particular experimental set-up is not possible, and hence the larger signal has been split in order to give some indication into the flow characteristics.

Evaluation of the time-average values for the flows considered reveals the individual time-averages and autocorrelation functions do not differ suggesting a stationary process. In addition, the time-average values are equal to the ensemble-averaged values of the measurements thus suggesting that the flows considered are ergodic processes. However, this conclusion is weak given that insufficient time records are available and this also hinders full statistical analyses. For the very limited number of repeat runs carried out the findings were as for the split signals, thus providing slightly increased credibility to the classification.

5.6.7 Frequency Measurement

Given the lack of data to generate adequate statistical analysis and the original simplistic approach of the experiment, a basic frequency analysis has been performed on the measurements. By evaluating the frequency content of the individual signals, any oscillations present in the wake of the valve predicted by the CFD should be apparent. The frequency content of the signals has been evaluated using a fast Fourier transform (FFT) algorithm, a special form of the discrete Fourier transform (DFT) that benefits from faster calculation time (Meade & Dillon, 1991). The FFT transforms the discrete time signal into a series of discrete points of the frequency spectrum and these are presented in the form of a histogram of coefficients for a given frequency. This is then evaluated for regions of concentrated coefficients or spikes in the graph that represent periodic structure within the flow. Such methods have been used in the earlier circular cylinder experiments in order to determine the shedding frequency of the flow.

Although calibration is not necessary for the analysis of frequency content, the signals analysed are those calibrated for the velocity measurements previously presented. Each record consists of a five-second signal sampled at 10 kHz leading to 50000 individual data points from which a frequency range of 0 to 5000 Hz has been evaluated using the FFT analysis. The results are presented for the frequency range $50 \leq N \leq 1000$ Hz in order to highlight only the frequencies of interest, although the full range of frequencies has been analysed. Typically the flows show high concentration of low-frequency activity that corresponds to the energy-carrying eddies of the turbulent flow (Bradshaw, 1971). As we are interested in the distinct oscillations of the flow due to the valve that are expected to be of high frequency, the low frequency oscillations have been filtered out.

Evaluation of the frequency content of the smaller-angle flows reveals no obvious dominant frequency components for the range of measurements. A typical transformation of the recorded signal to the frequency domain is shown in Figure 5.22 for a 5.8° throttle opening at the centre of the domain. The figure shows little activity

in terms of geometrically induced oscillations, but shows a broad spread of frequency content that corresponds to background turbulence. Such findings are typical of the small-angle flows with no clear indication of any transient or periodic flow features found. This is in agreement with the computational results, that showed evidence of small-scale vortices, although these were difficult to detect and should they exist here it is likely that they would be lost to the background noise of the flow.

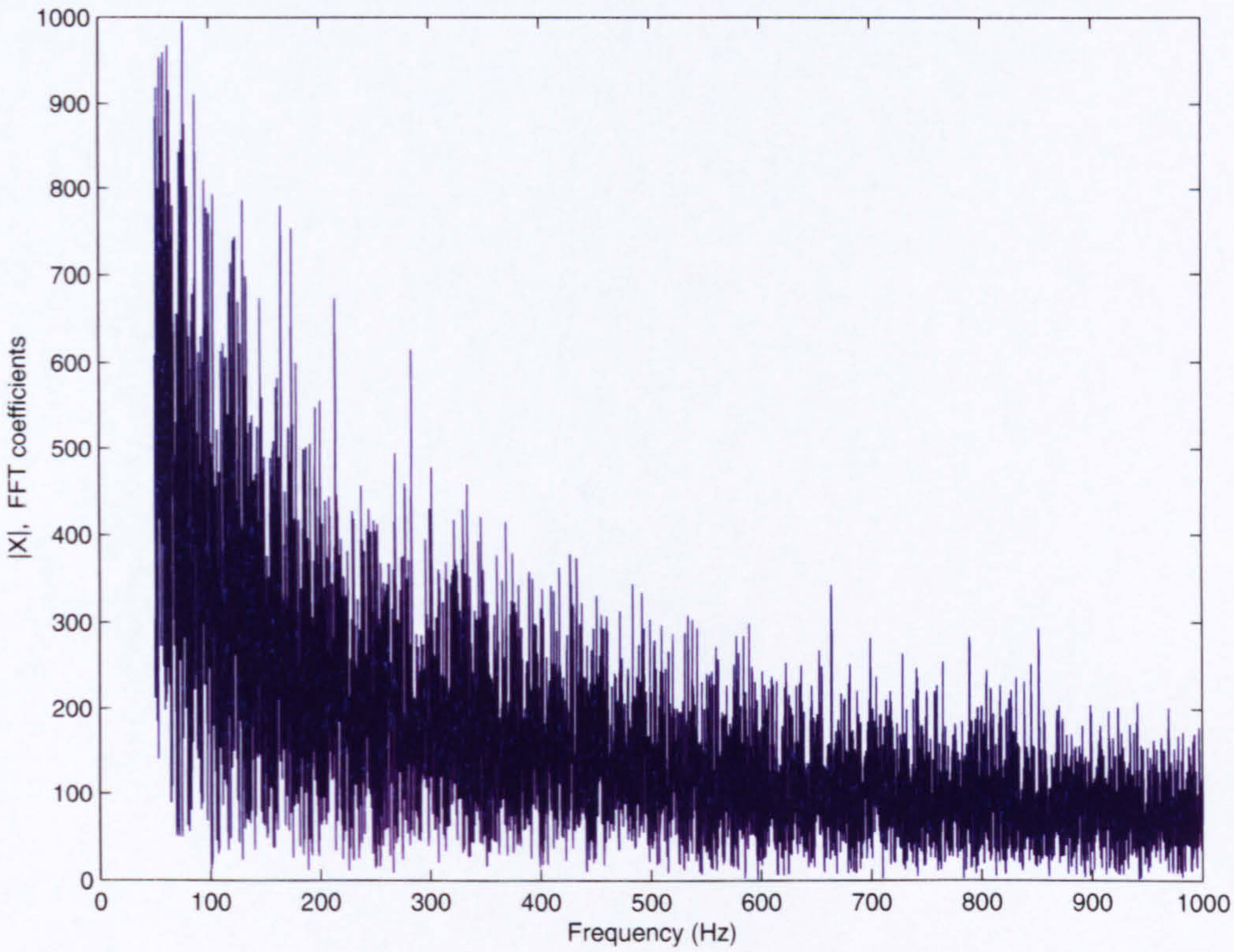

Figure 5.22: Frequency content of the flow through a valve at 5.8° at the centre of the 1D measurement plane. The figure shows no indication of periodic or transient flow features, only the broad frequency content of background turbulence.

At the larger openings similar observations are found with several signals showing little in the way of dominant frequency components. However, at the largest openings evidence has been found to suggest some form of periodic flow exists. For the flows through a valve at 47° and 60°, there are clear dominant frequencies for each of the flow rates considered, and for the 19° and 30° flows there are dominant features at the lower flow rates considered. In addition, for the flow at 12.5°, there exists one or

two regions where a dominant frequency has been found; however, given the level of background noise for this flow, the value should be treated with caution. Figure 5.23 shows the frequency domain for the flow through a valve at 47° with 15 m s^{-1}inlet velocity, measured at the 1D plane downstream of the valve leading edge.

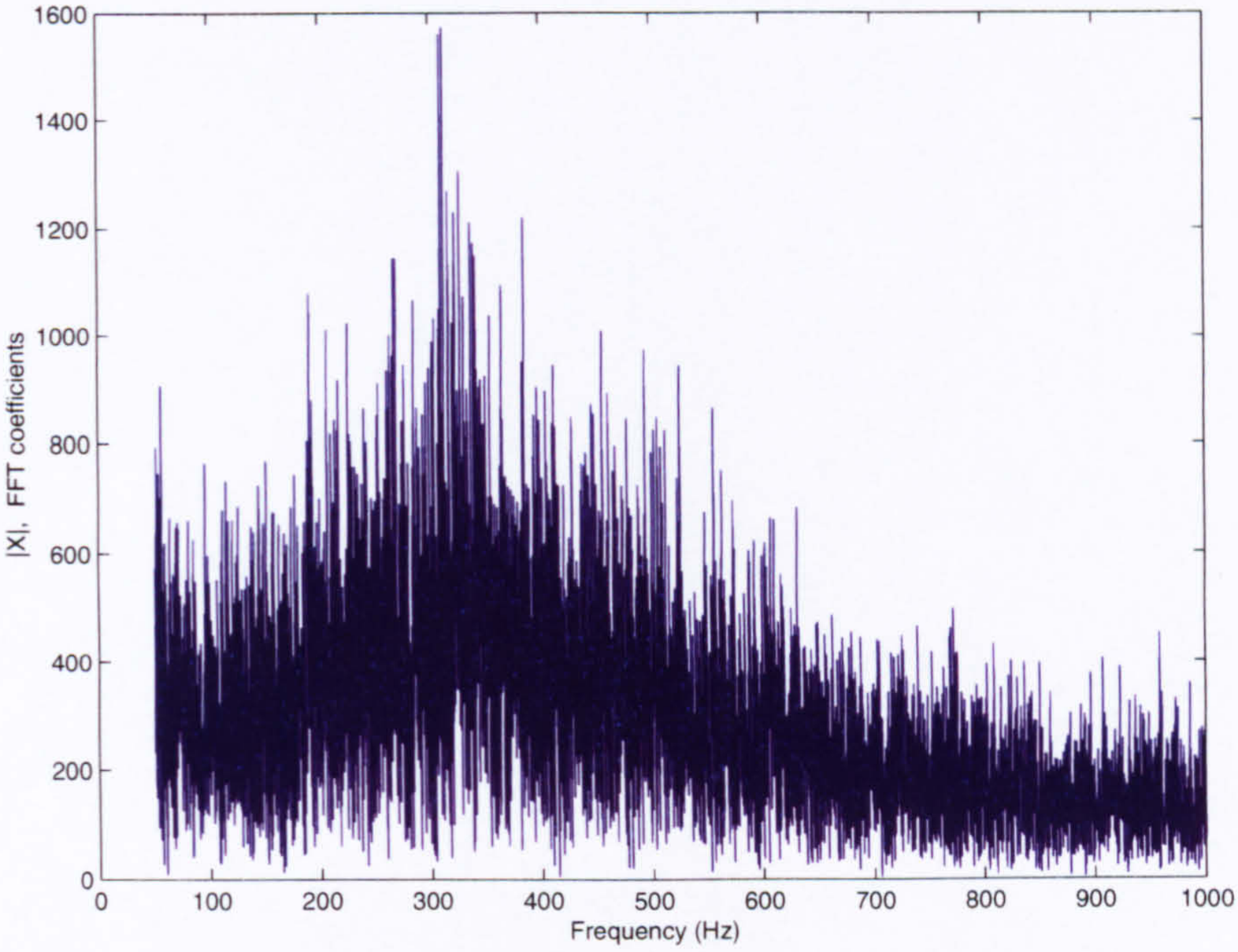

Figure 5.23: Frequency content of the flow passing through a valve opened at 47° with low inlet velocity showing evidence of periodic flow structure.

Clearly a high degree of activity is occurring with the considerable bunching of frequency components with an approximate peak of approximately 300 Hz. Similar graphs of frequency domain are found for the other measurements, with bunching of components about a central peak. A distinct single peak is not observed for any measurement, although at the lower velocities the concentration of frequency components is greater leading to improved peak definition. The poor bunching of the frequency components is partially explained by the measurement analysis considering both the fluctuating and unsteady components of the flow.

Figure 5.24 shows the variation of dominant frequency with throttle opening angle for the range of flows considered. The plot shows the three different flow rates consid-

ered, with the "high" value being the standard flow rate, and that simulated using the CFD. Despite the limited number of points in the graph a clear trend is shown with a decrease in dominant frequency as the throttle valve opens further. This contradicts the findings of the CFD that suggest the reverse is true with increasing angle leading to an increased vortex shedding frequency. The values of frequency are also considerably higher than those found for the CFD predictions. The trend also shows that for the 60° flows the frequency drop is not as great, and this stems from the fact that the flow rates for this angle has been calculated as opposed to measured or simulated. In addition the drop in frequency at 12.5° is because of the different data source for the smaller-angle flows leading to large difference in flow rates. As discussed above, only a few measurements for this angle show evidence of activity and hence this point should be questioned. To further analyse the data and to provide a more meaningful trend, Figure 5.25 plots the variation of throttle inlet velocity with the dominant frequency of the flow.

Figure 5.25 reveals a near linear relationship between the inlet velocity and frequency of the wake oscillation, although this is only assumed as lack of data points per curve makes this difficult to justify. Despite the lack of data points the trend does appear to hold for each set of results. Thus the frequency of the flow appears to depend on both the throttle angle and the inlet flow velocity that therefore raises the question as to whether the frequency of oscillation in the valve wake can be predicted if these criteria are known. As discussed previously, the vortex shedding from a bluff body or circular cylinder can be estimated through the Strouhal number of the flow (equation (5.2)) and this is now calculated for the throttle flows to establish whether a similar relationship holds.

The characteristic dimension used in calculation of the Strouhal number are typically a cylinder diameter or a bluff body height. Here, the apparent height of the throttle valve is used as the characteristic height, that is, the projected height of the valve presented to the oncoming flow. The free-stream velocity is usually taken as the characteristic velocity for the flows in question, as opposed to a local flow velocity. Thus

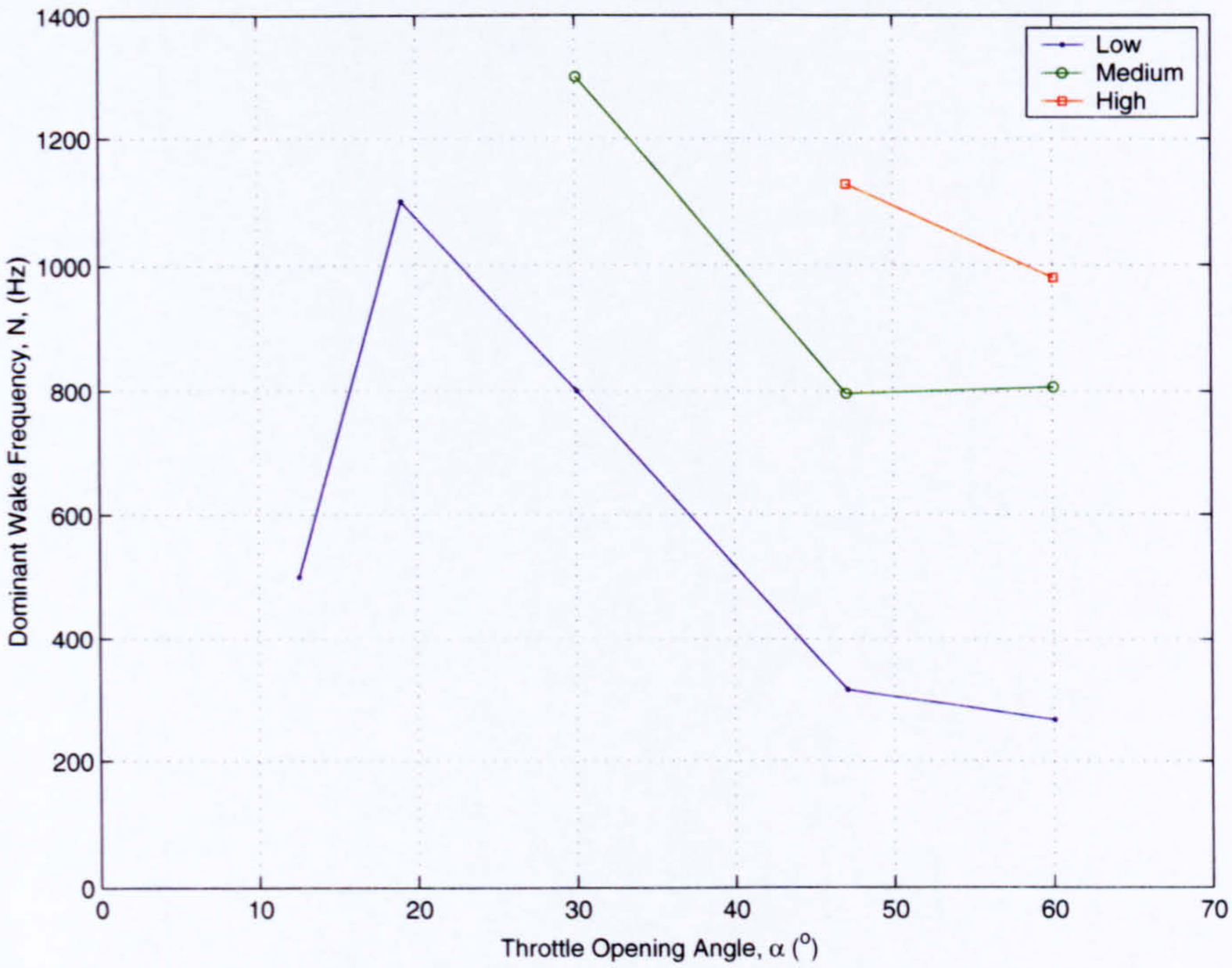

Figure 5.24: Variation of dominant frequency with throttle opening angle for low, medium, and high flow-rates.

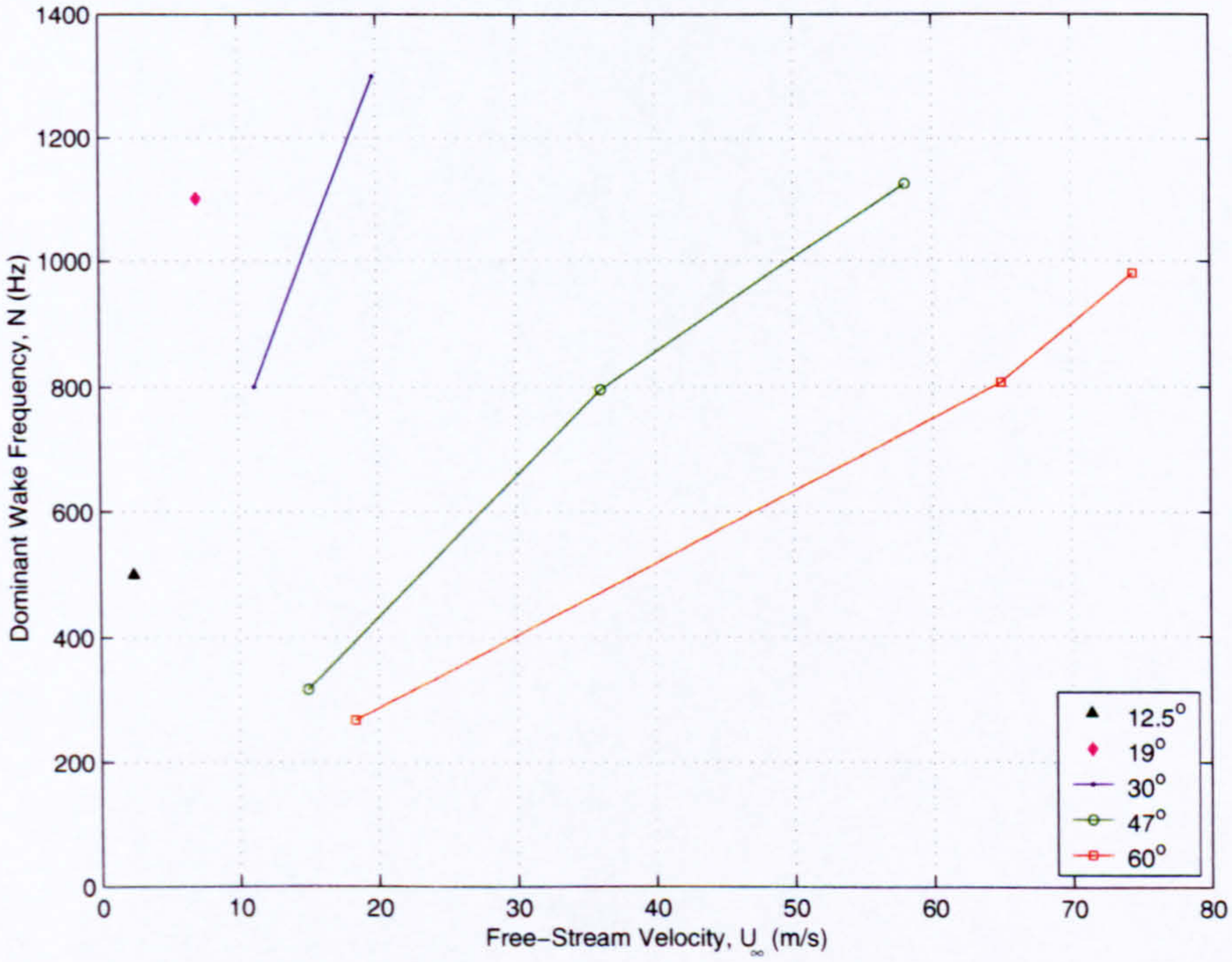

Figure 5.25: Variation of dominant flow frequency with throttle inlet velocity for large angle throttle openings, and low, medium, and high flow rates.

for the calculations presented here, the Strouhal number has been calculated using the apparent height of the valve, $D\cos(\alpha)$, and the mean inlet velocity, U_∞. The resulting values are plotted in Figure 5.26 against throttle angle.

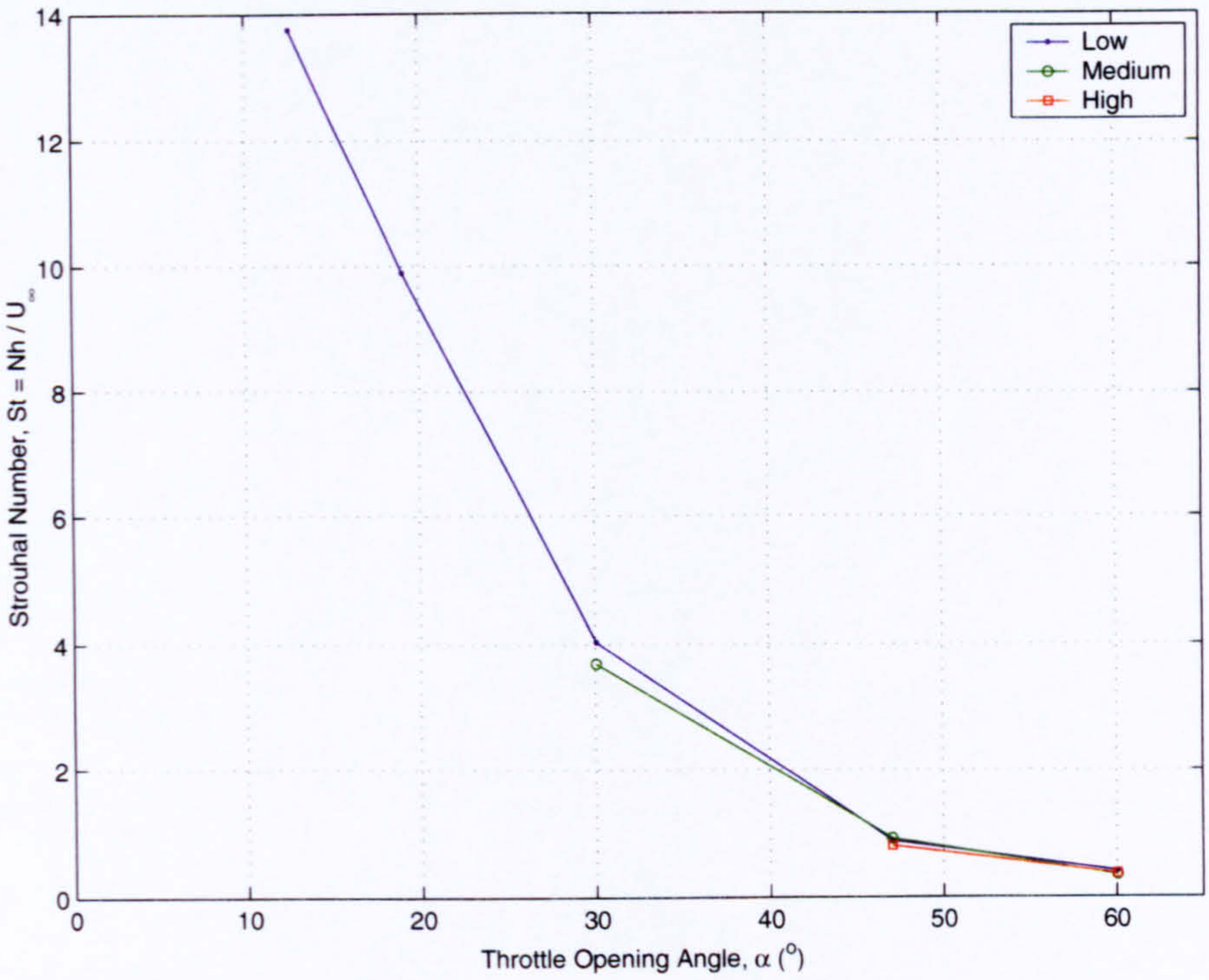

Figure 5.26: Strouhal number for the range of throttle angles calculated using inlet velocity and apparent valve height, for low, medium, and high flow rates.

Although the graph shows a variation of St with throttle angle, the values of St for the three different flow rates considered collapse to the same curve, thus suggesting a Strouhal relationship holds for a particular throttle angle. Variation of Strouhal number is not normally seen for cylinder or bluff-body flows and the discrepancy here is due to the proximity of the throttle walls influencing the local velocity around and downstream of the valve. Such Strouhal relationships are usually based on the body in question being exposed to a free-stream flow in an unbounded domain that allows full flow development. As discussed previously, the Strouhal number for unbounded cylinder flows is actually a function of the Reynolds number but varies so slowly that it is normally considered constant (Tritton, 1988). This is confirmed by the review of

cylinder flows by Williamson (1996) who shows that the Reynolds number dependence is most significant at low Reynolds numbers. Sallet (1969) also shows similar results in a review of several authors' work.

Typically, a flat plate swept through an incidence range will show variation of vortex shedding frequency with angle and velocity, but the data points will collapse to the same Strouhal number. For an inclined flat plate, Abernathy (1962) provides the Strouhal number for a range of incidence angles and a range of plate chords and shows that the Strouhal number lies in the range $0.185 \leq \mathrm{St} \leq 0.244$ for an incidence range of $30^\circ \leq \theta \leq 90^\circ$ (note that $\theta = 90^\circ$ corresponds to $\alpha = 0^\circ$ here). For the measurements carried out here the Strouhal number has a maximum of approximately 14 for the 12.5° flow, and collapses to an approximate minimum value of 0.47 for the 60° flows, hence even the smallest values are at least 100% larger than those expected for an unbounded flow.

Igarashi (1999), however, investigates the effect of blockage ratio on the vortex shedding performance of several bluff bodies and shows that as the blockage ratio increases so Strouhal number rises. This is attributed to a modification of the local oncoming velocity as a result of the increased blockage, and the author notes that the increase in blockage ratio had no effect on the frequency of vortex shedding.

Igarashi (1999) shows that for a blockage ratio of 0.5, the Strouhal number for the flow quadruples in size, and thus the considerable increase here is reasonable. Evaluation of the valve blockage ratio for the cases considered shows a minimum blockage of 0.41 for the 60° opening and a maximum of 0.99 for the 3.5° opening, and a blockage ratio of 0.95 for the lowest angle showing evidence of flow oscillation (12.5°). It is unsurprising, then, that the Strouhal number reaches higher values at the smaller openings where the blockage ratio is seen to increase massively. Also noted is that at high blockage ratios (≥ 0.47), the formation of the jet-like flows between the body and walls of the domain cause any flow oscillations to cease. As the blockage ratio here exceeds this limit there is a possibility that the same damping of the oscillations occurs. However, the shedding phenomenon here is of a different nature to the typical shedding found from a thick

bluff body.

A modified Strouhal number can be defined that takes into account the blockage ratio of the valve and this too has been carried out by Igarashi (1999). The resulting Strouhal number shows less variation with blockage, and performing the same task here yields a similar reduction in variation, but does not collapse all points and hence is not used further here. Both Abernathy (1962) and Yeung & Parkinson (1997) use a modification based on the variation of static-pressure coefficient that shows improved collapse for various bluff bodies. This method has not been employed here as the pressure measurements are not adequate enough for the purpose and limited pressure measurements are available at the low flow rates.

Thus it can be seen that the throttle-body walls have a significant effect on the flow past the valve plate, and in particular the vortex shedding from the valve. A relationship does, however, exist between the shedding frequency of the vortices, the mean flow speed and the throttle angle, through the Strouhal number; albeit with specific values corresponding to a particular valve geometry and opening angle or blockage ratio.

The following chapter compares the experimental measurements and computational predictions and discusses their merits and inadequacies.

Chapter 6

Comparison of Computational Predictions with Experimental Measurements

6.1 Introduction

The results of the computational predictions are here compared to the experimental measurements and the findings discussed. In order to aid in visualising the orientation of the probe the reader is referred to Figure 5.6 that is repeated in Figure 6.1 below for clarity.

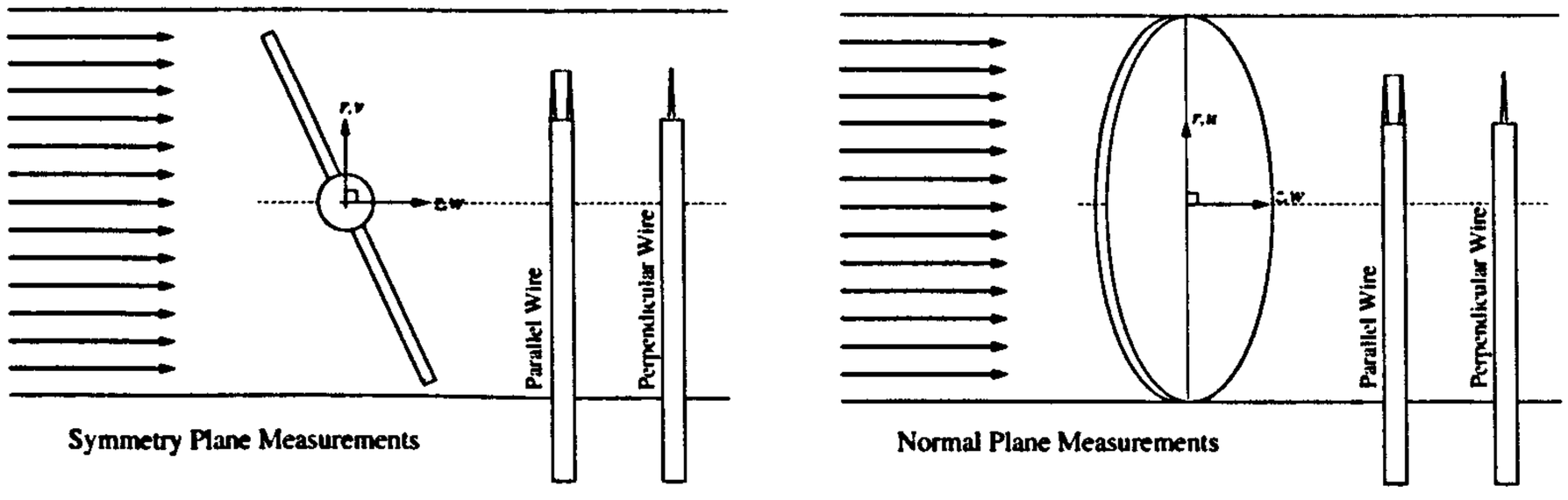

Figure 6.1: As Figure 5.6: Schematic showing the orientation of the hot-wire probe and sensing element relative to the throttle body and mean flow direction. Symmetry plane measurements are represented to the left, and normal plane measurements to the right.

6.2 Pressure Drop Across The Valve

Figure 6.2 compares the predicted and measured static-pressure drop of the flow through the throttle valve for the range of throttle opening angles investigated here. The static-pressure drop has been calculated as the difference between the static pressure recorded at locations 1D upstream and 1D downstream of the valve. Pressure measurements are the averaged values recorded from a single pressure tapping in the wall of the domain that is located at the level of the pivot. Hence the computationally predicted pressures have been found from similar locations.

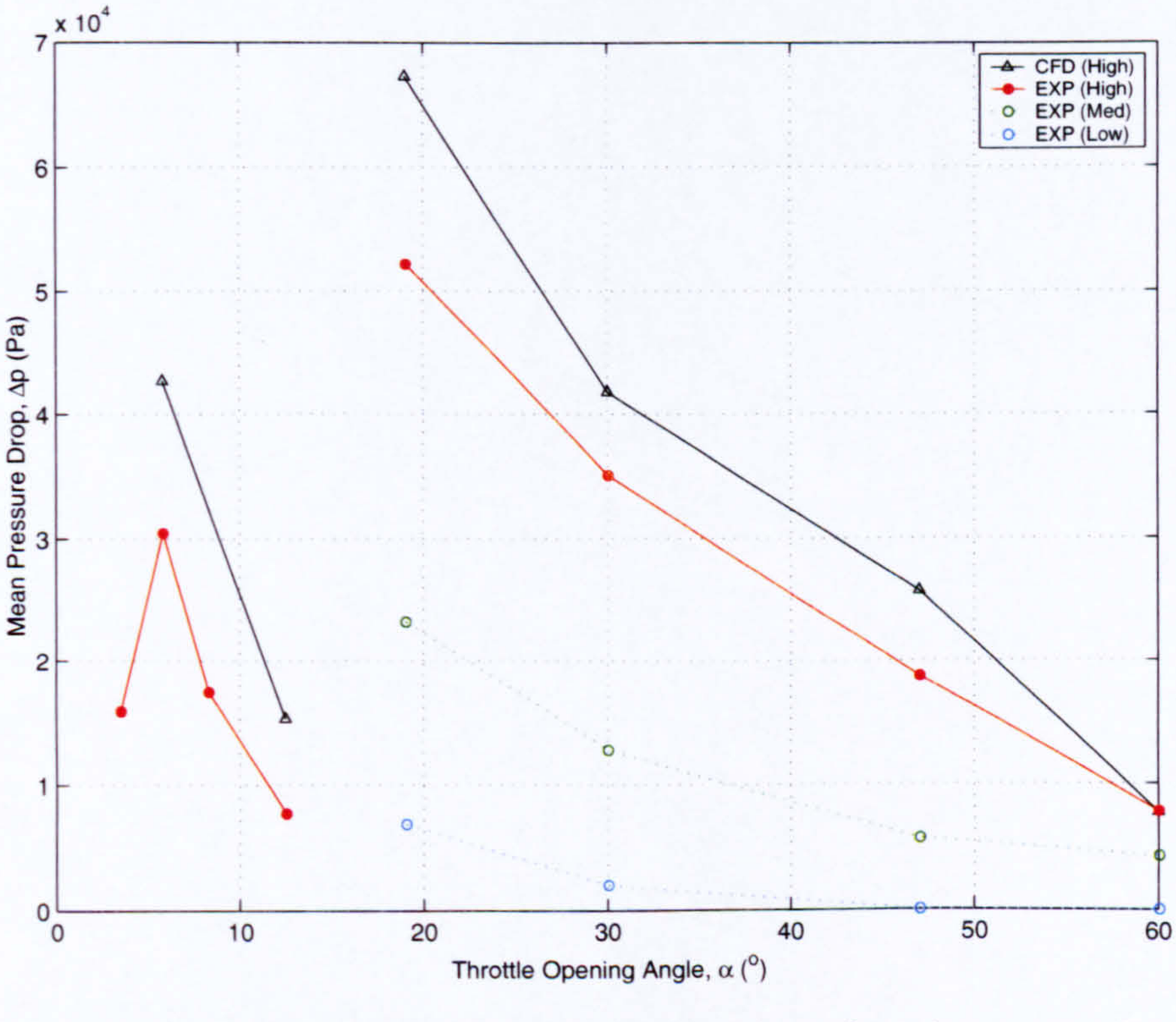

Figure 6.2: Comparison of the predicted and measured static pressure drop across the throttle valve for the range of throttle openings considered. Pressure drop has been calculated as the difference between static pressure 1D upstream and 1D downstream of the valve taken at the wall of the domain. CFD predictions are shown as magenta and black triangles with thick line for the small and large angle flows respectively. The experiments are split into small and large angle flows and are presented for the low, medium and high flow rates.

The figure compares the predicted pressure drop for the small- and large-angle

flows against the measured pressure drop for the three different flow rates considered. The CFD corresponds to the high flow rate of the experimental values and should be compared to these. The low- and medium-flow rate measurements are presented for completeness. As the valve opens, and the flow rate increases, the pressure drop across the valve reduces, which is seen for both the small- and large-angle flows. The experimentally measured values show an asymptotic reduction in pressure drop for the flow through large throttle openings where the valve presents minimal blockage. The predicted flows show a similar trend with a reduction in pressure drop for an increased valve opening for both the small- and large-angle openings. A good qualitative agreement exists between the predicted and measured pressure drop (at the high flow rate) with only the predicted flow through a 60^{o} opening deviating from the trend. Quantitatively this value shows excellent agreement with the measured values; however, the point is spurious as the remaining predicted values consistently over-predict the pressure drop by 20% to 40%. Although the predictions incorrectly predict the pressure drop across the valve, the global trend is correctly predicted, hence promoting confidence in the predicted flows.

6.3 Comparisons of the Velocity Magnitude Profiles

Comparisons are now made of the velocity-magnitude profiles of the flow downstream of the valve as predicted by the CFD and those measured with the HWA system. The experimentally measured velocity-magnitude profiles presented in chapter 5 are the sum of two velocity components that depend on the orientation of the hot-wire sensing element. These have been presented as the time-average of the recorded signals and they will be presented here in the same manner. As the measurements have been made separately across each half of the domain the results presented here show a slight mis-match in the velocity magnitude at the centreline that corresponds to a mis-match of the inlet mass-flow rate between the individual experimental runs. In addition, the measurements at each of the downstream locations have been made at separate instances and therefore the presented profiles are a result of six individual experimental runs. As

in the previous chapter, error bars are used to represent the uncertainty in the physical measurements. Also, the measured profiles in the plane normal to the symmetry plane have been generated by reflecting the profile about the symmetry plane, and have a reduced number of measurement locations.

The results of the computational predictions are presented as the instantaneous value taken from the last time-step of each simulation. Time-averaging of the data has not been performed owing to the large disc storage requirements of the data files, and although sensor points can be defined within the model to monitor the data this has not been carried out. In order to give a fair comparison to the measured values, the computational profiles are presented as the combination of the two dominant velocity components, as measured by the hot-wire probe for a given orientation.

6.3.1 Small Throttle Valve Openings

Perpendicular Wire Measurements in the Symmetry Plane

Here the probe body is perpendicular to the flow direction and valve pivot, and the hot-wire element is also aligned perpendicular to the flow direction. For this hot-wire and traverse orientation the recorded signals represent the combined axial and downwash components of the velocity and therefore the computationally predicted profiles are presented as the magnitude of these combined components, i.e. $|U| = \sqrt{v^2 + w^2}$.

The general trend for the small-angle flows is that the CFD under-predicts the velocity magnitude and fails to accurately predict the sharp velocity gradients found in the experimental measurements. However, the predictions do capture the general flow field, showing regions of high-energy flow at the walls and low velocities in the centre of the domain. Figure 6.3 compares the predicted and measured velocity-magnitude profiles of the flow downstream of a 5.8° throttle opening at the 1D, 2D and 3D measurement planes.

The figure indicates that the predictions show reasonably good quantitative agreement with the experimentally measured values at the centre of the domain, particularly for the flow at the 1D measurement plane. In the same plane, the sharp velocity gradi-

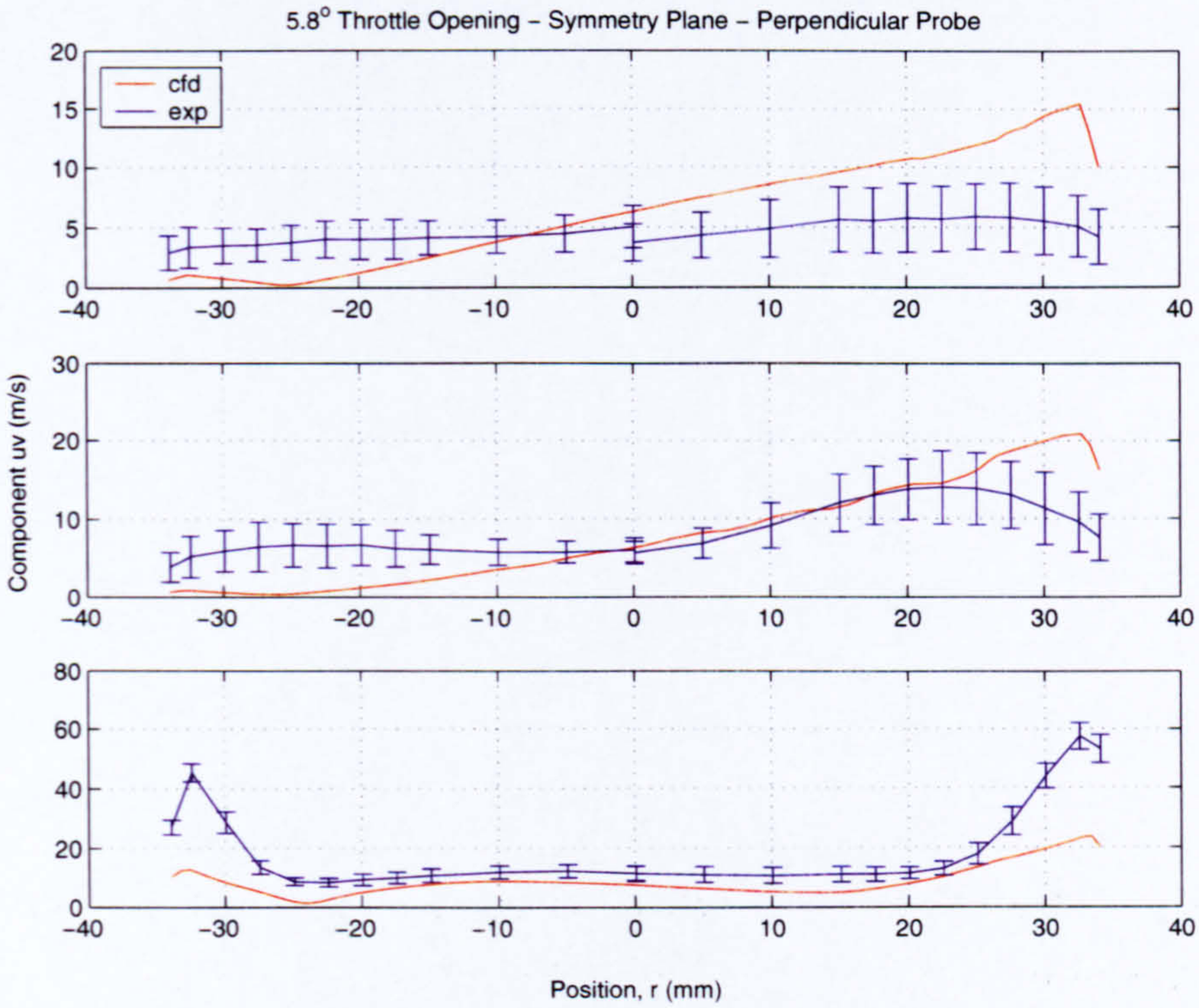

Figure 6.3: Comparison of the predicted instantaneous velocity magnitude profiles against the time-averaged experimental measurements made in the symmetry plane of the valve for a 5.8° throttle opening. The hot-wire element is aligned perpendicular to the mean flow direction and the computational prediction is the product of the axial and upwash components of the velocity. From bottom to top, 1D, 2D, and 3D measurement planes, with positive distance representing the leading-edge side of the valve. The CFD is shown as the solid red line, and the experimental values as the solid blue line with corresponding error bars representing the uncertainty in the measurements.

ents toward the walls of the domain are grossly underpredicted, although this improves downstream where the measured gradients are less severe. Predictions of the flow at the plane 3D downstream show the worst agreement with the measurements with the CFD predicting a high velocity gradient where the measurements indicate only a slight gradient. However, considering the offsets in the mass flow of the experiment and the fair spread in the data, the predicted values still show reasonable agreement with the measurements.

Comparisons of the predicted and measured velocity magnitude profiles for the remaining small-angle flows are similar to the comparisons made in Figure 6.3. Each

flow shows excellent agreement at the centre of the domain at the 1D measurement plane with the predicted velocities within 5% of the experimentally measured values. The flow at 12.5° shows particularly good agreement in this region with overlap of the two curves. Toward the walls of the domain, each of the remaining flows show the predictions failing to capture the steep velocity gradients of the measurements. Further from the valve the trends are again similar to those of Figure 6.3 with the predictions at 8.3° showing similar profiles to those at 5.8°, while the 12.5° flow predictions capture the velocity gradients at the 2D plane but prove more diffuse by the 3D plane.

Levels of uncertainty in the experimental measurements tend to decrease as the throttle opening angle increases, and increase as the flow moves further from the valve. These factors result from changes to the mean flow at each of the throttle angles and downstream locations. As the valve opens, the mean flow through the valve increases, and although the absolute level of uncertainty may change little, the level of uncertainty in comparison to the mean flow rate therefore reduces. Similarly, as the flow convects downstream the mean velocity decreases away from the valve and hence the relative uncertainty increases. For example, at this orientation, the uncertainty in measurements at the 1D plane for the 5.8° opening reaches 22%, whilst at the 3D measurement plane this increases to 55%, despite the absolute uncertainty in each measurement remaining the same at approximately ± 2.3 m s^{-1}.

Parallel Wire Measurements in the Symmetry Plane

The probe is now rotated about its body so the wire element is parallel to the flow direction. With this hot-wire probe and traverse orientation the measurements record the cross-flow and downwash components of the velocity and therefore the CFD profiles are presented as the combined magnitudes of these components, i.e. $|U| = \sqrt{u^2 + v^2}$. Figure 6.4 compares the predicted flows to the measurements for a 5.8° throttle opening.

It is immediately apparent from Figure 6.4 that the agreement between predicted and measured velocity profiles is not as good as those of the perpendicular wire orientation. Of note is that the measured profiles show weak similarity to those of the

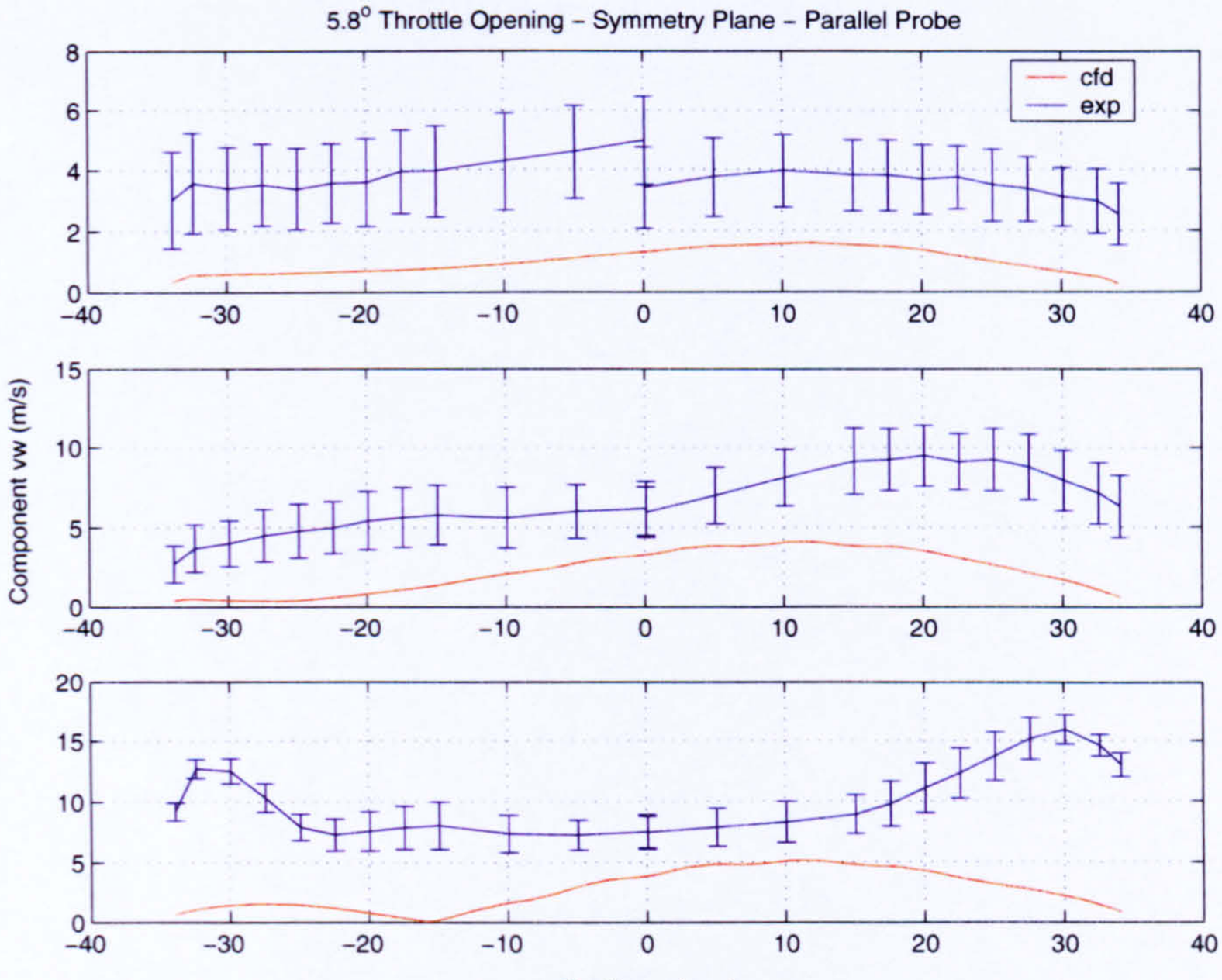

Figure 6.4: Comparison of the predicted instantaneous and measured velocity magnitude profiles in the symmetry plane of the valve for a 5.8° throttle opening. Flows correspond to those of Figure 6.4 for a parallel probe wire orientation.

perpendicular orientation while the predicted profiles contrast more greatly to those of Figure 6.3. This is also apparent for the 8.3° flow that shows very similar predicted and measured profiles to those shown here, and hence similar agreement is found. For the 12.5° flows the similarity between the parallel and perpendicular measurements is still apparent, however, the predictions also show slight similarity to the perpendicular predictions.

In all cases, the flow at the 1D measurement plane shows the weakest agreement. The measurements suggest high velocities exist at the domain walls that are more likely the influence of cross-flow velocity components than downwash components owing to the proximity of the probe to the wall. This rise in velocity toward the walls may also represent the influence of axial velocity on the readings that would result from a poorly positioned probe. Each of the computational predictions, however, do not reflect this

and show higher velocities toward the centre of the domain, although biased toward the leading-edge side. It is difficult to ascertain whether this is an increased component of downwash or prediction of a different flow structure at this time, although this is discussed later.

At the 2D and 3D measurement planes the qualitative agreement of the two profiles is improved, despite the CFD underpredicting the velocity magnitude of the measurements by 90% in the worst cases. The CFD predicts similar profiles to that at the 1D plane with higher velocities toward the centre of the domain and shows gradual dissipation of the flow as it moves downstream. At these downstream locations, the 12.5° flow prediction shows improved capture of the measured velocity gradients to those of Figure 6.4 and to those of the 8.3° flow.

In terms of measurement uncertainty, each of the small-angle flows follows a similar trend with greater uncertainty far from the valve, and a fairly even level of uncertainty across the span of measurements. This holds for both hot-wire orientations although the level of uncertainty in the measurements is less for a parallel orientated wire. The findings above show that measurements made at the 2D and 3D plane, where local velocities are small (0-10 m s^{-1}), the level of uncertainty is of the order of 40% to 50%, and hence too high to allow strong conclusions to be drawn. At these locations, at the small openings, the flow shows no strong physical features that can be distinguished by the hot-wire system. There is evidence to suggest a velocity gradient across the domain, but a qualitative figure can not be accurately determined with the equipment and methods used here.

Perpendicular Wire Measurements Normal to the Symmetry Plane

Comparisons are now made of the predicted and measured flows in the plane normal to the symmetry plane of the valve at the level of the valve pivot. The probe body is orientated perpendicular to the flow direction and parallel to the valve pivot while the wire element lies perpendicular to the flow direction. Note as previously (see chapter 5), the experimental results are reflected about the symmetry plane and fewer measurement lo-

cations have been used, therefore the resolution of the measured profiles is considerably less than those made in the symmetry plane. The use of reflected data is made more acceptable by the time-averaging process that tends to show a symmetric profile for the flow across the valve. In this orientation the hot-wire records the axial and cross-flow components of the velocity and so the CFD is presented as the combination of these signals, $|U| = \sqrt{v^2 + w^2}$.

Comparison of the predicted and measured profiles at this wire orientation reveals significant differences between the two for each of the small-angle throttle openings. This is true both in terms of qualitative and quantitative agreement. In order to highlight these differences, Figure 6.5 compares the velocity magnitude profiles for a 5.8° valve opening.

Figure 6.5 clearly shows that there is a significant qualitative disagreement between the CFD and measured profiles. The predictions tend to indicate a higher velocity toward the centre of the domain with any offset from the centreline a result of the presentation of instantaneous values. In contrast, each of the experimental profiles downstream of the valve indicates a more uniform flow field. At the 2D and 3D downstream locations the measurements indicate a very slight drop in velocity magnitude at the domain centre that contrasts with the predictions. Closer to the valve, at the 1D plane, these trends are reversed with the predicted flow showing a significant drop in the central velocity while the measurements indicate a more elliptic profile. Here, the predictions suggest high near-wall velocities that are an indication of the jetting of the flow past the sides of the valve, and the formation of attached eddies leads to the drop in velocity magnitude seen inboard of the walls in the profiles (see Figure 3.8). Downstream, the predicted flows have a strong central velocity but tend to show re-circulation toward the walls and hence the profiles reflect this as a reduced velocity magnitude. The measurements do not reflect these findings.

For the 8.3° valve opening the comparisons are very similar to those of Figure 6.5, with the CFD predicting the same profile shapes although the measured profiles are marginally more elliptic in shape. Significant contrast is found for the 12.5° flow,

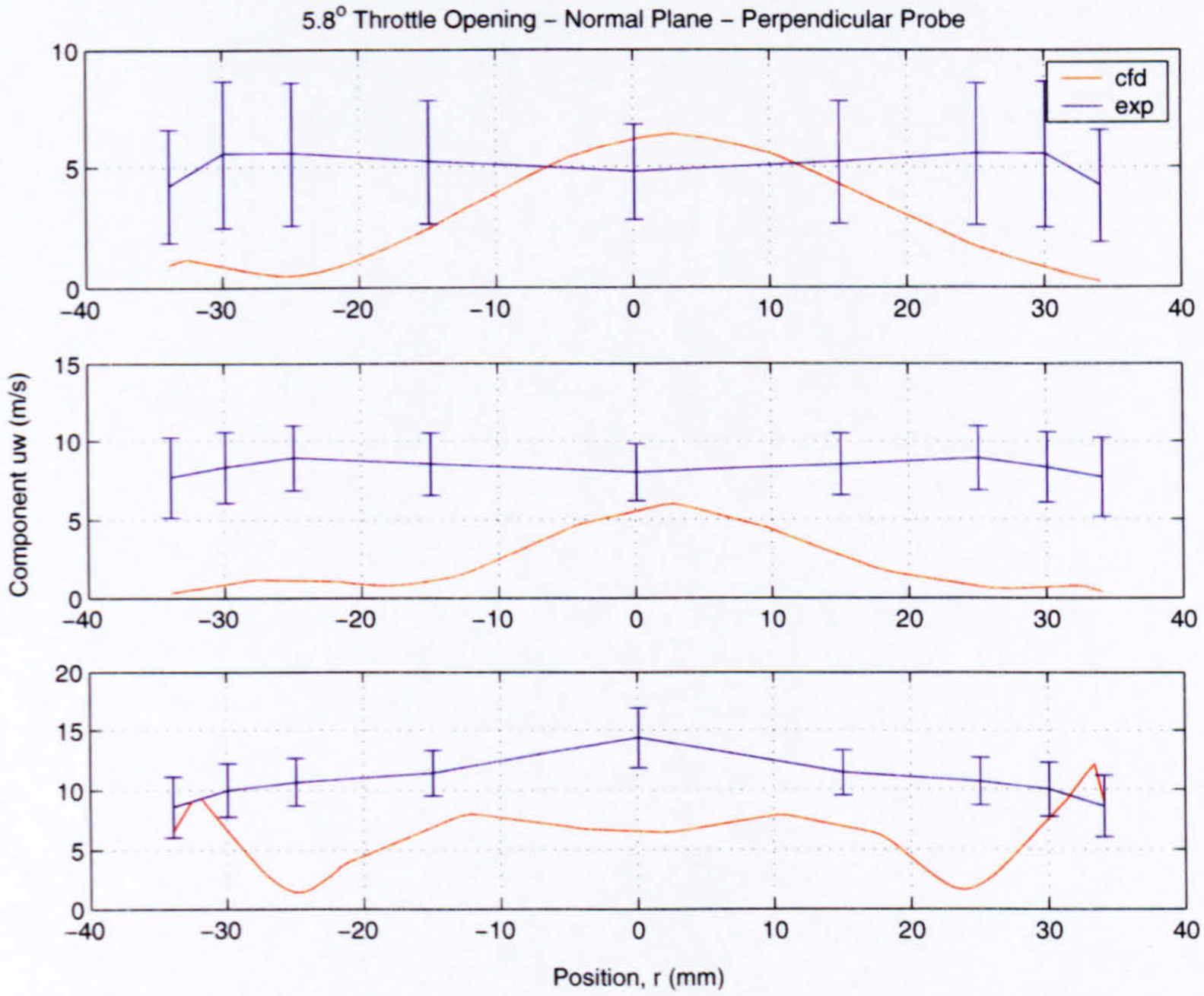

Figure 6.5: Comparison of the predicted instantaneous and time-averaged measured velocity magnitude profiles normal to the symmetry plane of the valve, at the level of the pivot, for a 5.8° throttle opening. Measurements have been made with a hot wire element orientated perpendicular to the mean flow direction. From bottom to top: 1D, 2D, and 3D measurement planes, predictions as solid red, and measurement as solid blue with bars representing the uncertainty of the measurements.

where, at the 1D plane, the measurements show significant evidence of the wall jetting previously described. Unfortunately this is poorly captured by the computationally predicted profiles that remain similar in shape to those presented here. Further downstream, the 12.5° flow predictions are flatter and at the 3D plane become asymmetric that suggests a poorly developed flow. As with all the small-angle flows the measured profiles remain similar (see Figure 5.9) and hence the agreement at this angle is poor.

Figure 6.5 again shows the level of uncertainty in the measurements to be high for this probe and traverse orientation, particularly far from the valve. At the 1D measurement plane there is approximately 20% uncertainty in the measurements, whilst at the 3D plane, this increases to approximately 50%. Given the low velocity magnitude

encountered far downstream (approximately 5 m s^{-1}) this leads to considerable scatter in the data, and thus as before, the measurements can not be used to accurately determine the velocity magnitude or the structure of the flow. This is also apparent for the remaining small-angle flows that are not presented and hence limits the comparison that can be made at these locations. At the 1D measurement plane the level of uncertainty is reduced, partially because of the increased velocities present, hence giving more confidence in the comparison to predicted data.

Parallel Wire Measurements Normal to the Symmetry Plane

In the final set of comparisons for the small-angle flows the hot-wire probe has been rotated about its body so the wire element is parallel to the flow direction and hence is sensitive to the cross-flow and downwash velocity components of the flow. This hot-wire orientation should therefore provide clear evidence of whether the predicted vortical structures are present in the measurements. The general findings show the CFD to underpredict the velocities in comparison to the measurements and show greater evidence of the vortical structures. Figure 6.6 presents the predicted $\left(|U| = \sqrt{u^2 + v^2}\right)$ and measured velocity-magnitude profiles for the 5.8° throttle opening.

Figure 6.6 again shows contrasting predicted and measured velocity magnitude profiles as found for the perpendicular wire orientation. The measurements remain largely uniform in nature with a slight elliptic shape to the profiles. Each of the downstream predicted profiles in contrast shows evidence of the twin vortex structures discussed in chapter 3. This is signified by the inflections in the profiles about the axis and the near symmetric nature of the profiles. Slight decay of the structure is apparent downstream of the valve, although the underlying shape remains. None of the experimentally measured profiles at this throttle angle reveal evidence of the vortex structures.

For the 8.3° valve opening the measured profiles are similar to those of the flow through a 5.8° opening (see Figure 5.10), although slightly higher in overall magnitude. At this angle, the predicted flow shows stronger evidence of the vortical structures close to the valve, but further downstream (2D plane) the structure decays and by the 3D

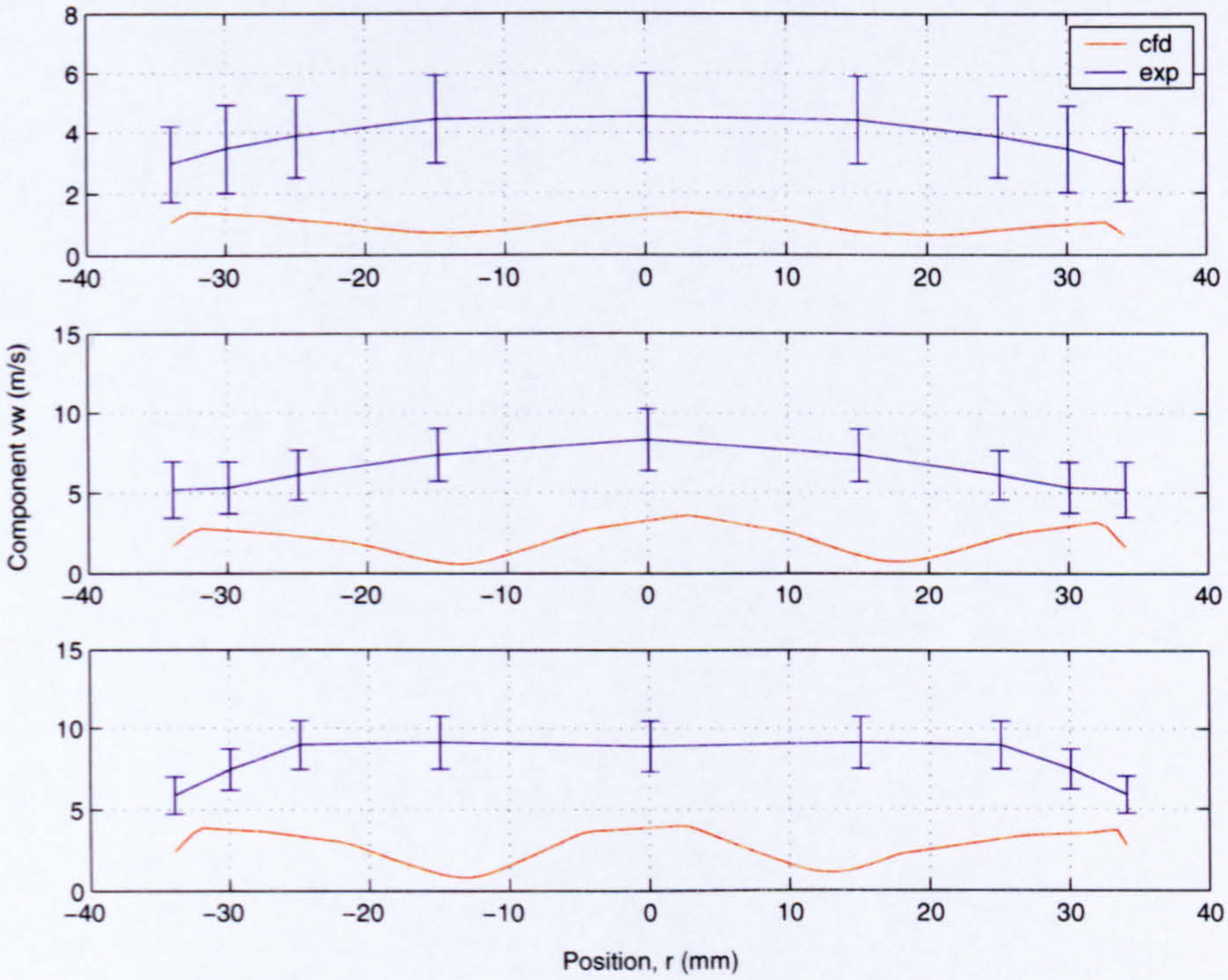

Figure 6.6: Comparison of the predicted instantaneous and measured velocity magnitude profiles normal to the symmetry plane of the valve, at the level of the pivot, for a 5.8° throttle opening. Profiles correspond to Figure 6.5 with a parallel hot-wire wire orientation.

plane there is no evidence of the vortical structures at all. At this plane the predicted profile has become elliptic, although at a significant reduction in velocity magnitude when compared to the experimental values (approximately 5% of that measured).

Finally, the predicted flow for a 12.5° throttle opening also shows strong evidence of the vortical structures at the 1D measurement plane, however, this is dissipated by the time the flow reaches the 2D plane. At the 3D measurement plane the vortex structure is again apparent and its presence questions the quality of this flow prediction. Measurements for this angle do, however, indicate the presence of the vortical structures at the 1D measurement plane. The measured velocity magnitudes are equal at the domain centre and walls, with a 50% reduction in magnitude between these regions. The predictions show the equivalent velocity magnitude at the centre, but reduced magnitude toward the wall. At locations 2D and 3D downstream of the valve the

measurements reveal the flow to have reverted back to the elliptic profiles suggesting the dissipation of the vortices.

6.3.2 Large Throttle Valve Openings

Perpendicular Wire Measurements in the Symmetry Plane

For the large-angle throttle openings the level of agreement between the predicted and measured flows varies with throttle angle and downstream location. As found for the small-angle flows, the CFD generally under-predicts the velocity magnitude and is more diffusive leading to greater differences to the measured flows at locations furthest from the valve. Figure 6.7 compares the predicted velocity profiles to the measured values for the flow through a 47° valve opening with each profile representing the combined cross-flow and axial velocity components of the flow.

It is apparent from Figure 6.7 that the flow predictions and measurements show more favourable agreement than for the small-angle flows, particularly at the 2D and 3D measurement planes. The predictions have successfully captured the velocity gradients toward the trailing-edge side of the domain although the fine detail is less well predicted. Quantitatively the CFD underpredicts the measurements by up to 20 m s^{-1} at the furthest locations from the valve, although at the 1D plane, where the agreement is worse, the discrepancy is nearer 50 m s^{-1} toward the centreline. This contrasts to the small-angle flows where the comparisons are improved toward the centre of the domain close to the valve. Qualitatively the agreement at the 1D plane is good, with the predicted velocity gradient following the trend of the measured data.

The level of uncertainty associated with the measurements is also greatly improved compared to the small-angle measurements. This stems primarily from the higher velocity magnitudes and higher velocity gradients associated with the large valve-openings. Measurements made in the strong flow leaving the valve trailing edge exhibit the least uncertainty that is expected owing to the uniformity of the flow in these regions. Where the flow is diverging, such as that leaving the leading edge of the valve, the measurements show greater uncertainty that can be attributed to the increased influence of the

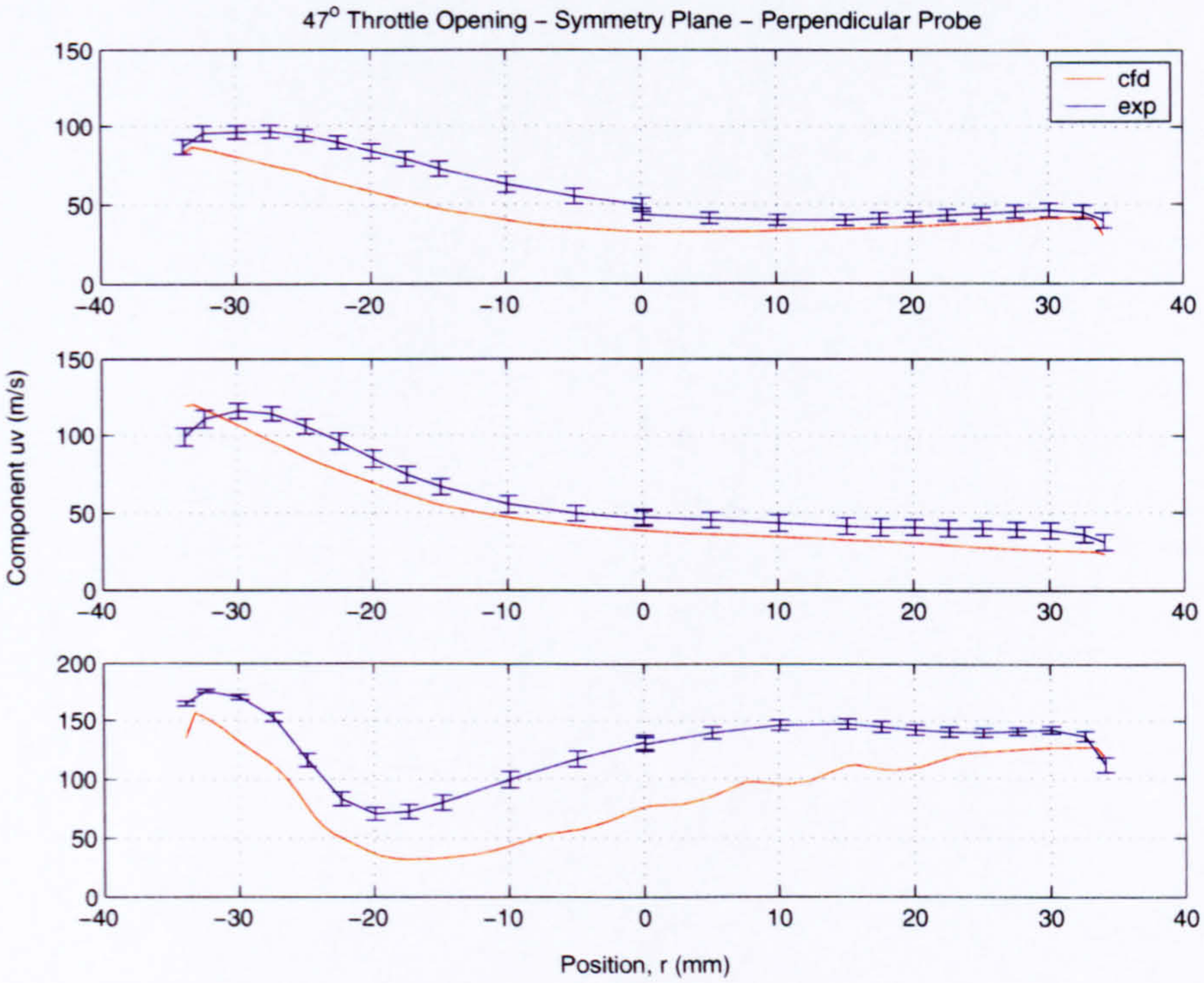

Figure 6.7: Comparison of the predicted instantaneous velocity magnitude profiles against time-averaged experimental measurements made in the symmetry plane of a valve for a 47° throttle opening. The hot-wire element is aligned perpendicular to the mean flow direction and the computational prediction is the product of the axial and upwash components of the velocity. From bottom to top, 1D, 2D, and 3D measurement planes, with positive distance representing the leading edge side of the valve. The CFD is shown as the solid red line, and the experimental values as the blue line with bars representing the uncertainty of the measurements.

second velocity component at this orientation. Overall, the levels of uncertainty are similar across the domain and the changes described are small. The change in uncertainty is also less acute as the measurements are made further downstream from the valve, with the similar levels of uncertainty at the 2D and 3D measurement planes.

Similar trends to those of Figure 6.7 are found for the flow through the valve at 30° with a slight improvement in agreement at the 1D measurement plane, and marginally worse predictions of the gradients at the 2D plane. In both cases the predictions do not become overly diffusive downstream of the valve and the agreement with the measurements is very good. The flow predictions at 19° and 60° are both more

diffusive downstream of the valve. For the 19° prediction, the flow appears less well defined and subsequently the velocity profiles are in poor agreement with the measurements at the 2D and 3D planes that remain similar to those shown here (see Figure 5.11 for reference). At the 1D plane the measured data show that flow leaving the leading edge of the valve is well defined and this is reflected by the predicted velocity profile and gradient that are reasonably well predicted with both leading- and trailing-edge flows captured. Predictions of the 60° flow show the velocity gradients to the leading-edge side of the domain to be less well defined at the 1D plane; however, the strong trailing-edge gradient is successfully captured, despite an underprediction of velocity magnitude. Further downstream the predictions show significant diffusion and hence at the 3D plane the profile is largely flat.

Overall, the comparisons reveal the CFD to quantitatively underpredict the measurements by between 10% and 60% across the range of angles considered and across the extent of the domain with the worse agreement found furthest from the valve. The diffuse nature of the downstream flows for the 19° and 60° predictions suggests that either the computational modelling techniques are inappropriate for such flows, or that the flows are under-developed and further modelling is required. Given that fully developed flow has been reasonably well modelled for the 30° and 47° flows, the latter scenario is assumed to be the cause of the poor agreement.

Parallel Wire Measurements in the Symmetry Plane

Similarly to the small-angle comparisons in this orientation, the large-angle flows reveal greater differences between the predicted and measured profiles than the perpendicular wire orientation, particularly further from the valve. Generally, the predicted profiles resemble those of the small-angle flows in their shape whilst the downstream measurements show weak similarity to their perpendicular counterparts. Figure 6.8 illustrates these points with the comparison of the predicted and measured profiles for the flow through a 47° valve opening.

The figure shows reasonable qualitative agreement of the predictions and measure-

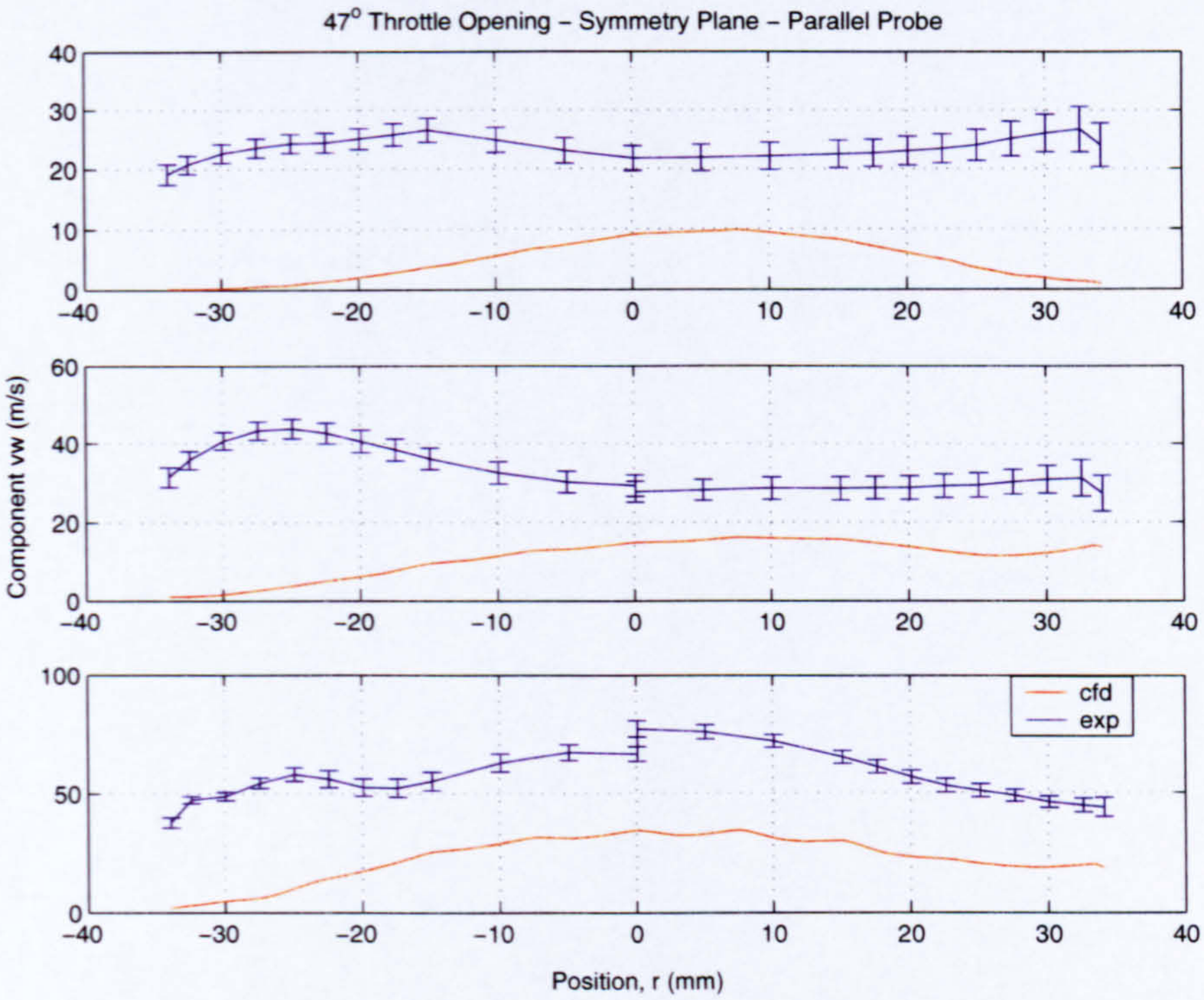

Figure 6.8: Comparison of the predicted instantaneous velocity magnitude profiles against time-averaged experimental measurements made in the symmetry plane of a valve for a 47° throttle opening. The plot corresponds to the flow of Figure 6.7 with a parallel wire orientation.

ments at the 1D plane despite the obvious under-prediction of velocity magnitude that remains reasonably consistent at 35 m s^{-1} and 45 m s^{-1} below the measurements across the trailing-edge and leading-edge sides of the domain respectively. This step across the domain is brought about through the use of separate experimental runs to construct the velocity magnitude profile. Only the relatively high velocity flow toward the trailing-edge side of the domain that is present in the measurements is not reflected by the predictions. This is more pronounced at the smaller of the large-angle flow measurements. Further downstream the differences are greater. The predictions clearly show similarities to the flow structure at the 1D plane as the flow moves downstream, although the flow becomes more diffused further from the valve. The measurements show that the strong flow toward the trailing-edge of the domain to remain present to the 2D plane, and although present at the 3D plane, this has also been diffused.

The measurements in the leading-edge side of the domain show that as the flow moves downstream it is diffused leading to a more uniform flow and flattening of the velocity profile. Therefore, the agreement between experiment and computation is only reasonable at the 1D measurement plane, while further downstream the variations lead to poor agreement.

Comparison of the remaining large-angle flows reveals similar trends to those described above. The predicted profiles exhibit increased velocity magnitudes toward the centre of the domain and very low velocity magnitude toward the trailing-edge side of the domain. As found for the perpendicular wire predictions, the 60° flow prediction is overly diffusive far downstream of the valve and the profiles are generally less well defined than those of Figure 6.8. Velocity profiles for the measurements made at the remaining large-angle openings also show similarities to those of Figure 6.8, but the two smallest valve openings show evidence of shear layers toward the trailing-edge side of the domain. The overall agreement between the predictions and measurements for this orientation is therefore poor, with only the flow at the 1D measurement plane providing reasonable agreement across the range of angles considered. For the two planes furthest from the valve the agreement is poor, with differing profile shapes and a clear underprediction of velocity magnitude. There is a possibility that the measurements may have been influenced by the axial velocity component given the stronger trailing-edge flow that is not predicted by the computations despite these providing reasonable agreement for the perpendicular wire orientation. This hypothesis is strengthened when considering the much higher measured velocity magnitudes than those predicted in comparison to the results at other orientations.

Perpendicular Wire Measurements Normal to the Symmetry Plane

For this wire and traverse orientation some common flow features are found between the measured and predicted flows across the range of throttle angles considered. Profiles resembling those of a classic twin-vortex structure are found for the majority of the throttle angles at the 1D measurement plane, which appear to dissipate by the 2D

measurement plane. However, these profiles are not an indication of the vortex structure, as the velocity components measured are the axial and cross-flow components, and hence the profiles correspond to shear layers and recirculations in the flow. Figure 6.9 shows the velocity magnitude profiles for the 47° valve opening that clearly depicts the change in flow structure between the downstream measurement locations.

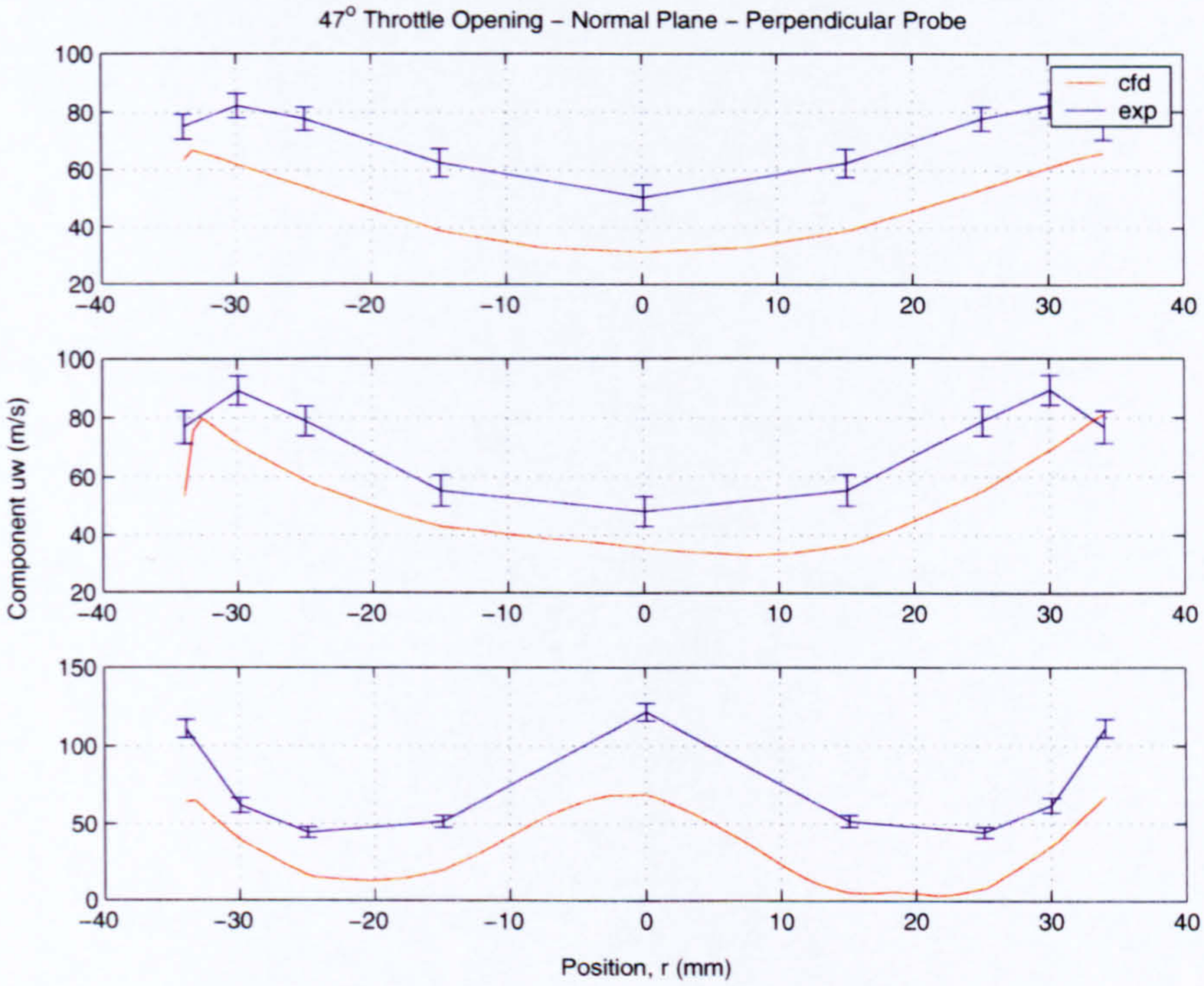

Figure 6.9: Comparison of the predicted instantaneous velocity magnitude profiles against time-averaged experimental measurements made normal to the symmetry plane of a valve for a 47° throttle opening. The hot-wire element is aligned perpendicular to the mean flow direction and the computational prediction is the product of the cross-flow and downwash components of the velocity. From bottom to top, 1D, 2D, and 3D measurement planes, with the CFD is shown as the solid red line, and the experimental values as the blue line with bars representing the uncertainty of the measurements.

Figure 6.9 shows good qualitative agreement between the predictions and measurements with similar profile shapes for each, and similar levels of dissipation present further downstream. Quantitatively the CFD again underpredicts the measurements, however, given the improvement in qualitative agreement, the predicted trends are improved for the large-angle flows. For both the measurements and predictions, the

distinctive shear-layer profiles are no longer present at the 2D and 3D measurement planes and inverted elliptic profiles are found. Evaluation of the predictions reveals that the high near-wall velocities at the 1D measurement plane represent the jetting of the flow past the sides of the valve, while the high central velocity represents the separated leading-edge flow sweeping down into the domain. At the 2D and 3D planes, the effect of the jetting is still apparent with high near-wall velocities, however, the downward directed leading-edge flow is no longer present and hence the core of the domain experiences much lower velocities (see Figure 3.5).

For the remaining large-angle flows, whilst the measurements show similar profiles to those presented here (see Figure 5.13 for reference), the predicted profiles show greater differences over the throttle opening range. At 19°, the predicted flow at the 1D plane shows a profile associated with regions of reversed flow and attached vortices as discussed in chapter 3. The predictions for this throttle opening differ most from those of the 47° flow, and hence these are also presented here in Figure 6.10.

Figure 6.10 shows that at the 1D plane, the predicted profile is similar to that shown in Figure 6.9, but the two troughs are inflected. At the 2D measurement plane, a region of high velocity is predicted in the centre of the domain with low near-wall velocities. This again represents the separated leading-edge flow, however, the smaller valve opening causes the acceleration of the flow past the leading edge to increase, and the overall level of downwash is reduced although spread further downstream. This is thus reflected in the velocity profile at the 3D measurement plane that also has raised velocities at the domain centre. Unfortunately, the experimental measurements show similar profiles to those of Figure 6.9, and hence totally contrast with the predictions. It is difficult to say whether the computational model is incorrectly modelling the flow, or whether the experimental measurements are incorrectly representing the flow features.

The predicted velocity profiles for the 30° throttle opening show similarities to both the 19° and 47° flow predictions. Generally, the shapes of the profiles are similar to those of the 47° flow predictions (Figure 6.9), however, the central domain shows marginally higher velocity magnitudes that resemble the profiles of the 19° predictions (Figure

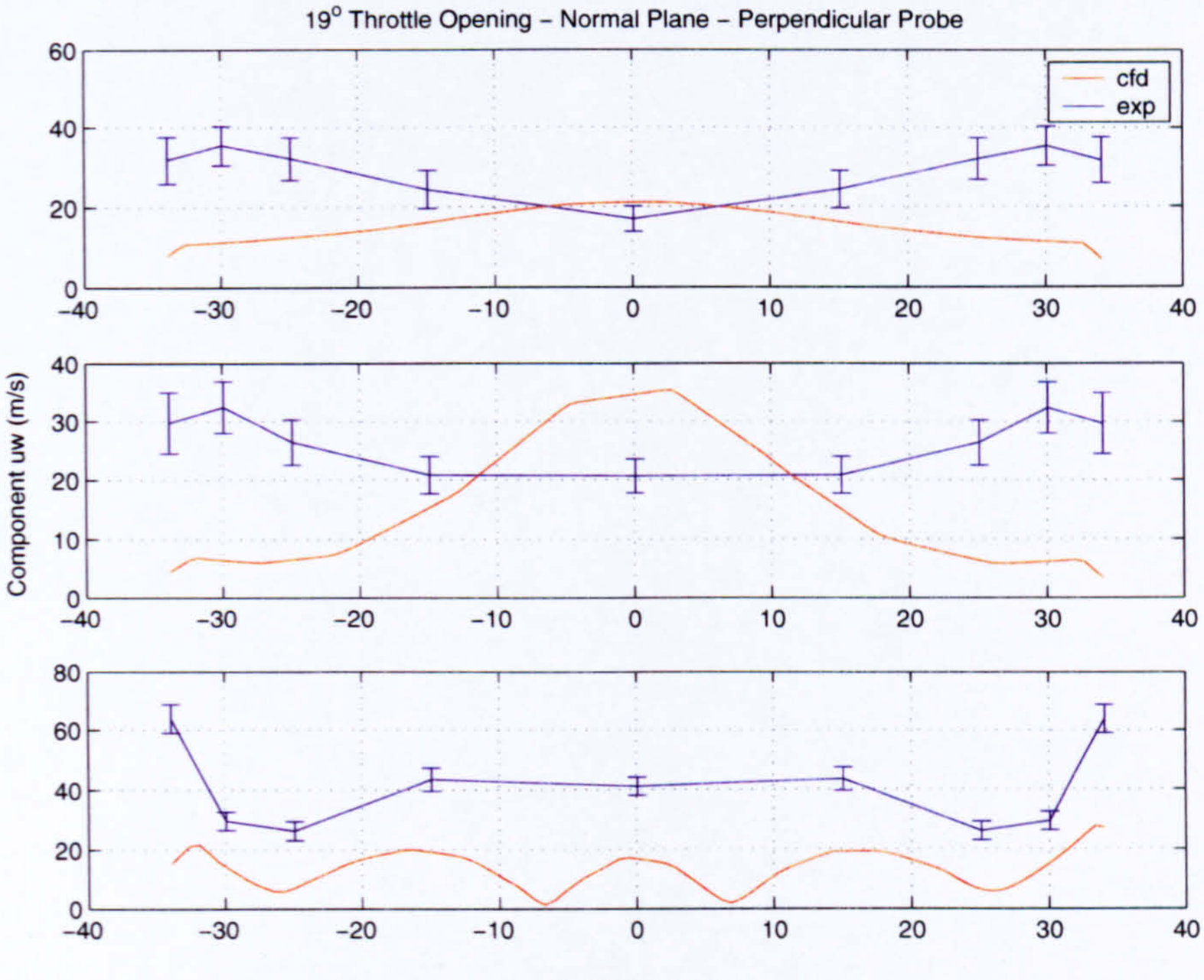

Figure 6.10: Comparison of the predicted instantaneous velocity magnitude profiles against time-averaged experimental measurements made normal to the symmetry plane of a valve with a perpendicular wire orientation for a 19° throttle opening.

6.10). The measured profiles remain similar to those of the 47° flow, and hence the overall agreement between these and the predictions is good. However, the similarities between the experimentally measured profiles, and the subtle differences between each of the predicted profiles, suggests that the measurements are insensitive to changes in the flow structure. The computational predictions are able to clearly distinguish between subtle changes in the flow structure, and the velocity profiles are generated using precise velocity components.

At 60°, the predicted velocity profile close to the valve is almost constant across the span of the domain with the exception of raised near-wall velocities. The much wider opening of the valve leads to reduced downwash, although there is still jetting of the flow past the sides of the valve. By the time the flow reaches the 3D measurement plane the velocity profile is uniform and any flow structure appears to have been damped out.

Experimentally these findings are not shown, and the resulting profiles are similar to those of the 47° flow. Agreement between the results therefore varies for each location downstream of the valve, but overall the agreement if poor for this valve angle. The computational modelling of this throttle opening appears underdeveloped in comparison to the measurements and the other flow predictions.

Parallel Wire Measurements Normal to the Symmetry Plane

For this final set of comparisons, the hot-wire orientation leads it to be sensitive to the cross-flow and downwash components of the flow and hence the presence of the twin axial vortices should be well represented by the velocity profiles. As shown in chapter 5, the measured profiles reveal this to be the case (see Figure 5.14), with each flow showing evidence of the vortices at the 1D measurement plane. Evaluation of the computationally predicted velocity profiles also shows strong evidence that these vortices exist and these are now compared. Figure 6.11 shows the predicted and measured velocity profiles for the 47° flow.

The predicted velocity profiles in Figure 6.11 clearly show evidence of the vortex structures at all three downstream measurement locations. Each profile also shows inflections at the axis that is a result of the directional ambiguity brought about by summation of the individual velocity components. Also apparent in the predicted profiles is a degree of asymmetry that varies at each of the measurement locations and highlights the transient nature of the flow. The measurements show strong evidence of the vortex structures close to the valve, but further away, this is diminished. At the furthest locations from the valve, the measured profiles have flattened out, however, there exists weak evidence of the vortices presence. The velocity magnitude of the measurements is consistently higher than those of the predictions, and this may again result from the influence of axial velocity. Should this be occurring, then evidence of the vortical structures would be swamped by the additional velocity component, and would also explain the lack of inflection in the profiles at the measurement planes furthest from the valve. Additionally the lack of resolution of the measurements hinders

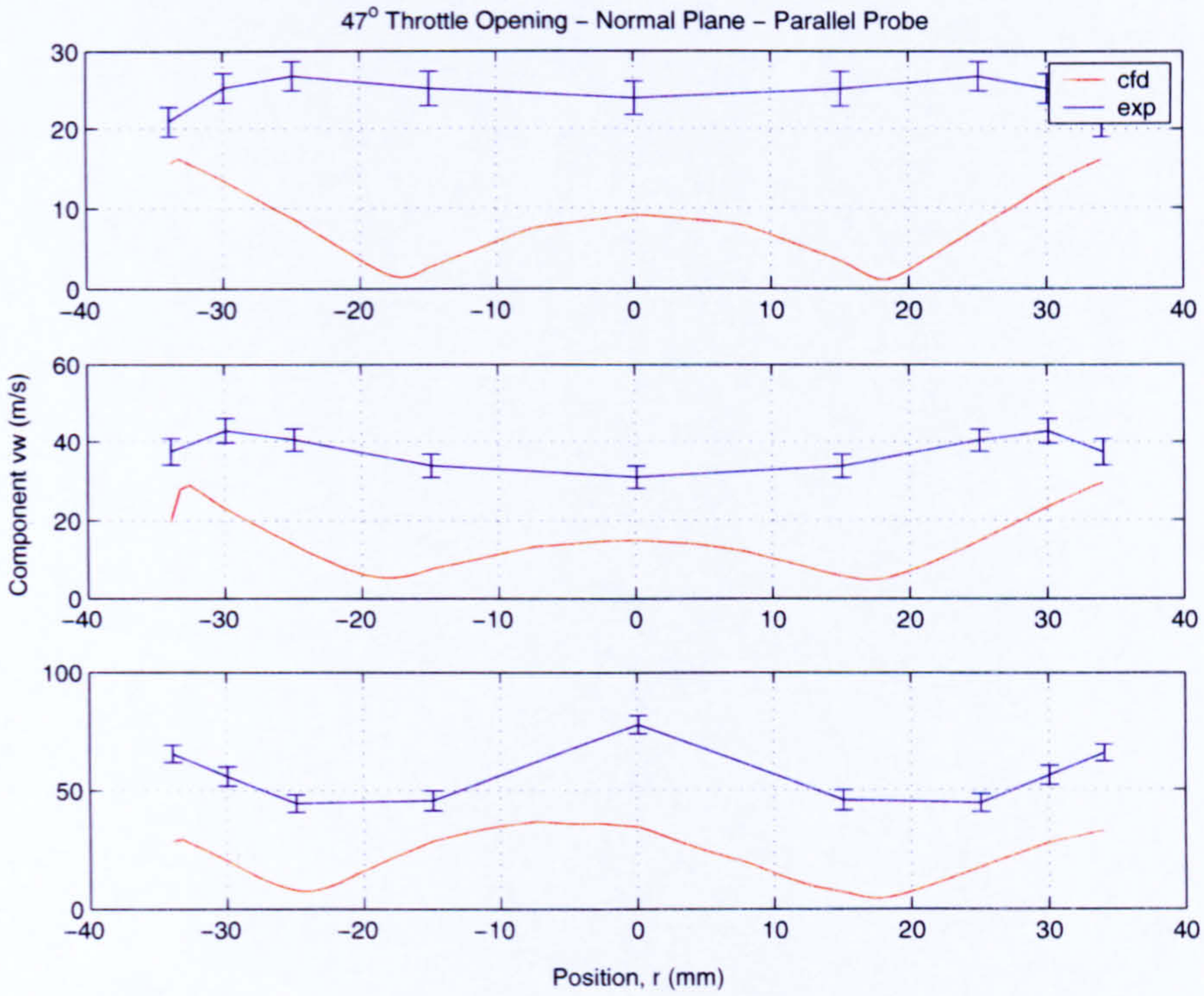

Figure 6.11: Comparison of the predicted instantaneous velocity magnitude profiles against time-averaged experimental measurements made normal to the symmetry plane of a valve for a 47° throttle opening. The plot corresponds to the flow of Figure 6.9 with a parallel wire orientation.

the comparison process. Thus, although the agreement is fair at the 1D measurement plane, elsewhere it is poor.

Very similar results to those of the 47° opening are found for both the 19°, and 30° flow predictions and measurements, although slight improvement in agreement is found at the 1D plane. Each of the predicted profiles shows strong evidence of the vortical structures, particularly at the 1D and 2D measurement plane, and slight damping of the structure at the 3D measurement plane. For the 60° valve opening the predicted profiles differ from the other large angle flows as is shown in Figure 6.12.

Figure 6.12 reveals that the measurements show similar trends to those of the other large-angle flows; however, the predicted profiles do not show as strong evidence of the vortical structures as has been found for the other predictions. Evaluation of the computational results reveals that the dominant vortical structures remain in proximity to

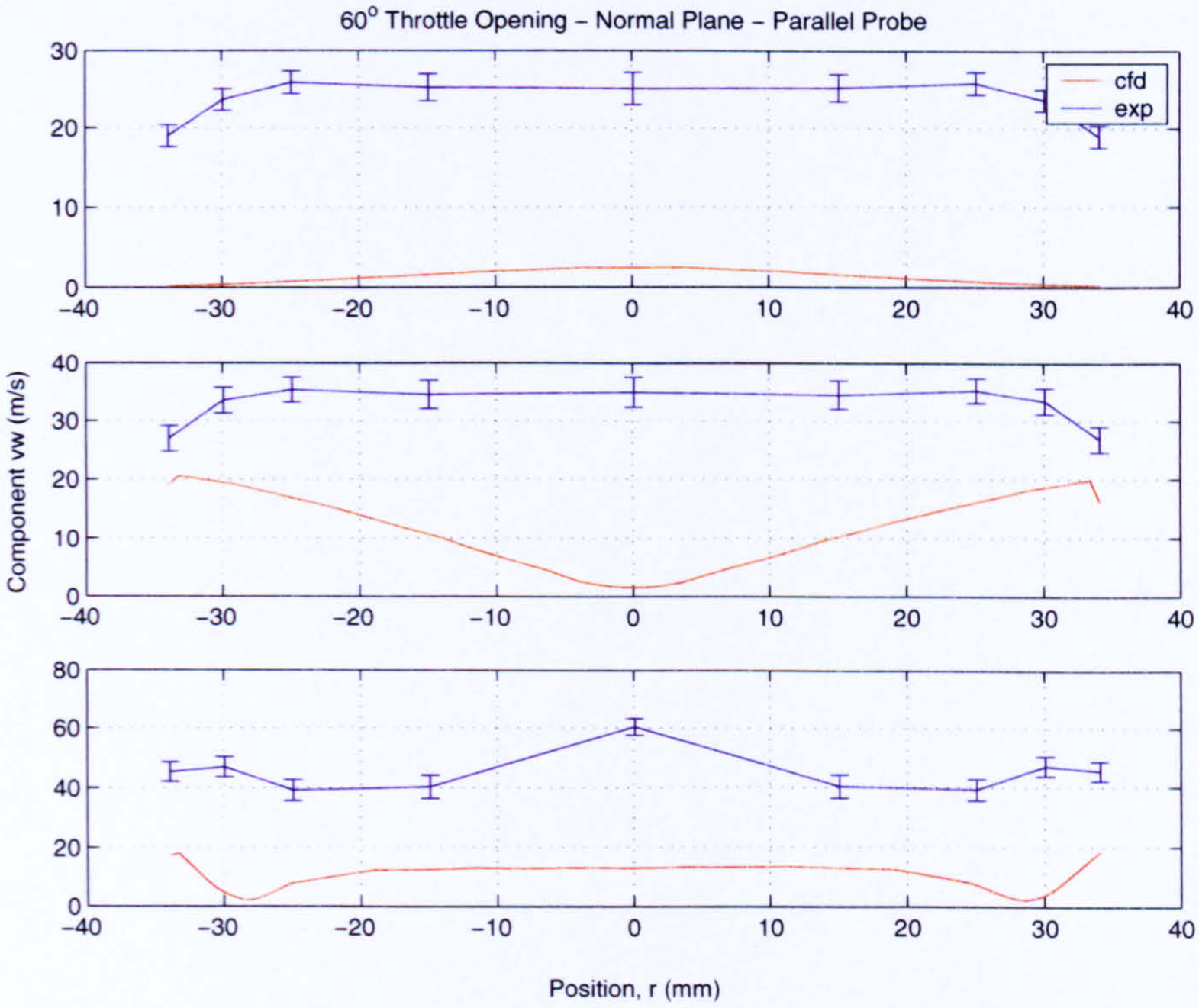

Figure 6.12: Comparison of the predicted instantaneous velocity magnitude profiles against time-averaged experimental measurements made normal to the symmetry plane of a valve with a parallel wire orientation for a 60° throttle opening.

the valve and that the downstream flow is less well developed than the other predictions. This is apparent from the figure that shows mild evidence of the structures and a very flat profile far downstream. This reflects the findings at each of the other orientations considered for this throttle angle.

6.3.3 Discussion of Results

The comparisons have revealed that several differences exist between the computational and measured velocity profiles, many of which depend on the particular orientation of the hot-wire sensing element and the direction of the hot-wire traverse. The key to the differences between the different orientations is the difference in presentation style of the two sets of results, i.e. the presentation of instantaneous predicted values and time-averaged measurements. This difference can have a significant effect on the velocity

profiles generated, depending on the dominant velocity components used to generate the profiles. To explain these differences, and to expand on them, it is beneficial to consider the different probe orientations separately.

Perpendicular Wire Measurements in the Symmetry Plane

In this hot-wire orientation the axial and downwash components of velocity are considered and, of these, the axial component is responsible for the transport of the flow through the domain and hence is generally the dominant component. However, the downwash component becomes more significant at different locations and throttle angles owing to the significant changes in flow structure that occur, and hence its influence on the velocity magnitude profiles can not be ignored.

Flows past the leading and trailing edge of the valve are dominated by the axial flow component and it has been shown that, depending on the throttle angle, either the leading- or trailing-edge flow dominates the shape of the velocity profile . Moving downstream sees these regions of high-energy flow diffuse into the surrounding regions of low-energy flow and the profiles reflect this with a reduction in peak magnitude and a subsequent widening of the pronounced shape.

Similarly, the downwash component tends to be at its strongest close to the valve and is largest toward the leading edge side of the valve owing to the divergent nature of the geometry. Small-angle throttle openings tend to generate regions of reversed flow immediately downstream of the valve that are not seen at the higher throttle openings. This significantly increases the downwash angle, but also reduces the dominance of the axial flow on the measurements in these regions. Directional ambiguity of the hot-wire measurements, and the similar manipulation of the computational data, means that these regions of reversed flow are not necessarily distinguished from the normal, non-reversed flow.

Time-averaging of the measurements should have little effect on the resulting velocity magnitude profiles as the axial and downwash components of the flow are predicted to remain predominantly steady through the symmetry plane with oscillations of signif-

icance only occurring in the cross-flow direction. This is reflected in the measurement uncertainty that remains relatively low and hence allows a well defined flow structure to be determined in comparison to the measurements made at the other wire orientations considered. Consequently, the comparisons made in the previous sub-sections are not significantly affected by these factors.

The main issue in the comparisons is the determination of what is being compared in each profile. At the 1D measurement plane for the small valve-openings, both the predicted and measured profiles match toward the centre of the domain whilst toward the walls the CFD appears to significantly underpredict the velocity magnitude. In the near-wall regions the flow is dominated by the axial component of the velocity owing to the acceleration of the flow past the valve, and also by the proximity of the walls limiting downwash. The hot-wire probe is readily able to capture the axial flow component in this orientation, thus the measured velocity gradients in proximity to the walls appear realistic. As the probe moves away from the wall, the sensing wire experiences greater influence of the downwash component of the flow and additionally, the predictions indicate that regions of reversed flow also exist for the small-angle valve openings. Thus in the regions toward the domain centre the measurements become more ambiguous. In order to alleviate this issue, the hot-wire probe should be calibrated to distinguish between velocity components, either through the use of yawed or multi-wire probes, or with a single-normal probe, through multiple readings with the probe rotated to capture the individual components of velocity.

Therefore, given the findings above, the following can be concluded. At large throttle openings, where the axial flow component is dominant, and reversed flow does not occur, the velocity magnitude profiles offer a good representation of the axial velocity component of the flow. At small throttle openings close to the valve, where the flow may experience reversal, and significantly higher levels of downwash occur, the resultant velocity profile becomes unclear. The reduced, or even reversed, axial flow component toward the centre of the domain, and the increased level of downwash, means that no single velocity component necessarily dominates, and the addition of the directional

ambiguity of the readings makes it more difficult to interpret the velocity profiles. At smaller throttle openings away from the valve, the downwash is no longer so strong and the axial flow component again dominates although not to such an extent as for the large throttle openings. Hence the measured velocity profiles offer a fair representation of the axial flow component of the flow. The computational predictions underpredict the velocity gradients toward the wall that suggest the model is overly diffuse in these regions. This may be the result of the modelling techniques used, such as the turbulence model, or be more fundamental in nature such as a lack of grid resolution in the regions of high gradients.

Parallel Wire Measurements in the Symmetry Plane

Rotation of the hot-wire probe such that the sensing element is aligned parallel to the mean flow direction, or domain axis, generates a signal that comprised the cross-flow and downwash components of velocity. The results of the computations and the flows found in previous studies (as discussed in chapter 3), indicate that the downwash component is dominant in the central region of the domain that results from the separated flow leaving the leading edge of the valve. Cross-flow velocity components tend to vary more readily with throttle angle and measurement location; however, for this orientation and measurement plane, cross-flow effects would only become significant if asymmetric or periodic flow features are encountered. Therefore, the combined velocity magnitude profiles should indicate an increased velocity magnitudes toward the centre of the domain as a result of the downwash and cross-flow, while a reduced velocity magnitude should exist toward the walls where axial flow dominates.

The velocity magnitude profiles presented in the previous sections have shown disagreement between the measured and predicted flows, both for the small- and large-angle valve openings. For each throttle angle considered, and for each measurement location, the computationally predicted velocity magnitude remains significantly lower than that measured. Additionally, the predicted profiles show weaker velocity gradients and reduced structure in comparison to the measurements. Each of the predicted pro-

files reflects the point raised above, i.e. a higher central velocity magnitude and reduced velocity magnitudes toward the wall of the domain. Any bias in the region of higher velocity is toward the leading-edge side of the domain. In contrast, the experimentally derived profiles not only show raised velocity magnitudes overall, but also show significant increases in velocity magnitude in proximity to the walls, particularly close to the valve. These discrepancies make establishing the more correct flow features difficult, and some explanations are considered.

Firstly, the CFD presents an instantaneous velocity profile that is derived from the final iteration of the solution, whilst the experimentally derived profiles result from the time-averaging of the measurement signals. When considering only the cross-flow component of velocity, the two methods of presentation can have significant affect on the resulting velocity profiles that brings additional uncertainty into any comparison. Cross-flow components in the computational predictions generate a positive and non-zero contribution to the velocity magnitude, or no contribution at all. The cross-flow contribution will therefore lie in the range of zero to maximum, which depends entirely on the time the solution ended. For the experiments, time-averaging of the cross-flow component, in absolute terms, would lead to a zero mean on account of the oscillation about the symmetry plane. However, the directional ambiguity of the hot-wire system means that a positive value for the cross-flow component is recorded, and that this is the time-mean component of the cross-flow component. Therefore, the experimentally derived profiles include the mean contribution of the cross-flow component for each set of measurements, while the predicted profiles include the instantaneous value that by its nature will vary over a range of values and be different for each throttle angle considered. This leads to greater uncertainty when comparing the profiles and inconsistencies between each of the profiles. The majority of these effects should only be of influence toward the centre of the domain where cross-flow becomes significant.

A second factor that may explain the differences between the predictions and measurements is the possibility of axial flow components contributing to the measurement signal, as has been previously discussed. Given the large differences in velocity mag-

nitudes and profile shapes between the data, this is a distinct possibility. Evaluation of the profiles (see Figures 6.4 and 6.8) shows that the discrepancy is greatest at the closest measurement plane to the valve, with the measurements showing much higher near-wall velocity magnitudes. Comparison of these profiles to those made with a perpendicular wire for the same valve openings (see Figures 6.3 and 6.7) reveals that, at the 1D measurement plane particularly, similarities exist between the measured profiles, while the predicted profiles show little in common. It appears as though the axial component of the flow is influencing the measurements at the walls, particularly toward the trailing-edge side of the domain. As discussed in the previous sections, it is in the near wall regions that the axial flow is dominant and hence its influence would be greatest in these regions. The further the measurements are made from the valve, the less the similarity of the parallel measurements to the perpendicular measurements. If the measurements are being influenced by the axial velocity as suggested, the influence will be reduced downstream owing to the lower magnitude of the axial component and hence the downwash and cross-flow components are not so readily drowned out. This is also reflected by the improved agreement between the measurements and predictions further from the valve, particularly for the smaller valve openings.

For the parallel wire measurements to be influenced by the axial velocity component requires that the wire be misaligned to the symmetry plane, rotationally misaligned with the domain axis, or a combination of both. In the case of mis-alignment with the symmetry plane, a probe positioned marginally to one side of the symmetry plane will record an artificially high velocity magnitude on account of the increased component of cross-flow. Flow past the valve tends to be symmetric about the geometric symmetry plane and as the flow passes over the leading edge of the valve it tends to converge at the centreline (see Figures 3.13 and 3.14 for reference). The convergent nature to the flow would be incident to the wire and hence an increased cross-flow component would be recorded from the misaligned probe. For the second scenario, an angular misalignment, the flow approaching the wire would again be at incidence and hence an increased cross-flow component would be recorded by the measurements. A combination of the two

effects could lead to a significant increase in the cross-flow component, or the two may partially cancel out; however, the misalignment will differ for each set of measurements and this leads to greater uncertainty in interpretation of the results.

Evaluation of the true probe yaw effects on the signal requires a full directional calibration of the probe to allow the influence of the individual velocity components to be determined. As only a simple calibration has been performed the latter is not possible, but using a very basic approach, where the velocity is presumed a function of wire orientation alone, a first-order approximation can be made for the influence of the axial velocity on an angular misalignment of the probe. With the probe aligned perfectly parallel with the flow direction there is no influence of the axial velocity on the probe, and at the extreme, when the probe is perpendicular to the flow, there is 100% influence of the axial and zero cross-flow influence. Thus, if a sine law relationship is assumed to hold between these two extremes where the velocity components are a function of the yaw angle alone, and that the mis-alignment of the probe is $\pm 5^{\circ}$ at most, then the signals may record approximately 9% of the axial velocity for a corresponding 0.4% reduction in the cross-flow velocity. Given that the axial velocity component is considerably larger than the cross-flow component, this provides a reasonable increase in the flow velocity that may well explain the resulting profiles.

For example, for the 5.8° flow of Figure 6.3, the peak near-wall velocity magnitude near the valve trailing-edge is approximately 50 m s^{-1}, which is assumed to be predominantly the axial component. Thus, assuming a 5° probe misalignment in the parallel orientation, this wound give rise to a 4.4 m s^{-1} increase in the recorded velocity magnitude in this region. Evaluation of Figure 6.4 shows that a reduction in velocity magnitude by this amount would significantly reduce the trailing-edge velocity peak. As the perpendicular profiles are dominated by high near-wall velocities, performing this calculation across the span of the measurements would have greatest influence in these regions and little change toward the centre of the domain. However, this alone would not be sufficient to remove the peaks entirely from the velocity profiles and therefore there is a high probability that the probe is also misaligned to the symmetry plane.

An additional source of error stems from supporting the hot-wire probe body perpendicular to the flow direction. Normally hot-wire probes are mounted such that the probe body lies parallel to the flow direction therefore minimising the blockage and disturbance caused by the probe. Here the probe has been mounted perpendicular to the flow for practicality as discussed previously. However, Bruun (1995) shows findings that suggest a probe body orientated perpendicular to the flow direction produces a 6-15% variation in velocity when compared to a parallel probe body orientation for the same flow. Therefore part of the discrepancy can also be attributed to this effect.

One further aspect that affects the measurements is that the free-stream conditions for each individual set of measurements varies slightly from case to case. As each set of measurements across the domain is made from two individual experiments, and hence the full set of profiles for one probe orientation consists of 6 individual experiments, there is an offset in free-stream conditions for each that can be seen in the velocity profiles. This is particularly obvious in measurements made furthest from the valve where velocities are low, for example the upper plot of Figure 6.4, and this leads to greater disagreement and uncertainty when comparing to the predicted profiles. This does not directly affect the measurement uncertainty, as this is related to the free-stream, but the resulting offset compromises the comparisons.

From the discussions above it is clear that several factors may be influencing the comparisons of the predicted and measured data. One further aspect to consider is the effect of combining the individual velocity components to form the velocity magnitude profiles. In order to evaluate these effects the individual velocity profiles need to be considered alongside the combined signal. This can only be achieved for the predicted flows here as the hot-wire has not been calibrated to extract the individual velocity components. Figure 6.13 shows the velocity profiles of the combined and individual velocity components for the predicted flow through a 47° throttle opening at the 1D measurement plane. The upper plot of Figure 6.13 is equivalent to the measurements made with a perpendicular wire orientation and the lower plot to those of a parallel wire orientation.

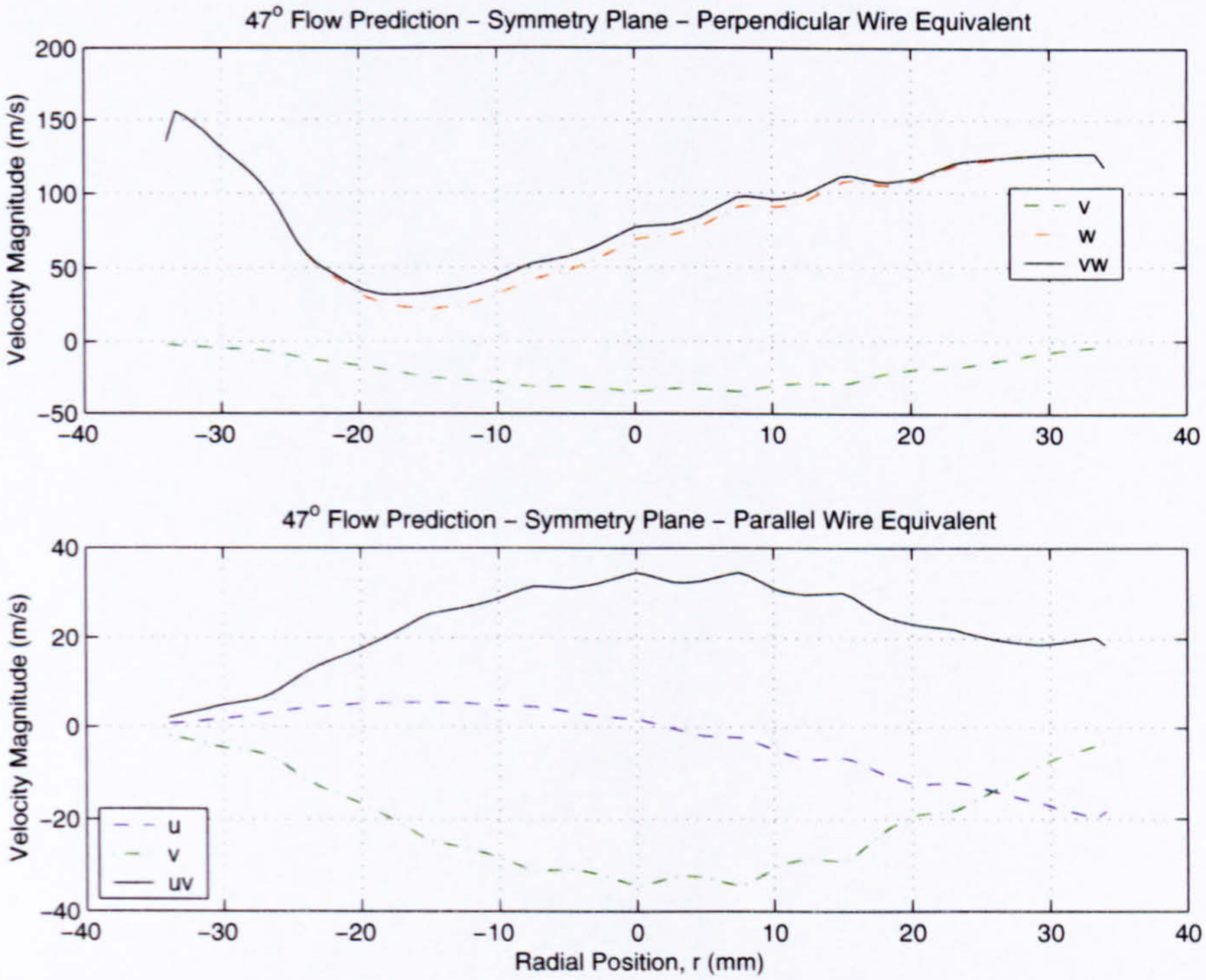

Figure 6.13: Predicted instantaneous velocity profiles for the flow through a 47° valve opening in the symmetry plane, 1D downstream of the valve. The upper plot shows the equivalent of perpendicular-wire measurements with the axial, downwash, and combined velocity components shown. The lower shows the equivalent to parallel-wire measurements with the cross-flow, axial, and combined components.

The figure shows that the equivalent predictions to the perpendicular wire measurements (upper plot) give good representation of the axial flow component at large angles owing to the relatively weak downwash component. The profiles equivalent to a parallel wire measurement (lower plot) show that the downwash component of the flow has greater influence on the combined profile than the cross-flow component, particularly at the domain centre. Toward the leading edge side of the domain, the cross-flow component is more significant and becomes dominant in immediate proximity to the wall. This only occurs for the large-angle predictions where vortex shedding is predicted; however, for the physical measurements the same effect would be seem when using a misaligned probe. Despite this, the cross-flow component is not strong enough to generate a combined velocity profile with high leading-edge peaks, and certainly not high

trailing-edge peaks, both of which are present in the experimentally derived velocity profiles.

The combination of effects discussed and the evaluation of the velocity profiles suggest that the experimental measurements are indeed influenced by the axial velocity component of the flow in this wire and traverse orientation. Given that probe position has not been accurately ascertained owing to the initial under-estimate of the importance of the measurements, the likelihood of probe misalignment is high. Hence, this would account for the similarities in the profiles between the perpendicular and parallel measurements. The possibility that the raised leading- and trailing-edge velocities in the measured profiles are a result of increased cross-flow caused by vortex shedding is also considered. However, the raised velocities are local to the domain walls, and any vortex shedding in these regions is unlikely to be damped out so rapidly toward the centre of the domain, and additionally the presence of the vortices in the strong shear flow leaving the trailing edge is unlikely. The predictions suggest this and show that vortex shedding and flow oscillations, although biased toward the leading edge side of the domain, have significant influence away from the walls. These oscillations could be incorrectly modelled by the computational model, or they may be over-damped in the wall regions owing to poor wall gridding, or through excess damping of the flow using the k-ε turbulence model. The latter has previously been shown to be overly diffusive in the prediction of periodic flow oscillations (Tucker, 2001; Nishimura & Kimura, 2001). Limitations in the experimental investigation permit further exploration of these ideas.

Perpendicular Wire Measurements Normal to the Symmetry Plane

Measurements made with the perpendicular wire orientation in the plane normal to the symmetry plane are sensitive to the cross-flow and axial velocity components of the flow. Of these, the axial flow is predicted to dominate for each throttle angle, despite the increased influence of the cross-flow component at smaller valve openings.

Agreement between the predictions and measurements has been shown to be greater for the large opening angles than for the small openings where agreement is poor.

Comparisons of the velocity profiles reveals two types of flow structure exist for both the experimental and predicted flows that depend on the valve opening angle. Similar profiles are found for the large valve openings where axial vortices are predicted to exist downstream of the valve. These are driven by the flow passing over the leading edge of the valve that descends into the domain before energising the near-wall flows and sweeping up the walls as the flow moves downstream (see chapter 3). This is reflected by the large-angle velocity profiles that show increased near-wall velocities downstream of the valve, and an increased central velocity closer to the valve corresponding to the flow leaving the leading edge. These characteristics are also found for the experimentally derived velocity profiles.

At small valve openings, the profiles indicate a change in the flow structure and there is no longer agreement between the predictions and measurements. The predictions show the flow in the centre of the domain to dominate, and again this is a result of the axial component of the flow leaving the leading edge of the valve. At the smaller angles, the flow passing the leading edge experiences severe separation that leads to increased levels of downwash and regions of reversed flow immediately downstream of the valve. The small troughs in the profiles are representative of the attached eddies on the downstream face of the valve, and the near-wall peaks in velocity are a result of the jetting of the flow between the valve and wall that form these eddies (see Figure 3.8). Further downstream the central flow dominates whilst the near-wall flows have significantly diminished. Although the axial vortices are still present, the separated leading edge flow provides less energy to the wall regions downstream of the valve. These patterns are not shown by the measurements at the small valve-openings. There is a marginal increase in the central velocity close to the valve that is just maintained downstream by all but the smallest valve angles. None of the measurements made for the small valve openings show any evidence of the wall jetting apart from the 12.5° flow.

Thus the velocity profile comparisons for small-angle flows are fairly inconclusive. It is possible that the experimental measurements are insufficient to capture the detail of the flow at the lower velocities found here, or that the predicted flow structure does

not exist. The former, in addition to the high level of uncertainty in the measurements, and the ambiguity of the readings, seems likely. Typically the mean velocity magnitude of the small-angle measurements for this hot-wire orientation are of the order of 5 to 15 m s^{-1}; however, the level of uncertainty in the measurements lies in the range 20 to 30% at the 1D measurement plane, and rises to 35 to 55% by the 3D measurement plane. This is a significant level of uncertainty that combined with the other factors discussed above, makes fair comparison to the predictions impossible. For the large-angle flows, the experimentally derived profiles are a reasonable indication of the axial flow component, particularly at the walls and centre of the domain.

Parallel Wire Measurements Normal to the Symmetry Plane

Here the cross-flow and downwash components of the flow are measured, as for the parallel-wire measurements made in the symmetry plane. Consequently, similar factors affecting those measurements are apparent here, such as probe misalignment issues, the influence of the individual velocity components, and the effects of time-averaging the cross-flow velocity component. Also, in a similar manner to the perpendicular wire measurements in the same plane, asymmetry in the predicted profiles results from the presentation of instantaneous data, that contrasts to the time-averaged and reflected experimental values. For this orientation, the downwash component of the flow provides a clear indication as to the presence of the twin axial vortices within the flow. These vortices are driven by the downwash of the flow leaving the leading edge of the valve; however, at the smaller angles the cross-flow component becomes increasingly significant and its affects must be considered.

For the flow predictions, the downwash component is clearly dominant in the centre and at the walls of the domain as a result of the axial vortices. Between these regions the velocity magnitude is reduced as the profile intersects the vortex cores, and hence no single component of velocity dominates. These findings hold for each throttle angle considered and for each plane downstream of the valve. The experimentally derived profiles, however, only show this trend for measurements made close to the valve at

large openings and the 12.5° opening. Away from the valve, the measurements generate flatter profiles more akin to those of the perpendicular measurements. Consequently, the trend in agreement is similar to those found for the perpendicular measurements, with improved agreement at large throttle openings.

Comparison of the profiles derived from parallel and perpendicular hot-wire orientations again reveal similarities between the two sets of data, particularly further from the valve for the small valve-openings (see Figures 6.5 and 6.6). Hence the possibility of probe misalignment is again questioned through the same arguments as discussed previously. However, at the larger openings this is not the case as the profiles show distinct differences to those generated with a perpendicular wire orientation (see Figures 6.9 and 6.11). In order to further investigate the differences and aid the interpretation of the results, the velocity magnitude profiles can again be broken down into their individual components. Figure 6.14 shows the velocity profiles of the combined and individual components of the predicted flows for an equivalent of a perpendicular and parallel wire orientation for a 47° throttle opening at the 1D measurement plane; these profiles correspond to those in Figures 6.9 and 6.11.

Although the combined profiles of Figure 6.14 show a similar shape, they clearly stem from different flow features. For the perpendicular-wire profile (upper plot), the cross-flow component can be seen to be very small (of the order of ± 10 m s^{-1}) in comparison to the axial component (approximately 0 to 70 m s^{-1}) and hence the combined profile is made up almost entirely of the axial flow component. The latter shows high velocities at the wall and centre of the domain with low values between that are a result of the locally attached vortices and reversed flow as shown previously in Figure 3.9. The equivalent to the parallel-wire measurements (lower plot of Figure 6.14), shows that the combined velocity profile is primarily a result of the downwash flow component, with the cross-flow component becoming only slightly more significant. In each case the cross-flow component only shows influence between the centre and walls of the domain, and thus away from these regions (i.e. at the domain centre and walls) the flow can confidently be assumed to represent either the axial or cross-flow component to the flow

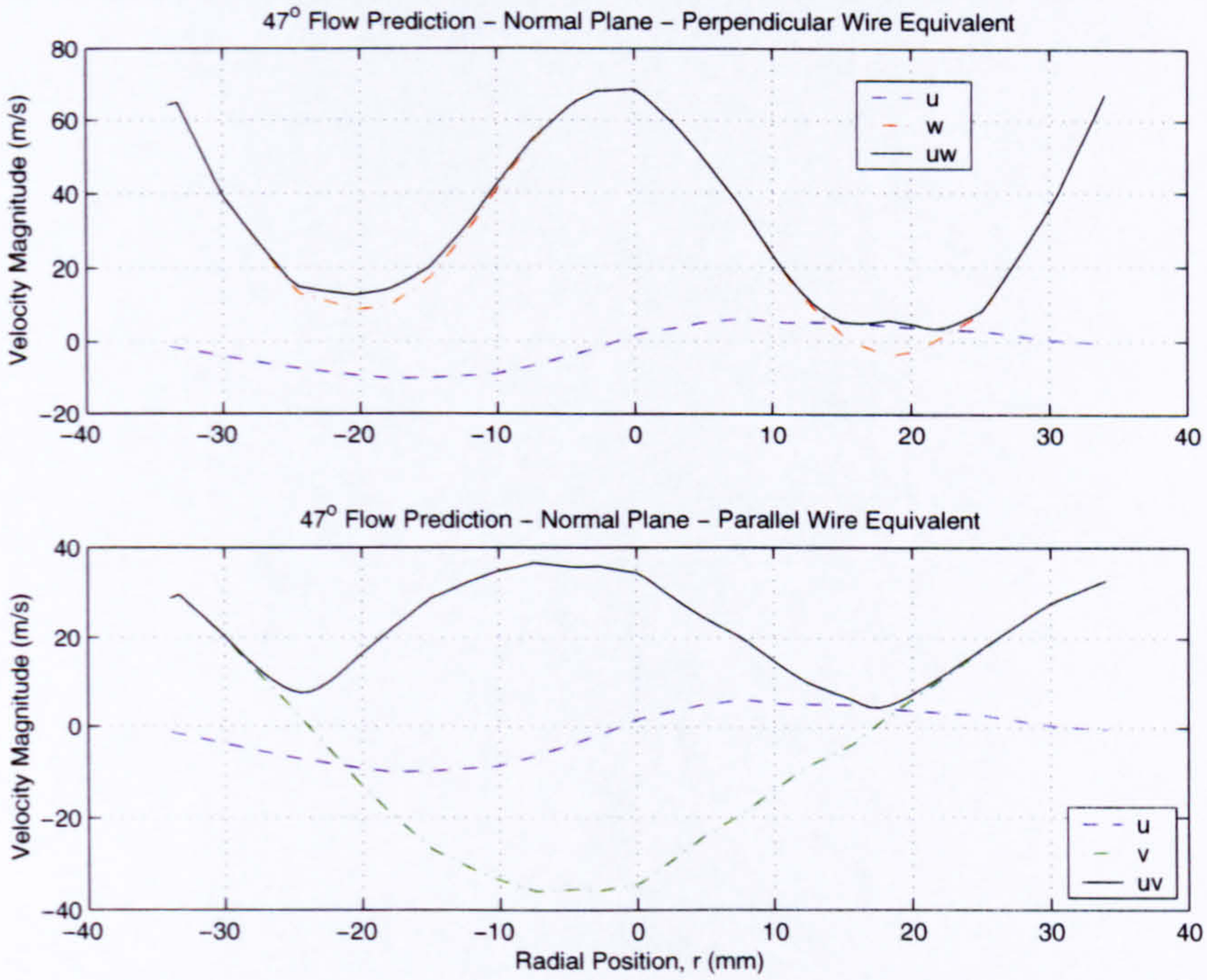

Figure 6.14: Predicted velocity profiles for the flow through a 47° valve opening in the plane normal to the symmetry plane at the level of the pivot, 1D downstream of the valve. The upper plot shows the equivalent of perpendicular-wire measurements with the axial, cross-flow and combined velocity components shown. The lower shows the equivalent to parallel-wire measurements with the cross-flow, downwash, and combined components.

when using a perpendicular or parallel wire orientation respectively.

The disagreement between the predictions and measurements for the small-angle flows is thus unlikely a direct result of probe misalignment. Calibration of the probe over a range of velocities, by nature of the calibration curve, causes the probe to be more sensitive to small changes of velocity toward the low end of the calibration velocity range; this is reflected in the sensitivity of the probe as described by equation (2.28). As such the probe will be sensitive to small changes in the flow field, which would be further amplified by any periodicity in the flow. These small scale changes are not apparent from the derived velocity profiles; however, the high level of uncertainty associated with the measurements may well be a reflection of this. As the uncertainty calculations include the evaluation of the time-history of the experimental signals, some of the small-scale changes in the flow will have been incorporated into the calculation. This, coupled with

the time-average of the data, and the limited resolution of the measurements creates significant ambiguity in interpretation of the measurements at low velocities.

For the large throttle openings, the measured velocity profiles indicate the presence of the axial vortices that suggests the profiles are dominated by the downwash flow component. Further from the valve the agreement to the predictions is worse, with the measurements showing flatter profiles. This suggests that the vortices may have burst, or that measurements made at higher velocities are more susceptible to probe misalignment and thus the downwash component have been partially drowned out by the influence of axial velocity.

6.4 Frequency Comparison

Examination of the flow predictions and experimental measurements has revealed periodic flow structures present in the flow downstream of the throttle valve. This has been confirmed by the frequency content analysis of the measured signals and predicted time-history, in addition to visualisation of the predicted flows. Each shows the frequency of the flow oscillation to be dependent on the throttle opening angle, although the experimental and predicted trends show reversed trends. Figure 6.15 compares the variation of frequency with throttle angle for the predicted and measured flows, with the experimental measurements shown for each of the three flow rates considered.

It is clear from Figure 6.15 that there is considerable differences between the measured and predicted frequency content of the flow. The CFD has shown that the periodic flow stems from vortex shedding from the valve and the subsequent oscillation of the flow from side-to-side in the domain. This has been shown to become increasingly significant at larger throttle openings, and the frequency of the vortex shedding increases with the throttle opening angle. The measurements show the reverse trend with the dominant oscillation frequency reducing as the valve is opened further. In addition the measured frequencies are considerably higher than those predicted by the CFD, with only the low flow-rate measurements showing any overlap with the predicted flows. The measured frequencies also show a step between the small-angle and large-angle flows;

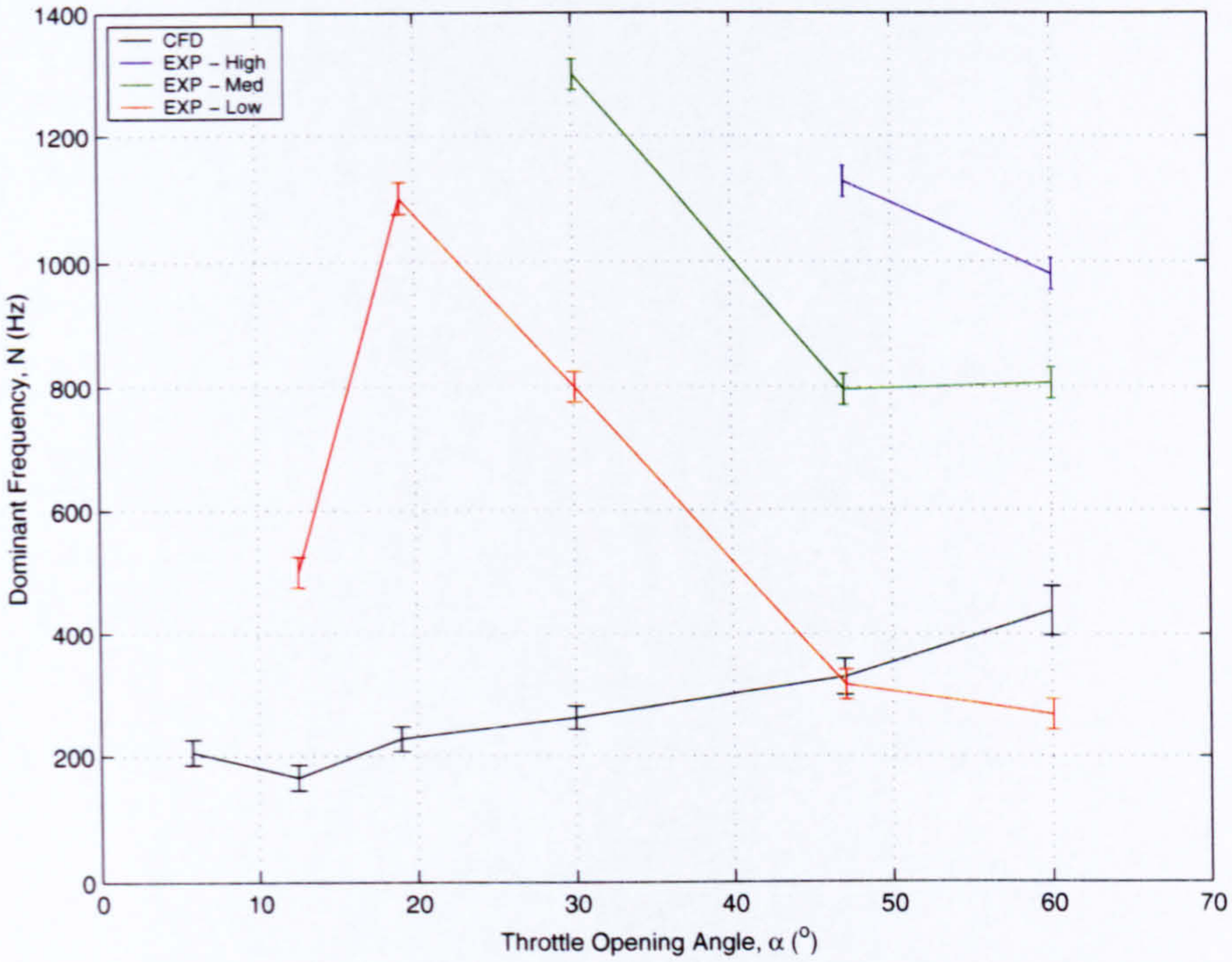

Figure 6.15: Comparison of predicted and measured frequency content of the flow behind the throttle valve for various throttle opening angles. Predicted values shown in black, with experimental values for the high, medium, and low flow rates shown in blue, green and red respectively.

however, the trend for the small-angle flows cannot be determined as no oscillations were found in the wake of the valve for the smallest openings. Computational predictions also show little data for the small-angle flows; however, this is partially due to insufficient run times limiting the quality of the results. Although, there is a drop in frequency for the predicted 12.5° flow that may indicate a change in trend between the small- and large-angle flows but there are insufficient data points to confirm this and the 12.5° flow has been shown to be overly diffuse downstream.

Results of the experiments do not provide sufficient information to establish the exact nature of the flow oscillation; however, the velocity profile comparisons suggest that the twin-vortex structures are present in the flow and hence the initial conclusion is that these are oscillating as predicted by the computational simulation.

Comparing the predicted oscillation frequencies to the work of Abernathy (1962), who studies the vortex shedding from bounded inclined flat plates of various sizes and

shapes, shows fair agreement of values for a range of equivalent incidence angles. Abernathy (1962) uses a small-section wind-tunnel to evaluate the lateral constriction of the flat plates that, although not offering the extreme blockage of the throttle valve, provides a fairer comparison than unbounded flows. Figure 6.16 compares the CFD predictions made here to the experimental observations of Abernathy (1962).

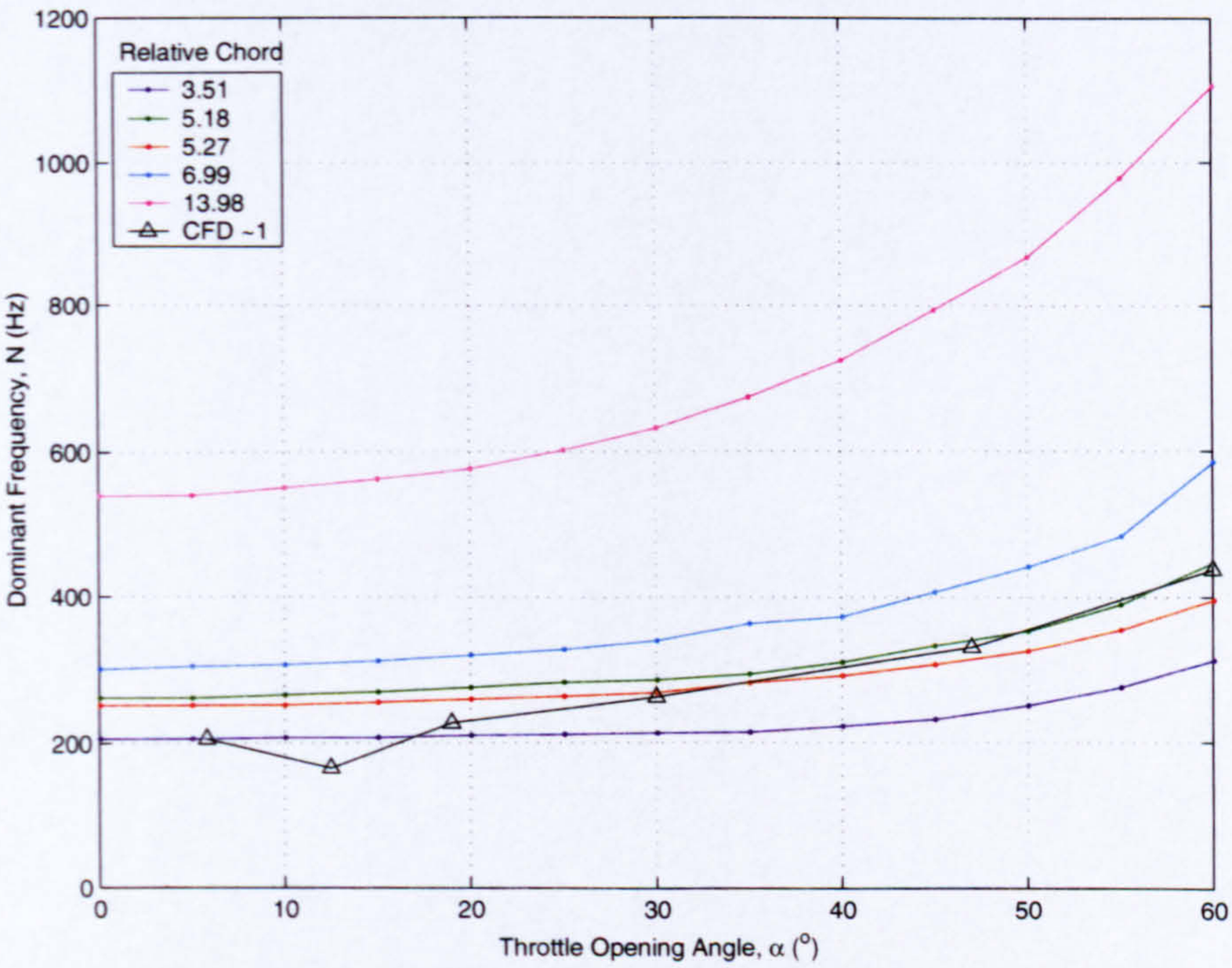

Figure 6.16: Comparison of predicted frequency content of the flow in the wake of the valve to values found by Abernathy (1962) for flows over an inclined flat plate in a small-section wind-tunnel. Predictions are shown in black with triangle markers, the work of Abernathy is presented by the relative chord of the flat plate with larger values representing reduced blockage, and unity representing full blockage.

The figure shows that the predicted frequency variation agrees well with the flat-plate study that offers confidence in the CFD predictions. The results of Abernathy (1962) suggest that the frequency of flow oscillation reduces for an increased blockage ratio, and also for a reduction in velocity (although the latter is not shown in Figure 6.16). Thus for the large blockage of the valve the frequency trend appears plausible and the increase in inlet velocity as the valve opens contributes to the steeper curve for

the CFD predictions in Figure 6.16.

A fairer comparison can be made through the Strouhal number that reflects the non-dimensional frequency of the vortex shedding. However, given the differences in plate size, blockage ratio, and inlet flow-rate, such comparisons invariably show large contrasts. Maximum values of Strouhal number for the computational predictions here are approximately St = 5 for a 5.8° throttle opening, while the equivalent flat-plate flow of Abernathy has a much lower Strouhal number of St = 0.24. Strouhal number for the predicted flows reduces as the valve opens further, thus reflecting the work of Abernathy (1962). At the largest openings (47° and 60°), where blockage becomes less apparent, the Strouhal number falls to values approaching those of the flat-plate flows, with St = 0.24 for the predictions and an equivalent flat-plate flow giving St = 0.185. Hence the blockage of the throttle body is still apparent, leading to over-prediction of the oscillation frequencies.

In conclusion it appears that the computational predictions are correctly predicting the trend in flow oscillation frequency, but absolute values of frequency can not be confirmed by experiment. The experimentally measured frequencies offer no correlation to the predicted values and also contrast to the values found in the literature. The poor correlation of the measured frequencies brings their validity into doubt, and it is unclear what these frequencies represent. However, the fact that the measured frequencies collapse to the same curve (see Figure 5.26) suggests that the recorded frequencies are an artifact of the flow and are thus physically correct. The frequencies found for the measurements appear to reflect the small-scale flow fluctuations as opposed to the vortex shedding from the valve and thus are an indication of the turbulence intensity of the flow.

The analysis of the measurements has therefore not been able to confirm the presence of vortex shedding in the downstream flow, although evidence does exist to confirm that the twin axial vortices are present downstream of the valve and extend throughout the outlet runner. Comparisons of the results to previous studies suggests that the valve is likely to shed vortices, even in the confines of the throttle body, and that the CFD

has successfully predicted the trend in the shedding. The measurements have failed to capture these vortices and this could be for various reasons. Firstly, the vortices may not exist in the physical flow; however, given that previous studies have shown these to exist, this is unlikely. It is also possible that the vortices do not exist in the confines of the flow-rig, owing to the set-up of the experimental investigation. The latter is perhaps the most plausible explanation given some of the issues discussed in the previous section, and the reasonably simple post-processing of the experimental data.

As has been discussed in the previous chapters, the presence of the hot-wire probe in the domain can have a significant effect on the flow through the valve. The probe affects the local flow field and thus there is a good chance that the presence of the probe has stemmed, or significantly altered, the vortex shedding from the valve. In particular, by entering the probe in the side of the domain the probe offers greater obstruction to the flow and also presents itself as a vortex-shedding body. Although these disturbance effects are believed to be of small-scale, they may be sufficient to alter the shedding characteristics from the valve.

Additionally, the flow domain may have adverse affects on the flow quality, and although tests have shown the flow to be acceptable, these have only been made where physically possible. Several joints exist, which if inadequately smoothed, will generate flow disturbance that will propagate downstream into the measurement domain. Further, there have been no checks to determine whether sufficient sealing is present at these joints and neither at any of the probe entry locations. Low pressure downstream of the valve will suck air into the domain through any gaps in the walls or joints, thus altering the flow characteristics and the resulting measurements. Previous work by the author has briefly investigated the effect of adding a breather tube to the throttle body that vented to atmosphere (Alsemgeest et al., 2000). By adding such a tube, the vortex shedding structures from the valve were found to be suppressed, whilst the large-scale vortices downstream of the valve remained. The vortex shedding therefore seems to be very sensitive to external effects and disturbances. Thus should a small leak be present between the throttle body and outlet runner, or via the hot-wire access points then this

could have a suppressive effect on the oscillatory flow.

6.5 Limitations of the Investigation

6.5.1 Limitations of the Experimental Investigation

The experiments carried out here have successfully measured the flow behind a throttle valve for a range of valve openings and overall confidence in the measurements is good for large valve-openings, but less so for small valve-openings. Measurements have been made of the hot-wire voltages over five-second intervals at each of the measurement locations for each of the throttle angles considered, and for two hot-wire orientations. These signals have been converted to the velocity-magnitude data through the hot-wire calibration equations as described in chapter 2. The converted data have been used to determine the turbulence intensity, skew and kurtosis of the flows, and the frequency content found through FFT analysis. The time-averaged data have been used to generate velocity profiles across the domain for each angle and location, and these have been compared to the predicted flows. Experimental uncertainty has been calculated for each set of measurements using statistical methods, and these have been used to access the quality of the results. The uncertainty in the measurements at small throttle openings, where low velocities exist, is particularly high thus reducing the confidence in the measurements. For large throttle-openings, the uncertainty in the measurements is significantly reduced, and hence confidence in the results is improved, and this is also reflected by improved agreement between the predictions and measurements. Overall the measurements have been a success at the larger throttle-openings, although some problem areas have been encountered that suggest the experimental investigation could be significantly improved. These factors affect the small-angle flows more significantly and some of these points are discussed below.

Flow-Rig Design and Manufacture

The flow rig itself has been carefully designed in order to generate a suitable flow for the measurements and to match the computational models. The design appears to have

been successful for the most part, although some aspects could be improved. Design and manufacture of the plenum chamber and contraction took a considerable amount of time and effort to complete, and the final manufactured items were not of the expected quality and this has undoubtedly resulted in a poorer than expected flow quality. With hindsight, some of these problems could be overcome by allowances in the design, and the use of more suitable manufacturing techniques. Unfortunately the plenum chamber was manufactured externally that meant no checks could be made to ensure that the design was being correctly followed and that the manufacturing processes were adequate. All other components were made in-house and hence the design of the parts involved consultation with technicians before final manufacture that ensured the parts assembled correctly as a whole.

A further problem with the experimental set-up is the limited air supply available that has lead to a short run-time for each set of measurements, particularly at the large throttle openings. In order to improve the flow measurements the available run-time of the experiments needs to be increased so that individual measurements can be made over longer periods, and more readings can be made at any one location. In addition, the increased run-time will mean that a constant and consistent flow is available for the range of measurements instead of several runs being required to evaluate the flow, as has been carried out here. A more systematic approach to the design of the experiment is required that assesses the quality of the design together with the proposed measurement instrumentation to provide a more suitable solution.

Hot-Wire Positioning

Tying in with the design and manufacture of the flow rig is the positioning of the hot-wire probe. Initially the hot-wire measurements were planned to record only the frequency of the flow oscillations and hence a very basic traverse system was designed and manufactured without consideration for more extensive measurements. Measurements made with the probe have, however, extended beyond these basic measurements to include velocity-profile measurements across the domain. In analysing the results it

has become clear that the measurements are limited by the single-normal probe and that by using a single-yawed or cross-wire probe, and suitable traverse system, a break-down of the velocity components could be more readily achieved. For the basic system used, the probe position and rotation has not been accurately defined that has lead to greater uncertainty in the measurements, and compromised the comparison to the predictions, as has been discussed. A further limitation of the measurements is the limited number of measurement locations used to generate a velocity profile, particularly for measurements made across the valve, i.e. normal to the symmetry plane. This in itself would require more accurate positioning of the hot-wire probe, both in the axial and rotational sense. Using an increased number of measurement locations would also require more time in which to undertake the experiments, increase the disc storage requirements, and also increase the flow requirements as discussed above. Ideally an automated traverse and capture system could be used to minimise the user intervention of the measurements, and such a system should improve the repeatability of the measurements.

The current traverse system has no physical alignment system to ensure that the probe wire is correctly orientated to the axial flow direction, rather relying on visual confirmation. This obviously leads to the possibility of fairly large mis-alignment given the small size of the probe wire, and very poor repeatability. Axial positioning of the probe is improved, however, the accuracy of the system is still limited and relies on visual calibration of the traverse. Misalignment of the probe from the centreline has not been accurately determined, and hence this leads to perhaps the greatest uncertainty in the position of the probe. These factors are apparent in the resulting velocity profiles with inconsistent agreement with the predicted flows. In order to improve the probe positioning, the traverse system needs to be designed with these factors in mind. Even if a full calibration of the system is not carried out, the position of the probe needs to be made consistent for all measurements to ensure that any errors are systematic and propagated through to the final results.

Flow-Rate Control

One of the primary sources of discrepancy between the experimental measurements and the predicted flows stems from the poor control of the inlet flow rate to the experimental system. Although the flow rate remains steady and constant once set, obtaining the correct flow rate proved incredibly difficult with poor repeatability. This leads to the stepped change in the velocity profiles previously seen in the comparisons and hence causing problems in establishing agreement to the predicted values. Longer run times in which to perform the measurements would partially alleviate this problem as the entire flow domain could be measured during one run. Although this does not overcome an incorrect inlet flow rate, the flow rate would at least be consistent throughout the measurements. In order to improve the control over the inlet flow rate, more sensitive regulation of the solenoid valves at the compressor outlet is required.

With an improved air delivery system in place the possibility exists to perform an hot-wire traverse across the entire domain without splitting the domain into two separate runs. This would, however, lead to complications with probe disturbance and probe access. Performing a traverse across the entire domain would cause a significant blockage to exist when far-wall measurements are made, and practically no blockage to exist for the near-wall measurements. Additionally, the geometry of the current probe is such that a step in the diameter is present between the probe and its support. Consequently, as the probe is withdrawn from the domain wall to perform the near-wall measurements there would be a high risk of additional flow disturbance through inadequate sealing around the probe. To alleviate these issues, a second set of measurements may be required that traverses in the reverse direction thereby allowing the effects of the blockage to be evaluated. Additionally the sealing of the walls would need to allow for a change in the probe diameter. Perhaps a more suitable solution is the use of a 90^{o} probe holder, thus allowing the probe body to align with the domain axis and hence present less local blockage to the flow. However, such a solution would need a more complicated traverse system and more careful calibration. Additionally, the length of

the probe holder required to alleviate the local blockage would make the probe and body susceptible to movement that would also hinder the measurements.

Pressure Measurement

Pressure measurements have been limited owing to the operational range and sensitivity of the pressure transducer used. The transducer was originally chosen for its ability to measure pressures over the full range of the experiment, including the inlet and plenum pressures. However, as the pressure measurement range of the transducer is large, its sensitivity to small changes in pressure is poor and hence the transducer measurements have been augmented through use of the micro-manometer system. However, the latter has only a limited range of measurement and this has lead to inconsistent measurement of the pressure for the range of throttle flows that has required additional analysis to correct for the change in instrumentation. Ideally the current pressure transducer would be used alongside a further transducer of more limited range and increased sensitivity to small-scale changes. Transducers with a faster response time would have been beneficial in order to capture some of the transient flow features. Despite the shortcomings of the measurements, the pressures have been successfully recorded and fair agreement has been found with the predictions.

Data Analysis and Presentation

The velocity-profile comparisons have used the time-averaged data to compare against the instantaneous predicted flows, which introduces large discrepancies between the two that have been discussed. An instantaneous velocity trace of the measured values has not been given owing to the limited run-times available and owing to the difficulty in obtaining a true instantaneous trace from a series of separate measurements. Ensemble averages of the flows would, perhaps, provide a more meaningful comparison and a fairer representation of the flow; however, it has not been possible to generate these owing to the insufficient run times and limited repeated measurements. Additionally the presentation of the time-averaged data for the predicted flows would also provide

more meaningful comparisons; however, the disc space requirements to do this are too large for the investigation, and alternate methods were unknown at the time.

Filtering of the signals may also have been beneficial in more accurately determining the measured flow structures by removing the unwanted noise and amplifying the signals of interest. In addition, the signal conditioner would perhaps have been better designed by not splitting the hot-wire signals and this has added additional complication to the analysis of the flows, and may even incorporate some hardware filtering to reduce noise in the system.

The uncertainty in the physical measurements has highlighted shortcomings in the experiment that could have been improved upon with more careful planning of the investigation at the design stage. Each of the small-angle measurements shows significantly higher levels of uncertainty than found for the large-angle openings, that stems primarily from the smaller velocities measured by the hot-wire anemometer. This is most notable for the measurements made normal to the symmetry plane of the valve where the velocities are at their lowest, particularly furthest from the valve. The level of uncertainties in these regions reaches $\pm 55\%$ in the worst cases that makes comparison to the predictions meaningless. These high levels of uncertainty are partially due to the factors described above, i.e. directional ambiguity of the hot-wire, lack of repeated measurements, and less than perfect filtering and analysis of the recorded data signals.

6.5.2 Limitations of the Computational Investigation

Similarly to the experimental investigation there are several shortcomings of the computational investigation that have become apparent throughout the investigation. Some of these are a direct result of insufficient resources, and others stem for poor modelling of the flows. Additionally several unexpected problems have arisen throughout the investigation.

Computational Resources

One of the main restrictions of the computational investigation has been the lack of sufficient computational resources. The computational simulations have been carried out using two alternate computer systems. The first is a Sun Ultra Sparc with 256 Mb of RAM, a single 166 MHz processor, and approximately 500 Mb of available disk space. This machine has been used for several of the simulations; however, the limited memory and storage of the machine have limited its use. The second machine used is an SGI Origin 2000 with 16 of 200 MHz processors, of which 8 were available for the simulations. This machine has 8 Gb of memory and several gigabytes of disc storage available thus making it a more suitable choice for the simulations. However, the machine is heavily used by many users and hence the full potential of the machine could not be exploited. All of the pre-processing and the majority of the post-processing has been carried out on the smaller of the machines, with the exception of the instantaneous velocity trace visualisations that have been performed on a third machine.

Such resources were found to be adequate for a steady-state solution; however, the use of transient calculations with a small time-step has resulted in very long computation times needed in order to obtain an adequate solution. To perform such simulations with sufficient grid resolution to adequately capture the flow physics requires a significant increase in resource, and hence the simulations here have been limited in grid density and solution time as discussed.

Grid Quality

Some of the poorer CFD results can be attributed to the overall grid quality of the models. All of the results presented are based on similar grid types and densities in order to be consistent throughout the investigation. However, these grids are not ideal and they have been limited by the computational overheads required to run a fully transient flow simulation. In order to ensure the simulations could be run practically, several restrictions have been placed on the mesh generation.

Firstly, the number of cells in the domain has been limited in order to reduce the

computational overheads of the models. The resulting simulations still show the main flow features of the flow; however, some of the small detail is not captured, as has been discussed. In addition the cell sizes are fairly large far downstream of the valve which will undoubtedly affect the quality of the solution, as the structure of the flow in this region is still of importance. This can be seen in some of the predicted velocity-profile plots where the profiles appear to span the domain is small discrete steps, and also through the more diffuse flows found far downstream for some predictions, particularly the 12.5° and 60° flows. The coarser grid resolution is also apparent in the results presented in chapter 3 where a "blocky" nature to some of the contour plots is observed. Refinement of the grids has been carried out for the models using an adaptive refinement as discussed (see also Figure 3.3). Thus the majority of the refinement of the grid is found in regions of high velocity and pressure gradients that are dominant close to the valve, leaving the downstream grid unchanged and hence no improvement in flow quality is found in these regions. Overall, the grids are considered to be a little coarse, and given additional resources a much greater level of refinement would be considered.

Individual cell quality has remained high for the models; this has been helped by the reduction in valve diameter improving the grid-generation process (see Figure 3.2). However, this region is still prone to poor cells being generated owing to the close proximity of the valve and walls, and hence smoothing and manual manipulation of the grid has been performed in order to reduce this. Poor cells in the crescent region have caused running issues throughout the investigation owing to their poor quality and the limited number of cells in the gap region. These poor-quality cells and the limited cell count are a result of the fairly large reference size imposed on the model to reduce the cell count and hence the computational overheads.

A further limitation of the computational grids is the lack of suitable near-wall cells, i.e. prismatic cells. The use of tetrahedral cells in the wall regions is not recommended as they do not necessarily provide a uniform near-wall distance that is required for the turbulence model. However, careful refinement of the near-wall tetrahedral cells has been performed to ensure that this effect is minimised. Evaluation of the solutions

indicates that the y^+ values lie within the specified range ($30 \leq y^+ \leq 100$), and that no significant banding was present that is often seen. Additionally, the velocity gradients in immediate proximity to the wall are normal to the surface, which is a further requirement of the turbulence model wall functions.

Related to the cell count is the length of the domain that has been reduced in order to further reduce the computational overheads, as has been briefly discussed in chapter 3. The length of the outlet runner has been reduced from 8D to 6D for all of the small-angle throttle openings, and also for the 19° and 30° throttle openings. Changes have been made to these models owing to the reduced flow rates present, and, particularly for the small-angle flows, most flow interactions occur closer to the valve. Extended outlet domains are normally used to allow for development and settling of the flow before reaching the outlet boundary far downstream. Therefore, by restricting the length of the outlet domain the flow is artificially constrained that can lead to the development of non-physical flows. Here, the flows appear to be adequately captured and show reasonable agreement with the experimental measurements. However, the domain length is inadequate, and even the 8D used should ideally be extended considerably to ensure full flow development. An extension of the domain could be accompanied by reduced grid density toward the outlet that itself introduces increased artificial diffusion to the solution and thus aids in the settling of the flow before reaching the outlet. A locally refined grid can be used in the region about the valve and for several diameters downstream to ensure that the flow is well-captured in the areas of interest. A further extension to the inlet flow would also prove beneficial to ensure full development of the inlet flows, although this would only be a precautionary step, as no problems have been found here with the inlet flows.

The use of experimentally derived inlet conditions can also be used to further improve the quality of the predictions. An iterative method can be followed whereby the computational model is continually improved on the basis of experimental validation. This would result in an excellent model of the physical flow; however, this would also require a significant increase in resource and time that is not normally achievable.

Boundary Conditions

The reduced outlet-runner length also has repercussions for the boundary conditions used in the model. As discussed in chapter 3, several combinations of boundary condition were evaluated before the final inlet-pressure combination was chosen for the simulations. Some of the problems found in using alternative boundaries are as a direct result of the short outlet length used. For example, the preferred boundary type of an outlet boundary could not be used as this requires that all the flow at the exit of the domain is directed outward and that the flow is predominantly aligned normal to the outlet plane. This is not necessarily the case for these flows owing to the vortices present in the flow. Although the outlet boundary can handle a small amount of inflow, the velocities in such regions are effectively reduced to zero by the code and hence this leads to an non-physical representation of the flow (Computational Dynamics Ltd., 2001). The use of the pressure boundary gives more freedom to the solution as it allows for inwardly directed flows and also non-uniform flow fields. The latter can pose a problem and lead to poor results and instability if a realistic pressure boundary is not specified. Here a uniform pressure field is applied across the outlet, which is in closer proximity to the valve than desired and hence places a further constraint on the flow. This may also account for some of the start-up issues that have occurred throughout the investigation, thus requiring the careful set-up of the models as discussed.

Time Dependent Modelling

Modelling the flow using a time-dependent solution requires a considerable increase in run time in order to obtain a flow solution, and can require considerably more disc storage space depending on the requirements of the investigation. This has been a problem here given the limited computational resources available, hence the compromises in grid density and domain length as discussed above.

Obtaining a stable solution has been a major issue for the computational predictions and this is caused by a number of factors. Use of a coarser grid should have only minimal effect on the stability of the solution, as the flow features should be smeared out, and

hence not cause concern. However, the restriction on domain length will certainly not be beneficial to the stability of the solution as discussed. Combining these factors with a transient calculation makes the problem worse as a suitable time-step needs to be used to adequately capture the flow. Given the limitations of the model tending to decrease the stability of the solution, smaller time-steps have had to be used to counteract this. Hence the CFL condition has been used as a guide in selection of an appropriate time step, in addition to the Courant number being used to monitor the flow solutions. The combination of these factors has lead to the implementation of very small time-steps that are of the order of milli-seconds. With such a small time-step it is clear that in order to obtain a suitable solution to the flow, massive run-times are required. Because of this, some of the predicted flows show poor results owing to insufficient time available for the calculations. Examples of this are the 12.5° flow prediction and the 60° flow prediction. The poor quality of these cases is apparent from the poor agreement with the experimental values, as has been discussed, and is evident from some of the figures presented earlier. However, all cases fall short of ideal owing to the run-times required to obtain a solution and the other problems outlined above.

The combined factors of the limited computational resource, coarse grids, short domain, restrictive boundaries and the time-dependent modelling is a major shortcoming of the CFD models used throughout the investigation. Insufficient run times have been used throughout and this has impaired the results to some degree. However, the flow oscillations appear to have converged, either by damping out or remaining constant, within the run times used, suggesting sufficient development of the flow solutions.

Turbulence Modelling

In addition, the simulations have highlighted a modelling problem that was unforeseen at the time the simulations were carried out, and has contributed to the stability and start-up problems encountered. Despite most fluid flows being time-dependent to some degree, the most common form of flow simulation carried out is the steady-state approach. This is often preferred owing to the reduced overheads involved, and the

need to obtain only the global flow characteristics that such a model is usually able to provide. In the majority of cases the flow is predicted using the RANS equations which attempt to model both the small-scale and large-scale flow structures that make up a turbulent flow. As these structures are highly flow dependent, this has lead to the growth of numerous turbulence models to suit specific flows and applications. Often, the RANS models are utilised for the prediction of time-dependent flows using their unsteady form, leading to the terminology of URANS modelling, i.e. using the unsteady Reynolds-averaged Navier-Stokes equations. Here the unsteady valve flows have been modelled using the URANS equations in conjunction with the k-ε turbulence model and this has led to additional problems.

The use of URANS models to predict flows with unsteady vortex-shedding is common, and Tucker (2001) offers an account of such work by an extensive number of authors. The work discussed covers the use of various one-equation and two-equation turbulence models including zonal models. In the majority of cases where the k-ε model has been used for the unsteady calculations it has provided poor results, with steady or highly damped flows typically predicted. The same author has also performed an investigation into the effects of using different turbulence models for the prediction of unsteady flows though an electronic device with complex geometry (Tucker, 2000). The findings show that all the turbulence models considered gave similar time-averaged velocities throughout the system, although greater differences were found for the temporal velocity variations. In addition, it was noted that the predicted amplitude of the unsteady structures reduced with an increase in turbulence viscosity. The k-ε model consistently performed poorly with the largest error of any of the models in terms of temporal velocity variations, and levels of turbulence intensity in the flow. Despite these shortcomings, the k-ε model is still regularly used for such predictions. Such findings are also reported by Constantinescu, Chapelet & Squires (2003) who model the vortex shedding from a sphere using URANS, LES, DES and experiments. In their work the k-ε model consistently shows poor results in comparison to other RANS models, and shows significant deviation from LES and DES models.

Here, vortex shedding has been captured despite the general poor performance of the k-ε model for the prediction of unsteady flows. The results have shown that for some cases the agreement with experimental data is poor, and there have been numerous problems with the initialisation and stability of some of the flows. Some of these problems have arisen through insufficient run times, poor mesh quality, and the diffusive nature of the k-ε model, all of which have been discussed. The limitations of the experimental investigation has also reduced the agreement between the predictions and measurements. However, a further aspect of the modelling has a greater significance for the predictions.

For URANS predictions of unsteady flows to be physically realistic, separation of the temporal scales must exist, i.e. the time scale of the time-dependent turbulent fluctuations (the turbulent time-scale), must be sufficiently far removed from the time scales of the flow oscillations. For steady-state calculations, the turbulence model normally accounts for any time dependence of the fluctuations to provide an overall mean flow. When using unsteady calculations this remains true, but any other oscillations in the flow are dealt with by the temporal terms in the discretised equations. Thus, if there is no separation of temporal scales, there is no distinction between the turbulent and main flow oscillations and hence the turbulence model will also model the main flow oscillations leading to double accounting of the flows.

The turbulent time scale of the predicted flows can be found by dividing the turbulent kinetic energy by the turbulence dissipation rate, i.e. $T_t = k/\varepsilon$, which has the dimensions of time (Speziale, 1998). Evaluation of the turbulence time scales and oscillation period ($T_f = 1/N$) reveals that the two are of similar magnitude for each of the predicted flows. Time scales for the turbulent fluctuations range from a tenth of a millisecond to 20 ms at the extreme. Vortex shedding from the valve has a frequency range of approximately 200 to 500 Hz that equates to time-scales from 2 to 5 ms, hence overlapping the turbulent time scales. However, the range of T_t varies with the valve opening angle, and with position in the domain. A reduction in T_t is found closer to the valve, thus increasing the difference between the two time scales. There appears to

Table 6.1: Average ratio of oscillation period to turbulent time-scales ($\overline{T_f}/\overline{T_t}$) for the predicted flows where vortex shedding has been found.

	Symmetry Plane				Normal Plane				All
Angle	1D	2D	3D	Avg	1D	2D	3D	Avg	Avg
5.8	1.46	0.72	0.56	0.91	1.24	0.56	0.46	0.75	0.83
12.5	4.22	1.81	0.65	2.23	2.96	1.65	0.67	1.76	1.99
19	7.65	4.25	1.85	4.58	5.33	3.05	1.49	3.29	3.94
30	8.26	3.90	1.52	4.56	6.39	3.05	1.48	3.64	4.10
47	6.41	2.63	1.59	3.54	5.35	2.68	1.69	3.24	3.39
60	1.30	0.79	0.28	0.79	1.03	1.39	0.34	0.92	0.86

be no trend in the variation of T_t with throttle opening angle; however, the small-angle, and the 60° flow predictions show notably higher values of T_t than the remaining flows.

Evaluation of T_t alone does not provide a sufficient information about the individual flows and hence the two time-scales are compared to give a more meaningful comparison. Table 6.1 shows values of $\overline{T_f}/\overline{T_t}$ for the range of flows where vortex shedding from the valve has been found. The table gives the ratio calculated using the average value of the time-scales found in one plane and axis combination, the average of these to give an angle-axis average, and a summed average for the entire flow field.

The tabulated values can be used as a guide to the quality of the flow with higher values representing greater separation of temporal scales and hence an improved prediction. The small-angle and 60° flows show that, on average, $T_t > T_f$, thus the turbulence model is poorly predicting the flows. The remaining flows show greater separation of temporal scales; however, these are still very small, and suitable separation of temporal scales would see this increase by one or two orders of magnitude. Given that the flow oscillations are likely to exist, and have been seen in previous investigations, the small separation of temporal scales found indicates that the URANS modelling of such flows, with the k-ε model in particular, is a poor combination and alternative methods need to be used to accurately predict the temporal flow features.

The use of URANS modelling need not be entirely discounted as alternative turbulence models have been shown to offer improved prediction of unsteady flows (Tucker, 2000; Constantinescu et al., 2003). Whether an alternate turbulence model would over-

come the overlap in the temporal scales is unclear. A more suitable alternative to the URANS modelling is the use of LES which is becoming a more viable option given the increased performance and reduced costs of computational resources. At the time of writing, the Smagorinsky LES model has become available as a beta-test feature of STAR, and is also available in other CFD codes, indicating the emergence of LES models into the mainstream engineering world. Another current development that may be applicable here is the use of DES, or Detached Eddy Simulation, which is a hybrid of the LES and URANS approach. The approach basically models near-wall flows using the RANS model and LES is used to resolve the large-scale flow away from walls (Constantinescu et al., 2003).

A similar approach to DES is offered by Davidson (2001), where a k-ω model is used to model the turbulence towards the wall and LES used to model the remaining flow. With this model the transition between the models lies in the log-law region of the flow, whereas for DES the RANS model is used to model the entire boundary layer and hence the transition point lies further from the walls. The model has been applied to a channel and hill flow with fair success; however, that author notes that the RANS modelling at the walls is incorrect as the modelled time-scales (T_t here) are larger than the resolved time-scales (T_f here). Davidson (2001) suggests that it is therefore incorrect to carry out unsteady RANS calculations for such flows, and it is more correct to denote the near-wall regions as VLES. VLES (Very Large Eddy Simulation) is a form of LES whereby the cutoff point between the sub-grid scale modelling and the resolved flows is closer to the large-scale spectrum of the flow (Tabor, 2001). Hamba (2001) deviates from the norm and uses LES to model near-wall flows and RANS models to model the bulk flow in a bid to reduce computational overheads with respect to a full LES calculation. Results were good provided the match point between the two models was suitably chosen. Speziale (1998) suggests that although LES offers benefits over the traditional two-equation RANS models, its use for high-Reynolds number flows is limited, as so much of the flow has to be modelled by the sub-grid-scale models, and hence recommends the use of Reynolds stress models for such flow simulations.

For the predictions carried out here, the near-wall flow is modelled using the wall functions of the k-ε turbulence model, and thus the near-wall cells are relatively coarse. Further afield the cell sizes increase on account of the restricted computational resource, and hence, fine details of the flow are not resolved but must also be modelled. Grid resolution places limits the smallest resolved length scales, and although the largest scales seen in the predictions are of the order of the diameter of the domain (i.e. the axial vortices), the smallest resolved scales are the order of several millimetres. Modelled length scales can be calculated through rearrangement of equation (3.4) applied within the modelling domain. In doing so, the largest modelled length scales for each of the predictions is found to be of the order of micrometers, and hence there is separation of length scales by some two to three orders of magnitude. Therefore, although separation of temporal scales does not exist, the relatively coarse grids used in the predictions gives rise to separation of length scales, and the predictions can be classified as VLES. However, alternate modelling approaches should offer improved modelling, particularly with the use of refined grids, and also avoid many of the problems encountered in establishing a solution.

CFD as a Design Tool

CFD has become widespread throughout academia and industry where its use as a non-intrusive predictive tool is valued and highly regarded. However, its emergence into industry has been accelerated more by the significant increase in computational power and resource, coupled with significant reductions in relative cost of hardware, as opposed to code maturity and modelling advancements. Many industrial applications still exploit steady-state RANS calculations using the k-ε turbulence model, or variants thereof, that have been the standard tools for CFD analysis for many years and are thus well used and well validated. More recently, the advent of increased computing power has lead to the emergence of more advanced turbulence modelling techniques into the mainstream, such as RSM and LES each with its own limitations. Use of such advanced models is often at the expense of accurate validation of the predictions and

full assessment of the modelling limitations and thus can easily lead to a bigger is better philosophy. CFD calculations are relatively easy to implement, particularly with some commercial applications; however, the solutions produced are only as good as the initial model definition and hence a poor definition will lead to poor results that may still look physically plausible.

In order to ensure that CFD is used effectively as a design tool, sufficient information must first be obtained to fully define the problem and a good understanding of the limitations of the model must be present. In conjunction with this, accurate experimental data should be available to allow the model to be validated. Without sufficient validation of the models the results and trends obtained could easily lead to incorrect design paths being followed that only becomes apparent after significant effort has been made. Typically such scenarios reflect poorly on CFD and the CFD engineer.

Where significant design iterations are proposed through use of a CFD model, further calibration of the model using several experiments should be carried out in order to ascertain whether the CFD model is able to correctly predict the global and local trends required. Only by performing such calibrations and validations can confidence be placed in the predicted solutions. Under circumstances where CFD is used for flow predictions on virtual components the results should be treated with caution, particularly if the design deviates significantly from previous designs. Where such models are then used for iterative design work, or trend prediction, and a final design is realised, then experimental validation should be performed on the design at the first available opportunity. This allows the quality of the predictions to be assessed and, where necessary, adjustment of the modelling variables can be made to improve the predictions. Provided that such steps are frequently carried out, the users are aware of the limitations of the models, and the CFD is not used blindly, then its use as a design tool is warranted.

Chapter 7

Conclusions and Recommendations

7.1 Conclusions

Computational predictions and experimental measurements have been made of the flow through an automotive throttle body for a range of valve opening angles and flow rates and the results presented herein. The combination of opening angles and flow rates used are based on engine simulations and experimental data from an instrumented engine.

Unsteady RANS modelling of the flows has been performed with a commercial finite volume code using unstructured tetrahedral grids. The standard derivation of the k-ε turbulence model has been used to predict the turbulent fluctuations within the flow. Temporal discretisation has been carried out using a fully-implicit first-order scheme, and spatial discretisation using a multi-dimensional second-order scheme.

A bespoke flow rig has been designed and built to allow experimental measurements to be made in the flow downstream of the throttle valve. The rig consists of a large plenum chamber and contraction that feed a series of tubes within which is situated the throttle body. Measurements have been made of the pressure drop across the valve and a hot-wire anemometry system used to measure the velocity magnitude at various locations downstream of the valve. Measurements have been made with the hot-wire sensing element orientated perpendicular and parallel to the free-stream flow direction, at locations spanning the width of the domain in, and normal to, the symmetry plane

of the throttle. The measurements have been made at distances of one, two, and three diameters downstream of the valve pivot, and the data obtained used to generate velocity magnitude profiles for each throttle angle, downstream location, and hot-wire orientation.

The computational predictions have revealed that the flow behind the valve is complex, highly three dimensional, and is dependent on the throttle opening angle. For each of the throttle angles considered, two large vortices are generated downstream of the domain with their core aligned with the domain axis. These vortices are formed by the flow passing over the leading edge of the valve diverging into the domain and subsequently sweeping around the circular walls. At smaller valve openings, a toroidal vortex forms immediately downstream of the valve that although not directly attached to the valve, is not predicted to shed. As the valve is opened, this vortex becomes attached downstream of the leading edge and is destroyed at the trailing edge by the strong shear flow present. Vortices that form around the side of the valve are able to detach and a periodic flow is seen to develop toward the leading edge side of the domain. The frequency of flow oscillation is found to increase as the throttle valve is opened further and the trend follows bluff body theory. The shedding of these vortices causes the flow passing over the leading edge to oscillate from side to side that subsequently causes the downstream axial vortices to oscillate also.

Experimental measurements have shown that the flow leaving the leading- and trailing-edges of the valve are the strongest flow features and that high velocity gradients exist in these areas. For the small throttle-valve openings, the flow leaving the leading edge of the valve tends to dominate the flow field close to the valve and remains dominant further downstream despite increased diffusion being apparent. Strong shear flows leaving the trailing edge of the valve are apparent close to the valve but are more readily diffused further downstream than the flows passing the leading edge of the valve. At larger opening angles, the flow past the trailing edge of the valve becomes the dominant flow feature and remains apparent far downstream of the valve. The geometry of the domain at the larger openings gives rise to greater divergence of the flow passing

the valve leading edge that leads to less severe velocity gradients in this region.

Measurements made across the valve normal to the symmetry plane have revealed little detail in the velocity profiles owing to the high level of uncertainty found for measurements made at low velocities. For the larger openings, the measurements show evidence of the axial vortices in the flow, but indicate that these are heavily dissipated, or even burst, downstream of the valve. Flow oscillations have also been captured by the measurements; however, analysis of the signals has revealed limited information about the transient flow features.

The computations overpredict the pressure drop across the valve by 20% to 40% for each throttle angle considered with the exception of the 60° throttle opening; however, the latter is believed to be a reflection of a poor model for this throttle opening. Despite the overprediction, the trend in pressure drop as the valve opens is correctly predicted for both the small and large throttle valve openings and hence the CFD correctly captures the bulk flow trends. Small-scale and transient changes in the pressure drop have not been compared as the measuring equipment used is insensitive to small changes and has a low response time.

In order to compare the predictions to the measurements, individual velocity components have been combined to form similar velocity profiles to those derived from the measurements. In this respect the CFD offers an exact combination of velocity components while the experimental measurements are governed by the accuracy of hot-wire probe position and orientation. In addition to the comparison of velocity profiles, comparison has also been made of the pressure drop across the valve, and the frequency of the flow oscillation.

Comparison of the velocity magnitude profiles has shown greater variation in agreement across the range of measurements that is dependent on throttle angle, measurement location and hot-wire orientation. In each case the computations have underpredicted the measured velocity magnitude regardless of the qualitative agreement. It has been found that the underprediction is a reflection of uncertainty in the measurements as opposed to poor modelling techniques. Regions of high velocity gradient are,

however, poorly predicted by the computations that is a reflection of the models used. Despite this, the general change in velocity gradient across the domain of the valve is well captured in all cases. Further from the valve the predictions tend to suffer from increased numerical diffusion that leads to poorer agreement with the measurements.

The best agreement overall has been found when comparing to the measurements in the symmetry plane of the valve using a perpendicularly orientated hot-wire probe. Under these conditions the velocity profile is a combination of axial and downwash flow components and, of these, it has been shown that the axial flow dominates the flow. For measurements made with a parallel hot-wire orientation, the resulting profiles show similarity to those of the perpendicular measurements thats suggest the axial component has influenced the readings. Comparison of the parallel measurements to the predictions shows the measured profiles to exhibit large near-wall velocities that strengthens this hypothesis.

Velocity profiles of the flow in the plane normal to the symmetry plane show greater disagreement with the experimentally derived profiles showing little detail in the flow at any location or for either probe orientation. Conversely, the computationally derived profiles show clear structure to the flow that reflects the 3D nature of the flow found from more detailed analysis. Both the predicted and measured velocity profiles show evidence of the downstream axial vortices, although the measurements only show this at the large throttle openings. The agreement in velocity magnitude and profile shape is good close to the valve, but further from the valve the experimental results show reduced evidence of the vortices. Previous studies have shown that these vortices do remain present further from the valve. It is apparent that the measurements are less sensitive to changes in the flow that are a result of poor and inconsistent hot-wire orientations leading to ambiguity in the readings. The agreement is made worse through high levels of measurement uncertainty, and comparison of time-averaged measured data to instantaneous predicted data.

Flow oscillations have been found for both the predictions and the measurements, although only for the largest throttle openings in the case of the latter. Unfortunately

the quantitative agreement in oscillation frequency between the two is very poor, and the trends in frequency change for the measurements are opposite to those of the predictions. The measurements show the oscillation frequency to be considerably higher than the predictions, and that the frequency reduces as the valve opens. Comparison to previous studies, however, indicates that the predicted oscillation frequencies agree with bluff-body flows that experience vortex shedding, even for near-wall bounded flows. It is believed that the experimental measurements are a reflection of small-scale flow fluctuations as opposed to large-scale oscillations occurring within the flow.

Limitations have been found in both the experimental and computational investigation that have reduced the quality of the results and lead to compromised comparisons being made. In order to allow the computations to be carried out given the available compute resources, restrictions have been placed on the domain size and the number of cells used. This results in relatively coarse grids and short computational domains that have given rise to the poor prediction of velocity gradients and the overly diffuse flows downstream of the valve. In order to reduce these shortcomings, a second-order spatial discretisation scheme has been used throughout the investigation. The use of slightly refined grids has shown that more detail is captured within the flow, but that any transient features are unaffected. However, as differences are still apparent, the solutions are grid dependent.

Temporal discretisation of the equations has been carried out using both first- and second-order temporal differencing schemes, however the results indicated no benefit in using the second-order accurate scheme and hence the first-order scheme was reverted to. Both schemes are unconditionally stable thus allowing the use of large time-steps; however, this benefit was not realised and very small time-steps have been employed in order to obtain a solution. This considerably increased the computational requirements for the investigation and consequently inconsistent solution times are found for the models.

Unsteady RANS modelling using the k-ε turbulence model has been questioned for the prediction of flows that contain vortex shedding. Although large-scale flow

oscillation have been predicted here, and such modelling combinations have been used in previous studies, their use can lead to spurious results if separation of temporal scales is not apparent. Here, the modelled and resolved temporal scales overlap hence the URANS terminology can not be applied; however, separation of length scales is apparent thus validating the combination and allows classification as VLES predictions. Alternative modelling approaches are likely to provide improved predictions given the diffuse nature of the k-ε turbulence model and its general poor performance in URANS predictions.

Overall the computational modelling of the flows has been successful. CFD has provided greater insight into the structure and behaviour of the flow than experimentation alone, and has thus been a valuable tool in the understanding of the flow through the throttle valve. It is clear that a great deal of information can be generated, and subsequently analysed, from one computational solution that would require several different experiments to provide the same level of information. This is one of the major strengths of CFD; however, it is also a potential weakness as poor modelling of the flow can lead to plausible results being generated.

Several limitations of the experimental investigations have been found that have lead to greater uncertainty in the results and made a large contribution to the disagreement with the predictions. The measurements have been affected by poor hot-wire positioning that has lead to ambiguity in the velocity profiles produced. Misalignment of the probe causes all three velocity components to influence the measurements and this is most apparent for the parallel wire orientations where the influence of the axial velocity component has been found in the resulting velocity profiles. This clearly highlights the need for accurate and consistent hot-wire probe alignment and orientation when making measurements.

Some of the velocity profiles show a step in magnitude at the centreline that is a result of poor flow-rate control and the combination of two separate experimental runs to generate a full traverse across the domain. For measurements normal to the symmetry plane, only half the domain has been traversed and the results subsequently

reflected about the centreline in order to generate a full velocity profile, and therefore these profiles do not provide a true representation of the flow. Additionally, insufficient measurement locations have been used in the generation of the velocity profiles hence reducing the resolution of the results.

Direct comparison of the predicted and measured profiles is further compromised through presentation of time-averaged experimental measurements and instantaneous predictions. Uncertainty in the measurements has been found to be high for low-velocity readings that is a result of the time-averaging of the results, the probe positioning error, and the ambiguity of the hot-wire anemometer.

The limitations of the experimental investigation show significant deficiencies that have reduced the quality of the results and the amount of usable information available. Insufficient planning of the investigation and an under-estimate of the importance of the measurements has lead to these limitations, and hence highlights the need for greater consideration for the design of the experiment. Additionally, the intrusive nature of hot-wire measurements is not best suited to confined flows with vortex shedding owing to the relatively high blockage of the probe and the possibility of the probe presence significantly affecting any flow oscillations. Therefore, with suitable design and planning of the experiments the level of accuracy in the measurements can be significantly increased, and through the use of non-intrusive measurement techniques such as LDA, the risk of flow disturbance can be minimised. Here, the measurements do not provide a sufficient level of detail to fully validate the computational predictions.

In order for computational modelling to be successful, the predictions must be validated by experiment in order to ensure that flows and trends are correctly predicted, and to allow adjustments to be made to rectify any shortcomings of the model. With careful validation of the models, the predictions are able to provide detailed information about the flow under investigation. Here, the level of agreement is mixed owing to the highlighted problems, but where these problems are minimal, the flow predictions and measurements show good agreement. Thus, although not providing full validation, the experiments offer sufficient information of the bulk flow to provide basic valida-

tion. The addition of the results of previous work have improved the validation of the computational investigation and placed confidence in the findings.

Although the CFD has not been used here to directly assess design changes, its use has highlighted the potential of the tool to do so. It is able to provide detailed, non-intrusive flow analysis for a wide range of applications and has the benefit of allowing extreme design changes to be carried out in a "what if" scenario. However, in order for CFD to be successfully used in this way, experimental validation is essential. Providing that such validations are carried out, and that the limitations of the modelling are understood, then CFD can be considered as a suitable design tool.

7.2 Recommendations for Further Work

In order to improve the quality of the investigation a number of changes need to be made to both the experimental and computational investigations. These issues have been discussed above and are summarised here. For the experimental investigation the improvements should incorporate,

- improved manufacture of components;
- improved assembly and sealing of components;
- increased number of measurement locations across the domain;
- increased number of measurement planes;
- accurate positioning of the valve, and rotational orientation;
- measurement of all three velocity components;
- longer run times in which to perform the experiments;
- finer control over inlet flow rates;
- improved measurement of pressures with transient features captured;
- more sophisticated data analysis techniques;

- alternate measurement techniques and methods.

For the computational investigation, the following improvements on the current methods are suggested,

- increased length of the inlet and outlet domains;
- increased grid density in the near wake of the valve, and a general increase overall;
- a full grid sensitivity study;
- evaluation of alternative cell types;
- application of an inlet-outlet boundary condition combination;
- increasing the run time of the solutions;
- use of an alternative turbulence model or modelling approach;
- increase the number of monitor-cell locations to show flow transients;
- calculate time-averaged features for comparison to experiment.

These factors will improve the current investigation without changing the overall aims of the investigation. Any future work relating to the current investigation would need to incorporate these improvements and include other aspects that have not been covered here.

Perhaps one of the most useful additions to the experimental investigation would be some form of flow visualisation that would enable the structure of the flow to be visualised and compared directly to the predicted flows. This could be performed using a basic method of flow seeding and the capture of the flows using a high-speed camera. Alternative means include the use of PIV that would not only provide useful information on the flow structure, but also give quantitative values for comparison. Other methods of measurements such as PIV and LDA should also be considered for their non-intrusive operation. An LDA system was considered for the experiments here, but the range of

velocities encountered in the flows was beyond the measurement range of the device. A higher-specification unit may provide an improvement over the HWA measurements performed.

A greater range of flow rates needs to be considered at each throttle opening, which may not tie in with the flows found in an engine, but would provide a more useful knowledge base and allow trends to be found that could be used for future engine design work. An increased range would also provide improved comparison to previous studies. By the same rational, the range of throttle opening angles also needs to be increased to give a broader range of information on throttle flows. In addition, the effect of opening or closing the throttle could be investigated as this is typical behaviour for the valve in a throttle body. As briefly discussed, the addition of a breather tube to the predicted flow tends to disrupt the flow through the valve, and as this is analogous to the crankcase breather system used in an engine, an experimental investigation into the effects would be beneficial.

Computational predictions also need to reflect the improved experimental values through the increased range of throttle angles and flow rates suggested. CFD lends itself to design changes and hence the breather tube study would more readily be investigated using the computational models, and using the most promising designs in the experimental investigation. Simulation of the various breather conditions can be used to show regions of poor flow, and in the case of reversed breather flow, where deposits and fouling of the valve are likely to occur. Similarly, design changes to the throttle body can also be made, such as the shape of the valve and walls of the throttle. The influence of the hot-wire probe on the flow could also be investigated with relative ease using the computational model, this would provide useful information into the any disturbance effects and also aid in determining suitable measurement locations that offer the least disturbance.

A study of various turbulence models used in RANS modelling may be a beneficial future task. However, given the general findings of previous studies using these models, the effort may be better placed in the evaluation of LES, DES, and other non-RANS-

based models. Another area of future work is the effect of the true boundary conditions on the flow. This could be simulated using measured engine flow data to define the computational boundary conditions. It may be that an unsteady flow field considerably changes the throttle flows.

The CFD predictions should include the investigation of alternative gridding methods, and certainly attempt to improve on the grids used here. Should tetrahedral cells be used, then prismatic cells should be placed on the walls, and where this causes problems as here, alternative means should be found to generate the mesh. This may include the use of a hybrid mesh of tetrahedral and hexahedral cells, or, preferably, the use of a completely hexahedral mesh.

Appendix A

Statistical Data Sources

This appendix contains details of the data sources used to gather information on transport and pollution. These are considered to be current figures as they have been sourced from online databases which are constantly updated.

A.1 Transport Trends

For the data concerning transportation trends and social attitudes towards transport (i.e. footnotes 2-5 within chapter 2) the majority of the information has been sourced from the *Office of National Statistics* (ONS) database. This can be found online at the following URL: http://www.statistics.gov.uk, and they claim that "National Statistics covers government data produced to the high professional standards set out in the Official Statistics Code of Practice".

Data used by the ONS has been sourced from various government departments and details of the sources and the data sets are listed below.

Department of Transport, Local government and the Regions (DTLR) is a UK government department. Details of the department, alongside reports and other information can be found at:

http://www.dtlr.gov.uk

Department of the Environment is actually the same department as the DTLR, and is often referred to by its abbreviated name or its alternate name, the De-

partment of the Environment, Transport and Regions (DETR).

Department of Environment, Northern Ireland (DOENI) is the Northern Ireland government division of the environment department. Details of can be found at:

http://www.doeni.gov.uk/

Vehicle Information Database is a database covering all registered vehicles throughout Great Britain. The database is held by the DVLA (Driver and Vehicle Licensing Agency) and passed on to the DTLR. Data is held on approximately 60 million vehicles, of which 28 million are currently licensed. The full data base covers the period end 1993 to end 1999, the latter updates on a yearly basis. Details can be found at:

http://www.statistics.gov.uk/statbase/Source.asp?vlnk=1415

National Travel Survey (NTS) is commissioned by the (DTLR) and has a data set of approximately 3,000 households per year. Detailed data collection started in 1988 with results published annually. Covers Great Britain. Full details can currently be found at:

http://www.statistics.gov.uk/statbase/Source.asp?vlnk=1333

A.2 Environmental Trends and Pollution

Information regarding atmospheric pollutants and the effect on the environment has been sourced from the online databases of the *UK National Air Quality Information Archive*, at http://www.aeat.co.uk/netcen/airqual/. The information presented on these pages comes from various sources around the British Isles, in particular:

The Department for Environment, Food and Rural Affairs (DEFRA) which is a UK government department. Information has been sourced from the environment division which can be found at:

http://www.defra.gov.uk/environment/index.htm

The Scottish Executive is the Scottish government. Details are obtained from the environmental air quality division, which is found at:

http://www.scotland.gov.uk/environment/airquality/

The National Assembly of Wales provides information from of its environmental division. Details are found at:

http://www.wales.gov.uk/subenvironment

The Department of Environment (DOE) of Northern Ireland. Details of their environmental division can be obtained at:

http://www.ehsni.gov.uk/EnvironProtect

Further information on pollution and air quality trends for the United Kingdom have been obtained from the *Environment Agency*, whose website can be found at http://www.environment-agency.gov.uk. Again this uses information provided by the sources listed above.

Bibliography

Abbass, M. K., Andrews, G. E., Bartle, K. D. & Williams, P. T. (1989), Condensible unburned hydrocarbon emissions from a DI diesel engine, *in* D. Spalding & N. Afgan, eds, 'Heat and Mass Transfer in Gasoline and Diesel Engines', Hemisphere Publishing Corp., New York, pp. 643–655.

Abbott, M. B. & Basco, D. R. (1989), *Computational Fluid Dynamics, An Introduction for Engineers*, Longman Scientific and Technical.

Abernathy, F. H. (1962), 'Flow over an inclined plate', *Transactions of the ASME, Journal of Basic Engineering* **84**, 380–388.

Addy, A. L., Morris, M. J. & Dutton, J. C. (1985), 'An investigation of compressible flow characteristics of butterfly valves', *Transactions of the ASME, Journal of Fluids Engineering* **107**, 512–517.

Adrian, R. J. (1991), 'Particle-imaging techniques for experimental fluid mechanics', *Annual Review of Fluid Mechanics* **23**, 261–304.

Adrian, R. J., Johnson, R., Jones, B. G. & Tung, A. T.-C. (1984), 'Aerodynamic disturbances of hot-wire probes and directional sensitivity', *J. Phys. E. Sci. Instrum.* **17**, 62–71.

Alsemgeest, R. W. (1998), The study of flow in a crankcase and throttle body using computational fluid dynamics, M.Res Thesis, School of Engineering, University of Warwick, Coventry, CV4 7AL, U.K.

Alsemgeest, R. W., Shaw, C. T., Richardson, S. & Pierson, S. (2000), 'Modeling the time-dependent flow through a throttle valve', *Transactions of the SAE,* Paper 2000-01-0659.

Anderson, J. D. (2000), Introduction to computational fluid dynamics, *in* 'von Karman Institute for Fluid Dynamics, Annual Lecture Series, Introduction to Fluid Dynamics.', von Karman Institute, Rhode Saint Genese, Belgium.

Anderson, Jr, J. D. (1982), *Modern Compressible Flow, with Historical Perspective,* McGraw-Hill, New York.

Anderson, Jr, J. D. (1991), *Fundamentals of Aerodynamics*, second ed, McGraw-Hill, New York.

Bansod, P. & Bradshaw, P. (1972), 'The flow in s-shaped ducts.', *Aeronautical Quarterly* **23**, 131–140.

Barbin, A. R. & Jones, J. B. (1963), 'Turbulent flow in the inlet region of a smooth pipe.', *Transactions of the ASME, Journal of Basic Engineering* **85**, 29–34.

Baruah, P. C. (1986), Combustion and cycle calculations in spark ignition engines, *in* J. H. Horlock & D. E. Winterbone, eds, 'The Thermodynamics and Gas Dynamics of Internal Combustion Engines', II, Oxford University Press, Oxford, U.K., chapter 14.

Batchelor, G. K. (1970), *An Introduction to Fluid Dynamics*, Cambridge University Press, Cambridge.

Benedict, R. P. (1980), *Fundamentals of Pipe Flow*, John Wiley & Son.

Booker, D. R. (2000), 'Particulate matter sizing', Presentation at the *IMechE International Conference on Computational and Experimental Methods in Reciprocating Engines*, IMechE Headquarters, London, U.K. 1-2 November.

Bradshaw, P. (1970), *Experimental Fluid Mechanics*, second ed, Pergamon Press.

Bradshaw, P. (1971), *An Introduction to Turbulence and its Measurement*, Pergamon Press.

Bruun, H. H. (1995), *Hot-Wire Anemometry, Principles and Signal Analysis*, Oxford University Press.

Bryer, D. W. & Pankhurst, R. C. (1971), *Pressure-Probe Methods for Determining Wind Speed and Flow Direction*, Her Majesty's Stationary Office, London, U.K.

Buchhave, P., George, W. K. J. & Lumley, J. L. (1979), 'The measurement of turbulence with the laser-Doppler anemometer', *Annual Review of Fluid Mechanics* **11**, 443–503.

Cantwell, B. J. (1981), 'Organised motion in turbulent flow', *Annual Review of Fluid Mechanics* **13**, 457–515.

Casey, M. & Wintergerste, T., eds (2000), *Special Interest Group on "Quality and Trust in Industrial CFD" : Best Practice Guidelines*, 1st ed, European Research Community On Flow, Turbulence And Combustion.

Chen, A., Ganti, G., Lee, K. C. & Yianneskis, M. (1994), A comparison of CFD predictions and LDA measurements of the flow through a generic inlet port., *in* 'European Joint Conference on Engineering Systems Design and Analysis', **64**, ASME, London, pp. 85–93.

Chen, J. L. & Chen, G. (1995), 'Throttle body at engine idle - tolerance effect on flow rate', *Transactions of the SAE*, Paper 951057.

Cohen, M. J. & Ritchie, N. J. B. (1962), 'Low-speed three-dimensional contraction design.', *Journal of the Royal Aeronautical Society* **66**, 231–236.

Cohn, S. D. (1951), 'Performance analysis of butterfly valves.', *Instruments* **24**, 880–884.

Collis, D. C. & Williams, M. J. (1959), 'Two-dimensional convection from heated wires at low Reynolds numbers', *Journal of Fluid Mechanics* **6**, 357–384.

Computational Dynamics Ltd. (2001), *STAR-CD V3.15 Methodology Manual*, London, U.K.

Computational Engineering International Inc. (2000), *Getting Started with Ensight 7.1*, Morrisville, NC, U.S.A.

Comte-Bellot, G. (1976), 'Hot-wire anemometry', *Annual Review of Fluid Mechanics* **8**, 209–231.

Comte-Bellot, G., Strohl, A. & Alcaraz, E. (1971), 'On aerodynamic disturbances caused by single hot-wire probes', *Transactions of the ASME, Journal of Applied Mechanics* **38**, 767–774.

Constantinescu, G., Chapelet, M. & Squires, K. (2003), 'Turbulence modeling applied to flow over a sphere', *AIAA Journal* **41**(9), 1733–1742.

Danbon, F. & Solliec, C. (2000), 'Aerodynamic torque of a butterfly valve - influence of an elbow on the time-mean and instantaneous aerodynamic torque', *Transactions of the ASME, Journal of Fluids Engineering* **122**, 337–344.

Davidson, L. (2001), Hybrid LES-RANS: A combination of a one-equation SGS model and a $k-\omega$ model for predicting recirculating flows, *in* 'ECCOMAS Computational Fluid Dynamics Conference 2001, Swansea, Wales'.

Dhariwal, H. C. (1997), 'Control of blowby emissions and lubricating oil consumption in I.C. engines.', *Energy Conservation Management* **38**(10-13), 1267–1274.

DISA Elekronik A/S (n.d.), *55M System with 55M10 CTA Standard Bridge*, Herlev, Denmark. Date unknown.

Downie, J. H., Jordinson, R. & Barnes, F. H. (1984), 'On the design of three-dimensional wind tunnel contractions.', *Aeronautical Journal* **88**, 287–295.

Drain, L. E., ed. (1980), *The Laser-Doppler Technique*, Wiley.

Durox (1999), 'Flow seeding with an air nebulizer', *Experiments in Fluids* **27**, 408–413.

Ebner, H. W. & Jaschek, A. O. (1998), 'The importance of blow-by measurements, measuring equipment required and implementation', *SAE Special Publications: Technical Paper 981081* **1364**, 61–66.

Eom, K. (1988), 'Performance of butterfly valves as a flow controller', *Transactions of the ASME, Journal of Fluids Engineering* **110**, 16–19.

Ferziger, J. H. & Perić, M. (1999), *Computational Methods for Fluid Dynamics.*, second ed, Springer.

Figliola, R. S. & Beasley, D. E., eds (1995), *Theory and Design for Mechanical Measurements*, second ed, Wiley.

Fisher, E. H. & Rhodes, N. (1996), 'Uncertainty in computational fluid dynamics', *Proceedings of the Institution of Mechanical Engineers, Part C: Journal of Mechanical Engineering Science.* **210**, 91–94.

Fraden, J. (1993), *AIP Handbook of Modern Sensors: Physics Designs and Applications*, American Institute of Physics, New York, U.S.A.

Freitas, C. J. (1995), 'Perspective: Selected benchmarks from commercial CFD codes.', *Transactions of the ASME, Journal of Fluids Engineering* **117**, 208–218.

Gay, B., Spettel, F., Jeandel, D. & Mathieu, J. (1973), 'On the design of the contraction section for a wind tunnel.', *Transactions of the ASME, Journal of Applied Mechanics* **40**, 309–310.

George, P. L. (1991), *Automatic Mesh Generation: Application to Finite Element Methods*, John Wiley & Sons.

Gibbings, J. C. (1964), 'Flow in contracting ducts.', *AIAA Journal* **2**, 191–192.

Gordon, R. & Imbabi, M. S. (1998), 'CFD simulation and experimental validation of a new closed circuit wind/water tunnel design.', *Transactions of the ASME, Journal of Fluids Engineering* **120**, 311–318.

Gosman, A. D. (1998), Quality assurance for industrial CFD codes, *in* '29th American Institute of Aeronautics and Astronautics Conference on Fluid Dynamics, Albuquerque, NM'.

Hamba, F. (2001), 'An attempt to combine large eddy simulation with the k-ϵ model in a channel-flow calculation.', *Theoretical and Computational Fluid Dynamics* **14**, 323–336.

Hayase, T. (1999), 'Monotonic convergence property of turbulent flow solution with central difference and QUICK schemes.', *Transactions of the ASME, Journal of Fluids Engineering* **121**, 351–358.

Heisler, H. (1995), *Advanced Engine Technology*, Edward Arnold, London.

Herbst, H. M. & Priebsch, H. H. (2000), 'Simulation of piston ring dynamics and their effect on oil consumption', *SAE Technical Paper 2000-01-0919.*

Heywood, J. B. (1988), *Internal Combustion Engine Fundamentals*, McGraw-Hill, New-York.

Hirsch, C. (1990), *Numerical Computation of Internal and External Flows*, 2: Computational Methods for Inviscid and Viscous Flows, John Wiley & Son.

Hirt, F., Iten, R. & Ziada, S. (1997), 'Flow-induced oscillations of a butterfly-valve: Prediction of the frequency behaviour', *ASME Aerospace Division (publ) AD, Fluid-Structure Interaction, Aeroelasticity, Flow-Induced Vibration and Noise, Volume II* **'53-2'**, 499–505.

Huang, C. & Kim, R. H. (1996), 'Three-dimensional analysis of partially open butterfly valve flows', *Transactions of the ASME, Journal of Fluids Engineering* **118**, 562–568.

ICEM CFD Engineering (1998), *ICEM-Tetra v3.1 Users Guide*, Berkeley, CA, U.S.A. http://www.icemcfd.com.

Igarashi, T. (1999), 'Flow resistance and Strouhal number of a vortex shedder in a circular pipe', *Japan Society of Mechanical Engineers* **42**(4), 586–595.

ISO (1991), 'Measurement of fluid flow by means of pressure differential devices - part 1: Orifice plates, nozzles and venturi tubes inserted in circular cross-section conduits running full.', *ISO Paper 5167-1.*

Issa, R. I. (1986), 'Solution of implicitly discretised fluid flow equations by operator splitting', *Journal of Computational Physics* **62**, 40–65. This paper is referenced from Versteeg *et al.* (1995).

Jaguar Cars Ltd. (1999), 'Personal communication'.

Jordan, S. A. & Ragab, S. A. (1998), 'A large eddy simulation of the near wake of a circular cylinder.', *Transactions of the ASME, Journal of Fluids Engineering* **120**, 243–252.

Jordinson, R. & Rodger, J. G. (1981), 'On an approximation to the flow through axi-symmetric contracting ducts.', *Aeronautical Quarterly* **32**, 72–81.

Khan, M. K., MacKenzie, K. A. & Bruun, H. H. (1987), 'The effect of blockage correction in hot-wire probe calibration facilities', *J. Phys. E. Sci. Instrum.* **20**, 1031–1035.

Kimura, T., Tanaka, T., Fujimoto, K. & Ogawa, K. (1995), 'Hydrodynamic characteristics of a butterfly valve - prediction of pressure loss characteristics', *ISA Transactions* **34**, 319–326.

King, L. V. (1914), 'On the convection of heat from small cylinders in a stream of fluid: Determination of the convection constants of small platinum wires with applications to hot-wire anemometry', *Phil. Trans. Roy. Soc.* **A214**, 373–432.

Knight, J. J., Lucey, A. D. & Shaw, C. T. (2001), 'On the aerodynamic loading and deformation of convertible car roofs', *SAE Technical Paper 2001-01-1269.*

Koch, F., Hardt, T. & Haubner, F. (2001), 'Oil aeration in combustion engines - analysis and optimization', *SAE Technical Paper 2001-01-1074*.

Kramers, H. (1946), 'Heat transfer from spheres to flowing media', *Physica* **12**, 60–81.

Krause, W., Spies, K. H., Bell, L. E. & Ebert, F. (1995), 'Oil separation in crankcase ventilation - new concepts through system analysis and measurements', *SAE Paper 950939, Transactions of the SAE*.

Lacor, C. & Hirsch, C. (1988), 'Numerical simulation of the three-dimensional flow around a butterfly valve.', *ASME Fluids Engineering Division Publ. FED, volume 69*, Flows in Non-Rotating Turbomachinery Components.

Lange, C. F., Durst, F. & Breuer, M. (1999), 'Correction of hot-wire measurements in the near-wall region', *Experiments in Fluids* **26**, 475–477.

Launder, B. E. & Spalding, D. B. (1974), 'The numerical computation of turbulent flows', *Computer Methods in Applied Mechanics and Engineering* **3**, 269–289.

Lee, D. J., Shaw, C. T. & Pierson, S. (1997*a*), Prediction of flow within inlet plenum systems and comparison with experiment., *in* C. Taylor & J. T. Cross, eds, 'Numerical Methods in Laminar and Turbulent Flow', **10**, Pineridge Press, pp. 915–926.

Lee, D. J., Shaw, C. T. & Pierson, S. (1997*b*), Simulation of Flow within Inlet Plenum Systems., *in* 'Proceedings of 5th International Conference of Associazione Tecnica dell Automobile, The Virtual Automobile and the Role of Experimentation', pp. 275–284.

Libby, P. A. & Reiss, H. R. (1951), 'The design of two-dimensional contraction sections.', *Quarterly of Applied Mathematics* **9**(1), 95–98.

Linford, A. (1961), *Flow Measurement and Meters*, second ed, E. & F. N. Spon Ltd., London, U.K.

Matsumoto, M. (1999), 'Vortex shedding of bluff bodies: A review', *Journal of Fluids and Structures* **13**, 791–811.

Mavriplis, D. J. (1997), 'Unstructured grid techniques.', *Annual Review of Fluid Mechanics* **29**, 473–514.

Meade, M. L. & Dillon, C. R. (1991), *Signals and Systems: Models and Behaviour*, second ed, Chapman and Hall.

Morel, T. (1975), 'Comprehensive design of axisymmetric wind tunnel contractions.', *Transactions of the ASME, Journal of Fluids Engineering* pp. 225–233.

Morel, T. (1976), 'Comprehensive design of axisymmetric wind tunnel contractions - discussion of paper.', *Transactions of the ASME, Journal of Fluids Engineering* pp. 131–133.

Morel, T. (1977), 'Design of two-dimensional wind tunnel contractions.', *Transactions of the ASME, Journal of Fluids Engineering* pp. 371–378.

Morris, M. J. (1987), An investigation of Compressible Flow through Butterfly Valves, Ph.D. Thesis, Department of Mechanical and Industrial Engineering, University of Illinois at Urbana-Champaign, Urbana, Ill, U.S.A.

Morris, M. J. & Dutton, J. C. (1989*a*), 'Aerodynamic torque characteristics of butterfly valves in compressible flow', *Transactions of the ASME, Journal of Fluids Engineering* **111**, 392–399.

Morris, M. J. & Dutton, J. C. (1989*b*), 'Compressible flowfield characteristics of butterfly valves', *Transactions of the ASME, Journal of Fluids Engineering* **111**, 400–407.

Morris, M. J. & Dutton, J. C. (1991), 'An experimental investigation of butterfly valve performance downstream of an elbow', *Transactions of the ASME, Journal of Fluids Engineering* **113**, 81–85.

Namazian, M. & Heywood, J. B. (1982), 'Flow in the piston-cylinder-ring crevices of a spark-ignition engine; effect on hydrocarbon emissions, efficiency and power', *SAE paper 820088, Transactions of the SAE* **91**, 261–288.

National Instruments Corporation. (2000), *Data Acquisition Basics Manual*, Austin, TX, U.S.A.

Nishimura, M. & Kimura, N. (2001), URANS computations for mixing phenomena of an oscillatory non-isothermal triple-jet, *in* 'ECCOMAS Computational Fluid Dynamics Conference 2001, Swansea, Wales'.

Norman, B. (n.d.), 'Hot-wire anemometer calibration at high subsonic speeds', *DISA Info.* pp. 5–19. Date and volume unknown.

Onorati, A., Ferrari, G. & D'errico, G. (2000), The coupling of one-dimensional and two-dimensional fluid dynamic models for the prediction of unsteady flows in IC engine duct-systems., *in* 'IMechE Conference Transactions: International Conference on Computational and Experimental Methods in Reciprocating Engines', IMechE, pp. 17–26.

Patankar, S. V. & Spalding, D. B. (1972), 'A calculation procedure for heat, mass and momentum transfer in three-dimensional parabolic flows.', *International Journal of Heat and Mass Transfer* **15**, 1787–1806.

Perry, A. E. (1982), *Hot-Wire Anemometry*, Oxford University Press.

Perry, A. E. & Morrison, G. L. (1971), 'Vibration of hot-wire anemometer filaments', *Journal of Fluid Mechanics* **50**, 815–825.

Perry, A. E., Smits, A. J. & Chong, M. S. (1979), 'The effects of certain low frequency phenomena on the calibration of hot wires', *Journal of Fluid Mechanics* **90**, 415–431.

Plint, M. A. & Böswirth, L. (1978), *Fluid Mechanics: A Laboratory Course*, Charles Griffin & Company Ltd., London, U.K.

Pope, A. & Goin, K. L. (1965), *High-Speed Wind-Tunnel Testing*, John Wiley & Sons.

Pozrikidis, C. (1997), *Introduction to Theoretical and Computational Fluid Dynamics*, Oxford University Press.

Prandtl, L. & Tietjens, O. G. (1934), *Fundamentals of Hydro- and Aeromechanics*, Dover Publications Inc., New York, U.S.A.

Prasad, A. & Williamson, C. H. K. (1997), 'Three-dimensional effects in turbulent bluff-body wakes.', *Journal of Fluid Mechanics* **343**, 235–265.

Rae, W. H. & Pope, A. (1984), *Low-Speed Wind-Tunnel Testing*, John Wiley & Sons.

Reese, R. J. & Kawahara, W. A. (1993), *Handbook of Structural Testing - Types of Structural Test.*, Fairmount Press.

Roache, P. J. (1997), 'Quantification of uncertainty in computational fluid dynamics', *Annual Review of Fluid Mechanics* **29**, 123–160.

Rockwell, D. (1998), 'Vortex-body interactions', *Annual Review of Fluid Mechanics* **30**, 199–229.

Saffman, P. G. & Baker, G. R. (1979), 'Vortex interactions', *Annual Review of Fluid Mechanics* **11**, 95–122.

Sallet, D. W. (1969), 'On the spacing of Karman vortices.', *Transactions of the ASME, Journal of Applied Mechanics* pp. 370–372.

Satoh, K., Kawai, T., Ishikawa, M. & Matsuoka, T. (2000), 'Development of method for predicting efficiency of oil mist separators', *SAE Technical Paper 2000-01-1234*.

Schäfer, F. & van Basshuysen, R. (1995), *Reduced Emissions and Fuel Consumption in Automobile Engines*, Springer-Verlag/Wien and the Society of Automotive Engineers, New-York.

Shames, I. H. (1992), *Mechanics of Fluids*, third ed, McGraw-Hill, New York.

Shaw, C. T. (1992), *Using Computational Fluid Dynamics*, Prentice Hall.

Shaw, C. T., Lee, D. J., Richardson, S. & Pierson, S. (2000), 'Modelling the effect of plenum-runner interface geometry on the flow through an inlet system.', *SAE paper 2000-01-0569, special publication SP-1511: Modeling of SI Engines.*

Shayler, P. J., Winborn, L. D. & Scarisbrick, A. (2000), 'Fuel transport to the crankcase, oil dilution, and HC return with breather flow during the cold operation of an SI engine.', *SAE Technical Paper 2000-01-1235.*

Siddall, R. G. & Davies, T. W. (1972), 'An improved response equation for hot-wire anemometry', *Int. J. Heat Mass Transfer* **15**, 367–368.

Sohankar, A., Norberg, C. & Davidson, L. (2001), 'Simulation of three-dimensional flow around a square cylinder at moderate Reynolds numbers.', *Physics of Fluids* **11**(2), 288–306.

Solliec, C. & Danbon, F. (1999), 'Aerodynamic torque acting on a butterfly valve. comparison and choice of a torque coefficient.', *Transactions of the ASME, Journal of Fluids Engineering* **121**, 914–917.

Speziale, C. G. (1998), 'Turbulence modeling for time-dependent RANS and VLES: A review', *AIAA Journal* **36**(2), 173–184.

Stratford, B. S. (1959), 'The prediction of separation of the turbulent boundary layer.', *Journal of Fluid Mechanics* **5**, 1–16.

Su, Y.-X. (1991), 'Flow analysis and design of three-dimensional wind tunnel contractions.', *AIAA Journal* **29**(11), 1912–1920.

Tabor, G. (2001), Modelling of complex flows with (V)LES., *in* 'ECCOMAS Computational Fluid Dynamics Conference 2001, Swansea, Wales'.

Tennekes, H. & Lumley, J. L. (1999), *A First Course in Turbulence*, MIT Press.

Tritton, D. J. (1988), *Physical Fluid Dynamics*, 2nd ed, Oxford University Press., Oxford.

TSI Inc. (1997), *Model 1127/1128 Air Velocity Calibrator Instruction Manual*, B ed, St. Paul, MN, U.S.A.

Tucker, P. G. (2000), 'Prediction of turbulent oscillatory flows in complex systems.', *International Journal for Numerical Methods in Fluids* **33**, 869–895.

Tucker, P. G. (2001), *Computation of Unsteady Internal Flows: Fundamentals Methods with Case Studies*, Kluwer Academic Publishers, Dordrecht, The Netherlands.

van Thinh, N. (1969), 'On some measurements made by means of a hot wire in a turbulent flow near a wall', *DISA Info.* **7**, 13–18.

Versteeg, H. K. & Malalasekera, W. (1995), *An Introduction to Computational Fluid Dynamics - The Finite Volume Method*, Longman Scientific and Technical.

Wang, J.-S. & Tullis, J. P. (1974), 'Turbulent flow in the entry region of a rough pipe.', *Transactions of the ASME, Journal of Fluids Engineering* **96**(I), 62–68.

Wang, Z.-X., Tortorelli, D. A. & Dantzig, J. A. (1996), 'Sensitivity analysis and optimisation of coupled thermal and flow problems with applications to contraction design.', *International Journal for Numerical Methods in Fluids* **23**, 991–1020.

Ward-Smith, A. J. (1980), *Internal Fluid Flow, the fluid dynamics of flow in pipes and ducts*, Oxford university Press.

Wentworth, J. T. (1968), 'Piston and ring variables affect exhaust hydrocarbon emissions', *SAE paper 680109,Transactions of the SAE.*

Whitehead, L. G., Wu, L. Y. & Waters, M. H. L. (1951), 'Contracting ducts of finite length.', *Aeronautical Quarterly* **2**, 254–271.

Widell, K. E. (n.d.), 'Stresses and deformations in hot-wire probes', *DISA Info.* pp. 14–17. Date and volume unknown.

Wilcox, D. C. (1994), *Turbulence Modeling for CFD*, DCW Industries Inc., La Canãda, California, U.S.A.

Williamson, C. H. K. (1996), 'Vortex dynamics in the cylinder wake', *Annual Review of Fluid Mechanics* **28**, 477–539.

Yao, Y. F., Savill, A. M., Sandham, N. D. & Dawes, W. N. (2000), Simulation of a turbulent trailing-edge flow using unsteady RANS and DNS, *in* '3rd Symposium on Turbulence, Heat and Mass Transfer', pp. 463–470.

Yeung, W. W. H. & Parkinson, G. V. (1997), 'On the steady separated flow around an inclined flat plate', *Journal of Fluid Mechanics* **333**, 403–413.

Zienkiewicz, O. C. & Taylor, R. L. (1989), *The Finite Element Method*, 1: Basic Formulation and Linear Problems, fourth ed, McGraw-Hill, New York.